CARBON STARS AND SILICON CARBIDE

A Dissertation presented to
the Faculty of the Graduate School
at the University of Missouri

In Partial Fulfillment
of the Requirements for the Degree
Doctor of Philosophy

---

by
ADRIAN CORMAN
Dr. Angela Speck, Dissertation Supervisor
MAY 2010

The undersigned, appointed by the Dean of the Graduate School, have examined the dissertation entitled:

CARBON STARS
AND SILICON CARBIDE

presented by Adrian Corman,
a candidate for the degree of Doctor of Philosophy and hereby certify that, in their opinion, it is worthy of acceptance.

Dr. Angela Speck

Dr. Aigen Li

Dr. Peter Pfeifer

Dr. Gregory Triplett

Dr. Henry White

For my mother and father, who taught me to be true to myself and to follow my dreams,
and who gave me the courage to study the stars.

ACKNOWLEDGMENTS

I would first like to thank my advisor, Dr. Angela Speck, who reminds me of William of Baskerville from *The Name of the Rose* in many ways, but especially when he says ”...during our whole journey I have been teaching you to recognize the evidence through which the world speaks to us like a great book.” She has been a mentor to me in many areas of my life and I feel extremely fortunate to have had her as a supervisor and as a friend. I wouldn’t be where I am today without her kind guidance.

I would like to thank Dr. Karly Pitman, Dr. Anne Hofmeister, and Dr. Kevin Volk, who have all had many illuminating conversations with me and all of whom are researchers who I deeply respect. It has been a great pleasure to work with them during my journey.

The other members of my research group also have my thanks, for keeping me sane during long days in the office and longer trips to conferences. I wish all of them the best of luck in their further endeavors.

I would also like to acknowledge NSF grant number 0607341, which helped to fund much of this research.

TABLE OF CONTENTS

ACKNOWLEDGMENTS . . . . **ii**

LIST OF TABLES . . . . **xi**

LIST OF FIGURES . . . . **xiii**

ABSTRACT . . . . **xviii**

CHAPTER . . . .

1 Introduction **1**

1.1 Beginnings 1

2 Stellar Evolution and AGB Stars **6**

2.1 Introduction 6

2.1.1 Surface temperature and size 7

2.1.2 Distance 8

2.1.3 Size 9

2.1.4 Hertzsprung-Russell diagram 10

2.2 Stellar evolution 11

2.2.1 Birth of stars 11

2.2.1.1 Molecular clouds 11

2.2.1.2 Hydrostatic equilibrium 16

2.2.1.3 Protostars 19

2.2.2 Main sequence 20

2.2.2.1 Proton-proton chain 21

        2.2.2.2 CNO cycle 22
        2.2.2.3 Life on the main sequence 24
    2.2.3 Red giants 24
        2.2.3.1 Below $\sim$2.5M$_\odot$ 26
        2.2.3.2 Degenerate matter 26
        2.2.3.3 Evolution as a red giant 30
        2.2.3.4 Above $\sim$2.5M$_\odot$ 31
    2.2.4 Horizontal branch 31
        2.2.4.1 Triple-alpha process 31
        2.2.4.2 End of the horizontal branch 33
    2.2.5 Asymptotic giant branch 33
        2.2.5.1 Pulsation 35
        2.2.5.2 Chemistry of AGB stars 37
        2.2.5.3 Dust shell formation 39
2.3 Death 41
        2.3.0.4 Degeneracy revisited 41
    2.3.1 Planetary nebulae 41
    2.3.2 White dwarf 42
2.4 Conclusion 43
3 Optical Properties of Solids 44
3.1 Introduction 44
3.2 Classical dispersion analysis 45
    3.2.1 Lorentz model 46
3.3 Light propagation through dust 52

3.3.0.1 Extinction 53
3.3.1 Radiative transfer 56
3.4 Spectral analysis 58
4 Silicon Carbide 61
4.1 Introduction 61
4.2 Physical properties of SiC 62
4.2.1 Crystal structure 62
4.2.2 Optical properties 63
4.3 SiC in astronomical environments 66
4.3.1 Meteoritic evidence 66
5 Observations of Carbon Stars and the Dust Condensation Sequence 69
5.1 Introduction 69
5.1.1 ∼11 μm feature 70
5.1.2 9 μm feature 73
5.1.3 Purpose 74
5.2 Observations 75
5.2.1 Source variability 75
5.3 Method 81
5.4 Results 94
5.4.1 The “9 μm” feature 94
5.4.2 The ∼ 11μm feature 96
5.4.3 The molecular bands 97
5.4.4 The effect of IRC+10°216 102
5.5 Modeling 107

5.6 Discussion . . . 111

5.7 Conclusion . . . 114

6 The Carbon Star V Cyg . . . 116

6.1 Introduction . . . 116

6.1.1 V Cyg . . . 117

6.2 Observations . . . 118

6.2.1 Spatially resolved spectra . . . 119

6.2.1.1 Long-slit spectroscopy . . . 119

6.2.1.2 Data processing . . . 120

6.2.2 Time resolved spectra . . . 121

6.3 Analysis . . . 123

6.3.1 Correlations . . . 127

6.4 Discussion . . . 127

6.5 Summary and conclusions . . . 136

7 Extreme Carbon Stars . . . 137

7.1 Introduction . . . 137

7.1.1 Extreme Carbon Stars . . . 138

7.1.2 SiC absorption features . . . 139

7.1.3 Previous Radiative Transfer Models of Extreme Carbon Stars . 141

7.1.4 Meteoritic evidence for non-SiC grain types . . . 144

7.1.4.1 Presolar “graphite” . . . 144

7.1.4.2 Other presolar carbides . . . 145

7.1.5 Investigation . . . 145

7.2 Observations and Data Processing . . . 146

7.2.1 The “30μm” feature 153

7.3 Radiative Transfer Modeling 153

7.3.1 Radial dust density distribution 154

7.3.2 Modeling grain-size distributions 155

7.3.3 Parameter space investigated 161

7.3.3.1 Degeneracies in radiative transfer modeling 161

7.3.4 Determining the Dust Condensation Temperature 163

7.3.4.1 Theoretical dust condensation models 163

7.3.4.2 P-T space in the condensation zone around extreme carbon stars 166

7.3.4.3 Comparison of P–T space for dust condensation models and sample stars 167

7.3.5 Constraining Dust Composition 168

7.4 Radiative Transfer Modeling Results 169

7.4.1 The effect of grain-size distribution 171

7.4.2 Dust Shell Thicknesses 172

7.4.3 Dust Shell Density Distribution 177

7.4.4 IRAS 17534−3030 178

7.4.5 Impact of the dust condensation temperature 179

7.4.6 Correlations between observed and model parameters 180

7.5 Conclusions 186

8 New Silicon Carbide Optical Constants 188

8.1 Introduction 188

8.1.1 Limitations of previously obtained optical properties of SiC . . . 189

8.1.2 Implications of these limitations on previous research 190

8.2 Experimental methods 191

8.2.1 Sample characteristics 191

8.2.2 Laboratory IR spectroscopic measurements 192

8.2.3 IR Data Analysis 193

8.3 Results 198

8.3.1 Laboratory reflectance spectra 198

8.3.2 Optical constants: $n(\nu)$, $k(\nu)$ 199

8.3.3 Calculated absorbance 202

8.4 Discussion 204

8.4.1 Comparisons to previous works 213

8.4.2 Differences between β- and α-SiC; implications for 2H 216

8.4.3 Recommendations for radiative transfer modelers 217

8.5 Conclusions 219

9 Size and Shape Dependent Optical Properties 222

9.1 Introduction 222

9.1.1 Theoretical background 223

9.1.2 Spherical particles 225

9.1.3 Distributions of non-spherical particles 226

9.1.3.1 Continuous distribution of ellipsoids 228

9.1.3.2 Continuous distribution of spheroids 232

9.1.4 Non-homogeneous particles 233

9.1.4.1 Distribution of hollow spheres 233

9.1.5 Size distributions and cross-sections 235

9.1.5.1 Single grain size 238

9.1.5.2 MRN 238

9.1.5.3 KMH 239

9.2 Implementation 240

9.2.1 Overview of absscat 241

9.2.1.1 Numerical integration 242

9.3 Application to newly derived SiC optical properties 246

9.3.1 Absorption and scattering efficiencies of SiC 247

9.3.1.1 Discussion 254

9.3.2 Radiative transfer modeling using shape and size dependent optical properties of SiC 257

9.3.2.1 Discussion 262

9.4 Summary and Conclusions 263

10 Summary and Future Work 265

10.1 Observations of carbon stars and the dust condensation sequence . . . 265

10.1.1 Future work 266

10.2 Extreme carbon stars 266

10.2.1 Future work 267

10.3 V Cyg 267

10.3.1 Future work 268

10.4 New SiC optical constants 268

10.4.1 Future work 268

10.5 Size and shape dependent optical constants 269

10.5.1 Future work 269

APPENDIX 271

A Source code for absscat 271

A.1 Package edu.missouri.stardust.absscat 271

A.1.1 Main.java 271

A.1.2 FileInput.java 284

A.1.3 Parser.java 289

A.1.4 Interpolator.java 306

A.1.5 Complex.java 317

A.1.6 Calculations.java 326

A.1.7 Integrator.java 343

A.1.8 Function.java 353

A.1.9 IterativeSimpsons 359

A.1.10 FileOutput.java 365

A.1.11 ConsoleOutput.java 371

A.2 Supplementary material and examples 393

A.2.1 Readme file 393

A.2.2 Example configuration files 399

A.2.2.1 Example1.inp 399

A.2.2.2 Example2.inp 400

BIBLIOGRAPHY 402

VITA 418

LIST OF TABLES

Table Page

5.1 Target sources 76
5.2 Underlying continuum temperatures obtained for both *IRAS* and *ISO*, as well as the periods, V_{max}, V_{min}, and variable types of all 26 sources. 86
5.3 Determination coefficient (R-squared) values of silicon carbide and molecular band linear regression correlations of all 26 sources and without IRC+10°216. 93
5.4 Determination coefficient (R-squared) values of linear regression correlations for the "9 μm" for all 26 sources 96
5.5 The parameters and their value ranges for the 1-D radiative transfer modeling 108

6.1 Parameters of the ISO SWS time-resolved spectra and fitted blackbodies 125
6.2 Parameters of the Gemini Michelle sliced spectra and fitted blackbodies 126
6.3 Correlations in the time-resolved spectra of V Cyg 127
6.4 Correlations in the spatially-resolved spectra of V Cyg 131

7.1 Previous models of extreme carbon stars with 11μm absorption features 143
7.2 Target list 147
7.3 Observed parameters of the target sources 152

7.4 Model and derived parameters 170
7.5 Compilation of CO mass-loss rates and expansion velocities, together with distances and luminosities of sample stars 174
7.6 Size and age of the extreme C-star dust shells 174

8.1 Experimental samples used for measuring SiC optical properties 195

9.1 Grain size distribution parameters 247
9.2 The parameter space investigated by radiative transfer models using the generated absorption and scattering efficiencies 257

LIST OF FIGURES

Figure Page

2.1 Stellar parallax 8

2.2 Schematic Hertzsprung-Russell diagram 10

2.3 Barnard 68 12

2.4 Schematic of a main sequence star 21

2.5 Schematic of a red giant 25

2.6 Schematic of a horizontal branch star 32

2.7 Schematic of an asymptotic giant branch star 34

3.1 Light propagating through a slab of dust 52

4.1 Tetrahedral structure of Si and C atoms in SiC 62

4.2 SiC sheet formation 63

4.3 Crystal structure of (2H) α-SiC and β-SiC 64

5.1 *IRAS* LRS and *ISO* SWS spectra of carbon stars together with their fitted underlying continua. 77

5.2 Continuum-divided *IRAS* LRS and *ISO* SWS spectra of carbon stars. 83

5.3 Continuum-subtracted *IRAS* LRS and *ISO* SWS spectra of carbon stars. 88

5.4 "9 μm feature" continuum-divided correlations. 95

5.5 SiC continuum-divided correlations 98

5.6 SiC continuum-subtracted correlations. 101
5.7 Molecular bands in continuum-divided spectra 103
5.8 Radiative transfer model results: T_{cont} vs. peak strength 109
5.9 Radiative transfer model results: composition vs. feature strength . . . 110

6.1 Long slit spectroscopy 120
6.2 Spectra of the dust shell around V Cyg showing the SiC feature at different positions 122
6.3 Spectra of the dust shell around V Cyg showing the SiC feature at different times 123
6.4 The light curve of V Cyg over the period of observation 124
6.5 Correlations in the time-resolved spectra of V Cyg, visual magnitude . 128
6.6 Correlations in the time-resolved spectra of V Cyg, fitted blackbody temperature 129
6.7 Correlations in the time-resolved spectra of V Cyg, peak to continuum ratio. 130
6.8 Correlations in the time-resolved spectra of V Cyg, peak position . . . 130
6.9 Correlations in the time-resolved spectra of V Cyg, FWHM 131
6.10 Correlations in the spatially-resolved spectra of V Cyg, fitted blackbody temperature 132
6.11 Correlations in the spatially-resolved spectra of V Cyg, peak to continuum ratio 133
6.12 Correlations in the spatially-resolved spectra of V Cyg, peak position . 133
6.13 Correlations in the spatially-resolved spectra of V Cyg, FWHM 134
6.14 A schematic diagram illustrating the slices over the dust shell and finer structure 135

7.1 Regions in the IRAS color-color diagram populated by extreme carbon stars 139

7.2 *ISO* SWS spectra of ten extreme C-stars. 148

7.3 *ISO* SWS spectra of sample extreme C-stars together with *IRAS* 12, 25, 60 and 100μm photometry points and *IRAS* LRS spectra. 149

7.4 *ISO* SWS spectra of sample extreme C-stars together with *IRAS* 12, 25, 60 and 100μm photometry points and *IRAS* LRS spectra (part 2). . 150

7.5 *ISO* SWS spectra of sample extreme C-stars together with *IRAS* 12, 25, 60 and 100μm photometry points and *IRAS* LRS spectra (part 3). . 151

7.6 The effect of grain-size distributions on the model spectral energy distribution 159

7.7 Pressure-Temperature space for the dust condensation region around extreme carbon stars 165

7.8 Extreme C-star best fit models (Part 1) 171

7.9 Extreme C-star best fit models (Part 2) 172

7.10 Extreme C-star best fit models (Part 3) 173

7.11 Degeneracy in the best fit models for IRAS 23166+1655 175

7.12 Correlations between the best-fit blackbody temperature and the modeled optical depth, the 11.3μm feature-to-continuum ratio, and the SiC feature position 182

7.13 Correlations between the modeled optical depth, the modeled %age SiC, and the calculated superwind timescale 183

8.1 Mid- and mid+far-IR laboratory specular reflectance as a function of wavenumber (wavelength) for $\vec{E}\|\vec{c}$ faces of α-SiC 196

8.2 Mid- and mid+far-IR laboratory specular reflectance for $\vec{E}\perp\vec{c}$ faces of β-SiC (dashed line), and two α-SiC samples 197
8.3 Reflectivity at near-normal incidence of 6H gray α-SiC ($\vec{E}\|\vec{c}$ orientation) and derived functions from classical dispersion analysis. 205
8.4 Reflectivity at near-normal incidence of 6H gray α-SiC ($\vec{E}\perp\vec{c}$ orientation) and derived n and k. 206
8.5 Reflectivity at near-normal incidence of moissanite (α-SiC, $\vec{E}\|\vec{c}$ orientation) and derived n and k fitted by 1 oscillator (ν = 802.0 cm^{-1}, FWHM = 4.0 cm^{-1}, f = 3.4). 207
8.6 Reflectivity at near-normal incidence of moissanite (α-SiC, $\vec{E}\perp\vec{c}$ orientation) and derived n and k. 208
8.7 Reflectivity at near-normal incidence of β-SiC and derived n, k. 209
8.8 Laboratory thin film absorbances divided by estimated sample thicknesses compared to calculated classical dispersion analysis absorbance coefficients for α-SiC 210
8.9 Laboratory thin film absorbances divided by estimated sample thicknesses, compared to calculated classical dispersion analysis absorbance coefficients for a 1 oscillator fit to β-SiC 211
8.10 Comparison of n and k values calculated via classical dispersion for single and multiple oscillator fits 212

9.1 Smooth particle shapes 224
9.2 Absorption and scattering efficiencies of α-SiC compared to Pegourie SiC, 0.1 μm single size grains. 248
9.3 Absorption and scattering efficiencies of α-SiC compared to Pegourie SiC, MRN grain size distribution. 249

9.4 Absorption and scattering efficiencies of α-SiC compared to Pegourie SiC, KMH grain size distribution. 250

9.5 Absorption and scattering efficiencies of β-SiC compared to Pegourie SiC, 0.1 μm single size grains. 251

9.6 Absorption and scattering efficiencies of β-SiC compared to Pegourie SiC, MRN grain size distribution. 252

9.7 Absorption and scattering efficiencies of β-SiC compared to Pegourie SiC, KMH grain size distribution. 253

9.8 Comparison of the absorption efficiencies of the parallel and perpendicular orientations of α-SiC 256

9.9 Synthetic spectra generated using new α-SiC vs. Pégourié SiC, spherical and CDE grain shapes 258

9.10 Synthetic spectra generated using new α-SiC vs. Pégourié SiC, CDS and DHS grain shapes 259

9.11 Synthetic spectra generated using new β-SiC vs. Pégourié SiC, spherical and CDE grain shapes 260

9.12 Synthetic spectra generated using new β-SiC vs. Pégourié SiC, CDS and DHS grain shapes 261

CARBON STARS
AND SILICON CARBIDE

Adrian Corman

Dr. Angela Speck, Dissertation Supervisor

ABSTRACT

Stars between about 0.8 and 8 times the mass of the Sun will eventually evolve become asymptotic giant branch (AGB) stars, where they pulsate and throw off mass from their atmospheres, forming dust shells in the space around them. AGB stars between about 2 to 4 solar masses can develop atmospheres that have an overabundance of carbon relative to oxygen (thus becoming carbon stars), which results in their dust shells containing mineral species dominated by carbonaceous compounds. One of these, silicon carbide (SiC) has been extensively investigated in an attempt to discover the conditions present in these dust shells. In this work, we investigate the nature and uses of SiC for astronomical research, and in particular what SiC can tell us about the dust shells around carbon stars. We investigate the SiC feature found in a collection of carbon stars, and then do the same for an additional set of 'extreme' carbon stars which are very close to the end of their lives. We investigate a single carbon star, V Cyg, in more detail, looking at the changes in the dust shell as functions of both position and time. We then examine existing optical constants for SiC, and obtain a new set of optical properties that eliminates limitations in the older data. Finally, we use small-particle absorption and scattering theory to produce a program which allows us to apply commonly used shape and size parameters to these new optical properties for use in radiative transfer modeling.

Chapter 1

Introduction

"I was trying to tell you that the search for explicative laws in natural facts proceeds in a tortuous fashion. In the face of some inexplicable facts you must try to imagine many general laws, whose connection with your facts escapes you. Then, suddenly in the unexpected connection of a result, a specific situation, and one of those laws, you perceive a line of reasoning that seems more convincing than others. You try applying it to all similar cases, to use it for making predictions, and you discover that your intuition was right. But until you reach the end you will never know which predicates to introduce into your reasoning and which to omit. And this is what I am trying to do now." - Umberto Eco

1.1 Beginnings

With the exception of hydrogen, helium, and a tiny amount of lithium created during the Big Bang, all the elements in the Universe come from nucleosynthesis inside stars. At the end of their lives these elements are ejected; either slowly and gently in the case of low to intermediate mass stars, or violently in the case of high mass stars. Elements from both kinds of stars become part of the interstellar medium in the form of dust and gas and eventually can form new stars and planets. The primary purpose of this work is to investigate the nature and evolution of SiC dust grains, in order to understand dust formation processes which pertain to many astrophysical environments.

With the emergence of IR astronomy in the late sixties, the importance of dust particles in the Universe began to be revealed. Dust is a vital ingredient in many astrophysical environments, because it plays an essential role in star formation processes, and contributes to several aspects of interstellar processes such as gas heating and the formation of molecules. In addition, since mass loss from evolved stars is driven by radiation pressure on dust grains, it is intimately linked to the precise nature of the circumstellar dust. Dust needs to be well understood in its own right, if we are to understand how it contributes to many aspects of astrophysics.

The major factors in determining the mineralogy (chemical composition and crystal structure), size and shape of dust grains are the temperature, chemistry and density of the gas from which it forms. The chemistry determines the type of atoms available to form the dust particles, whereas the density determines how likely these atoms are to come into contact and make dust particles, and the temperature determines which solid-state species are stable enough to form. The chemistry, density and temperature of a dust-forming circumstellar shell are in turn determined by the nature of the central star, including its metallicity and its initial mass, and by the evolution of the star. An evolution in the nature of the dust produced may, in turn, influence the stellar evolution, indicating a feedback relationship between the changes in the star and dust formation in its circumstellar envelope. The evolution of these stars cannot be fully understood until we determine the precise nature of their circumstellar dust.

The mineralogy of dust grains in space is typically studied by means of IR spectroscopy. The IR wavelength regime is particularly suited to determining mineral compositions because the dust in a circumstellar envelope absorbs the mostly optical light from the central star and re-radiates it at IR wavelengths. Dust particles of a given size, shape, temperature, structure and composition, have their own characteristic IR spectrum. We can thus use the IR spectra of candidate dust species studied in the laboratory to identify IR spectral features observed in astronomical environments.

Astromineralogy has undergone a surge in popularity in recent years mostly as a result of superior spectroscopic observations from the Infrared Space Observatory, (*ISO*; Kessler et al., 1996) and *SST* (for astromineralogy reviews, see Speck et al., 1997; Speck, 1998; Speck et al., 2000; Molster, 2000; Henning, 2003; Kwok, 2004, and references therein). However, most of these studies have concentrated on the mineralogy of O-rich stars. Carbon stars have been largely neglected. Furthermore, these studies have been limited by the paucity of available laboratory spectra and optical constants. Moreover, many of these studies have yielded differing results, and methods must be sought to differentiate between proposed mineral carriers of the various features (such as spatially resolved spectroscopy). There are other constraints or lines of evidence that can be used to aid our studies of dust in space, including spatial distributions of materials, theoretical models for dust formation and evidence from meteoritic studies of presolar grains.

In this work, we are concerned with low to intermediate mass stars (LIMS), which start their lives with masses between approximately 0.8 and 8 solar masses (a solar mass is denoted by $M_{\odot}$). About 95% of all stars are LIMS (Kwok, 2004). In particular we will study LIMS late in their lives, when they lose large amounts of mass and form circumstellar shells of dust and gas. This is called the Asymptotic Giant Branch or AGB phase of the star's evolution.

Stars evolve chemically during the AGB phase, and this strongly influences the type of dust produced. The most important parameter which determines the dust composition is the carbon-to-oxygen ratio in the star's atmosphere. LIMS stars start out with oxygen-rich atmospheres, but the star's core produces carbon which can be dredged to the surface by powerful convection currents. For stars between about 2 to 4 $M_\odot$, enough carbon can be mixed into the star's atmosphere by this process to make the carbon-to-oxygen ratio greater than one, and we refer to such stars as *carbon stars*; these stars make up about 1/3 of all AGB stars, though the exact proportion depends on the metallicity[1] (Matsuura et al., 2005).

The carbon-to-oxygen ratio strongly affects the chemistry in the dust shell because one of the first things that forms out of the outflowing gas is the extremely stable carbon monoxide (CO) molecule. The formation of CO will consume most of the carbon and oxygen in the gas, and the less abundant element will be almost entirely bound up by this process, making it unavailable for later chemistry.

For a carbon star, the primary solid-state constituent of the dust shell is carbon, though the exact crystal structure of the carbon (or if it is in fact amorphous) is still uncertain. The second most common constituent, silicon carbide (SiC), has been detected in the spectra of many carbon stars (e.g. Hackwell, 1972; Treffers & Cohen, 1974), and is useful because it displays a characteristic spectral peak at about 11μm, unlike the carbon which has no diagnostic spectral feature in the infrared (IR).

In this work, we will investigate astronomical SiC and what it can tell us about the dust shells that form around carbon stars. We will begin by examining the evolution of LIMS stars, and then turn our attention to the properties of SiC. This will lead us to an investigation of the SiC feature found in a collection of carbon stars, and then we will do the same for an additional set of 'extreme' carbon stars which are very close to the end of their lives. We will investigate a single carbon star, V Cyg, in more detail, looking at the changes in the dust shell as functions of both position and time. We then examine existing optical constants for SiC, and obtain a new set of optical properties that eliminates limitations in the older data. Finally, we use

---

[1] In astronomy, all elements with atomic number greater than 2 are called metals. The metallicity is a measure of the amount of these elements present in a star.

small-particle absorption and scattering theory to produce a program which allows us to apply commonly used shape and size parameters to these new optical properties for use in radiative transfer modeling.

Chapter 2

Stellar Evolution and AGB Stars

"Looking at these stars suddenly dwarfed my own troubles and all the gravities of terrestrial life. I thought of their unfathomable distance, and the slow inevitable drift of their movements out of the unknown past into the unknown future." - H.G. Wells

2.1 Introduction

Before going into the details of how stars are formed, live their lives, and eventually die, it would be wise for us to first take a few moments to consider how we know what we do about them.

With the exception of our own sun, the only direct information we have about stars comes from the light we receive from them and their surroundings. Even before applying any advanced techniques to analyze the light from a star, two properties of it are immediately apparent; how bright the light is, and its color.

2.1.1 Surface temperature and size

Since stars are reasonable approximations to blackbodies, we can relate the star's color with its surface temperature by Wien's Law,

$$\lambda_{peak} T = 2.898 \cdot 10^{-3}\,\mathrm{m} \cdot \mathrm{K} \tag{2.1}$$

Now that we have the temperature in addition to the brightness, we will be tempted to use the Stefan-Boltzmann equation

$$L = A\sigma T^4 \tag{2.2}$$

where L, the luminosity, is the total power output of the emitting object, A is the surface area of the emitting object, σ is the Stefan-Boltzmann constant ($\sigma \approx 5.67 \cdot 10^{-8}\,\mathrm{W} \cdot \mathrm{m}^{-2} \cdot \mathrm{K}^{-4}$), and T is the surface temperature of the object. However, we must be cautious here, because the brightness we observe when we look at a star in the sky differs from the star's true luminosity not only because we only see visible wavelengths and the star gives off radiation at all wavelengths, but also because the brightness we see falls off as a function of distance according to the inverse square law

$$F = \frac{L}{2\pi r^2} \tag{2.3}$$

where F is the flux we observe, and r is the distance between us and the star. Additionally, we would have to take account of the absorption of light by our own atmosphere and the interstellar medium between us and the star, but for this discussion we will ignore these factors (and from this point onwards the flux and luminosity will always refer to the flux or luminosity over all wavelengths).

2.1.2 Distance

To obtain the luminosity of a star, we must to find a way to determine its distance from us. In general, this is very difficult (and consequently distances are not known accurately for many stars), but one technique that can be used for relatively nearby stars (within about $3.084{\cdot}10^{19}$m; see below) is a measurement of the stellar parallax, which is shown in figure 2.1.

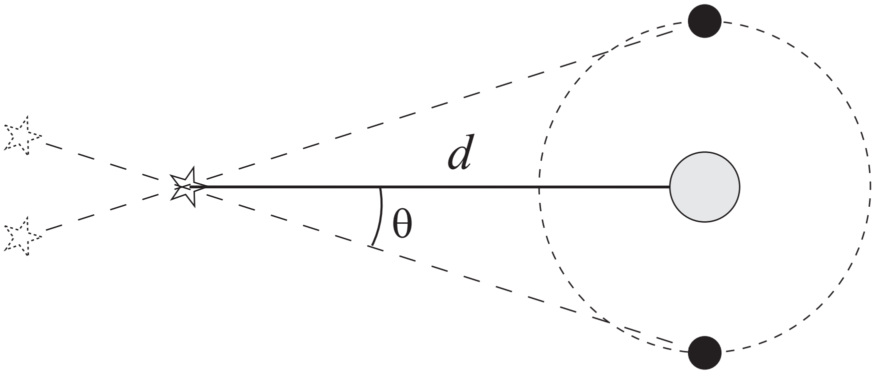

Figure 2.1: Stellar parallax. The large gray sphere is the Sun, the small black sphere is the Earth, and the dashed circle represents the Earth's orbit; d is the average distance between the Earth and the star being observed, and θ is the parallax angle.

If we imagine an observer on the Earth looking at a nearby star, the apparent position of that star in the sky will change (relative to much more distant stars) as the Earth moves in its orbit around the Sun; if we take measurements of the apparent position of the star at 6 month intervals as shown in figure 2.1, then the apparent change in position of the star between those two measurements will be at its maximum. Using trigonometry, we can relate this apparent positional change and the distance to the star by

$$d = \frac{r_{a.u.}}{\sin\theta} \tag{2.4}$$

where $r_{a.u.}$ is the average distance between the Earth and the Sun ($\sim 149.6{\cdot}10^9$m).

Because θ is extremely tiny for any object outside our solar system (the closest star to our solar system has $\theta < 1$ arcsecond; Carroll & Ostlie, 1996) we can make use of the small angle approximation $\sin\theta \approx \theta$ to obtain

$$d = \frac{r_{a.u.}}{\theta} \tag{2.5}$$

Since $r_{a.u.}$ is well known, this lets us determine the distance to objects to within our ability to measure θ; the distance given by θ of one arcsecond is referred to as a parsec (denoted by pc; about $3.09 \cdot 10^{16}$m or 3.26 light-years). Unfortunately, the best measurements of θ carried out so far (by the Hipparcos satellite) have only achieved an astrometric accuracy of about 0.001 arcseconds, so the furthest distance that could be determined by this method was 1000 pc, which is about 5% of the diameter of our galaxy (Carroll & Ostlie, 1996). Measurements beyond this distance involve the use of more complicated, indirect techniques that are beyond the scope of this discussion.

2.1.3 Size

Returning to our star, if we assume that its distance is known and that stars closely approximate spheres, we can return to equation (2.2) and obtain

$$\begin{aligned} L &= A\sigma T_{\text{eff}}^4 \\ &= 4\pi r^2 \sigma T_{\text{eff}}^4 \Longrightarrow r = \left(\frac{L}{4\pi\sigma T_{\text{eff}}^4}\right)^{\frac{1}{2}} \end{aligned} \tag{2.6}$$

where r is the radius of the star and T_{eff} is the effective surface temperature (T_{eff} is the temperature at which a perfect blackbody would emit the same total amount of electromagnetic energy as the star). Thus, we now know the star's size as well.

2.1.4 Hertzsprung-Russell diagram

Now that we have these relationships, our next step is to plot these values for many stars in a useful way and see what conclusions we can draw from it. If we make a plot of T_{eff} (increasing to the left) vs. $\log(L)$ (conventionally given relative to the luminosity of the Sun, denoted by $L_{\odot}$), we obtain what is called a Hertzsprung-Russell or H-R diagram, a schematic example of which is shown in figure 2.2.

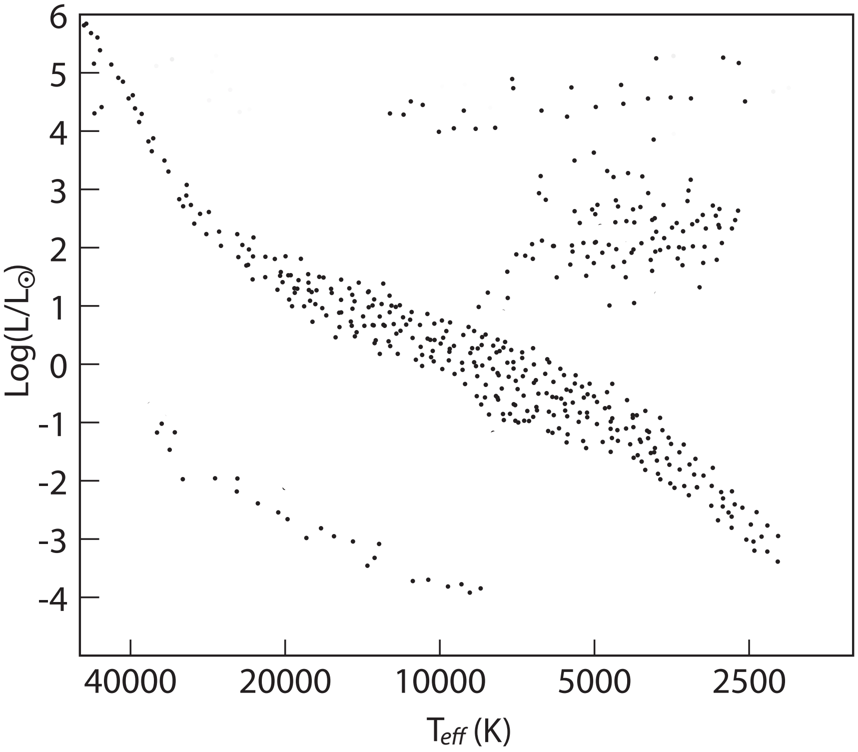

Figure 2.2: A schematic Hertzsprung-Russell diagram.

It is clear that stars tend to group in certain regions of this diagram; as we will see as we begin to explore the life cycle of stars, these regions correspond to different periods of a star's life. Though not explicitly marked on figure 2.2, from equation (2.6) we can also easily obtain size information from inspection of a H-R diagram. For example, the stars grouped to the lower left of the diagram are very hot, but have low luminosity; thus, we can deduce that they are small compared to other stars on the diagram. By the same logic, the stars in the upper right of the diagram are relatively cool but very luminous, thus they must be large.

2.2 Stellar evolution

A star's mass almost entirely determines how that star will live out its life (primarily because the mass determines what fusion reactions can occur in the core, and how fast those reactions run). For this reason, it is convenient to treat the evolution of low-to-intermediate mass stars (stars between 0.8 $M_\odot$ and 8 $M_\odot$) separately from the evolution of high mass stars (stars above about 8 $M_\odot$). The difference in evolution, however, mostly occurs near the end of a star's life; as will be discussed below in section 2.3.0.4, this is because the core of a star near the end of its life is composed of degenerate matter, and only star of high enough mass can overcome the degeneracy. The earlier part of a star's life is much the same for both low and high mass stars.

2.2.1 Birth of stars

2.2.1.1 Molecular clouds

Though we normally think of the vast spaces between the stars as only containing vacuum, it is actually filled with an extremely tenuous gas and dust called the interstellar medium. This material both originates from stars (apart from that left over from the big bang) and forms new stars, in a cycle of creation and destruction that has been occurring for billions of years.

In some regions of space, this gas and dust can become dense enough to become optically thick at visible wavelengths (that is, most or all of the visible emission we see from that region comes from the gas and dust, not objects located behind; the concept of optical depth will be discussed in more detail in chapter 3). Though there are different kinds of these optically thick clouds in space, when considering star formation we are interested in what are called molecular clouds, so named because they are optically thick enough for H_2 to form and survive (outside the cloud, ultraviolet radiation tends to dissociate H_2; see Carroll & Ostlie, 1996). An example of a small, dense molecular cloud (also called a Bok globule) can be seen in figure 2.3.

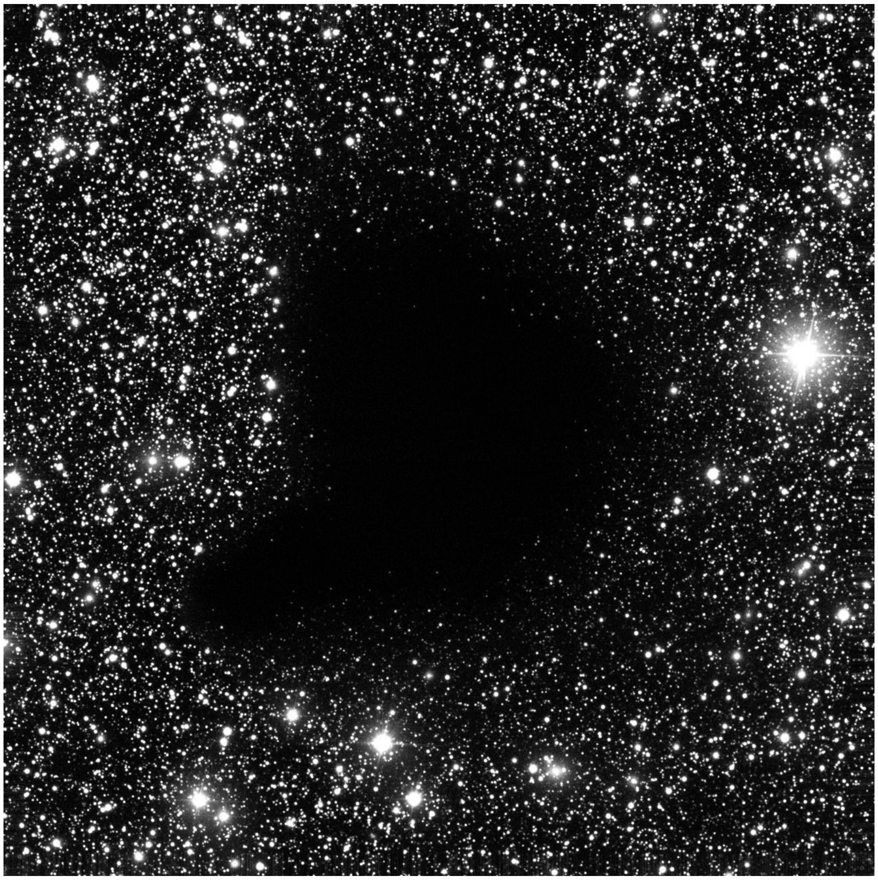

Figure 2.3: Barnard 68, a molecular cloud of gas and dust optically thick enough to block the light from stars behind it. Sometime in the future this cloud will likely form several low mass stars. Image courtesy of the European Southern Observatory.

Because such a cloud is only held together by gravity, if it is in equilibrium (i.e. neither expanding nor contracting) it satisfies the virial theorem (the following discussion is based on the discussion in Carroll & Ostlie, 1996)

$$2K + U = 0 \tag{2.7}$$

where K is the internal kinetic energy of the cloud and U is the gravitational potential energy of the cloud. If $2K$ is larger than U, the cloud will expand; if it is smaller, then the cloud will collapse. Therefore, we want to examine the boundary condition given by equation (2.7) in more detail. If we assume a spherical cloud of uniform density (for ease of analysis) the gravitational potential energy is approximately given by (Carroll & Ostlie, 1996)

$$U \sim -\frac{3GM_{\mathrm{C}}^2}{5R_{\mathrm{C}}} \tag{2.8}$$

where R_{C} is the radius of the cloud, M_{C} is the mass of the cloud, and G is the gravitational constant. If we assume that the cloud is an ideal gas (a reasonable approximation considering the large particle separation), we can apply the equipartition theorem to obtain the kinetic energy of the cloud

$$K = \frac{3}{2}NkT \tag{2.9}$$

where N is the total number of particles in the cloud, T is the temperature of the cloud, and k is Boltzmann's constant. We can rewrite N as

$$N = \frac{M_{\mathrm{C}}}{\mu m_{\mathrm{H}}} \tag{2.10}$$

where μ is the mean molecular weight of the cloud relative to hydrogen, and m_{H} is the mass of a hydrogen atom (we use this definition for convenience because any such cloud will be mostly composed of hydrogen). Therefore, we can rewrite equation (2.7) as

$$\frac{3M_{\mathrm{C}}k\mathrm{T}}{\mu m_{\mathrm{H}}} + -\frac{3GM_{\mathrm{C}}^2}{5R_{\mathrm{C}}} = 0 \implies \frac{k\mathrm{T}}{\mu m_{\mathrm{H}}} = \frac{GM_{\mathrm{C}}^2}{5R_{\mathrm{C}}} \tag{2.11}$$

The equality in equation (2.11) holds when the cloud is in equilibrium; for it to collapse, we must replace it by an inequality (the potential energy must be greater than the kinetic energy), giving us

$$\frac{k\mathrm{T}}{\mu m_{\mathrm{H}}} < \frac{GM_{\mathrm{C}}^2}{5R_{\mathrm{C}}} \tag{2.12}$$

Because we assumed a constant initial density (which we shall denote by ρ_0), we can rewrite R_{C} as

$$\begin{aligned} \text{Volume} &= \frac{M_{\mathrm{C}}}{\rho_0} \\ \frac{4}{3}\pi R_{\mathrm{C}}^3 &= \frac{M_{\mathrm{C}}}{\rho_0} \implies R_{\mathrm{C}} = \Big(\frac{3M_{\mathrm{C}}}{4\pi\rho_0}\Big)^{\frac{1}{3}} \end{aligned} \tag{2.13}$$

which allows us to express equation (2.11) entirely in terms of mass. Substituting, we obtain

$$\begin{aligned} \frac{k\mathrm{T}}{\mu m_{\mathrm{H}}} &< \frac{GM_{\mathrm{C}}^2}{5(\frac{3M_{\mathrm{C}}}{4\pi\rho_0})^{\frac{1}{3}}} \\ M_{\mathrm{C}}^{\frac{2}{3}} &> \frac{5k\mathrm{T}}{\mu m_{\mathrm{H}} G} \cdot \Big(\frac{3}{4\pi\rho_0}\Big)^{\frac{1}{3}} \\ M_{\mathrm{C}} &> \Big(\frac{5kT}{\mu m_{\mathrm{H}} G}\Big)^{\frac{3}{2}} \cdot \Big(\frac{3}{4\pi\rho_0}\Big)^{\frac{1}{2}} \end{aligned} \tag{2.14}$$

If a cloud has a mass fulfilling the inequality in equation (2.14), it will collapse in on itself (the critical value where both sides of equation (2.14) are equal is known as the Jeans mass). This can happen in several ways; one is for the cloud to have a shock strike it, increasing the density (this can be the result of nearby star formation or from the extremely violent death of a nearby massive star). Examining equation (2.14), we can see that if the ρ_0 density term on the right side of the inequality is increased, the required mass for collapse decreases; thus, any increase in density will make a cloud in equilibrium collapse.

We can obtain another important result by considering what happens to the cloud as it collapses if there are any local regions of higher density, even if only by a small amount (small enough to not invalidate our approximation of constant density). As the cloud collapses, these regions will become more dense along with the rest of the cloud (the same number of particles are in a smaller space); as a result, these regions can themselves fulfill the inequality in equation (2.14), causing them to locally collapse independently of the rest of the cloud. This will cause the cloud to fragment into smaller collapsing regions (which themselves can fragment if large enough); this helps to explain why stars tend to be found in groups of similar chemical composition called clusters. In addition, at least half of all stars are gravitationally bound to one or more additional stars (a system of two such stars is called a binary system, for example), and this can also be explained by the fragmentation of the initial molecular cloud (Carroll & Ostlie, 1996).

Though the preceding discussion incorporated several important assumptions (the cloud is perfectly spherical, motionless, of uniform composition and density) that are not accurate representations of the situation actually present in molecular clouds. However, it serves to give a qualitative understanding of the process involved in collapse.

2.2.1.2 Hydrostatic equilibrium

Before we continue further, we need to develop a concept that we will return to several times in this discussion, that of hydrostatic equilibrium. This occurs when the energy generated in the core of a star produces a pressure gradient which exactly balances the force of gravity pulling the star's matter inwards. If we imagine an infinitesimal cylinder of the star's matter with mass dm, height dr, and base of area A, located at distance r from the star's center, we can use Newton's Second Law to write the net force on the cylinder as (this discussion follows Carroll & Ostlie, 1996)

$$\mathrm{d}m\frac{\mathrm{d}^2 r}{\mathrm{d}t^2} = F_{\mathrm{gravity}} + F_{\mathrm{top}} + F_{\mathrm{bottom}} \tag{2.15}$$

where F_{gravity} is the gravitational force on the cylinder, F_{top} is the force of pressure on the top of the cylinder, and F_{bottom} is the force of pressure on the bottom of the cylinder. The pressure on the top and bottom of the cylinder are of opposite sign, and differ by a term $\mathrm{d}F_{\mathrm{pressure}}$ which represents the change in the force of pressure over the distance $\mathrm{d}r$. Thus, we can write

$$F_{\mathrm{top}} = -(F_{\mathrm{bottom}} + \mathrm{d}F_{\mathrm{pressure}}) \tag{2.16}$$

Substituting this into equation (2.15), we obtain

$$\begin{aligned}\mathrm{d}m\frac{\mathrm{d}^2 r}{\mathrm{d}t^2} &= F_{\mathrm{gravity}} - (F_{\mathrm{bottom}} + \mathrm{d}F_{\mathrm{pressure}}) + F_{\mathrm{bottom}} \\ \mathrm{d}m\frac{\mathrm{d}^2 r}{\mathrm{d}t^2} &= F_{\mathrm{gravity}} - \mathrm{d}F_{\mathrm{pressure}} \qquad (2.17)\end{aligned}$$

The gravitational force on the cylinder is given by

$$F_{\text{gravity}} = -G\frac{M_{\text{inside}}\,\mathrm{d}m}{r^2} \tag{2.18}$$

where G is the gravitational constant, and M_{inside} is the mass of the star inside radius r. To obtain the force due to the pressure, we observe that by definition

$$P = \frac{F_{\text{pressure}}}{A} \tag{2.19}$$

where P is the pressure. Because the area A of the cylinder does not change with r, we can write the differential pressure as

$$\mathrm{d}P = \frac{\mathrm{d}F_{\text{pressure}}}{A} \longrightarrow \mathrm{d}F_{\text{pressure}} = A\,\mathrm{d}P \tag{2.20}$$

Substuting these expressions into equation (2.17), we can see that

$$\mathrm{d}m\frac{\mathrm{d}^2r}{\mathrm{d}t^2} = -G\frac{M_{\text{inside}}\,\mathrm{d}m}{r^2} - A\,\mathrm{d}P \tag{2.21}$$

The expression for $\mathrm{d}m$ can be easily obtained by observing that the mass in the cylinder is simply the volume of the cylinder times the density of the material in the cylinder (which in this approximation is assumed to be constant), simply giving

$$\mathrm{d}m = \rho A\,\mathrm{d}r \tag{2.22}$$

Substituting this into equation (2.21) gives us

$$\begin{aligned} \rho A\,\mathrm{d}r\frac{\mathrm{d}^2r}{\mathrm{d}t^2} &= -G\frac{M_{\text{inside}}\,\rho A\,\mathrm{d}r}{r^2} - A\,\mathrm{d}P \\ \rho\frac{\mathrm{d}^2r}{\mathrm{d}t^2} &= -G\frac{M_{\text{inside}}\,\rho}{r^2} - \frac{\mathrm{d}P}{\mathrm{d}r} \qquad (2.23) \end{aligned}$$

This is the equation of motion for the cylinder in the radial direction. Because we are examining the situation of hydrostatic equilibrium where the star is neither expanding nor contracting, the cylinder is motionless and the $\frac{\mathrm{d}^2 r}{\mathrm{d}t^2}$ is therefore zero. Thus, for hydrostatic equilibrium,

$$\frac{\mathrm{d}P}{\mathrm{d}r} = -G\frac{M_{\mathrm{inside}}\ \rho}{r^2} \tag{2.24}$$

For a star to maintain the same radius, a pressure gradient given by equation (2.24) must exist. This pressure gradient is a result of the temperature gradient that exists due to energy coming from the star's core. If we assume the star is an ideal gas (which as we will see below can be inappropriate in the case of the star's core, but is valid for most of the star's atmosphere - and in any event, the general concept holds true for the entire star), then the gas pressure generated by the temperature (i.e. kinetic energy) of atoms in the star can be written as

$$P_{\mathrm{gas}} = \frac{NkT}{V} \tag{2.25}$$

where k is Boltzmann's constant, and N is the number of particles in volume V, at temperature T. Substituting equation (2.10), we can rewrite this as

$$P_{\mathrm{gas}} = \frac{M_{\mathrm{V}}kT}{\mu m_{\mathrm{H}}V} \tag{2.26}$$

where M_{V} is the mass contained in V. Under the assumption that the density in V is constant, this becomes

$$P_{\mathrm{gas}} = \frac{\rho kT}{\mu m_{\mathrm{H}}} \tag{2.27}$$

This gas pressure is not, however, the only pressure present as a result of the temperature. Such a large number of photons are present in a star that the radiation pressure due to the photon gas cannot always be neglected. It can be shown that the pressure generated by a photon gas of temperature T is given by (see, for example, Huang, 1987)

$$P_{\text{photons}} = \frac{\pi^2 k^4}{60\hbar^2 c^3} T^4 \tag{2.28}$$

resulting in a total pressure of

$$P_{\text{total}} = \frac{\rho k}{\mu m_{\text{H}}} T + \frac{\pi^2 k^4}{60\hbar^2 c^3} T^4 \tag{2.29}$$

Converting this equation from an equation involving T to one involving r is complicated by the fact that convection can play an important role in the interiors of some stars, making a solution extremely difficult. However, for our purposes, it is enough to have investigated the general concepts of hydrostatic equilibrium; whenever the energy generated by the star (and therefore the temperature/pressure gradient) is enough to overcome the gravitational force, the star will expand until the equilibrium is once again reached. Whenever the energy generated is not enough to overcome gravity, the star will contract until the energy output is again large enough to balance equation (2.24).

2.2.1.3 Protostars

As the material in a cloud (cloud will now refer to the collapse of a region that will form a single star; this could be one of the fragments mentioned above), collapses inwards, the material begins to rise in temperature as well as density, particularly in the center. Additionally, as the cloud collapses, it will start to spin increasingly fast. This is due to conservation of angular momentum; since it is to be expected that the progenitor cloud would have *some* angular momentum (even if only a small amount), the cloud must spin faster as its radius decreases to maintain the same momentum. Another result of this is that the cloud will become increasingly disk shaped, aligned with the rotational plane of the cloud. As the system evolves, some of the material in the disk will fall into the star, some will accrete together, forming planets and other objects that remain in orbit around the star, and most of the rest is dispersed into space by a stellar wind of very rapidly moving charged particles streaming out from the star's surface.

The center of the star forming in the cloud eventually becomes dense and hot enough for hydrogen to begin fusing into helium (described below); this causes the core to heat up even more, halting the collapse of the core and the star around it as it begins to reach a state of hydrostatic equilibrium. When this occurs, the star is said to be on the main sequence.

2.2.2 Main sequence

A star on the main sequence, by definition, is generating energy by fusing hydrogen into helium in its core. A schematic of a main sequence star can be seen in figure 2.4.

Hydrogen fusion in a main sequence star happens through two processes that are present in all main sequence stars, but the fraction of the star's energy generated by each depends on the mass of the star; the proton-proton chain provides the majority of the energy for a star below about 1.3 $M_\odot$, while the CNO cycle provides the majority of the energy for a star more massive than this.

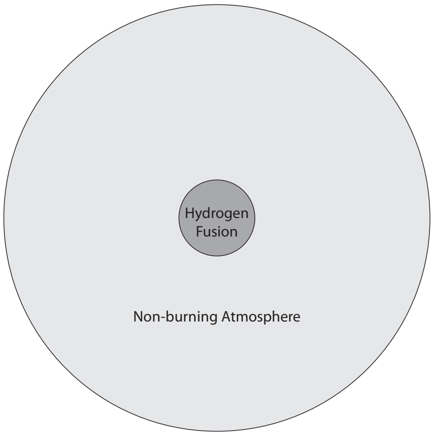

Figure 2.4: Schematic diagram of a main sequence star. The relatively tiny core of the star is fusing hydrogen into helium, and is surrounded by a much larger atmosphere that does not participate in the fusion processes. This schematic is not to scale.

2.2.2.1 Proton-proton chain

$$ {}^{1}_{1}\mathrm{H} + {}^{1}_{1}\mathrm{H} \rightarrow {}^{2}_{1}\mathrm{H} + e^{+} + \nu_e $$

$$ {}^{2}_{1}\mathrm{H} + {}^{1}_{1}\mathrm{H} \rightarrow {}^{3}_{2}\mathrm{He} + \gamma $$

$$ {}^{3}_{2}\mathrm{He} + {}^{3}_{2}\mathrm{He} \rightarrow {}^{4}_{2}\mathrm{He} + 2\ {}^{1}_{1}\mathrm{H} $$

$$ {}^{3}_{2}\mathrm{He} + {}^{4}_{2}\mathrm{He} \rightarrow {}^{7}_{4}\mathrm{Be} + \gamma $$

$$ {}^{7}_{4}\mathrm{Be} + e^{-} \rightarrow {}^{7}_{3}\mathrm{Li} + \nu_e $$

$$ {}^{7}_{3}\mathrm{Li} + {}^{1}_{1}\mathrm{H} \rightarrow 2\ {}^{4}_{2}\mathrm{He} $$

$$^{7}_{4}\mathrm{Be} + {}^{1}_{1}\mathrm{H} \rightarrow {}^{8}_{5}\mathrm{B} + \gamma$$

$$^{8}_{5}\mathrm{B} \rightarrow {}^{8}_{4}\mathrm{Be} + e^{+} + \nu_e$$

$$^{8}_{4}\mathrm{Be} \rightarrow 2\,{}^{4}_{2}\mathrm{He}$$

When combined, these branches produce energy at a rate proportional to roughly T^4 (here and for the remainder of this chapter, T when used to refer to nuclear processes is the core temperature).

2.2.2.2 CNO cycle

The CNO cycle also converts hydrogen into helium; difference is that the CNO cycle uses carbon, nitrogen, and oxygen atoms as catalysts that are needed for the reaction, but are not consumed (though the isotopic ratios of these atoms do change; Carroll & Ostlie, 1996).

$$^{12}_{6}\mathrm{C} + ^{1}_{1}\mathrm{H} \rightarrow ^{13}_{7}\mathrm{N} + \gamma$$

$$^{13}_{7}\mathrm{N} \rightarrow ^{13}_{6}\mathrm{C} + e^{+} + \nu_e$$

$$^{13}_{6}\mathrm{C} + ^{1}_{1}\mathrm{H} \rightarrow ^{14}_{7}\mathrm{N} + \gamma$$

$$^{14}_{7}\mathrm{N} + ^{1}_{1}\mathrm{H} \rightarrow ^{15}_{8}\mathrm{O} + \gamma$$

$$^{15}_{8}\mathrm{O} \rightarrow ^{15}_{7}\mathrm{N} + e^{+} + \nu_e$$

$$^{15}_{7}\mathrm{N} + ^{1}_{1}\mathrm{H} \rightarrow ^{12}_{6}\mathrm{C} + ^{4}_{2}\mathrm{He}$$

$$^{15}_{7}\mathrm{N} + ^{1}_{1}\mathrm{H} \rightarrow ^{16}_{8}\mathrm{O} + \gamma$$

$$^{16}_{8}\mathrm{O} + ^{1}_{1}\mathrm{H} \rightarrow ^{17}_{9}\mathrm{F} + \gamma$$

$$^{17}_{9}\mathrm{F} \rightarrow ^{17}_{8}\mathrm{O} + e^{+} + \nu_e$$

$$^{17}_{8}\mathrm{O} + ^{1}_{1}\mathrm{H} \rightarrow ^{14}_{7}\mathrm{N} + ^{4}_{2}\mathrm{He}$$

When combined, these branches produce energy at a rate proportional to roughly T^{20}, which is why this becomes the dominant energy process for higher mass stars; the cores of these stars have a higher temperature than those of lower mass stars. We can also see from this that the metallicity of a star can play a role in which of these processes is dominant; a star with a low metallicity may not have enough carbon atoms to make the CNO cycle run at the same rate as a higher metallicity star.

2.2.2.3 Life on the main sequence

A star will spend the majority of its lifespan on the main sequence; this is because hydrogen fusion generates the most energy per atom, and also because the star contains more hydrogen (by far) than any other element. Stars do, however, experience some changes during this time, because converting hydrogen into helium decreases the mass fraction in the core (i.e. the pressure given by equation (2.27) decreases; or to look at it another way, when four hydrogen atoms become one helium atom there are fewer total atoms available to participate in the gas pressure). This causes the core to slowly decrease in size, resulting in the density and temperature increase required to increase the fusion reaction rate and thus the energy output enough to return the core to a state of hydrostatic equilibrium. Thus, the energy output of the core is always slowly increasing, and so the star slowly becomes more luminous over time.

2.2.3 Red giants

Eventually, the star will have consumed all the hydrogen available in the core, which means it is no longer able to generate energy through hydrogen fusion. As a result, the core begins to collapse (though this takes place relatively slowly) and increases in temperature and density. The material around the core also contracts inwards and is heated by the core, and eventually a shell of hydrogen around the core becomes dense and hot enough to begin fusing hydrogen into helium. This is the same process that once occurred in the core, but now the reactions occur at a much greater rate due to the continual temperature increase generated by the core collapse. Because of this, several orders of magnitude more energy is generated by this shell of fusion than was previously generated by the core; the envelope of the star outside the shell is heated by this, which increases the temperature/pressure gradient. This causes the star to expand (simultaneously increasing the right side of equation (2.24) and decreasing the left side) until it has once again reached a state of hydrostatic equilibrium. A star in this condition is called a red giant, and a schematic diagram of such a star can be seen in figure 2.5.

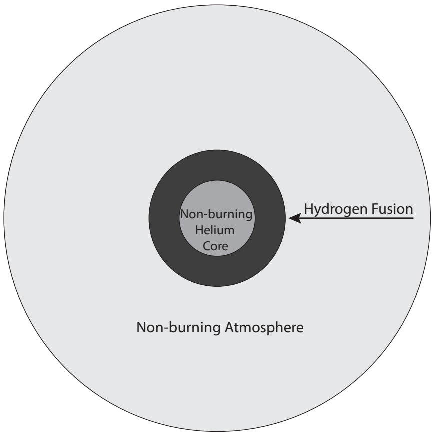

Figure 2.5: Schematic diagram of a red giant. The now inert core of helium is surrounded by a shell where hydrogen is being fused into helium, itself surrounded by a very much larger inert envelope. This schematic is not to scale.

Though the star is now generating more energy in its interior, the surface layers of the star are much further away from the center due to the expansion, and the star has a lower surface temperature than it did during the main sequence. However, the expansion is so great that the increase in surface area more than compensates for the decrease in temperature, and these stars are more luminous than when they were on the main sequence.

The subsequent evolution of low-to-intermediate mass red giants varies slightly depending on their mass, and we shall treat red giant stars of mass $<\sim 2.5 M_\odot$ separately from that of higher mass red giants.

2.2.3.1 Below ~2.5M$_\odot$

The core of these red giant stars cannot continue shrinking forever, because eventually its volume will have decreased to the point where it must be treated as *degenerate matter*; that is, the pressure due to quantum mechanical interactions between the electrons in the core dominates the pressure due to the temperature, as explained below.

2.2.3.2 Degenerate matter

Because electrons are fermions, they are subject to the Pauli exclusion principle and therefore there can only be one electron in each quantum state. To see why this causes the core of a red giant to resist further collapse, we must use quantum mechanics.

First, consider a collection of N non-interacting electrons bound inside a cube with sides of length L, where the potential is zero inside the cube and infinite outside. The allowed energies of each electron are given by

$$E_{n_x n_y n_z} = \frac{\hbar^2 \pi^2}{2m_e L^2}(n_x^2 + n_y^2 + n_z^2) \tag{2.30}$$

where $n_x = 1, 2, 3, \ldots$, $n_y = 1, 2, 3, \ldots$, and $n_z = 1, 2, 3, \ldots$ are the quantum numbers of this system and m_e is the electron mass. Let us now define a vector $\vec{w}$ in the following way:

$$\vec{w} = n_x \vec{x} + n_y \vec{y} + n_z \vec{z} \tag{2.31}$$

If we imagine a three-dimensional vector space with $\vec{w}$ as its basis, then each point (w_x, w_y, w_z) in the space corresponds to an allowed energy

$$E_{\vec{w}} = \frac{\hbar^2 \pi^2 \parallel \vec{w} \parallel^2}{2m_e L^2} \tag{2.32}$$

Now, consider an energy level E_{max}, corresponding to the situation where every quantum state with energy below E_{max} is filled with an electron and no electron has energy above this (i.e. the ground state of this system). This energy corresponds to the vector $\vec{w}_{\text{max}}$ in the $\vec{w}$ space. If N is large, then the number of allowed states with energies below E_{max} can be very closely approximated by the fraction of the volume of a sphere of radius $\parallel \vec{w}_{\text{max}} \parallel$ which lies within the $\vec{w}$ space. We must also include a factor of two, however, because each energy state can contain two electrons, one for each value of the spin. Therefore, the total number of states below E_{max} is (observing that only $\frac{1}{8}$ of the sphere lies within the $\vec{w}$ space)

$$N_{\text{states}} = 2 \cdot \frac{4}{24} \pi \cdot \parallel \vec{w}_{\text{max}} \parallel^3 \tag{2.33}$$

However, we defined E_{max} as the ground state of this system, so by definition the number of filled states is given by the number of electrons, N, and thus $N_{\text{states}} = N$. Therefore, we can write

$$N = 2 \cdot \frac{4}{24} \pi \cdot \parallel \vec{w}_{\text{max}} \parallel^3 \implies \parallel \vec{w}_{\text{max}} \parallel = \left(\frac{3N}{\pi} \right)^{\frac{1}{3}} \tag{2.34}$$

Substituting this into equation (2.32) gives

$$\begin{aligned} E_{\text{max}} &= \frac{\hbar^2 \pi^2 \parallel \vec{w}_{\text{max}} \parallel^2}{2m_e L^2} \\ &= \frac{\hbar^2}{2m_e L^2} \cdot (3N\pi^2)^{\frac{2}{3}} \end{aligned} \tag{2.35}$$

Finally, if we substitute the volume of the cube for the length (using $V = L^3 \implies L^2 = V^{\frac{2}{3}}$) we obtain

$$E_{\text{max}} = \frac{\hbar^2}{2m_e} \cdot \left(\frac{3N\pi^2}{V}\right)^{\frac{2}{3}} \tag{2.36}$$

This is known as the Fermi energy (which we shall now denote by E_{F}), and it marks the division between occupied and unoccupied states of this system. For the volume of this system to decrease, some of the electrons must have enough energy to transition to states above the Fermi energy; if they cannot obtain this energy, then the volume cannot be compressed. Of course, any collection of electrons with temperature above absolute zero (certainly electrons in a star's core!) will statistically have some electrons with an energy above the Fermi energy, and so there will be deviation from this result. However, in the cases where we are applying this concept, the Fermi energy is very large and such a small fraction of the electrons are above this level that the assumption of the ground state is quite good. On the other hand, even matter at high temperature will have some electrons below the Fermi energy, and so the resistance to compression is always present (simply vastly smaller than the thermal pressure in any non-degenerate matter).

We can calculate the pressure that results from this effect by considering the work done by this pressure if it expands the cube by $\mathrm{d}V$

$$\mathrm{d}W = P\,\mathrm{d}V \tag{2.37}$$

The work done, $\mathrm{d}W$, is equivalent to the change in the total energy of this system, $\mathrm{d}E_{\text{total}}$. Therefore, we must calculate the total energy of the system, and we can do so in the following manner. Consider that the Fermi energy gives us the energy of the highest filled state of this system of N electrons. This is true for any value of N, however, so the Fermi energy of a system of n electrons gives us the energy of the two nth electrons. Therefore, we can obtain the total energy of the system by integrating the Fermi energy over all N

$$\begin{aligned}
E_{\text{total}} &= \int_0^N E_{\text{F}}(n)\mathrm{d}n \\
&= \frac{\hbar^2}{2m_e} \cdot \left(\frac{3\pi^2}{V}\right)^{\frac{2}{3}} \cdot \int_0^N n^{\frac{2}{3}}\mathrm{d}n \\
&= \frac{\hbar^2}{2m_e} \cdot \left(\frac{3\pi^2}{V}\right)^{\frac{2}{3}} \cdot \frac{3}{5}N^{\frac{5}{3}} \\
&= \frac{\hbar^2}{2m_e} \cdot \left(\frac{3\pi^2 N}{V}\right)^{\frac{2}{3}} \cdot \frac{3}{5}N \\
&= \frac{3}{5}NE_{\text{F}} \qquad (2.38)
\end{aligned}$$

In order to use this in equation (2.37) we must calculate the derivative of this with respect to V

$$\begin{aligned}
\frac{\mathrm{d}E_{\text{total}}}{\mathrm{d}V} &= \frac{3}{5}N \cdot \frac{\mathrm{d}E_{\text{F}}}{\mathrm{d}V} \\
&= \frac{3}{5}N \cdot \frac{\hbar^2}{2m_e} \cdot \left(3N\pi^2\right)^{\frac{2}{3}} \cdot -\frac{2}{3}V^{-\frac{5}{3}} \\
&= -\frac{2NE_{\text{F}}}{3V} \qquad (2.39)
\end{aligned}$$

The negative sign is exactly what we should expect; as the volume increases, the total energy decreases. Therefore, using equation (2.37) we can obtain the expression for the pressure

$$P = \frac{\mathrm{d}W}{\mathrm{d}V} = -\frac{\mathrm{d}E_{\mathrm{total}}}{\mathrm{d}V} = \frac{2NE_{\mathrm{F}}}{3V} \tag{2.40}$$

2.2.3.3 Evolution as a red giant

The fact that the core of a red giant becomes degenerate has two important results. First, the core stops collapsing, because the gravitational force due to the core itself and the matter around it is not strong enough to overcome the degeneracy pressure. Second, because the degeneracy pressure is essentially independent of the temperature (they only interact through the very small increase in available quantum states below E_{F} when some electrons obtain enough energy to transition above this area), so the core can freely increase in temperature without expanding and cooling.

Eventually, the core will become hot enough for helium to begin fusing into carbon (this process is described in section 2.2.4.1 below). Degenerate matter is a good conductor of heat, so as soon as helium fusion begins it spreads extremely rapidly to the entire core. But because the core is degenerate, the rapid temperature increase does not expand and cool the core, and the rate of the fusion reactions increase . This causes the temperature to increase, which again increases the reaction rate, and so on, causing the core to release a massive pulse of energy called the helium flash; these events happen over a period of only a few seconds (Freedman & Kaufmann, 2005). This liberates enough energy to break the degeneracy (many electrons can now transition above the Fermi energy) which means that the pressure due to temperature again dominates, forcing the core to rapidly expand and stabilize the rate of helium fusion.

2.2.3.4 Above $\sim$2.5$M_\odot$

Low-to-intermediate stars of a higher mass evolve in nearly the same way as their lower mass counterparts, but because they are more massive their cores reach a temperature high enough to begin helium fusion before their cores become dense enough to become degenerate. As a result, helium fusion begins much more gradually in the cores of these stars, and they transition onto the next stage of their evolution without generating a helium flash.

2.2.4 Horizontal branch

Regardless of how it began, a star at this stage is now fusing helium into carbon in its core, and such a star is said to be on the horizontal branch (so named because a star on this stage moves in a relatively horizontal line on the H-R diagram). These stars are in some respect analogous to stars on the main sequence, because they are again producing energy in their core. However, in addition to the core helium fusion, the hydrogen burning shell is still active, although the rate of the hydrogen fusion reactions greatly decreases due to the core expansion. This causes the total energy output of the star to decrease, so the luminosity decreases, and the star itself shrinks (which increases the surface temperature). A schematic of a star on the horizontal branch is depicted in figure 2.6.

The method by which the core converts helium into carbon is called the triple-alpha process, and is described below.

2.2.4.1 Triple-alpha process

The triple-alpha process converts three atoms of helium (hence the name triple-alpha) into one of carbon, by the following process:

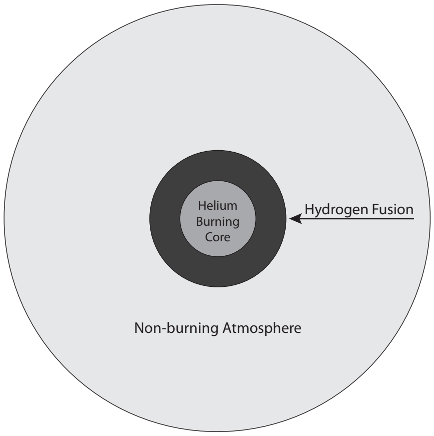

Figure 2.6: Schematic diagram of a horizontal branch star. The core of the star is now fusing helium into carbon, and is surrounded by a shell where hydrogen is being fused into helium, itself surrounded by a much larger inert envelope. This schematic is not to scale.

$$^{4}_{2}\mathrm{He} + ^{4}_{2}\mathrm{He} \rightleftharpoons ^{8}_{4}\mathrm{Be}$$

$$^{8}_{4}\mathrm{Be} + ^{4}_{2}\mathrm{He} \rightarrow ^{12}_{6}\mathrm{C} + \gamma$$

This reaction has a rate proportional to $\sim T^{41}$ (Carroll & Ostlie, 1996), so the energy output is extremely sensitive to fluctuations in the temperature.

At this high a temperature there are other, more minor fusion reactions occurring in the core; for stars of the masses we are interested in, the most important of these occurs when the carbon atom generated in step two of the triple-alpha process captures another helium atom, generating oxygen:

$$^{12}_{6}\mathrm{C} + ^{4}_{2}\mathrm{He} \rightarrow ^{16}_{8}\mathrm{O} + \gamma$$

2.2.4.2 End of the horizontal branch

Eventually the star will run out of helium in its core, just as it once ran out of hydrogen. However, this happens much more rapidly; there are fewer helium atoms available than there were of hydrogen, and each reaction generates less energy (so the reaction rate has to be higher to produce enough energy to maintain hydrostatic equilibrium). The exhaustion of the helium fuel causes the core to collapse again until it becomes degenerate (this happens to all stars between 0.8 and 8 $M_\odot$), heating up a region of helium around the core (recall that helium is being produced by the hydrogen burning shell, see figure 2.6), which then begins to fuse through the triple-alpha process. A star where this occurs is said to be an asymptotic giant branch star, because at this point its movement on the H-R diagram is roughly aligned with the evolutionary track it made as a red giant.

2.2.5 Asymptotic giant branch

Just as a star on the horizontal branch is analogous to a main sequence star, an asymptotic giant branch star (or AGB star) is analogous to a red giant in that the energy production in the star is coming from a region around the core. Now, however, the structure is more complicated. At the center of the star is a degenerate core of carbon (and depending on the mass a varying amount of oxygen), surrounded by a shell of helium being fused into carbon, itself surrounded by a shell fusing hydrogen into helium. A schematic of this kind of star can be seen in figure 2.7

The energy production in the interior of an AGB star is more complicated that it might first appear, because typically both shells are not active at the same time (or, at least, one shell is generally producing the dominant amount of energy at a time). This happens for the following reason. The helium burning shell is much thinner than the

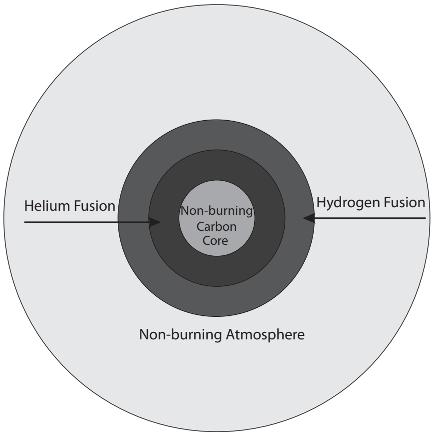

Figure 2.7: Schematic diagram of an asymptotic giant branch star. The now inert core of carbon is surrounded by a shell where helium is being fused into carbon, itself surrounded by a shell where hydrogen is being fused into helium, all of which is surrounded by a much larger inert envelope. This schematic is not to scale.

hydrogen burning shell, and as we will see below it can rapidly run out of helium fuel, causing the fusion reaction in the helium burning shell to cut off. During this period, the hydrogen burning shell is the only energy producing part of the star. The helium generated through the hydrogen fusion falls into the the region that was formerly helium burning, increasing its temperature and density. The density can increase so much that this region, though still dominated by the thermal pressure, can become degenerate enough to weaken the temperature dependence of the pressure. Eventually, this leads to a kind of low-order helium flash, when the region becomes hot enough to fuse helium again, and the small amount of degeneracy present helps to make the energy generation rate quite rapid. This causes the layers above this shell to expand, which cools the hydrogen burning shell and can even turn it off completely. The luminosity of the star increases greatly while the helium burning shell is active. This period is relatively short, however, and soon the helium shell will reduce its energy output and finally deactivate, making the outer layers of the star contract, which will heat the hydrogen shell burning region and reactivate it. This process will continue throughout the rest of the star's life.

The pulsations described above have a period that is dependent on the mass of the star, but is in the region of thousands of years for higher mass stars, and can be tens or hundreds of thousands of years for lower mass stars. There is however another mechanism that makes these stars pulsate, and on a very much smaller timescale.

2.2.5.1 Pulsation

To understand this pulsation mechanism, we must first think about what makes up the star's envelope. The primary constituent of the envelope is hydrogen; helium makes up almost all the rest. There are also, however, other elements present, some of which were present when the star formed (based on the composition of the molecular cloud that the star formed from) and as we shall see in section 2.2.5.2 below some of these were created during the star's lifetime. We will begin by first considering the hydrogen. Normally, a hydrogen atom has a single electron, but at high enough temperature (like in the interior of a star) the electron can receive enough energy to escape the atom, ionizing it. Because the star's temperature increases with depth, we can imagine a radius below which all the hydrogen atoms have lost their electrons (becoming fully ionized). In the same way, we can imagine a radius above which the temperature is not high enough to strip the electron from the atom and so there is no ionization (i.e. the atoms are neutral). These radii, however, do not coincide. Between them there is a layer of the star's material where there is a partial ionization; some of the hydrogen atoms are ionized, and some are not. This is referred to as the partial ionization zone. In this region, a small increase in temperature can cause a large change in the ionization state.

As we shall see in chapter 3, the opacity κ of a material determines how well it can absorb the light passing through it. In a star, the relationship between the opacity, the density, and the temperature for most of the star's envelope is given by (Carroll & Ostlie, 1996)

$$\kappa \propto \frac{\rho}{T^{3.5}} \tag{2.41}$$

This is called Kramers' Law. If we compress some of the star's material, we increase its density, which tends to increase the opacity; however, because the temperature also increases as it is compressed, the total opacity will decrease. This law also holds for the partial ionization zone, but now the ionization state has an important consequence related to the opacity. Imagine such a zone being compressed (for example, in the contraction phase of a pulsation); the density increases, also increasing the opacity. In this case, though, a large fraction of the energy from the compression that would normally go towards heating the zone is now used to increase the ionization state of the zone. As a result, the temperature increase is not enough to overcome the density increase, and the opacity *increases*. This causes the zone to absorb more energy from the interior of the star, and so it expands outwards, pushing the material above it.

As the zone expands, it cools and decreases in density; this does not continue indefinitely however because eventually the gas in the zone will cool enough that electrons will start to recombine with the ionized atoms. This releases energy, heating the zone. The heating due to the recombination counteracts the temperature decrease due to the expansion; once again the density term in Kramers' law is dominant, and the decrease in density results in a decrease in opacity. The zone is now absorbing less energy from the interior of the star, and so it falls back towards the center, resulting in compression, and the cycle starts over again.

Elements other than hydrogen can also have partial ionization zones, but this situation is slightly more complex because while hydrogen has only a single electron, heavier elements have more and thus can have more than one partial ionization zone (one for each ionized electron; for example, helium has two). The location of the ionization zones will depend on the temperature of the star. If the star is relatively cool, the zones will be deep inside the star; if the star is relatively hot, they will be near the surface. The precise location of the zones is important because if an ionization zone is located too deeply within a star, the envelope above the zone will be too massive for the zone to push effectively. The opposite case occurs if the zone is located too near the surface; if there isn't enough mass above the zone, then it doesn't have enough material to push to create a significant pulsation.

2.2.5.2 Chemistry of AGB stars

In the previous section we noted that a star can contain elements in its atmosphere that were generated after it formed. We will now investigate how this occurs. In section 2.2.4.1 we examined the triple-alpha process that converts helium into carbon; this is sporadically occurring in the helium burning shell. When the helium burning shell (discussed at the beginning of section 2.2.5) is active, it releases such a large amount of energy that it cannot all be radiated away; powerful convection currents develop which can mix the elements generated by the helium burning shell up into the region between the fusing shells and up into the hydrogen burning shell, and eventually up into the envelope of the star. This is known as the third dredge up (the previous two take place at earlier phases of the star's life and won't be considered here). It is somewhat of a misnomer because it implies that this happens only once; in fact, it can happen multiple times throughout the AGB phase as the helium shell activates (each one of these events is known as the third dredge up).

This involves more elements than were originally present in the core because as the material moves through and becomes trapped between the fusing shells during different stages of the convection, it is subjected to a relatively intense neutron flux that leads to neutron capture events and the generation of heavier elements. This is called the *s*-process (*s* for slow, as opposed to the *R* for the rapid nucleosynthesis process that occurs in supernovae). Here we will consider only the carbon.

A star which forms in our galaxy has an initial ratio of carbon to oxygen ratio in its envelope (called the C/O ratio) of ∼0.4 (Thompson et al., 2006), but this changes due to the third dredge up. For stars between ∼2 to $4M_\odot$ enough carbon will be dredged up into the outer envelope to increase the C/O ratio above 1; such stars are known as *carbon stars* or C stars. This mass dependence can be understood by examining what happens in the interior of stars outside ∼2 to $4M_\odot$. In stars below this limit, two processes interact to prevent the C/O ratio from increasing beyond one; first, such stars make less carbon in the helium burning shell and also more slowly, and second the convection currents in these stars are less powerful and don't extend as deeply than those in more massive stars, so less material is brought up out of the core. In stars above $\sim 4M_\odot$, the explanation lies in the details of the CNO cycle that is occuring in the hydrogen burning shell and the effect this has on the carbon as it passes through. The steps of the CNO cycle take place rapidly until $^{14}_{7}N$ is generated. This is a stable isotope with a small cross section, so it takes a long time for the rest of the cycle to occur (and thus regenerate the carbon). So when the carbon passes through the hydrogen burning shell, if the reaction rate of the initial parts of the cycle is rapid enough (implying high temperature and thus high mass) much of the carbon will be consumed and locked into $^{14}_{7}N$. Only in stars below $\sim 4_\odot$ can enough carbon survive the journey to make the star's atmosphere carbon rich.

A final point to consider here is the effect of metallicity on the ability of a star to become carbon rich. Imagine two equal-mass stars of the same C/O ratio, but with one having a greater metallicity than the other. This means that, though the ratios of these elements is the same for both these stars, the actual number of carbon and oxygen atoms are greater in the higher metallicity star (recall that metallicity, by definition, is a measure of the number of atoms heavier than hydrogen and helium in a star). Therefore the higher metallicity star will have to dredge up more carbon than the lower metallicity star for the same change in the C/O ratio. This makes it easier for a low metallicity star to become carbon rich.

2.2.5.3 Dust shell formation

AGB stars are large and therefore have a low surface gravity, which means that material lifts off the star's surface and flows outward with each pulsation. This material cools as it moves away from the star, and condenses to form molecules and dust grains. Once the material condenses, it is subject from the radiation pressure generated by the star which pushes the dust outwards even more (Lamers & Cassinelli, 1999). As a result of this extra push, the pressure near the star decreases, and so more material flows off the star's surface. The rate the star loses mass due to the pulsations is thus closely related to the formation of dust.

The nature of the dust that forms around the AGB star is strongly dependent on the chemistry of the star's atmosphere. As the material from the star's surface cools, carbon monoxide molecules are formed; this formation will continue until either all of the carbon or oxygen is consumed, depending on which is more abundant. Because carbon monoxide is extremely stable, this essentially locks in the element with lesser abundance, removing it from further reactions. This explains the importance of the C/O ratio, because the subsequent chemistry of the dust shell is dominated by whichever of those elements survives.

Determining what dust forms, and in what order (known as the dust condensation sequence) is complicated because there are many factors to consider; the gas pressure, temperature, C/O ratio, nitrogen abundance, and metallicity all play a role (Lodders & Fegley, 1995; Sharp & Wasserburg, 1995), and these factors themselves are influenced by other factors (for example, the gas pressure depends on the mass-loss rate, temperature, and the outflow velocity).

Carbon grains, either in the form of amorphous or graphitic carbon, dominate the dust shell around a carbon star; however, it is difficult to probe through observations because it does not have a diagnostic spectral feature in the infrared. The next most important grain which forms is silicon carbide (SiC), and as we shall see in the following chapters it is extremely interesting for research because it does have a diagnostic spectral feature in the infrared, at $\sim$11 μm.

Dust shells are expected to have heterogeneities and anisotropies in their density structure as a result of pulsation-driven dust formation and the ensuing hydrodynamic turbulent effects (e.g. Woitke 2006). These dust formation models suggest that carbon star mass-loss should be modulated on several timescales, especially that of the pulsation cycle. In addition, pulsations give rise to shocks in the outflowing gas, which are predicted to have a strong effect on local conditions (e.g. Cherchneff 2006) and thus could affect the type of dust that forms.

The spatial scale of heterogeneities arising from turbulence and shock is expected to be small. These small spatial-scale structure present observational challenges. For example, local density increases are expected to result from the pulsation-driven mass loss. However, the timescale for pulsation is much shorter than the timescale over which the star has been losing mass. Thus, spectroscopic studies include dust produced by several/many consecutive pulsation cycles. Moreover, these inhomogeneities in the density structure are expected to be wiped out over time by the subsequent hydrodynamic interactions (Villaver et al. 2002a,b).

2.3 Death

As mass flows out from the star, the radius of the star decreases due to the loss of material. Because the surface of the star is increasingly close to the star's center, it grows in temperature over time and thus also in luminosity. Additionally, the surface gravity of the star is also decreasing because of the loss of mass. As a result, the mass loss rate increases over time (Carroll & Ostlie, 1996); the dust shell around the star will eventually have enough material in it that it absorbs all the light coming from the star, itself emitting in the infrared. Eventually the star loses so much of its envelope that it can no longer throw off much material, and as the rest of the shell continues to spread and becomes less dense the star once more becomes visible.

2.3.0.4 Degeneracy revisited

Earlier in the star's life, it overcame the degeneracy in its core to begin helium fusion there. Why does this not occur now, allowing the star to fuse carbon? The answer lies in the star's mass. The temperature of a star's core increases with its mass in order to maintain hydrostatic equilibrium; stars below $\sim$8 $M_\odot$ are not massive enough to generate the temperature needed to start carbon fusion. Without this source of energy, there is no way to break the degeneracy, and so the only source of energy for the star is the

2.3.1 Planetary nebulae

At this point, the star has shed nearly all of its envelope, leaving behind the core, still surrounded by a hydrogen fusing shell. The star's temperature at this time is so great that it can emit ultraviolet photons which ionize the material the star threw out during the AGB phase; this causes the gas in the shell to generate visible light.

Additionally, a powerful stellar wind develops, which has a velocity much higher than the earlier material thrown out by the star. This wind sweeps up material, compressing it and forming much of the material into a shell-like relatively thin layer around the star (Kwok, 2000); for reasons not entirely understood, however, this shell of material around the star can form very complicated structures. The name planetary nebulae was coined because seen in a small telescope these objects look somewhat like the disc of a planet. They have no relationship to planet formation, except in the indirect way of spreading material into the interstellar medium that may eventually become part of a new star.

2.3.2 White dwarf

The planetary nebula phase of a star's life is very short, a few tens of thousands of years at most, because the hydrogen fusing shell cannot continue generating energy for long. When it exhausts the available fuel, there is no longer any source of energy and the now dormant core of the star begins to slowly cool. The remaining extremely hot core is called a white dwarf. Because a hot object emits energy at a rate much higher than a cooler one, the white dwarf initially cools relatively quickly, losing the ability to emit enough ultraviolet photons to ionize the material around it, which gradually becomes invisible (at least to visible wavelengths) and continues drifting away, spreading out into the interstellar medium.

The white dwarf itself is very small, and so it has a low luminosity for its temperature (these are the objects found to the bottom left of figure refhrdiagram). Because of this, it can remain hot for a very long time; white dwarfs older than our galaxy still have surface temperatures of thousands of kelvins (Fontaine et al., 2001).

2.4 Conclusion

We have seen how stars form out of gas and dust between the stars; and we have also seen how near the end of their lives these stars throw off nearly all their mass, which spreads out into space and can eventually become incorporated into molecular clouds and new generations of stars. Indeed, as we will see later in this work, we have even discovered some of this material in our own solar system by examining meteorites. The life, evolution, and death of these stars helped to create everything around us.

Chapter 3

Optical Properties of Solids

"This art [astronomy] which is as it were the head of all the liberal arts and the one most worthy of a free man leans upon nearly all the other branches of mathematics. Arithmetic, geometry, optics, geodesy, mechanics, and whatever others, all offer themselves in its service." - Nicolaus Copernicus

3.1 Introduction

Almost everything we know about dust in space comes from the interactions between light and that dust; almost the entire rest of this work is related to light interactions in some form or another. We will therefore examine some basic principles behind these interactions, starting with a method used later in this work for determining the optical properties of solids, and then continuing on to a basic discussion of how light propagates through dust.

3.2 Classical dispersion analysis

In order to understand how light interacts with a dust grain, we must first understand how we can determine the optical properties of a material through laboratory measurements. One such method, used later in chapter 8, is called classical dispersion analysis. Before we begin, we should recall some basic electrodynamics that will soon become useful; from Maxwell's equations, we can write

$$D = \epsilon_0 E + P \tag{3.1}$$

where D is the electric displacement, ϵ_0 is the electric permittivity of free space, and P is the polarization. If we now assume that we are dealing with a linear, homogeneous, and isotropic material under the influence of electric field E, we can write

$$P = \epsilon_0 \chi E \tag{3.2}$$

where χ is the electric susceptibility of the material we are investigating. Combining these two equations, we obtain

$$\begin{aligned} D &= \epsilon_0 E + \epsilon_0 \chi E \\ &= \epsilon_0 (1 + \chi) E \\ &= \epsilon E \end{aligned} \tag{3.3}$$

The term $(1 + \chi) = \epsilon$ is the relative permittivity of the material and is known as the dielectric function. The dielectric function is a function of the frequency of the electric field impinging on the material, and in general it is complex valued (in order to correctly represent the lag between the electric field and the reaction of the material). With these preliminaries complete, we can now examine the classical dispersion method. We will begin our investigation of this method by constructing a seemingly crude, but actually quite powerful model of electrons in matter called the Lorentz model.

3.2.1 Lorentz model

The Lorentz model is very simple; imagine an electron of mass m and charge q connected to a spring with spring constant k, and assume that the other end of the spring is fixed. The force on the electron from the spring is $F = -kx$, where x is the displacement of the electron. The equation of motion of the electron is thus given by

$$m\frac{\mathrm{d}x^2}{\mathrm{d}t^2} = -kx \tag{3.4}$$

This has the solution (neglecting the phase)

$$x = A\sin(2\pi\nu_0 t) \tag{3.5}$$

where A is the amplitude of the motion, and

$$\nu_0 = \frac{1}{2\pi}\sqrt{\frac{k}{m}} \tag{3.6}$$

is the natural frequency of the motion. Now, let us make this simple model more complicated by adding in a damping force b which resists the movement of the electron (in other words, it acts like a frictional force). This is represented by

$$F_d = -b\frac{\mathrm{d}x}{\mathrm{d}t} \tag{3.7}$$

Also, we now wish to allow the electric field to influence the electron; we shall assume that E is harmonic with frequency ν. From the Lorentz Force Law, we can write the force on the electron due to E as

$$F_{\mathrm{E}} = qE \tag{3.8}$$

as there is no magnetic field in our model. To derive the new equation of motion, we must include both this force and the damping force, giving us

$$m\frac{\mathrm{d}x^2}{\mathrm{d}t^2} = -kx - b\frac{\mathrm{d}x}{\mathrm{d}t} + qE \tag{3.9}$$

To solve this equation it is first convenient to rearrange the terms in the following way

$$\frac{\mathrm{d}x^2}{\mathrm{d}t^2} + \frac{b}{m}\frac{\mathrm{d}x}{\mathrm{d}t} + \frac{k}{m}x = \frac{qE}{m} \tag{3.10}$$

We can see that the coefficient in front of the x-term is just the square of ν_0. Additionally, let us define $\gamma = \frac{b}{m}$; this is called the damping coefficient. If we rewrite the equation of motion using these terms, we obtain

$$\frac{\mathrm{d}x^2}{\mathrm{d}t^2} + \gamma\frac{\mathrm{d}x}{\mathrm{d}t} + \nu_0^2 x = \frac{qE}{m} \tag{3.11}$$

This is called the Abraham-Lorentz equation. To obtain the solution we should explicitly include the harmonic nature of the electric field by writing

$$E = E_0 \cos(\nu t) \tag{3.12}$$

Doing this immediately gives us a clue to the solution, as it suggests a test function of

$$x = A\cos(\nu t - \phi) \tag{3.13}$$

where ϕ is the phase. Let us substitute this function into the equation of motion, which results in

$$\begin{aligned} -\nu^2 A\cos(\nu t-\phi) - A\nu\gamma\sin(\nu t-\phi) + A\nu_0^2\cos(\nu t-\phi) &= \frac{Aq}{m}\cos(\nu t-\phi) \\ A(\nu_0^2-\nu^2)\cos(\nu t-\phi) - A\nu\gamma\sin(\nu t-\phi) &= \frac{AqE_0}{m}\cos(\nu t-\phi) \end{aligned} \tag{3.14}$$

If we now apply the trigonometric identities $\sin(\nu t-\phi) = \sin(\nu t)\cos(\phi) - \cos(\nu t)\sin(\phi)$ and $\cos(\nu t-\phi) = \cos(\nu t)\cos(\phi) + \sin(\nu t)\sin(\phi)$, this becomes

$$\begin{aligned} &(A(\nu_0^2-\nu^2)\cos(\phi) + A\nu\gamma\sin(\phi) - \frac{qE_0}{m})\cos(\nu t) + \\ &\qquad A((\nu_0^2-\nu^2)\sin(\phi) - \nu\gamma\cos(\phi))\sin(\nu t) = 0 \end{aligned} \tag{3.15}$$

This equality is always true, so the terms in front of $\sin(\nu t)$ and $\cos(\nu t)$ must both be zero. Thus,

$$A(\nu_0^2-\nu^2)\cos(\phi) + A\nu\gamma\sin(\phi) - \frac{qE_0}{m} = 0 \tag{3.16}$$

and

$$A((\nu_0^2-\nu^2)\sin(\phi) - \nu\gamma\cos(\phi)) = 0 \tag{3.17}$$

We now have two equations and two unknowns, so we can solve for A and ϕ. Doing so, we obtain

$$A = \frac{qE_0}{m} \cdot \frac{1}{\left((\nu_0^2 - \nu^2)^2 + \gamma^2\nu^2\right)^{\frac{1}{2}}} \tag{3.18}$$

and

$$\phi = \arctan\left(\frac{\gamma\nu}{\nu_0^2 - \nu^2}\right) \tag{3.19}$$

Now, these equations are useful in this form (particularly the phase), but unfortunately they is not very helpful for our present requirements. It is somewhat tedious, but using trigonometric identities (such as $\cos(\arctan(y)) = \frac{1}{\sqrt{1+y^2}}$), it is possible to show that

$$x = \frac{qE_0}{m} \cdot \frac{1}{\nu_0^2 - \nu^2 - i\gamma\nu} \tag{3.20}$$

Let us return our attention to electrodynamics. The dipole moment $\hat{p}$ of a single electron is just the charge of the electron times the displacement of the electron. However, the dipole moment is also the polarizability $\hat{\alpha}$ times the electric field, so we can write (additionally removing the vector nature of these equations, which we have been ignoring)

$$\hat{\alpha} = \frac{q^2}{m} \cdot \frac{1}{\nu_0^2 - \nu^2 - i\gamma\nu} \tag{3.21}$$

Finally, we can return to the electrodynamic relations we observed at the beginning of this section. For a single oscillator, the polarization is just the polarizability, and therefore

$$\begin{aligned} D &= \epsilon_0 E + P \\ &= \epsilon_0 E + \hat{p} \\ &= \epsilon_0 E + \hat{\alpha} E \end{aligned} \tag{3.22}$$

But $D = \epsilon E$, so this becomes

$$\begin{aligned} \epsilon &= \epsilon_0 + \hat{\alpha} \\ &= \frac{q^2}{m} \cdot \frac{1}{\nu_0^2 - \nu^2 - i\gamma\nu} \end{aligned} \tag{3.23}$$

This equation is at the heart of classical dispersion analysis, and it is extremely powerful because ϵ determines the optical properties of the material, and the unknown values γ and ν_0 can be determined through an examination of resonances in the reflection spectrum of the material (as we shall see in chapter 8). Of course, a real spectrum will have multiple resonances, and we can include that into this model by imagining additional oscillators with different γ and ν_0. One can show that the value of ϵ for such a collection of oscillators is just the summation of the individual ϵ terms (Bohren & Huffman, 1983). In practice, one would fit a curve generated by equation 3.23 to the resonances in the spectrum, and thus obtain an accurate value for ϵ.

The dielectric function is useful in its own right, but because in general we are more used to thinking about the complex refractive index m, we will now examine the relationship between these two parameters. By definition,

$$m = \frac{c}{v_{\mathrm{p}}} \tag{3.24}$$

where c is the speed of light in vacuum and v_{p} is the phase velocity of light in the medium. If we return to Maxwell's equations, we can show that the phase velocity is given by

$$v_{\mathrm{p}} \frac{c}{\sqrt{\epsilon\mu}} \tag{3.25}$$

where μ is the magnetic permeability of the material. Almost all solid materials have a μ very close to one (though other environments like plasmas do not), so we can write

$$v_{\mathrm{p}} = \frac{c}{\sqrt{\epsilon}} \tag{3.26}$$

But from the definition of the complex refractive index, we can rewrite this as

$$\frac{c}{m} = \frac{c}{\sqrt{\epsilon}} \tag{3.27}$$

$$m = \sqrt{\epsilon} \tag{3.28}$$

And thus we see that the relationship between the complex refractive index and the dielectric function is straightforward.

3.3 Light propagation through dust

In section 2.2.5.3, we examined the dust shells that form around AGB stars, and in particular the shells that form around carbon stars. All the research we will consider in later chapters is in some way connected to the way light travels through this dust, so we must examine the fundamentals of light propagation through such a medium.

Consider light with flux F_λ propagating through a slab of dust of density ρ and thickness dx, with the resulting flux emerging from the other slide denoted by F'_λ. This is illustrated in figure 3.1 below.

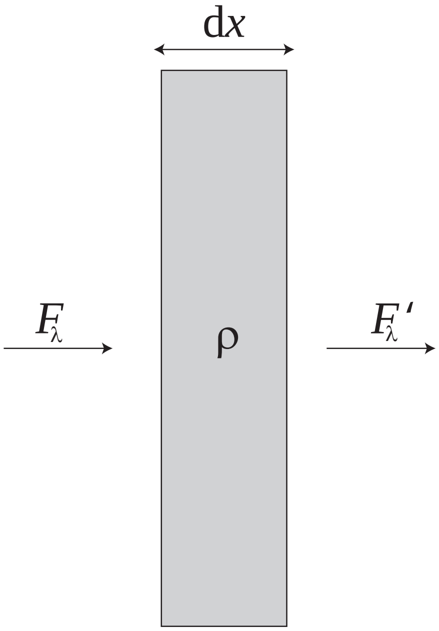

Figure 3.1: Light propagating through a slab of dust. See discussion for an explanation of terms.

We can write the change in the flux, dF_λ as the beam of light passes through the slab as

$$\mathrm{d}F_\lambda = F'_\lambda - F_\lambda \tag{3.29}$$

What causes this change in flux? The three processes we will consider here are absorption, scattering, and emission (there are other possible processes like florescence, but we will not consider them here).

3.3.0.1 Extinction

If we ignore the contribution from the dust emission, we expect the flux emerging from the right side of the slab to be less than the flux that entered on the left for two reasons. First, some of the light will be absorbed by the dust (through heating of the material or destruction of molecules, for example). Second, the light will be scattered; though some of the scattered light will still pass through the right side of the slab, some will scatter out through the left. In order to describe these processes, called extinction, we can define the wavelength-dependent opacity κ_λ such that

$$\mathrm{d}F_\lambda = -\kappa_\lambda \rho F_\lambda \,\mathrm{d}x \tag{3.30}$$

Integrating, we obtain

$$F_\lambda(x) = Ce^{-(\kappa_\lambda \rho x)} \tag{3.31}$$

With C as the constant of integration. We can easily determine the value for this constant by observing that at $x = 0$, $F_\lambda(0) = C$, thus giving

$$F_\lambda(x) = F_\lambda(0)e^{-(\kappa_\lambda \rho x)} \tag{3.32}$$

with $F_\lambda(0)$ as the flux before it interacts with the slab. From this, we can see that the flux will exponentially decrease in intensity as it passes through the dust. This is called Beer's Law. We now define the wavelength-dependent optical depth τ_λ as

We define the wavelength-dependent optical depth τ_λ as

$$\mathrm{d}\tau(\lambda) = \kappa(\lambda)\rho\mathrm{d}x \tag{3.33}$$

Often the optical depth is denoted in a more specific way by explicitly giving the wavelength at which the optical de; for example, many optical depths in this work are at 10 μm, and so are denoted by $\tau_{10\mu m}$. We can now substitute this definition into equation (3.32) to obtain

$$F_\lambda(x) = F_\lambda(0)e^{-\tau_\lambda(x)} \tag{3.34}$$

From this, we can see that the optical depth is a measure of how much light is being absorbed per unit distance; with a high optical depth, the exponential term will make the flux fall off quickly. Optical depth is a useful concept because often we wish to know how well and how far light is penetrating into a body of dust; the opacity alone doesn't give us this information, because the density and how much material the light goes through also are important. For example, consider fog; the fog itself is relatively diffuse, which is why it doesn't hinder seeing nearby objects, but objects further away are obscured. This is because the optical depth is higher for objects further away. We can see this more explicitly by integrating equation 3.33

$$\tau_\lambda = \int_0^l \kappa(\lambda, x)\rho(x)\,\mathrm{d}x \tag{3.35}$$

where l is the length of our line of sight. In general, when we are looking through dust with $\tau < 1$ we say that the dust is optically thin; if greater than this we say it is optically thick.

Let us return to equation (3.32). We can obtain this result in another way that has useful consequences. Imagine radiation in the form of an ideal sinusoidal wave passing through the dust. This wave takes the form

$$A = A_0 e^{-i(\omega t - \frac{2\pi x}{\lambda})} \tag{3.36}$$

where A_0 is the amplitude, ω is the angular frequency, and λ is the wavelength. The energy contained in this wave is proportional to A^2. As this wave enters the dust, it slows by an amount governed by the complex index of refraction; we can express this in the wave equation by writing

$$\begin{aligned} A &= A_0 e^{-i(\omega t - \frac{2\pi m x}{\lambda})} \\ &= A_0 e^{-i(\omega t - \frac{2\pi [n+ik]}{\lambda})} \\ &= A_0 e^{-i(\omega t - \frac{2\pi n}{\lambda})} e^{-(\frac{2\pi k}{\lambda})} \end{aligned} \tag{3.37}$$

The first exponential is just a wave traveling with a velocity dependent on n (precisely what we expect), and the second term is an exponential falloff. This is the same exponential falloff found in equation (3.32), except this time we are only dealing with the opacity due to absorption, which is κ_{abs}, the absorption coefficient. Since the exponential term in equation (3.32) is the same as the term here (except now that we have switched to the absorption coefficient we no longer need to include ρ, as this is already included in the term), we can write

$$-\kappa_{\text{abs}}x = -\frac{2\pi kx}{\lambda} \tag{3.38}$$

$$\kappa_{\text{abs}} = \frac{2\pi k}{\lambda} \tag{3.39}$$

Now, consider what happens at the interfaces of the slab. Some of the light will be reflected, some will be absorbed, and some will pass through the dust; there are two reflections we are concerned with here, the one that occurs when the light passes into the slab and the one that occurs when the light meets the boundary on the right. At each of these interfaces, the light will reflect back a fraction R of the total energy; therefore the transmitted light T at each interface is $(1 - R)$. In addition, the light continues to be absorbed as it continues through the dust. Therefore, the equation for the amount of transmitted light is (assuming the same fraction of light is reflected at each interface).

$$T = (1 - R)^2 e^- \kappa_{\text{abs}} \tag{3.40}$$

This equation tells us that we can obtain a value for κ_{abs} from measuring the amount of transmitted light, and from this and equation (3.39) the value of k also.

3.3.1 Radiative transfer

The discussion above is somewhat simplistic, because it only considers the change in the flux due to the opacity of the dust; there is also a change in the flux due to the thermal emission of the dust itself. Let us define the emission coefficient j_λ such that the increase in flux $\mathrm{d}F_\lambda$ as it passes through the slab is given by

$$\mathrm{d}F_\lambda^{\text{emission}} = j_\lambda \rho \, \mathrm{d}x \tag{3.41}$$

This allows us to write the total change in flux as

$$\mathrm{d}F_\lambda = j_\lambda \rho \, \mathrm{d}x - \kappa_\lambda \rho F_\lambda \, \mathrm{d}x \tag{3.42}$$

Now, divide this expression by $-\kappa_\lambda \rho \, \mathrm{d}x$ to obtain

$$-\frac{1}{\kappa_\lambda \rho} \cdot \frac{\mathrm{d}F_\lambda}{\mathrm{d}x} = F_\lambda - \frac{j_\lambda}{\kappa_\lambda} \tag{3.43}$$

The fraction j_λ/κ_λ is known as the source function, S_λ. Now, examine the term on the left side of equation (3.43). Using the definition of optical depth, we can rewrite this as

$$-\frac{1}{\kappa_\lambda \rho} \cdot \frac{\mathrm{d}F_\lambda}{\mathrm{d}x} = -\frac{\mathrm{d}F_\lambda}{\mathrm{d}\tau_\lambda} \tag{3.44}$$

Rewriting equation (3.43) gives us

$$\frac{\mathrm{d}F_\lambda}{\mathrm{d}\tau_\lambda} = S_\lambda - F_\lambda \tag{3.45}$$

This is called the *transfer equation* and it forms the basis for radiative transfer. We can also integrate to obtain the transfer equation in another form

$$F_\lambda(\tau_\lambda) = F_\lambda(0) e^{-\tau_\lambda} + \int_0^{\tau_\lambda} S_\lambda(z_\lambda) e^{-(\tau_\lambda - z_\lambda)} \, \mathrm{d}z_\lambda \tag{3.46}$$

The transfer equation is, in general, very difficult to solve; a great deal of effort has gone into developing solutions and techniques to use the transfer equation; a classic work on the subject is Chandrasekhar (1950). For some situations and geometries exact solutions exist, but usually some kind of numerical method is needed.

3.4 Spectral analysis

Now let us investigate the methods we will use when analyzing the spectra produced by dust in space (and in particular, the dust shells around C stars). The emission at wavelength λ from a dusty region with optical depth $\tau(\lambda)$ and a single temperature T is

$$F(\lambda) \propto B(\lambda, T)[1 - e^{(-\tau(\lambda))}]$$

where $B(\lambda, T)$ is the Planck function.

When the source is optically thick, $F(\lambda) \propto B(\lambda, T)$, otherwise $F(\lambda) \propto B(\lambda, T) \times \kappa(\lambda)$, where $\kappa(\lambda)$ is the grains' wavelength dependent absorption coefficient. The source will emit as a blackbody when either $\tau(\lambda) \gg 1$ or $\kappa(\lambda)$ is wavelength independent (gray opacity). When the optical depth is low, and the absorption coefficient is $\kappa(\lambda) \propto \lambda^{-\beta}$ so that

$$F(\lambda) \propto B(\lambda, T) \times \lambda^{-\beta}$$

The index β depends on the size, structure, and composition of the dust grains.

As discussed above, the spectrum is essentially given by: $F(\lambda) \propto B(\lambda, T) \times \kappa(\lambda)$, where $\kappa(\lambda)$ is the grains' wavelength dependent absorption coefficient. However, $\kappa(\lambda)$ is made up of an amalgam of optical behaviors of the various grain sizes, shapes and compositions within the dust shell. Therefore there are two interpretations of how to extract the absorption/emission properties of the circumstellar dust from a given spectrum. The spectrum can be interpreted as a product of the underlying continuum and an extinction efficiency factor for the entire spectrum,

$$F_\lambda = BB_\lambda \times Q_\lambda \tag{3.47}$$

or as though the entire spectrum is made up of the sum of products of individual components.

$$F_\lambda = [BB_{Carbon} \times Q_{Carbon}] + [BB_{SiC} \times Q_{SiC}] + [BB_{other} \times Q_{other}] \tag{3.48}$$

where BB is the temperature-dependent Planck function and $Q \propto$ absorbance.

Using the continuum-divided spectrum assumes the type of spectrum described by Equation 3.47. Dividing the entire spectrum by the fitted underlying continuum, leaves only the absorption/extinction efficiency of the dust (assuming all dust species have the same blackbody temperature). In this case, we effectively end up with an optical depth spectrum which is equivalent to an extinction efficiency for some sort of composite grains that represents all the grains present. Using this technique implicitly assumes that SiC is the dominant cause of wavelength dependent changes to the optical depth, and fails to account for different sizes, shapes and/or temperatures within the SiC grain population.

In the case of Equation 3.48, subtracting the product of underlying continua and absorbances of everything but SiC would leave only SiC's spectrum. In this case, the continuum is taken to be due to the prevalent carbon grains (which do not have diagnostic mid-IR features and thus Q is constant with wavelength). This implies that the continuum-subtracted spectrum is due to SiC, but neglects the fact that SiC will also contribute to the continuum. Both scenarios are oversimplifications of the true situations and it is difficult to know which approach is most appropriate.

In reality the situation is even more complex:

$$F_\lambda = \sum_{i=1,j=1}^{n,m} BB_i \times Q_j \tag{3.49}$$

where each BB_i represents a single dust (or stellar) temperature, and each Q_j represents the extinction efficiency for a single grain type as defined by its size, shape, composition and crystal structure. Such a complex situation can only be completely addressed using radiative transfer modeling (which assumes optical data are available for all relevant dust grain species).

Chapter 4

Silicon Carbide

"En plus de ce phosphure cristallisé nous avons rencontré, dans les résidus qui ont résisté aux attaques alternées d'acide fluorhydrique concentré et d'acide sulfurique bouillant, des cristauz hexagonaux verts, caractéristiques, de siliciure de carbone.

C'est la premié fois que ce siliciure de carbone est rencontré dans la nature." - Henri Moissan

4.1 Introduction

Silicon carbide (SiC) is the focus of much of the remainder of this work due to its diagnostic spectral feature at ∼11 μm, and so we should carefully examine the nature and properties (particularly the optical properties) of this substance before proceeding further. The first theoretical prediction that SiC could exist in nature was made over 180 years ago by Berzelius (1824), but more modern investigation has focused on SiC's usefulness as a high temperature, wide band-gap semiconductor (O'Connor & Smiltens, 1960; Levinshtein et al., 2001; Saddow & Agarwal, 2004, only a few of many examples). This extensive research on SiC is useful for our purposes, but we must keep in mind that conditions in a terrestrial lab are very different from those found in astrophysical environments, and care must be taken before using the results of that research.

4.2 Physical properties of SiC

4.2.1 Crystal structure

SiC comes in ∼250 different crystalline forms or polytypes (Mitra et al., 1969; Liu et al., 2004). All polytypes of SiC possess tetrahedral linkage of the Si and C atoms (Taylor & Jones, 1960, and see figure 4.1 below), which combine to form sheets; it is the alignment of these sheets as they stack which determines the particular polytype.

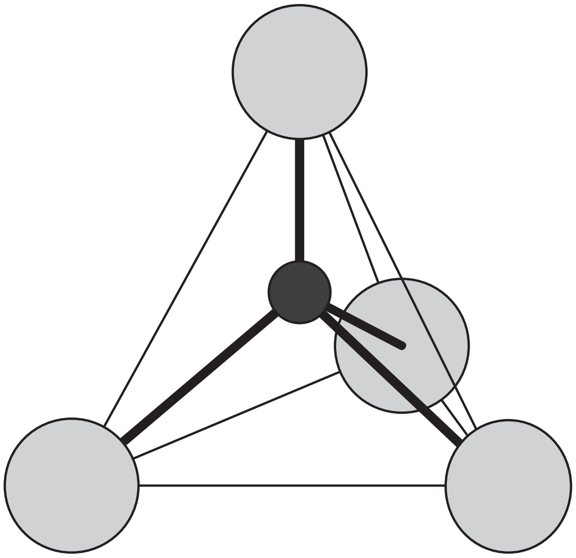

Figure 4.1: Tetrahedral structure of Si and C atoms in SiC; the light gray spheres are Si, the dark gray sphere is C, and the thick lines represent the atomic bonding of this structure (the thin lines are provided as an aid to seeing the tetrahedral structure).

An illustration of how the tetrahedral structures produce sheets can be seen in figure 4.2.

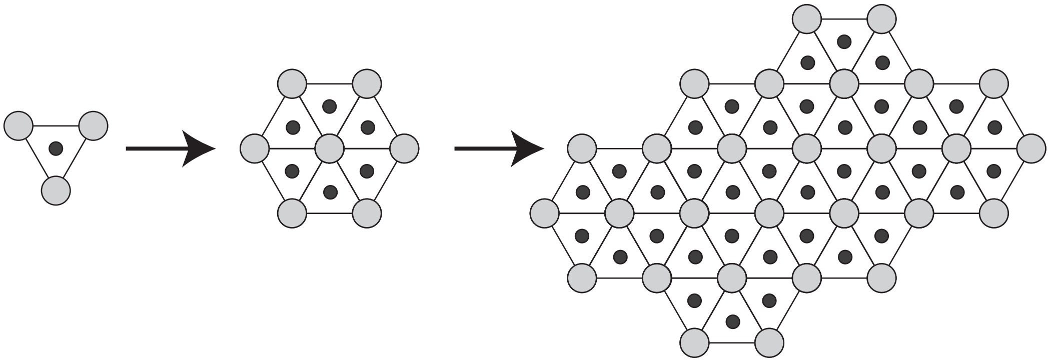

Figure 4.2: Schematic of how the tetrahedral structures of the Si (large gray spheres) and C atoms (small dark spheres) form sheets in SiC; the tetrahedrons are being viewed from one side, and the fourth Si atom is omitted for clarity.

This discussion will examine only the face centered cubic form of SiC (known as the 3C or β polytype) and the 2H and 6H forms of α-SiC, which are two different combinations of cubic and hexagonal layering patterns (Pitman et al., 2008). The structure of these polytypes is shown in Figure 4.3.

4.2.2 Optical properties

The most obvious optical property of SiC (at least in the infrared) is a distinctive feature at $\sim 11\mu$m, which has been observed around nearly every C star. (Pitman et al., 2008). This is useful, because this feature of should have different properties depending on several factors; the polytype or mixture of polytypes present, the concentration of SiC, and the temperature, as a few examples. This has led to the hope that the $\sim 11\mu$m feature could be used as a diagnostic tool to determine the conditions present in the dust shell, and a great deal of research has focused on SiC for this reason.

The structural differences between SiC polytypes affect their interaction with light in two ways. First, light which passes through a sample of β-SiC has no preferred direction due to the symmetry of the crystal lattice, but light interacting with α-SiC experiences different effects depending on if the light's electric field vector is

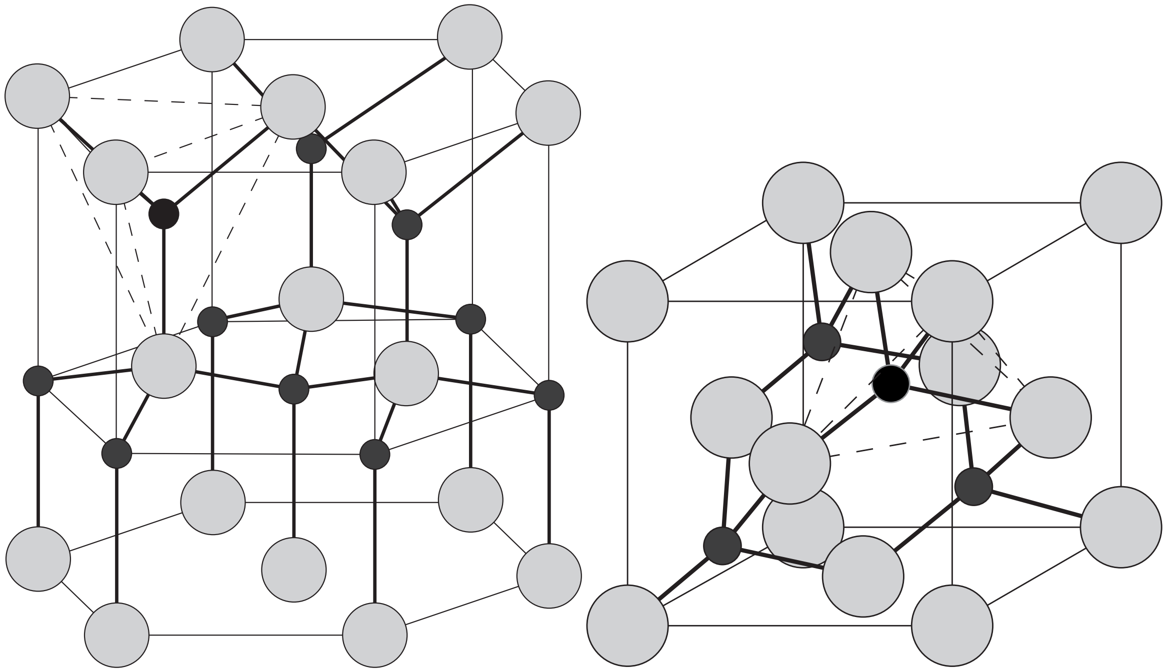

(a) (2H) α-SiC

(b) β-SiC

Figure 4.3: Crystal structure of (2H) α-SiC and β-SiC. The larger light gray spheres are Si, the smaller darker spheres are C. Thick lines represent the atomic bondings between Si and C, the thin lines are an aid to seeing the lattice structure, and the dashed lines are an aid to seeing one of the tetrahedral elements (around the dark black C atom) of the lattice. In the case of β-SiC, the sheets described in the text and in figure 4.2 are arranged diagonally in this view.

perpendicular to the crystal's c axis (called the ordinary ray) or parallel to c (called the extraordinary ray).

Second, the different SiC polytypes have different numbers of vibrational modes, also because of the symmetry of the lattices (Patrick, 1968; Feldman et al., 1968). Because the polytypes are related to each other through the different stackings of layers, it is possible to determine the number, type, and frequency of the vibrational modes of a polytype by comparing the size of its unit cell with that of β-SiC (Burns, 1990). Phonon dispersion curves of β-SiC have been determined using symmetry analysis and Raman spectroscopic measurements of various polytypes (Nakashima & Harima 1997). In Raman measurements, the transverse optic (TO) component of each

IR mode, or minimum in ϵ_2, manifests as a peak that is distinct from the longitudinal optic (LO) component, or maximum in $\mathrm{Im}(1/\epsilon)$. However, IR activity is complicated by several factors.

1. Energy in an IR experiment is absorbed at all frequencies between the TO and LO components.
2. Si-C pairs that produce LO activity when $\vec{E}\perp\vec{c}$ are the same pairs that produce TO activity when $\vec{E}\|\vec{c}$.
3. Some modes are strong, and some are weak. Although symmetry considerations do not predict intensities, the main Si-C stretch in β-SiC should dominate the IR spectra of the various hexagonal and rhombohedral polymorphs.
4. Stacking disorder may contribute additional modes expected for other polymorphs (e.g., 15R modes may occur in 6H crystals).
5. Acoustic overtones and accidental degeneracies are always possible in IR spectra.

Many measurements of the optical properties of SiC have been made; quite a few have been used for astronomical research (Spitzer et al., 1960; Philipp & Taft, 1960; Lipson, 1960; Dorschner et al., 1977; Friedemann et al., 1981; Borghesi et al., 1985; Orofino et al., 1991; Papoular et al., 1998; Mutschke et al., 1999; Andersen et al., 1999b); as will be discussed in chapter 8, these measurements all have various limitations. A new set of SiC optical constants is presented in that chapter which overcome these limitations.

4.3 SiC in astronomical environments

Over 40 years ago, equilibrium condensation models predicted the formation of SiC in carbon rich astrophysical environments (Friedemann, 1969; Gilman, 1969). Equilibrium condensation models such as these attempt to determine the temperature (and therefore in the case of condensation around stars the distance from the parent star) at which a given molecule can begin to be found in the solid phase; equilibrium refers to the assumption made that the vapor and condensate are in equilibrium at the point of condensation. These models can sometimes also be used to determine the cooling history of a molecule, which determines (in part) if that molecule will be found in an amorphous or crystalline form. The assumption of equilibrium is relatively simplistic because non-equilibrium condensation is also possible (for example, nucleation processes can decrease the condensation temperature, see Tanaka et al., 2000), but these models were qualitatively confirmed by the detection of SiC's characteristic 11 μm spectral feature (discussed in section 4.2.2) a few years later around C stars (Hackwell, 1972; Treffers & Cohen, 1974). Observations of many C stars since that time have shown that SiC is nearly always present around these stars, though it appears to only make up a very small percentage of the interstellar medium, which is taken as evidence that almost all SiC grains are destroyed sometime after leaving the environment around their parent star (Whittet et al., 1990).

4.3.1 Meteoritic evidence

Despite the tremendous distance separating our solar system from the other stars, we can still obtain actual physical samples of astrophysical SiC (and other minerals) by carefully examining meteorites for the presence of grains that were produced before our solar system formed (such grains are called ”presolar grains”). As discussed in

Clayton & Nittler (2004), presolar grains can be distinguished from grains that formed along with our solar system by an analysis of the isotopic composition of those grains. Because of the chemistry that occurred during the formation of our solar system, the isotopic ratio C^{12}/C^{13} (as an example) of material involved in that chemistry should be close to the interstellar average of 89; carbon atoms found in presolar SiC grains have been observed with C^{12}/C^{13} of anywhere between 5 and 5000, very strongly suggesting that these grains were formed outside our solar system (Hoppe & Ott, 1997; Clayton & Nittler, 2004). In addition, isotopic ratios of specific grains including SiC have been identified as coming from the nuclear processes that only occur inside particular types of stars (many references can be found in Clayton & Nittler, 2004).

In fact, the first identification of natural SiC (as opposed to the synthetic SiC which was in use as an abrasive at that time) was made through an investigation of meteorites by Moissan (1904, and in his honor naturally occurring SiC is sometimes called "moissanite"; this term is also now used for synthetic SiC used as a gemstone). Much later SiC was the first presolar grain to be found in meteorites (Bernatowicz et al., 1987) and remains the best studied (Bernatowicz et al., 2006, and references therein); an important reason for this is that SiC is impervious to acidic assault, and so one can relatively easily obtain SiC grains from a meteorite by simply dissolving it in acid and looking at the remnants for the SiC grains.

The two decades of work on presolar SiC have led to several important conclusions, among which are Bernatowicz et al. (2006);

1. Most ($\sim 99\%$) SiC presolar grains were formed around C stars.

2. $\approx 95\%$ of the SiC grains that could be identified as coming from AGB stars appear to have originated around low-mass carbon stars ($<3\,\mathrm{M}_\odot$), based on nucleosynthesis models of isotopic compositions.

3. All the presolar SiC grains are crystalline (not amorphous).

4. Most (≈80%) presolar SiC grains are of the β polytype, with the remainder comprised of the 2H α polytype or intergrowths of these two polytypes (this analysis was performed by using high-resolution transmission electron microscopy to examine the lattices of presolar grains; see also Daulton et al., 2003).

5. With one exception, SiC grains have not been found in the cores of carbon presolar grains (unlike other carbides: TiC, ZrC, and MoC); in other words, presolar SiC grains are virtually never found coated with carbon.

6. The grain size distribution of the SiC grains includes both very small and very large grains ($1.5\,\mathrm{nm} \rightarrow 26\,\mu\mathrm{m}$), with most grains in the 0.1–1μm range.

It is important to remember, though, that this kind of evidence has to be given careful thought before being used in other kinds of analysis. As an example, consider the grain size distribution given in 6. above. One might uncritically use this size distribution as the actual SiC grain size distribution present around carbon stars; however, this leads to discrepancies with actual observations (Speck et al., 2009). It is possible that grains of certain sizes are preferentially destroyed as they move through the interstellar medium, or the techniques used to obtain and analyze the grains may be biased towards some grain sizes over others. So, one can see that though the meteoritic data is extremely useful, it is only through a combination of both meteoritic and observational evidence that the most accurate results can be obtained.

Chapter 5

Observations of Carbon Stars and the Dust Condensation Sequence

"True learning must not be content with ideas which are, in fact, signs, but must discover things in their individual truth." - Umberto Eco

5.1 Introduction

In section 2.2.5 we briefly examined the dust shell that forms around AGB stars with C/O ratio > 1, and then in section 4.3 we discussed this in more detail; in particular, we looked at the many studies of the $\sim$11 μm feature and the contradictory conclusions reached by that research. In an attempt to resolve these contradictions, we analyzed the spectra of a collection of C stars, examining not only the $\sim$11 μm feature but also the molecular bands present in the spectra of these stars, and a $\sim$9 μm feature that was also investigated in several of the previous studies.

This research was previously published in Thompson et al. (2006), for which this author was a co-author.

5.1.1 $\sim$11 μm feature

The chararacteristic $\sim$11 μm SiC feature present in the spectra of C stars has been discussed extensively (Baron et al., 1987; Willems, 1988; Chan & Kwok, 1990; Goebel et al., 1995; Speck et al., 1997; Sloan et al., 1998; Speck et al., 2005). Datasets including the Infrared Astronomical Satellite (*IRAS*; Neugebauer et al., 1984) Low Resolution Spectrometer (LRS), the Infrared Space Observatory (*ISO*; Kessler et al., 1996) Short Wavelength Spectrometer (SWS; de Graauw et al., 1996) and the United Kingdom Infrared Telescope (UKIRT) have been used to study the $\sim$11 μm feature. However, in most cases the dataset used for the analyses comprised *IRAS* LRS spectra. All these analyses looked at the strength and peak position of the $\sim$11 μm feature.

One justification for the many studies of the $\sim$ 11 μm spectral feature is that it is of some interest to know which polytypes of SiC can form around C stars (and the exact spectral feature these polytypes would produce), because the crystal structure of SiC grains contains important information about the environment these grains formed within and also their cooling history. This problem has not yet been fully resolved (Speck et al., 1999; Pitman et al., 2008), and theoretical analysis is made more complicated by the fact that the polytypes which form depend not only on the temperature but also on the gas pressure in the surrounding environment (Daulton et al., 2002). In the kind of environment we expect to find around C stars, however, it is predicted that below about 2400 K the β polytype of SiC is most likely to form. When heated to above 2400 K β-SiC will transform into 6H α-SiC, but it is energetically unfavorable for the reverse process to occur (Speck et al., 1997, and references therein).

Though the majority of the results have been based on the same *IRAS* LRS data, the apparent trends are not consistent from one study to the next. Furthermore, there have been several hypotheses proposed to explain the apparent trends in the shape, strength and position of the SiC feature which seem to be contradictory. Each analysis took a slightly different approach, some simply subtracting a stellar continuum from the *IRAS* LRS spectra (e.g. Sloan et al., 1998). Some analyses divided the spectra by the continuum (either the dust continuum or the assumed stellar continuum); and some both divided and subtracted by continua (e.g. Willems, 1988). The justifications for each approach are discussed in section 3.4 . Given the range of analytical techniques used, it is not entirely surprising that the results are not altogether consistent. There is a trend that appears to be consistent amongst all analyses, i.e. that the $\sim$11 μm SiC feature gets weaker as the underlying dust continuum temperature ($T_{\rm cont}$) decreases. Both Baron et al. (1987) and Chan & Kwok (1990) suggested this behavior is due to SiC grains becoming coated by a mantle of the more abundant amorphous carbon. This hypothesis is however not supported by meteoritic evidence, which shows that SiC grains from carbon stars are rarely coated in carbon (Clayton & Nittler, 2004, and references therein). To date only a single presolar SiC grain with a carbon mantle has been found (discussed below in section 4.3.1). Speck et al. (1997) put forth the idea that the reason for the behavior of the emission/absorption feature is that there is SiC self-absorption by cooler particles further out in the circumstellar dust shell (see also Cohen, 1984). These cooler dust grains absorb what was emitted by warmer SiC grains closer to the star. Speck et al. (1997) used ground-based UKIRT CGS3 data and showed that every star in their sample whose $T_{\rm cont} < 1200$ K was best fitted by self-absorbed SiC, whether the $\sim$11 μm feature was in net emission or net absorption.

Whereas the trend of the $\sim$11 μm SiC feature strength with $T_{\rm cont}$ appears to be fairly consistent between studies, the variation in position of this feature with $T_{\rm cont}$ has been found to behave differently in the separate analyses. Baron et al. (1987) found that, as $T_{\rm cont}$ decreases and the peak-continuum strength of the $\sim$11 μm feature diminishes, the peak position moves from 11.3 μm to 11.7μm. Speck et al. (2005) showed that such shifts in the peak of the $\sim$11 μm SiC feature may be attributable to a combination of optical depth and grain sizes. SiC absorption features tend to peak at shorter wavelengths ($\sim 10.8\mu$m). Speck et al. (2005) suggest that the only way to see a shift in the absorption feature to 10.8 μm is if the absorbing grains are larger than the emitting grains. This suggests that grains forming in circumstellar shells get smaller as the parent stars evolve. Willems (1988) found stars with high $\mathrm{T_{cont}}$ have their $\sim$11 μm feature located at 11.7 μm, while features at 11.3 μm are associated with lower $\mathrm{T_{cont}}$. This result is the opposite of that presented by Baron et al. (1987). Goebel et al. (1995) concur with Willems (1988) regarding the trend of the position of $\sim$11 μm emission feature (i.e. it peaks at longer wavelengths for higher $\mathrm{T_{cont}}$).

In addition to these analyses using *IRAS* data, Speck et al. (1997) performed a similar analysis on 32 ground-based UKIRT CGS3 data and found no correlation between the SiC peak wavelength and the continuum temperature, but did find one between SiC peak-to-continuum ratio (strength) and $\mathrm{T_{cont}}$. Using 19 *ISO* SWS spectra, Sloan et al. (2006) found that the 'central' wavelength of the SiC feature increases monotonically to about 11.6 μm as the continuum temperature decreases in agreement with Baron et al. (1987).

The difference in trends with $\mathrm{T_{cont}}$ may be attributable to the differences in the adopted values of $\mathrm{T_{cont}}$. The poor resolution and wavelength coverage of *IRAS* may lead to underestimation of the continuum, and the effect is not necessarily constant across the spectrum. For instance, there are well-known molecular absorption bands that coincide with the short wavelength cut-off for *IRAS* (due to HCN, C_2H_2 and CS). These absorptions, together with the lower sensitivity at these wavelengths, lead to an apparent dip in the *IRAS* spectra around 7-8 μm, as demonstrated in Figure 5.1f. This short wavelength drop-off in *IRAS* LRS spectra mimics a lower temperature blackbody continuum. This may explain why our minimum $\mathrm{T_{cont}}$ values for *IRAS* data appear to be considerably higher than those of previous studies using the same dataset (see section 5.3). For example, Baron et al. (1987) had $500 \gtrsim T_{\rm cont} \gtrsim 3000$ K. In addition, to the choices of continua, their application to the problem at hand (division by and/or subtraction of) leads to further problems in comparing the results. These issues are discussed in more detail in section 5.3.

Dissimilar analyses and interpretations of the same data yield no clear correlations between changes in spectral features and the evolution of dust, though it has been agreed that the spectra of carbon stars change with the evolution of the star. Therefore, there are some accepted trends: early in the carbon star phase, there is a low mass-loss rate, an optically thin shell, and a strong, narrow, and sharp $\sim$11 μm SiC feature. As the mass-loss rate increases, the shell becomes optically thicker, and the emission feature broadens, flattens, and weakens, until, eventually it appears in absorption (Speck et al., 1997, 2005).

5.1.2 9 μm feature

Another apparent spectral feature of carbon stars appears at $\sim 9\mu$m. Willems (1988) suggested that this feature is of molecular origin because its strength correlates with the strength of the 3 μm molecular absorption band. However, Willems (1988) used NIR data observed at a different epoch to the IRAS data (see Noguchi et al., 1981). Given the intrinsic variability of AGB stars (see section 5.2.1), this correlation may be meaningless. Correlations (or lack thereof) of various spectral parameters with the strength of the 3 μm molecular absorption band are investigated in section 5.4.3. Baron et al. (1987) and Goebel et al. (1995) found that this feature emerges as $T_{\rm cont}$ decreases; Sloan et al. (1998) found that the 9 μm feature is associated with higher $T_{\rm cont}$. However, the definition of $T_{\rm cont}$ varies, making it difficult to interpret differing trends. It is possible that the emergence of the $\sim 9\mu$m feature is an artifact caused by underestimation of molecular absorption bands (Aoki et al., 1999). This is investigated in section 5.4.1.

5.1.3 Purpose

The differing interpretations of the *IRAS* LRS data probably arise from a combination of different 'best fit' underlying continua and the application of these continua (i.e. division by or subtraction of, etc.). It has been suggested that the low resolution of *IRAS* LRS data precludes the identification of the potentially strong molecular bands due to HCN, C_2H_2 and CS, and thus hinders the proper identification of the continuum level in these data (Aoki et al., 1999). The limited wavelength coverage of the *IRAS* LRS data exacerbates the problem. Since one of the major components of the analysis uses $T_{\rm cont}$, the choice of continuum is crucial. Strong molecular absorptions can artificially increase the apparent strength of the SiC feature. The relative strengths of the absorption features can also vary (Jørgensen et al., 2000) causing complications in fitting the continuum temperature.

Here we present a reassessment of the 'best-fit' continuum for 26 known carbon stars using the *IRAS* LRS data as well as *ISO* SWS spectra in order to determine the true effect of molecular bands on the identification of the continuum temperature. Using the newly-defined continua, we generate both continuum-divided and continuum-subtracted spectra and analyze the trends (or lack thereof) using the shape, strength and position of the SiC feature and associated mid-IR features (section 5.3). In addition, using the *ISO* SWS spectra, we determine whether there are any trends associated with the relative strength of the molecular bands. We also investigate whether the apparent $\sim 9\mu$m feature is real or an artifact (section 7.4). Furthermore, we present radiative transfer modeling to show that, in fact, we should not expect to see such trends (section 5.5). The reasons for this are addressed in section 5.6.

5.2 Observations

We examined spectra of 26 known carbon stars observed spectroscopically using both *IRAS* LRS and *ISO* SWS (See table 5.1.).

The raw *ISO* data were extracted from the *ISO* data archive, and the *IRAS* dataset was obtained from Kevin Volk's website[1] (Volk et al., 1991). For the *ISO* data we used pipeline version OLP 10.1 from the *ISO* data archive. Individual spectral sub-bands were cleaned from glitches (caused by cosmic ray particles) and other bad data sections. Next they were flat-fielded, sigma-clipped (using the default values $\sigma = 3$) and rebinned, the final spectral resolution ($R = \lambda/\Delta\lambda$), which ranged from 200-700, depending on the scanning speed of the SWS grating during the observation (Leech, 2003). The resulting spectra are shown in Fig 5.1.

5.2.1 Source variability

In the majority of our sources, the spectra from both *ISO* and *IRAS* are essentially identical. However, in several cases (∼25%), spectra taken by *ISO* and *IRAS* are not overlapping. This is simply due to the fact that these sources are intrinsically variable.

Given the intrinsic variability of our sources, one might expect to see as many as half our sample sources to show different spectra at different epochs. The sources for which the *ISO* and *IRAS* spectra are offset are: HV Cas, V384 Per, IRC+10°216, Y CVn, RU Vir, RY Dra, LP And (see figure 5.1b, f, k, m, n, o & y). Comparing these

---

[1] http://www.iras.ucalgary.ca/∼volk/getlrs_plot.html

Table 5.1: Target sources.

IRAS Name	Other Name(s)	ISO TDT Number	Spectral Class	Variable Type
00172+4425	VX And	42801502	C4,5 (N7)	SRa
01080+5327	HV Cas	62902503	C4,3−C5,4e (Ne)	M
01246−3248	R Scl	41401514	C6,5ea (Np)	SRb
02270−2619	R For, AFGL 337	82001817	C4,3e (Ne)	M
03075+5742	V623 Cas	64601230	C4,5J (R5)	Lb
03229+4721	V384 Per	81002351	C (N)	M
03374+6229	U Cam	64001445	C3,9−C6,4e (N5)	SRb
05028+0106	W Ori	85801604	C5,4 (N5)	SRb
05421+2424	TU Tau, AFGL 812	85403210	C5,4 (N3)	SRb
06226−0905	V636 Mon	86706617	C	M
09452+1330	IRC+10°216, CW Leo	19700159	C9,5	M
12226+0102	SS Vir	21100138	C6,3e (Ne)	SRa
12427+4542	Y CVn, AFGL 1576	16000926	C5,4J (N3)	SRb
12447+0425	RU Vir	24601053	C8,1e (R3ep)	M
12544+6615	RY Dra	54300203	C4,5J (N4p)	SRb
15477+3943	V CrB	57401003	C6,2e (N2e)	M
17556+5813	T Dra	42902712	C6,2e−C8,3e (N0e)	M
18476−0758	S Sct	16401849	C6,4 (N3)	SRb
19017−0545	V Aql, AFGL 2314	16402151	C5,4−C6,4 (N6)	SRb
20396+4754	V Cyg	08001855	C5,3e−C7,4e (Npe)	M
21168−4514	T Ind	37300427	C7,2 (Na)	SRb
21358+7823	S Cep	75100424	C7,4e (N8e)	M
21399+3516	V460 Cyg	42201734	C6,4 (N1)	SRb
21440+7324	PQ Cep	42602373	C6−,3e (N)	M
23320+4316	LP And, IRC+40540	38201557	C8,3.5e	M
23438+0312	TX Psc, AFGL 3147	75700419	C7,2 (N0)(Tc)	Lb

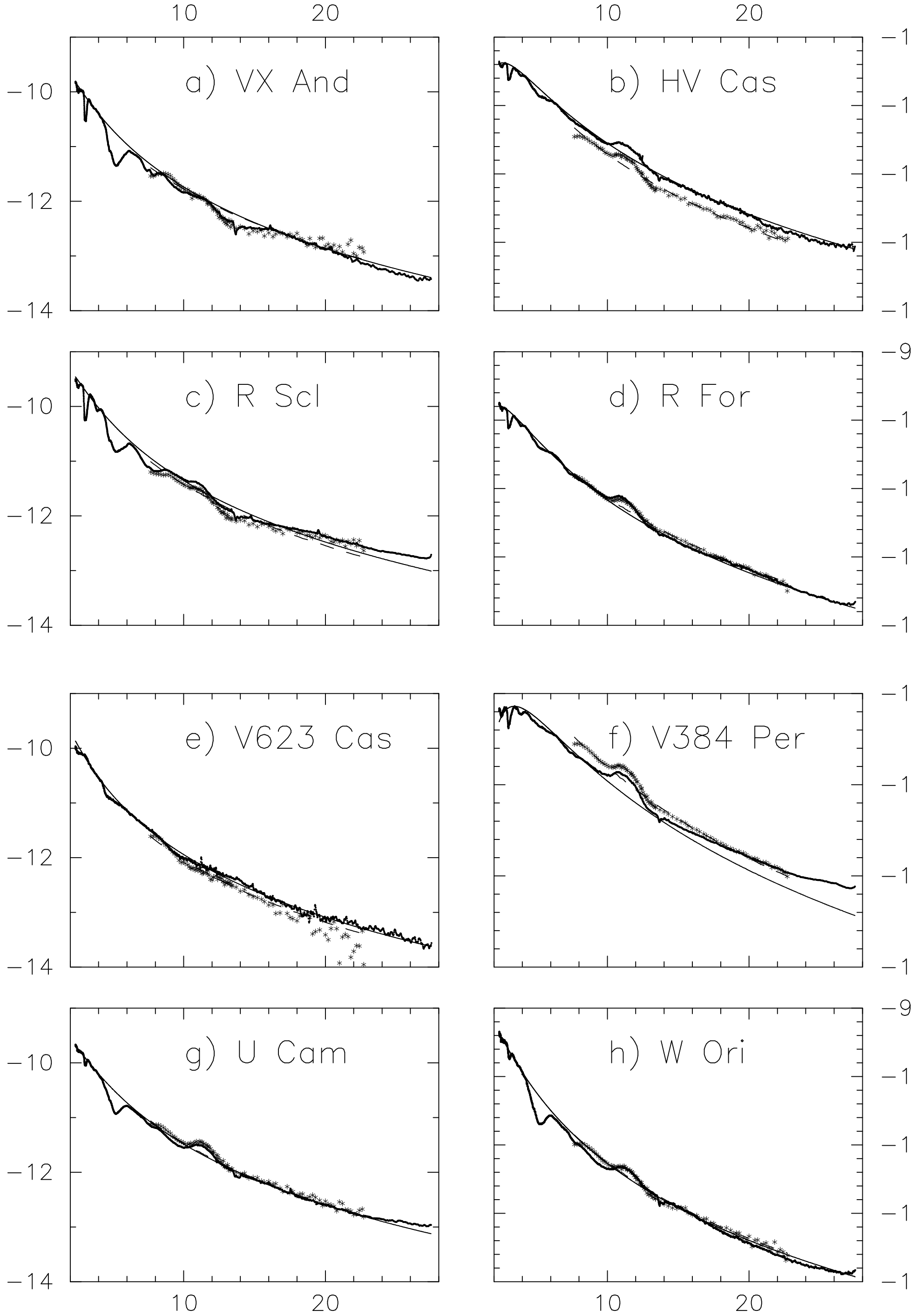

Figure 5.1: *IRAS* LRS and *ISO* SWS spectra of carbon stars together with their fitted underlying continua. x-axis is wavelength (μm); y-axis is Log[Flux density (W m$^{-2}\mu$m^{-1})]; *IRAS* LRS data = asterisks "*".; *ISO* SWS data = small dots; fitted continuum to *ISO* SWS = dashed line; fitted continuum to *IRAS* = solid line.

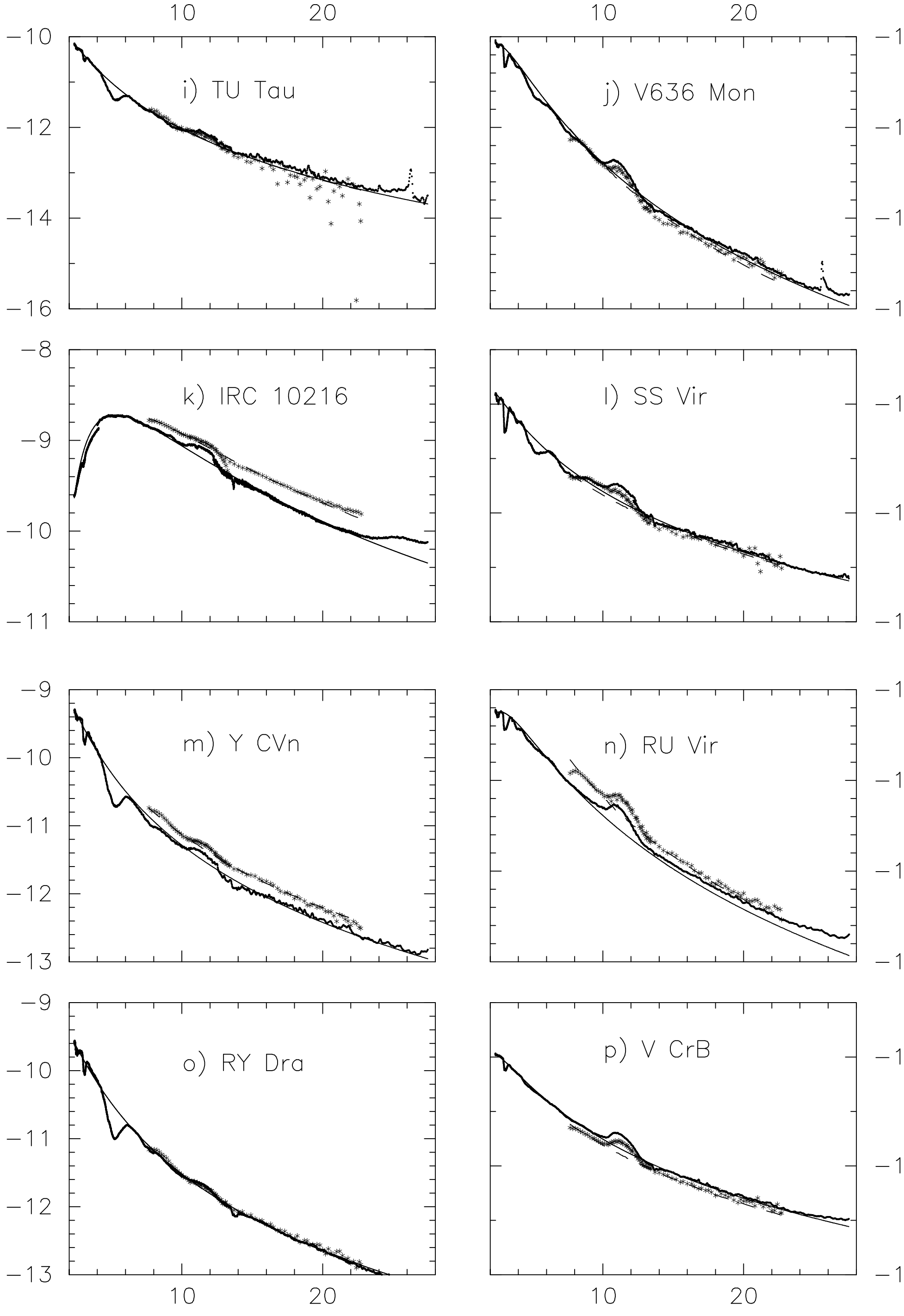

Figure 5.1: *IRAS* LRS and *ISO* SWS spectra of carbon stars continued.

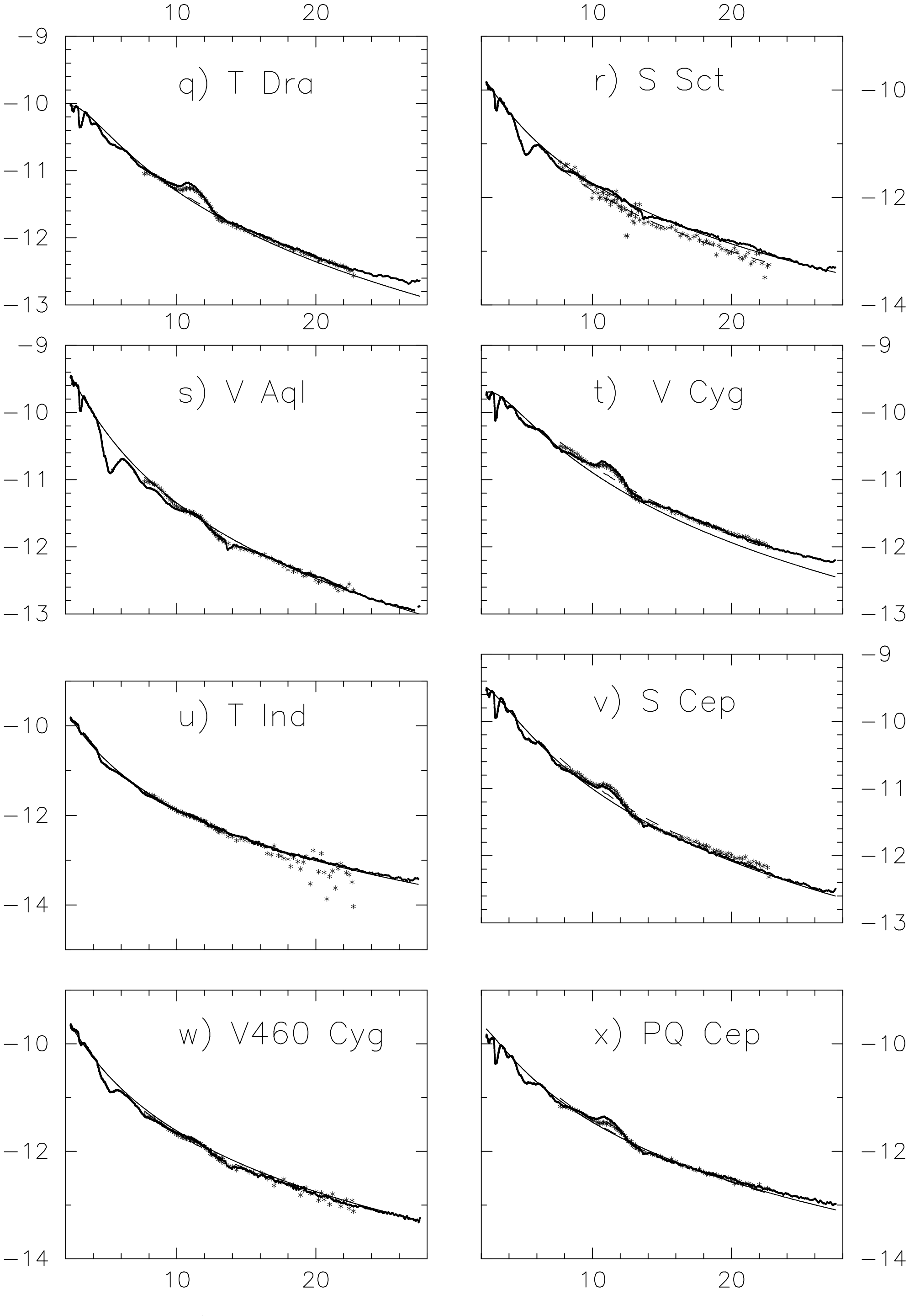

Figure 5.1: *IRAS* LRS and *ISO* SWS spectra of carbon stars continued.

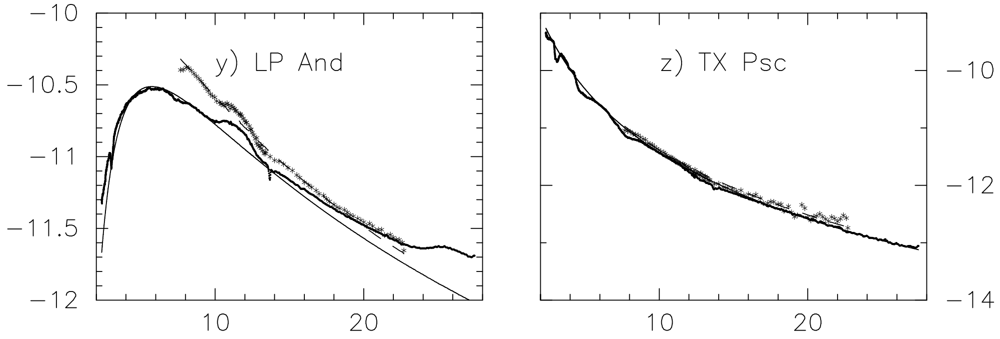

Figure 5.1: *IRAS* LRS and *ISO* SWS spectra of carbon stars continued.

seven sources to the entire sample, 5 of these are Mira variables (see table 5.2), have very long periods ($>$ 433 days), and are intrinsically brighter than the average of the entire set. Approximately half the Mira variables in our sample show offset spectra, whereas $\lesssim$15% of spectra of the non-Mira variables display this characteristic. Clearly the large amplitude variations of Mira variables has larger effect on the IR spectrum of these stars than does the smaller amplitude changes in non-Mira variables.

It is worth noting that the continuum-divided spectra of HV Cas (figure 5.2b) are essentially identical for both *ISO* and *IRAS*, whereas the other six sources for which *ISO* and *IRAS* spectra are offset, show varying degrees of difference in their continuum-divided spectra. This phenomenon can also be seen in analyses of "extreme" carbon star spectra. The UKIRT CGS3 ground-based mid-IR spectrum of AFGL 3068 has a markedly different brightness and slope to that observed by *ISO* (see Speck et al., 1997; Clément et al., 2003; Speck et al., 2005; Pitman et al., 2006). The underlying continuum temperature was seen to change from ∼380 K (Speck et al., 1997) to ∼295 K (Clément et al., 2003; Pitman et al., 2006) in these observations. However, the continuum-divided spectra are essentially identical for both epochs (Pitman et al., 2006), implying that while the energy flow through the circumstellar shell has changed, the absorbance properties of the dust remain unaltered. This phenomenon is also observed for AFGL 5625 (Speck et al., 1997; Clément et al., 2005; Pitman et al., 2006).

Examining the continuum-divided spectra in figure 5.2 we can see that some spectra are identical for both *IRAS* and *ISO* data, whereas, even some sources with almost identical "undivided" spectra look quite different once their spectra have been continuum-divided. Therefore, the effect of the variability of the underlying AGB stars on the intrinsic nature of their circumstellar dust is not clear, and certainly not consistent from star to star. In some cases, the bulk absorbance properties of the dust remain more or less unchanged, and in others they are markedly different. This observation is potentially devastating to any attempt to decipher carbon star dust condensation sequences.

5.3 Method

In order to re-analyze and compare with previous studies, we fitted continua to our spectra. Continua are assumed to be either blackbodies or modified blackbodies (i.e. $B \times \lambda^{-\beta}$)

Initially we applied our technique to the *IRAS* dataset without reference to the *ISO* data. For each spectrum, the variables of continuum temperature, β, and normalization wavelength were adjusted to find an underlying continuum that fitted the spectrum well. While the default continuum was a pure blackbody, it was also possible to change the emissivity law to produce a modified blackbody.

In general, pure blackbodies were more successful than modified blackbodies, though some of the modified blackbody continua for the *IRAS* spectra fit as well as the pure blackbodies. Once the underlying continuum fitting for the *IRAS* data was accomplished, we applied the fitting technique to the *ISO* data. It was not possible to achieve good fits to the *ISO* data using modified blackbodies. The continuum-fitting of the *ISO* data was performed without reference to the *IRAS* data in order to compare the independent results from each dataset.

The results of continuum-division and continuum-subtraction of our spectra are shown in figures 5.2 and 5.3.

The predominance of the pure blackbody continua suggests that the dust is optically thick close to the star and we are seeing the surface at the temperature of underlying continuum where the shell transitions from optically thin to optically thick.

After assigning continua to all 26 spectra for both *IRAS* and *ISO*, the $\mathrm{T}_{\mathrm{cont}}$ values for a single source as assessed from both *IRAS* and *ISO* were compared (See table 5.2.). The difference between the continuum temperatures for *IRAS* and *ISO* were compared to the absolute temperature. No correlations were found.

It is clear from the values in table 5.2 that the spread in ΔT is similar for both Miras and non-Mira variables. The difference in temperatures for the two datasets (ΔT) could be due to the poor resolution and wavelength coverage of *IRAS* or perhaps to the intrinsic variability of the star. There are well-known molecular absorption bands that coincide with the short wavelength cut-off for *IRAS*. These absorptions, together with the lower sensitivity at these wavelengths, lead to an apparent dip in the *IRAS* spectra around 7-8 μm, as demonstrated in Figure 5.1f. This short wavelength drop-off in *IRAS* LRS spectra mimics a lower temperature blackbody continuum. Because of the possible impact of molecular bands, we ignored wavelengths shortward of $\sim 8.5\mu$m in fitting our continua. This may explain why our minimum $\mathrm{T}_{\mathrm{cont}}$ values for *IRAS* data appear to be considerably higher than those of previous studies using the same dataset. For example, Baron et al. (1987) had $500 \lesssim \mathrm{T}_{\mathrm{cont}} \lesssim 3000\,\mathrm{K}$.

As suggested by Aoki et al. (1999), it is possible that the cause of the difference in temperatures for the two datasets (ΔT) is due to varying molecular absorption band

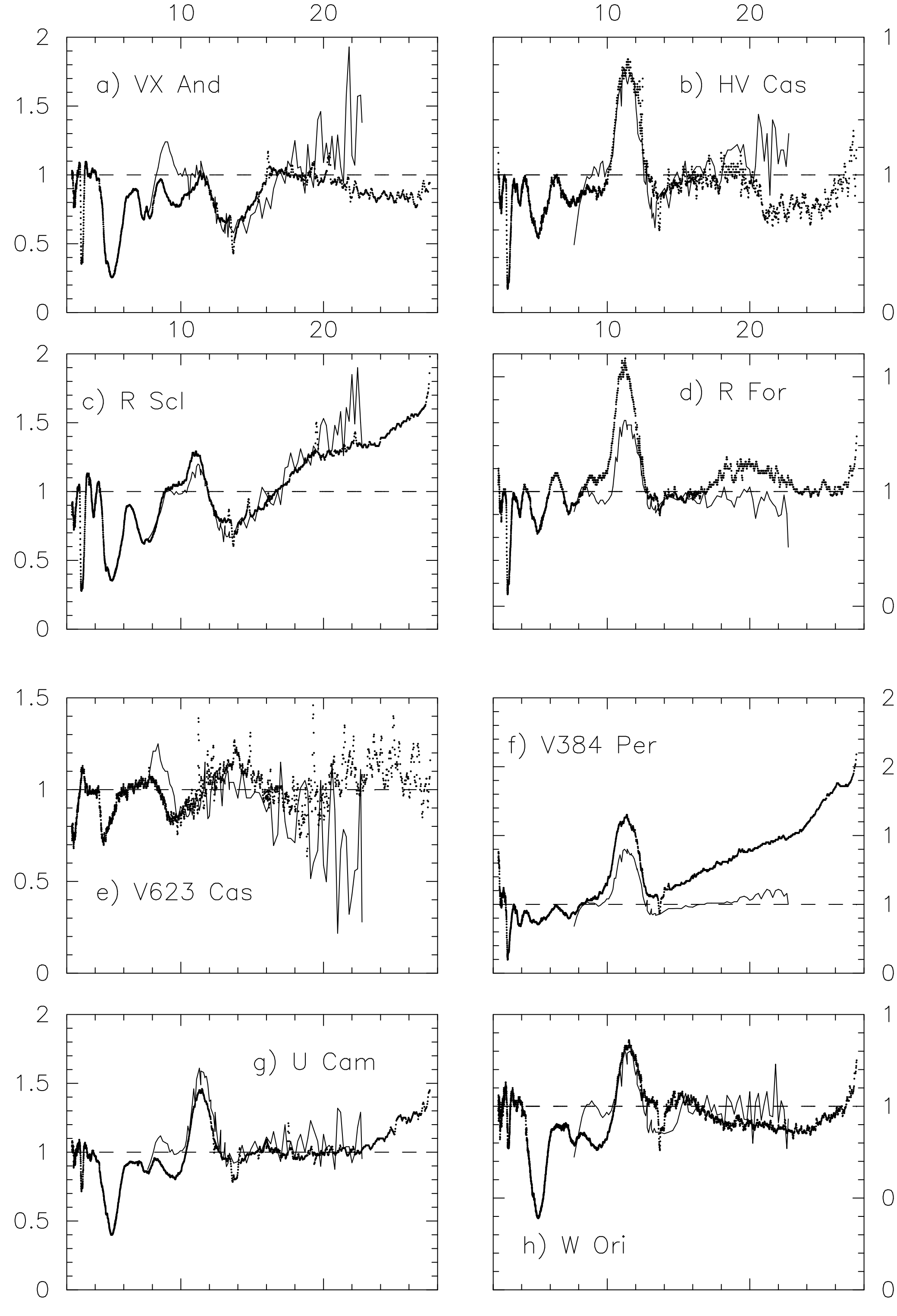

Figure 5.2: Continuum-divided *IRAS* LRS and *ISO* SWS spectra of carbon stars. x-axis is wavelength (μm); y-axis is dimensionless; *ISO* SWS = bold dots; *IRAS* LRS = solid line; dashed line denotes $y = 1$.

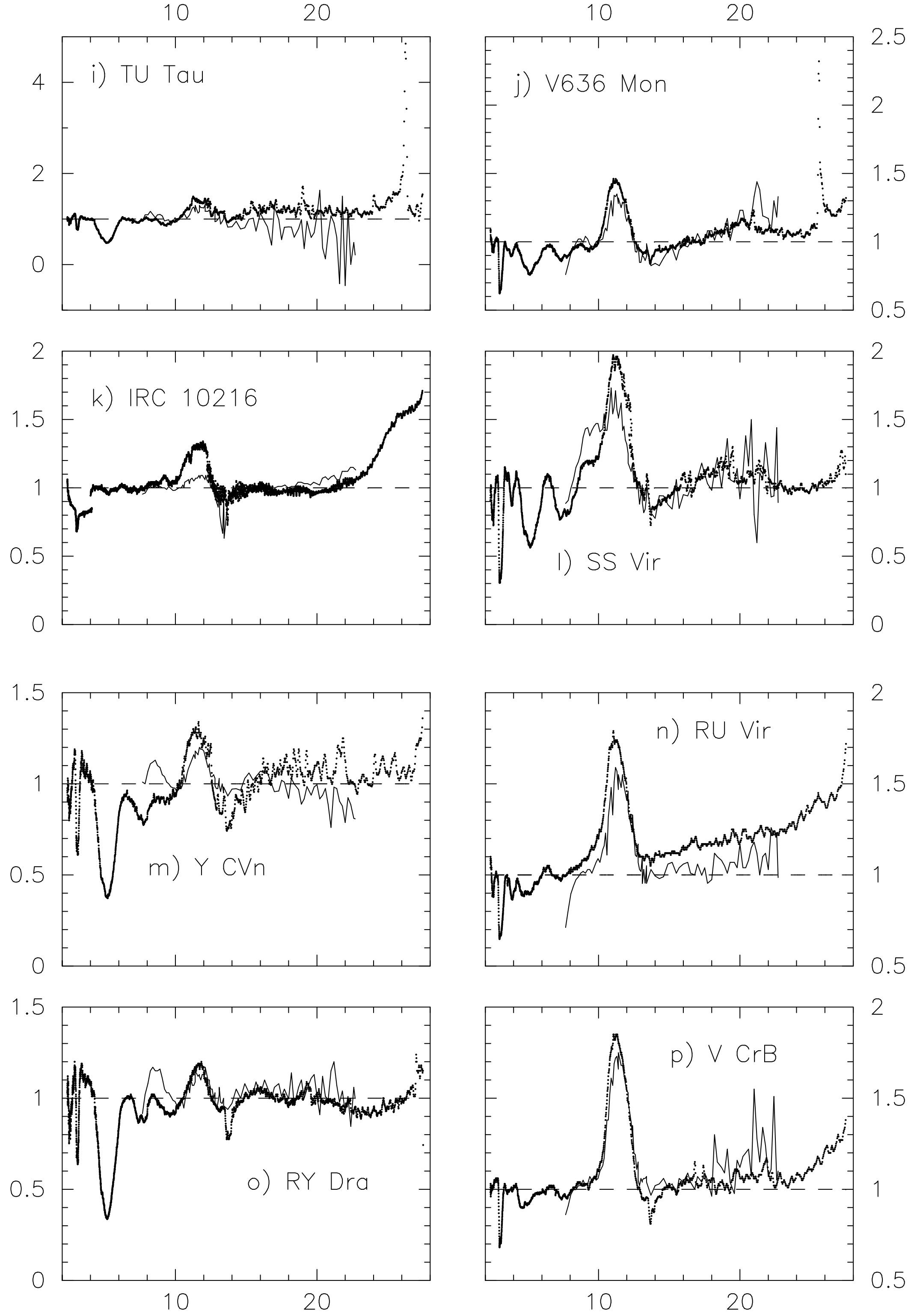

Figure 5.2: Continuum-divided spectra continued.

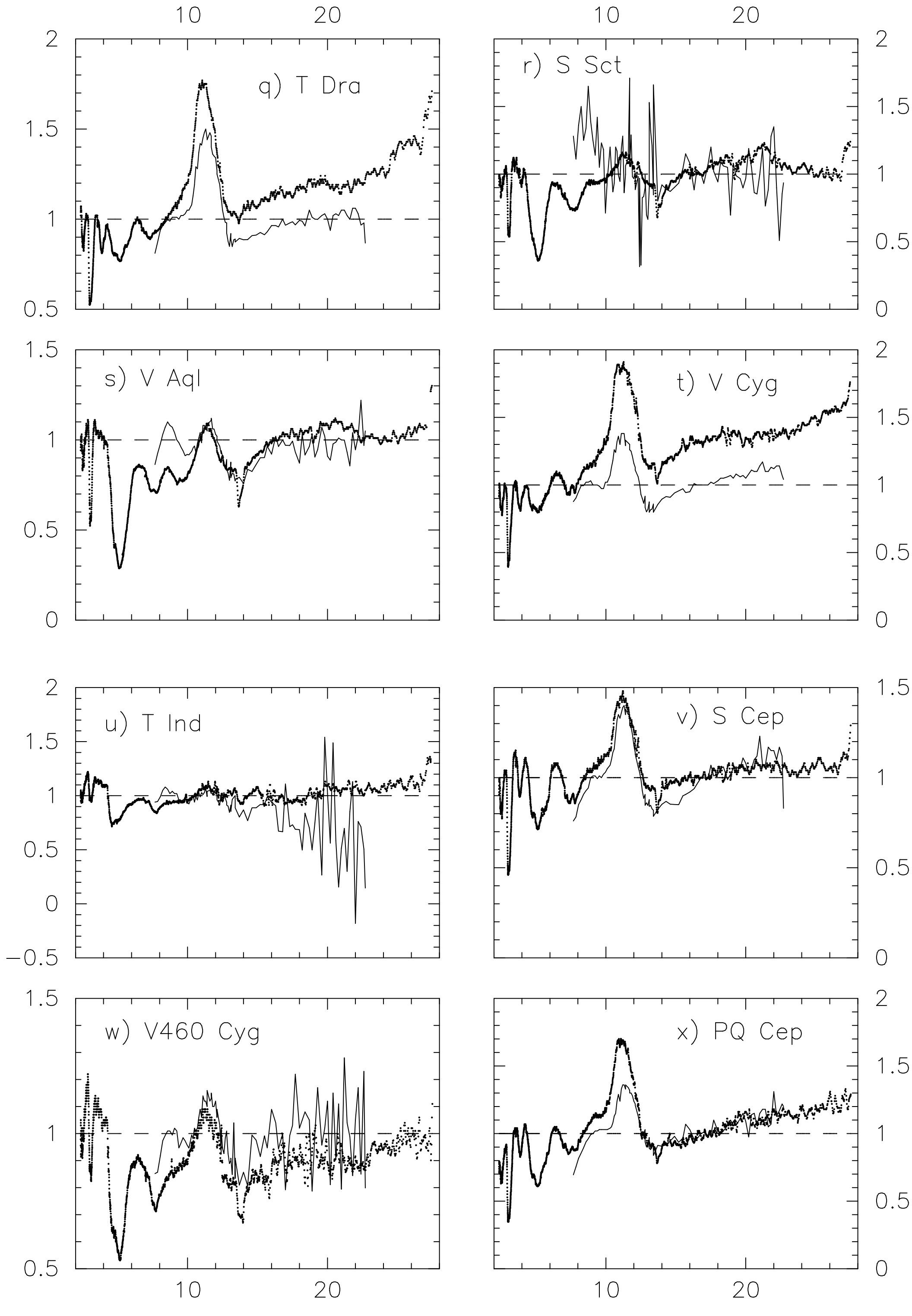

Figure 5.2: Continuum-divided spectra continued.

Table 5.2: Underlying continuum temperatures obtained for both *IRAS* and *ISO*, as well as the periods, V_{max}, V_{min}, and variable types of all 26 sources.

Source Name	T_{IRAS}	T_{ISO}	ΔT	Period (days)	V_{max}	V_{min}	Variable Type
VX And	1475	2165	+690	369	7.8	9.3	SRa
HV Cas	1455	1100	−355	527	12.9	17.2	M
R Scl	2150	2115	−35	370	9.1	12.9	SRb
R For	1100	1272	+172	388.73	7.5	13	M
V623 Cas	2800	2850	+50	—	9	9.8	Lb
V384 Per	920	843	−77	535	11.3	14.2	M
U Cam	1950	1850	−100	—	11	12.8	SRb
W Ori	1900	2140	+240	212	8.2	12.4	SRb
TU Tau	2850	2050	−800	190	5.9	9.2	SRb
V636 Mon	1725	1217	−508	—	6.2	9.8	M
IRC+10°216	480	550	+70	630	10.96	14.8	M
SS Vir	1500	1900	+400	364.14	6	9.6	SRa
Y CVn	1425	2475	+1050	157	7.4	10	SRb
RU Vir	2225	1075	−1150	433.2	9	14.2	M
RY Dra	1850	2200	350	200	6.03	8	SRb
V CrB	1450	1475	+25	357.63	6.9	12.6	M
T Dra	960	1175	+215	421.62	7.2	13.5	M
S Sct	2450	2100	−350	148	9.63	10.9	SRb
V Aql	1675	2100	+425	353	6.6	8.4	SRb
V Cyg	1085	1120	+35	421.27	7.7	13.9	M
T Ind	1980	2660	+680	320	7.7	9.4	SRb
S Cep	1550	1400	−150	486.84	7.4	12.9	M
V460 Cyg	2450	2350	−100	180	5.57	7	SRb
PQ Cep	2800	1735	−1065	—	10.5	15.5	M
LP And	660	505	−155	—	16.9	20.6	M
TX Psc	2350	3475	+1125	—	4.79	5.2	Lb

T_{IRAS} is the continuum temperature in K found by fitting a blackbody to the *IRAS* LRS data; T_{ISO} is the continuum temperature in K found by fitting a blackbody to the *ISO* SWS data; ΔT is the difference between the fitted continua temperatures for *ISO* and *IRAS* for a single source.

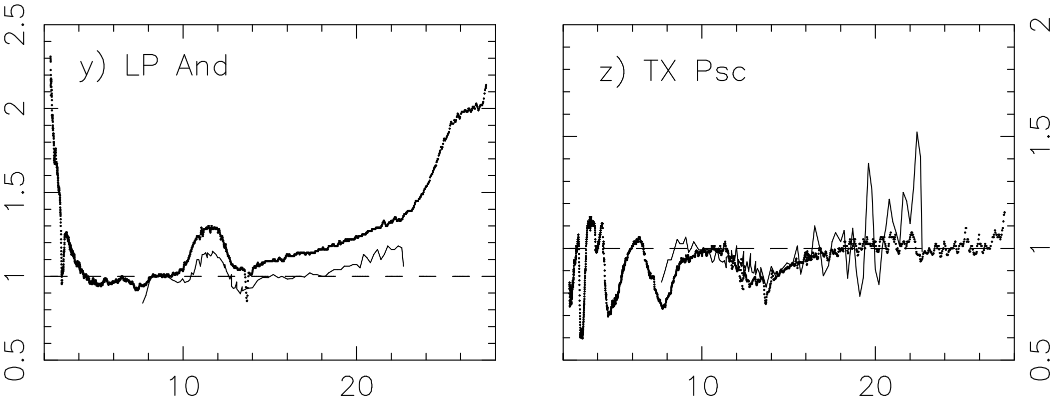

Figure 5.2: Continuum-divided spectra continued.

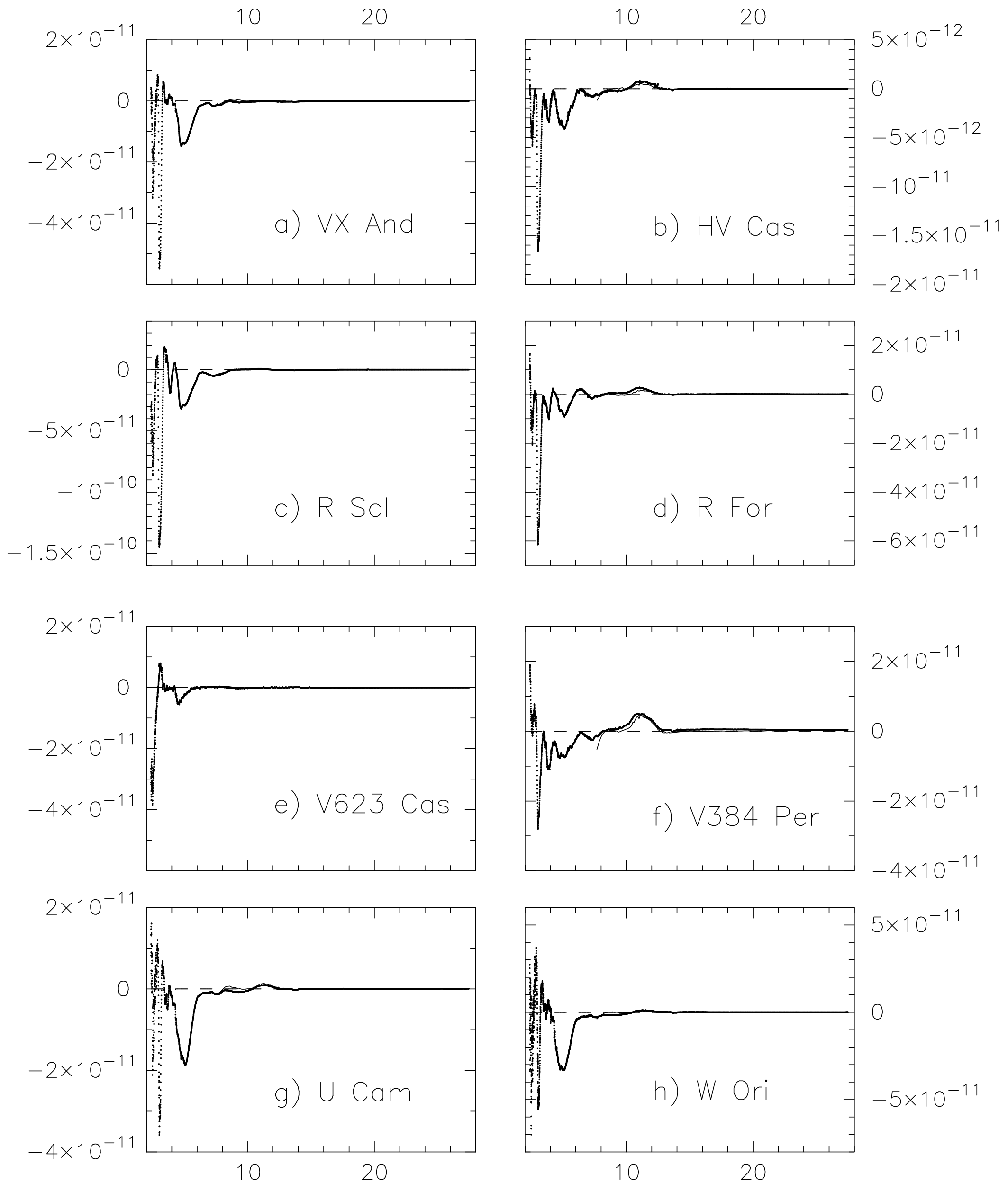

Figure 5.3: Continuum-subtracted *IRAS* LRS and *ISO* SWS spectra of carbon stars. x-axis is wavelength (μm); y-axis is Spectra minus Continuum in $\mathrm{W\,m^{-2}\mu m^{-1}}$); *ISO* SWS = bold dots; *IRAS* LRS = solid; dashed line denotes $y = 0$.

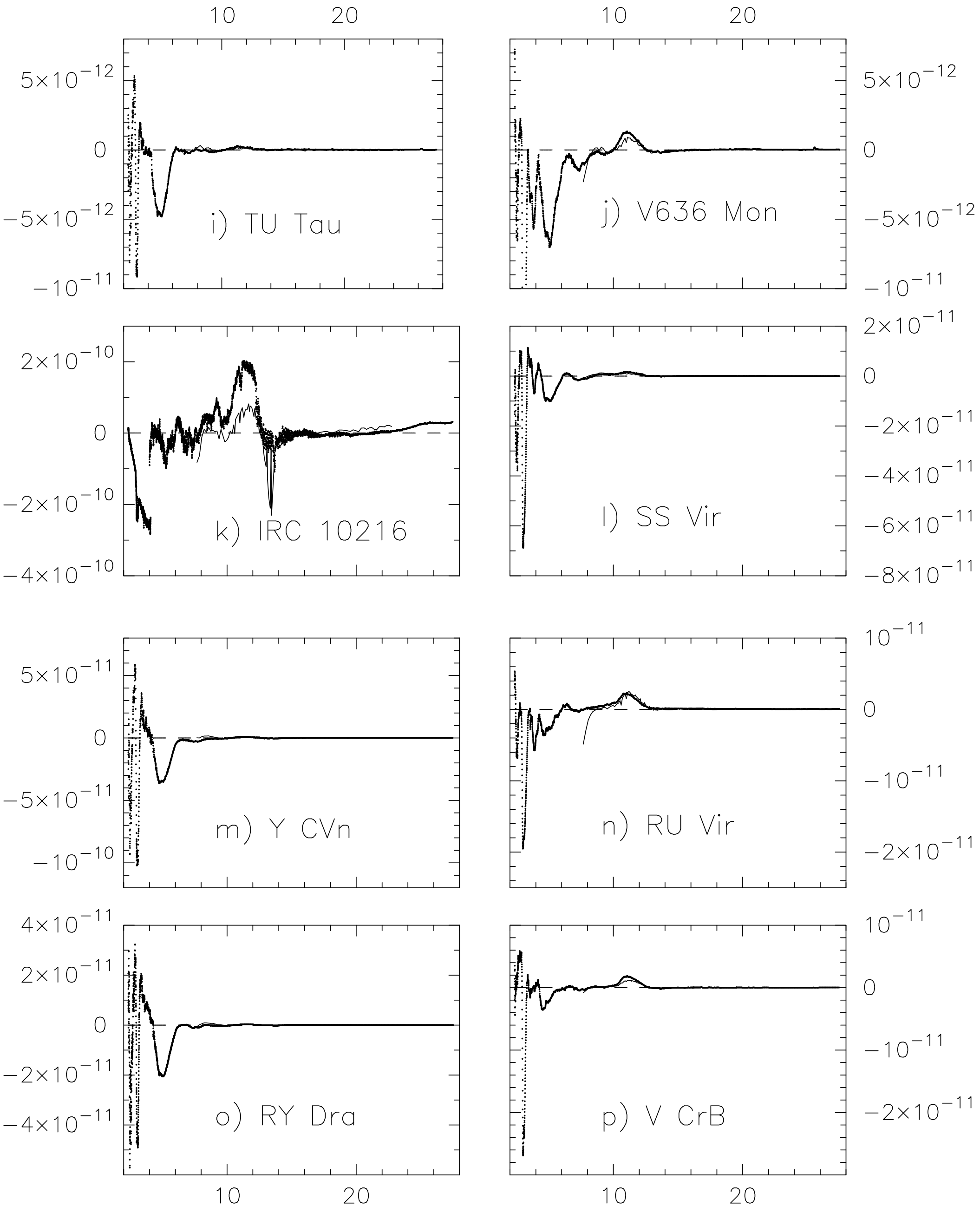

Figure 5.3: Continuum-subtracted spectra continued.

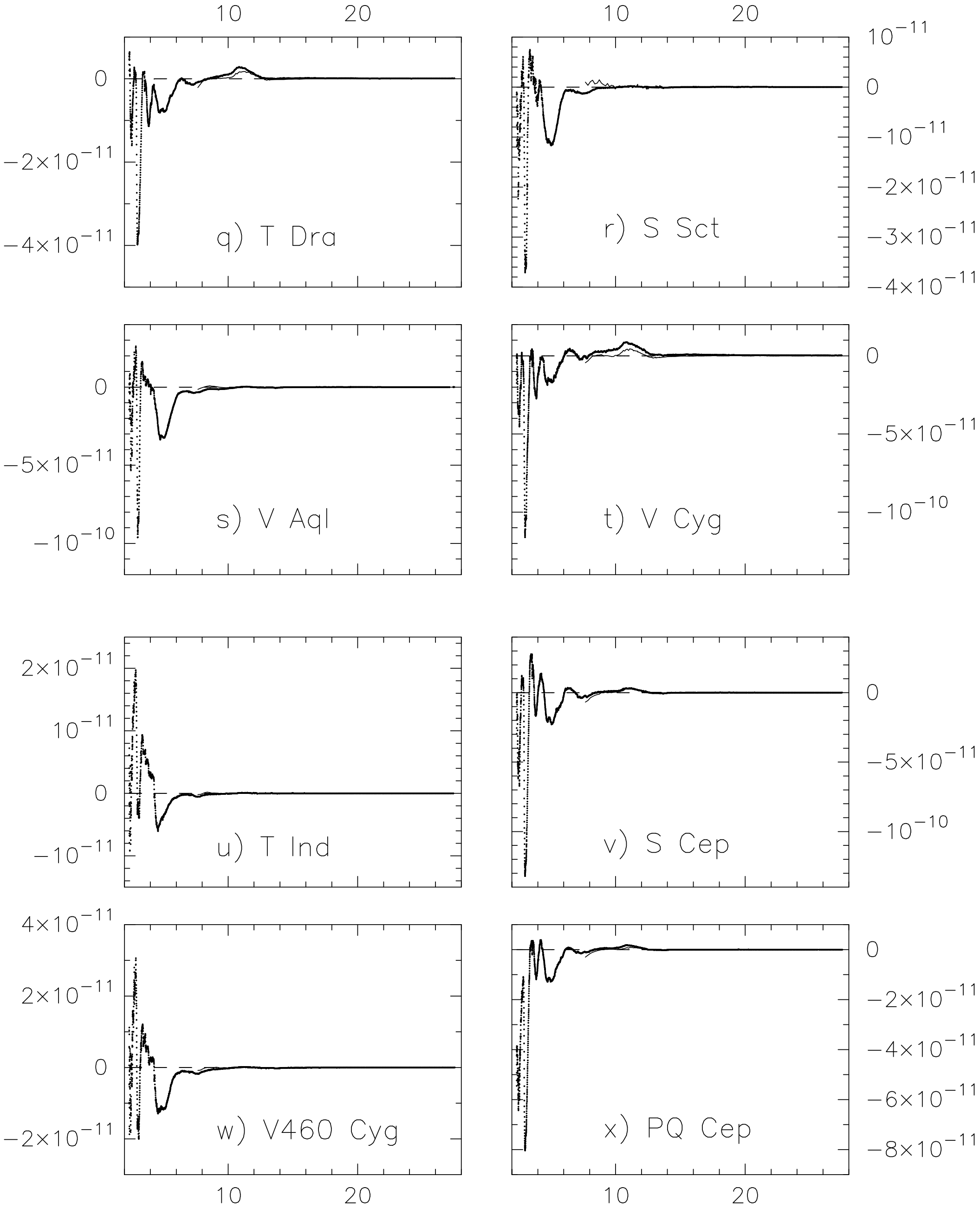

Figure 5.3: Continuum-subtracted spectra continued.

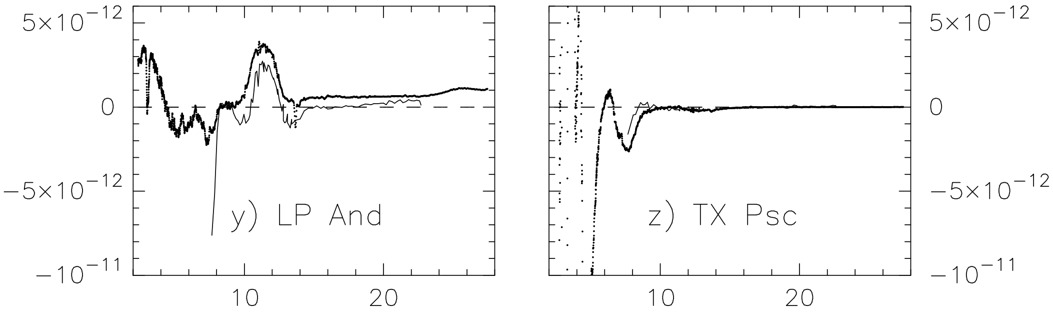

Figure 5.3: Continuum-subtracted spectra continued.

strengths. Furthermore, Jørgensen et al. (2000) showed that the relative strengths of different molecular bands varies, complicating this issue. Table 5.3 shows that there are no correlations between the $3\,\mu$m, 7–8$\,\mu$m or $13.7\,\mu$m molecular band strengths and underlying continuum temperatures ($T_{\rm cont}$, see also section 5.4.3).

To ensure our results are robust, we conducted the experiment using both continuum-divided and continuum-subtracted spectra (hereafter divided spectra and subtracted spectra respectively; see the discussion in section 3.4).

Each spectrum was divided by its assigned continuum in order to determine the characteristics of the solid-state spectral features (See Figure 5.2.). By applying this technique, the features are apparent from the underlying continuum. It is very important to have an accurate continuum temperature because the parameters that define the spectral features in continuum-divided spectra are greatly affected by the choice of continuum. The continuum-divided spectra were then analyzed in great detail looking for possible correlations between the SiC peak position, peak strength, and the assigned underlying continuum temperature. In addition, we also looked for similar correlations with molecular bands due to HCN, C_2H_2 and CS. Finally, the divided spectra of a single source for *IRAS* was compared to that of *ISO* to see how similar the results were. In addition to using continuum-divided spectra, we used continuum-subtracted spectra which were obtained using the same continuum used to produce the continuum-divided spectra (See Figure 5.3.).

Table 5.3: Determination coefficient (R-squared) values of silicon carbide and molecular band linear regression correlations of all 26 sources and without IRC+10°216.

	IRAS		*ISO*	
SiC Divided Correlation Type	Spectra (All 26)	Spectra less IRC+10°216	Spectra (All 26)	Spectra less IRC+10°216
Strength vs Peak position	0.1644	0.1355	0.3512	0.3567
Peak position vs T_{cont}	0.0036	0.0338	0.0044	0.0348
T_{cont} vs Strength	0.0002	0.0128	0.2710	0.3428
BC Strength vs BC position	0.2044	0.1775	0.3407	0.3454
BC position vs T_{cont}	0.0035	0.0317	0.0026	0.0282
T_{cont} vs BC Strength	0.0004	0.0134	0.2680	0.3388

	IRAS		*ISO*	
SiC Subtracted Correlation Type	Spectra (All 26)	Spectra less IRC+10°216	Spectra (All 26)	Spectra less IRC+10°216
Strength vs Peak position	0.0812	0.2487	0.0198	0.3304
Peak position vs T_{cont}	0.0365	0.1336	0.2165	0.3193
T_{cont} vs Strength	0.1893	0.3560	0.1397	0.4522
BC Strength vs BC position	0.0835	0.2226	0.0223	0.3318
BC position vs T_{cont}	0.0383	0.1383	0.2269	0.3377
T_{cont} vs BC Strength	0.1890	0.3542	0.1396	0.4475

	ISO	
3 μm Band Divided Correlation Type	Spectra (All 26)	Spectra less IRC+10°216
T_{cont} vs Strength	0.0154	0.0247
3 μm Strength vs SiC Strength	0.081	0.0788

	ISO	
7–8 μm Band Divided Correlation Type	Spectra (All 26)	Spectra less IRC+10°216
T_{cont} vs Strength	0.4184	0.3777
7–8 μm Strength vs SiC Strength	0.3356	0.3910
7–8 μm Strength vs 9 μm Strength	0.0007	0.0083

	ISO	
13 μm Band Divided Correlation Type	Spectra (All 26)	Spectra less IRC+10°216
T_{cont} vs Strength	0.0511	0.0799
13 μm Strength vs SiC Strength	0.2797	0.2756

BC = Barycentric

5.4 Results

5.4.1 The "9 μm" feature

Using the divided and the subtracted spectra for each source, we have sought the infamous 9 μm "feature". By inspection of the continuum-divided and continuum-subtracted spectra (figures 5.2 and 5.3.), it is clear that sometimes there appears to be some excess emission at $\sim 9\mu$m and sometimes a deficit. In order to assess whether there is really a feature, we used the continuum-divided spectrum and sought the highest flux point in the 9–10 μm region. We then determined the strength of the "feature" (i.e. the flux-to-continuum ratio) at this point. The resulting "features" have strengths in the range 0.7 to 1.4. This spread is indicative of there not being a feature at this wavelength, and the ranges arises from uncertainty in fitting the continuum. In addition, if we examine continuum-divided spectra for which there is a clear $\sim 9\mu$m feature in the *IRAS* spectra (e.g. VX And, U Cam, Y CVn, RY Dra and V Aql, see figure 5.2 a, g, m, o and s) the *ISO* spectra either do not show the feature, or it is clearly an artifact of molecular absorptions. In section 5.2.1, we discussed the possible affect of stellar variability on the observed dust feature. This effect is far from understood and further complicates interpretation of the $\sim 9\mu$m feature which may appear in the *IRAS* data but not that of *ISO* or *vice versa*.

To confirm the that the $\sim 9\mu$m is indeed an artifact of uncertainties in continuum fitting, we looked for correlations between the feature strength and underlying continuum temperature $T_{\rm cont}$ and between the $\sim 9\mu$m feature and the SiC feature strengths. Finally we sought a correlation between the $\sim 9\mu$m feature strength and the strength of the HCN, C_2H_2 and CS molecular bands at 3, 7–8, and 13.7 μm. The results are shown in figure 5.4 and correlation parameters are listed in table 5.4. There are no clear correlations which leads us to suggest that the $\sim 9\mu$m feature probably does not exist.

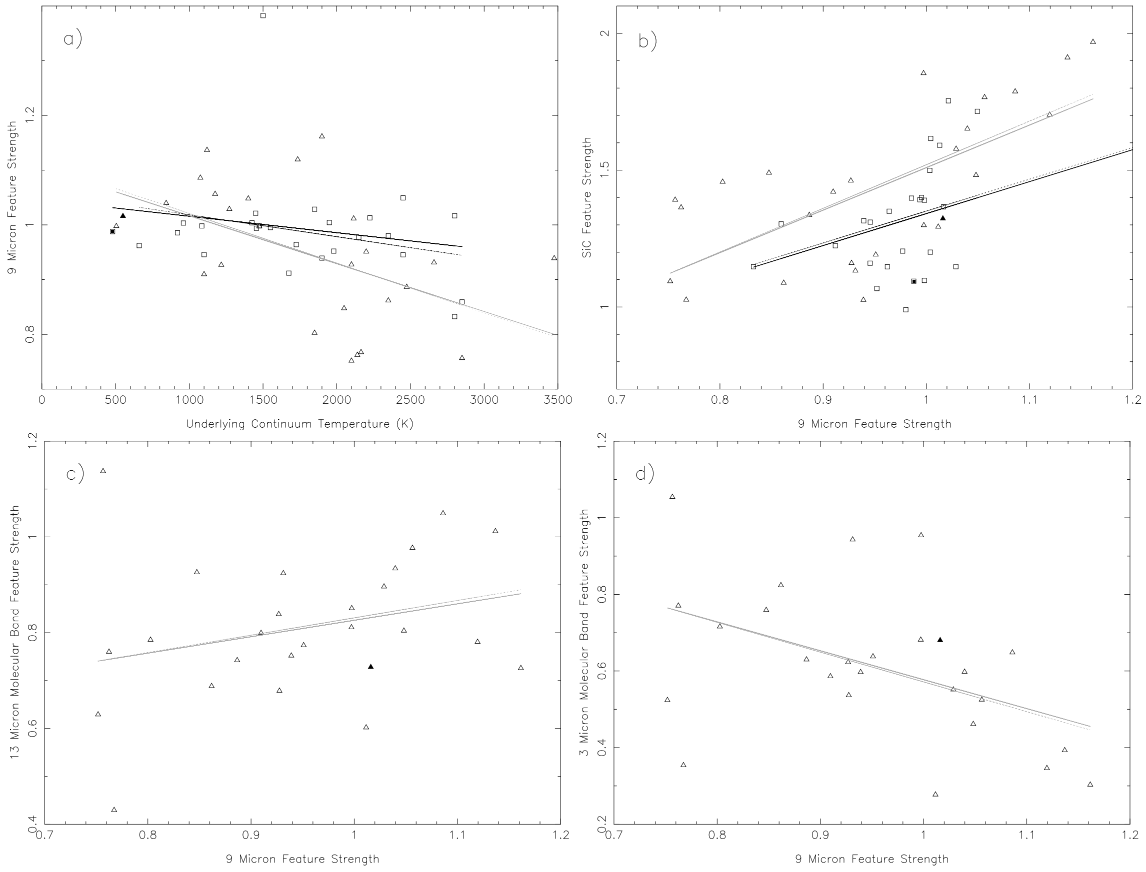

Figure 5.4: "$9\,\mu$m feature" continuum-divided correlations. a) $T_{\rm cont}$ vs. $\sim 9\mu$m peak strength; b) $\sim 9\mu$m peak strength vs. SiC feature strength; c) $\sim 9\mu$m peak strength vs. C_2H_2 $13.7\,\mu$m band strength; d) $\sim 9\mu$m peak strength vs. HCN $3\,\mu$m band strength; In each panel, *IRAS* LRS points = open square; *ISO* SWS points = open triangle; *IRAS* LRS IRC+10°216 point = filled square; *ISO* SWS IRC+10°216 point = filled triangle; Correlation line including IRC+10°216 = solid line; Correlation line not including IRC+10°216 = dotted line; *IRAS* LRS correlations = black lines; *ISO* SWS correlations = gray lines.

An alternative interpretation would be that the $\sim 9\mu$m feature is sometimes real and sometimes an artifact, but the lack of correlation with any other spectral parameter precludes determination of the origin of such a feature. Speck et al. (2005) suggested that the feature was associated with carbon impurities in amorphous SiC.

Table 5.4: Determination coefficient (R-squared) values of linear regression correlations for the “9 μm” for all 26 sources

Correlation	*IRAS* Spectra	*ISO* spectra
9 μm Strength vs $T_{\rm cont}$	0.0115	0.0001
9 μm Strength vs SiC strength	0.2408	0.1921
9 μm vs 3 μm Molecular Band Strength	—	0.2046
9 μm vs 7–8 μm Molecular Band Strength	—	0.0087
9 μm vs 13 μm Molecular Band Strength	—	0.0144

The occasional appearance of the feature would then be due to the physical conditions within the circumstellar shell conspiring to produce such material.

5.4.2 The $\sim 11\mu$m feature

Using the divided and the subtracted spectra for each source we analyzed the shape, strength and position of the ~11 μm SiC feature (See Figures 5.2 and 5.3.).

For each spectrum of both *IRAS* and *ISO*, the continuum temperature (as determined by the best-fit blackbody) as well as four parameters of the ~11 μm SiC feature were measured; the peak position, peak strength (peak-to-continuum ratio), barycentric peak position, and barycentric strength-to-continuum ratio. We then sought correlations between any and all of these parameters, and with $T_{\rm cont}$; i.e.: 1) SiC feature strength versus SiC peak position; 2) SiC peak position versus $T_{\rm cont}$; 3) SiC feature peak strength versus $T_{\rm cont}$; 4) SiC barycentric strength-to-continuum ratio versus SiC barycentric peak position; 5) SiC barycentric peak position versus $T_{\rm cont}$; and 6) SiC barycentric strength-to-continuum ratio versus $T_{\rm cont}$. The correlations or lack thereof are plotted in Figures 5.5 and 5.6. We used the coefficients derived from linear regression in determining whether the above pairings of spectral parameters indeed yield correlations[2] (see table 5.3 for the coefficent values.).

The largest correlation coefficient value obtained was 0.4522, therefore there are very weak correlations at best. The only "correlations" for which the coefficients are >0.4 are for the SiC strength (peak or barycentric). This fits with the only trend agreed upon by previous studies.

According to Speck et al. (2005), self-absorption of the $\sim 11\mu$m feature may lead to asymmetric features. Therefore, we have investigated whether there are any apparent trends in the shape of the SiC feature with $T_{\rm cont}$. For symmetrical features the barycentric and peak positions will coincide, and asymmetric features will have these two positions offset. In order the determine whether shape effects correlate with $T_{\rm cont}$, we have taken the difference between peak position and the barycentric peak position and divided by the barycentric peak position. This value was then correlated with the continuum temperature. Likewise we took the barycentric strength, subtracted the peak strength and divided by the barycentric strength and correlated with $T_{\rm cont}$. This method was applied only to the SiC $\sim 11\mu$m feature because the molecular bands' peak and barycentric positions were the same. No correlations were found, implying that there is no clear trend for the shapes of $11\,\mu$m feature to vary with $T_{\rm cont}$, and thus with optical depth.

5.4.3 The molecular bands

In addition to the sought correlations for the SiC feature, we examined whether there are any correlations between the various spectral parameters and the molecular ab-

---

[2] Note that a correlation is assumed to exist if $R^2 > 0.5$. R^2 values less than 0.5 imply that less than 50% of the data point positions can be explained by the relationship given my the linear regression trendline. This also implies that the linear correlation coefficients R must be $\gtrsim 0.7$

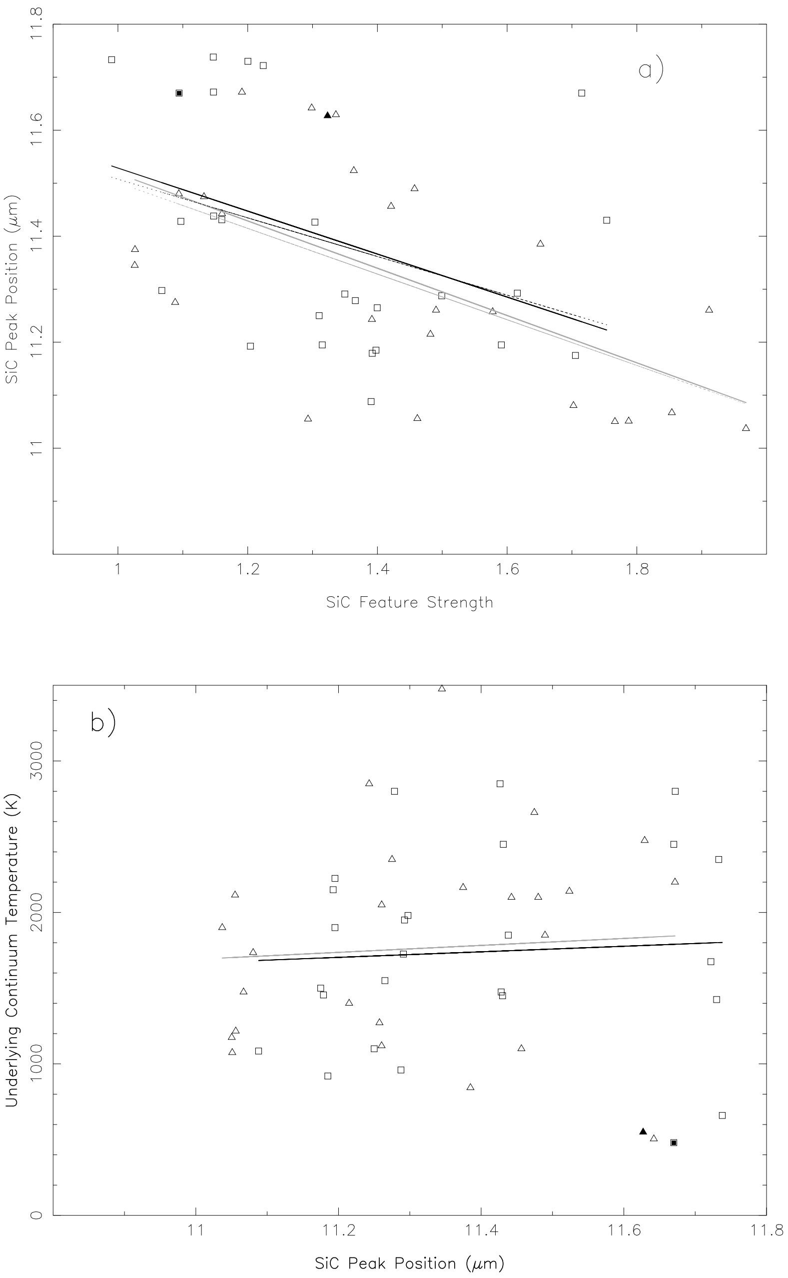

Figure 5.5: SiC continuum-divided correlations. a) SiC peak strength vs. SiC peak position; b) SiC peak position vs. T_{cont}; c) T_{cont} vs. SiC peak strength; d) SiC barycentric strength vs. SiC barycentric position; e) SiC barycentric position vs. T_{cont}; f) T_{cont} vs. SiC barycentric strength. In each panel, *IRAS* LRS points = open square; *ISO* SWS points = open triangle; *IRAS* LRS IRC+10°216 point = filled square; *ISO* SWS IRC+10°216 point = filled triangle; Correlation line including IRC+10°216 = solid line; Correlation line not including IRC+10°216 = dotted line; *IRAS* LRS correlations = black lines; *ISO* SWS correlations = gray lines.

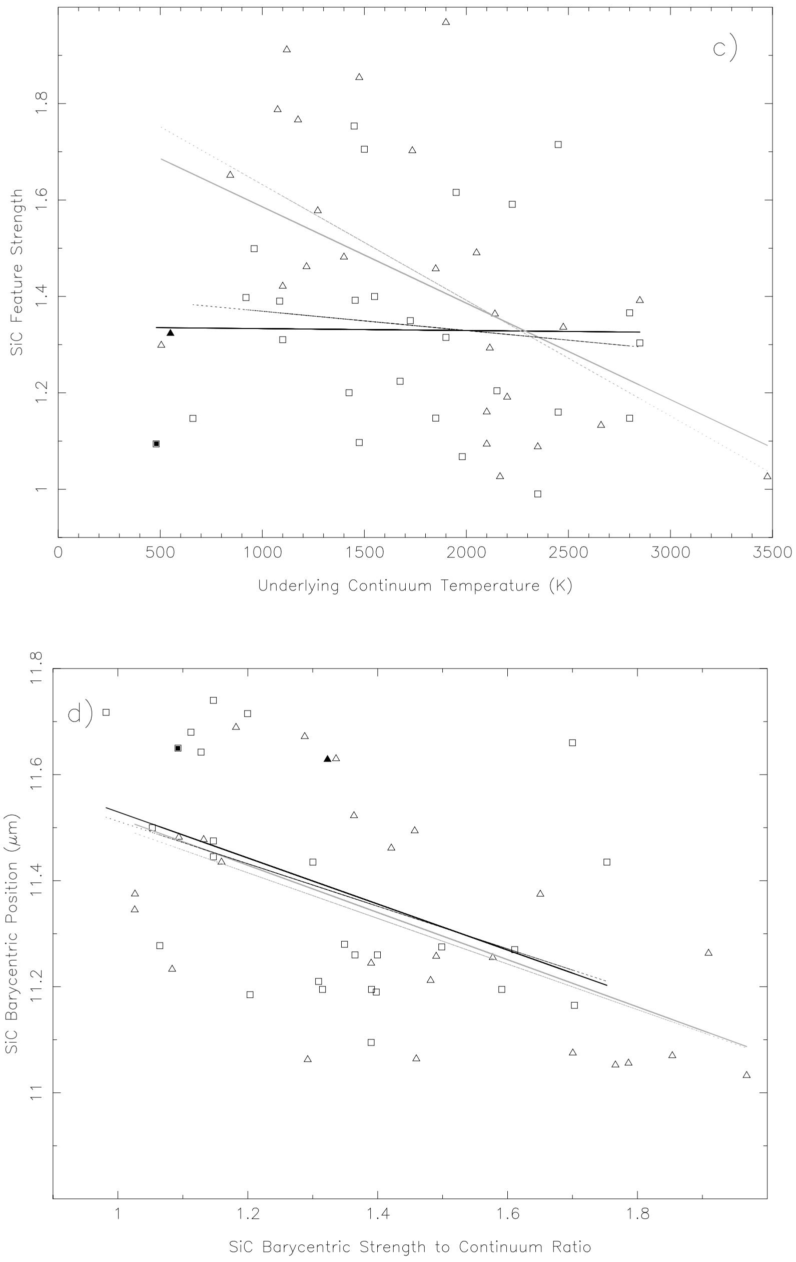

Figure 5.5: SiC continuum-divided correlations continued.

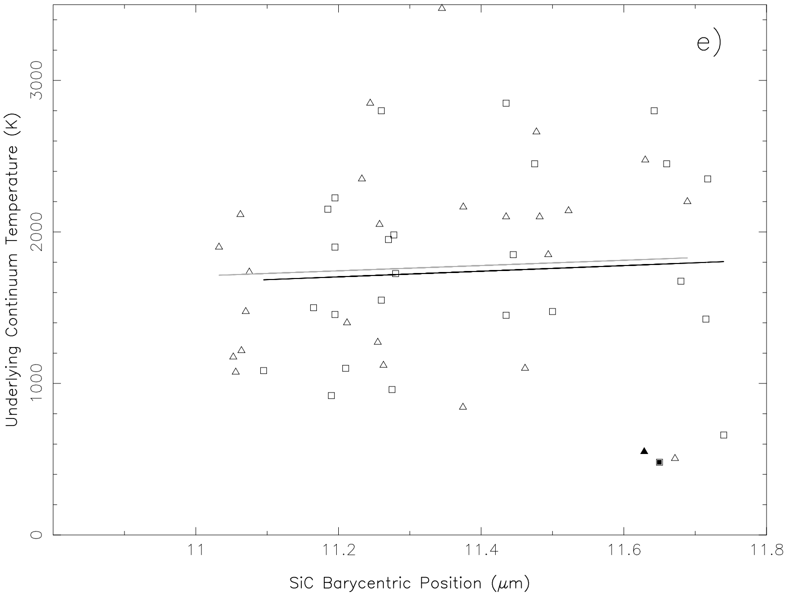

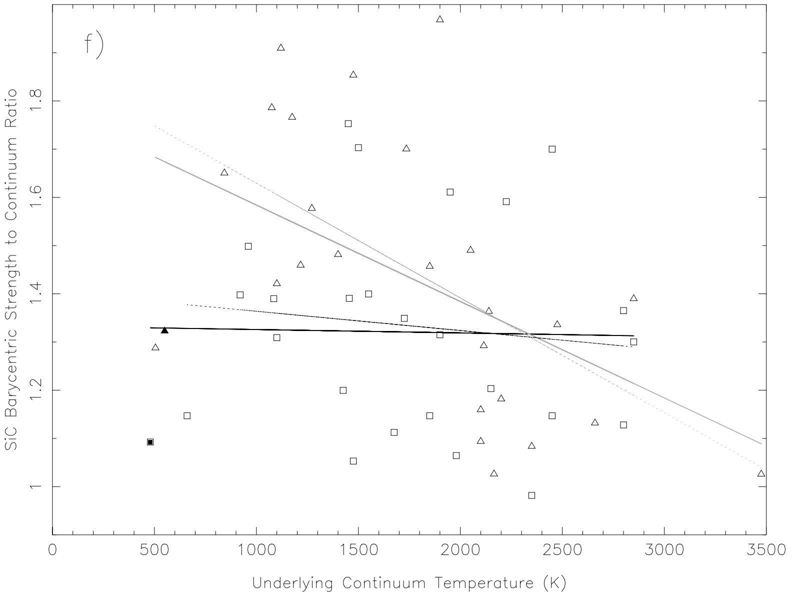

Figure 5.5: SiC continuum-divided correlations continued.

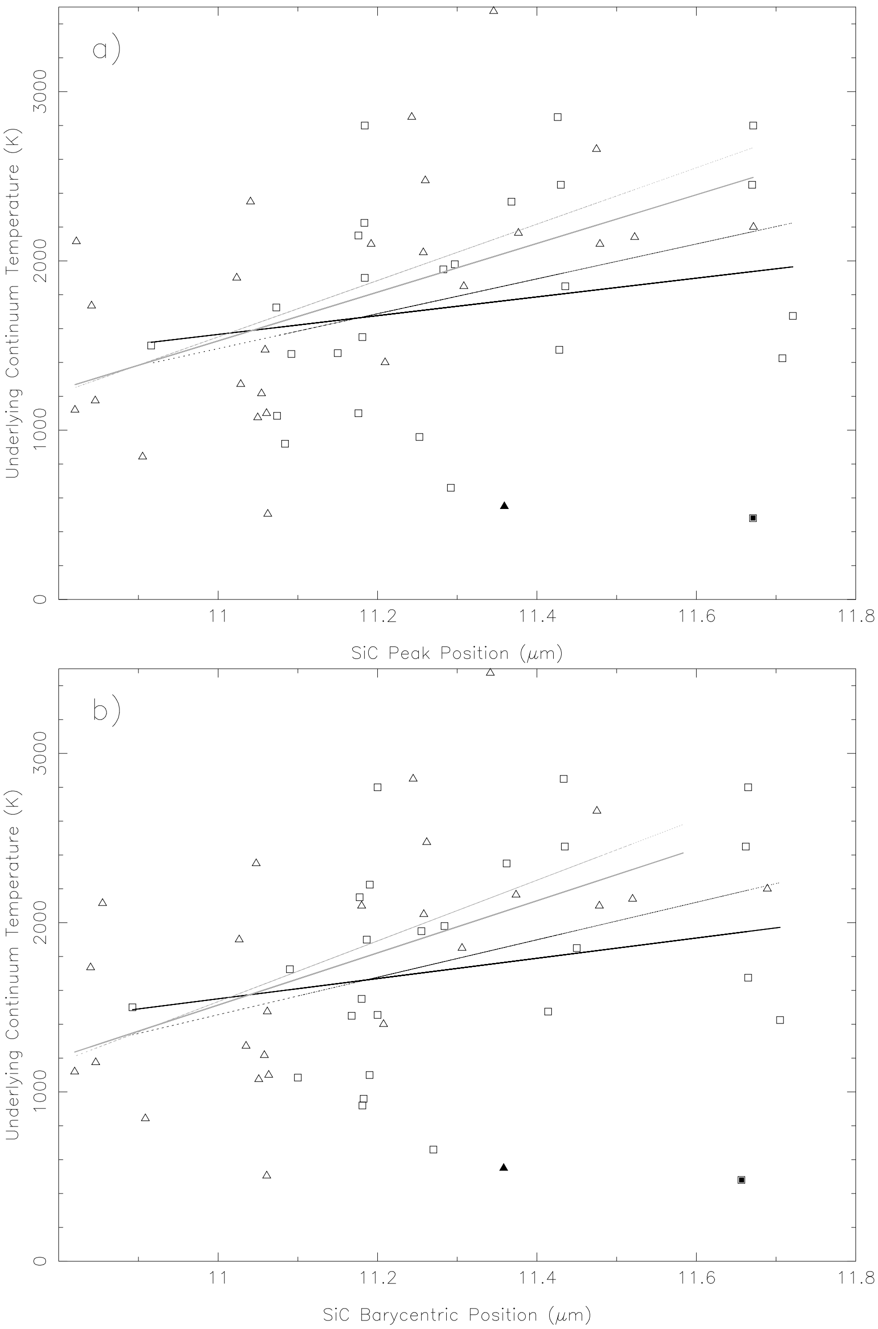

Figure 5.6: SiC continuum-subtracted correlations. a) SiC peak position vs. T_{cont}; b) SiC barycentric position vs. T_{cont}. In each panel, *IRAS* LRS points = open square; *ISO* SWS points = open triangle; *IRAS* LRS IRC+10°216 point = filled square; *ISO* SWS IRC+10°216 point = filled triangle; Correlation line including IRC+10°216 = solid line; Correlation line not including IRC+10°216 = dotted line; *IRAS* LRS correlations = black lines; *ISO* SWS correlations = gray lines.

sorption bands. These bands are located at 3 μm (due to HCN) 7–8 μm (due to a blend of HCN, CS and C_2H_2) and 13.7 μm (due to C_2H_2; Aoki et al., 1999; Jørgensen et al., 2000). This time we sought trends between the strength of the molecular bands, T_{cont} and SiC feature strength. We also sought correlations with the ΔT, i.e., difference between the T_{cont} as determined using *ISO* and using *IRAS* spectra. This was to determine whether the difference in fitted continua could be attributed to the strengths of the molecular bands. Correlations for the molecular bands are weak to non-existent (See figure 5.7.). The only correlation with a coefficient > 0.4 is for the strength of the 7–8μm band and T_{cont}. In light of the results of Jørgensen et al. (2000), further analysis of the molecular bands, and in particular the ratios of the band strengths, may yield some interesting results. Such analysis is beyond the scope of the present work.

5.4.4 The effect of IRC+10°216

While attempting to find correlations between the various parameters, we chose to investigate the effect of discarding the source IRC+10°216 as it often appears as an outlier in the correlation plots and could possibly skew the results. The dataset excluding IRC+10°216 provided slightly better correlations for all the comparisons involving the SiC feature (both divided and subtracted spectra). However, there was not a discernible change in the correlations of the molecular bands regarding the use of IRC+10°216. And in all cases, the linear regression coefficient is low enough to preclude an actual correlation. The data used for correlation analyses and the fitted correlations are shown in figures 5.5, 5.6 and 5.7 as well as table 5.3. In conclusion, no pair of spectral parameters could be contrived that yielded a correlation. This is a distinctly different result from previous work. The highest correlation coefficients

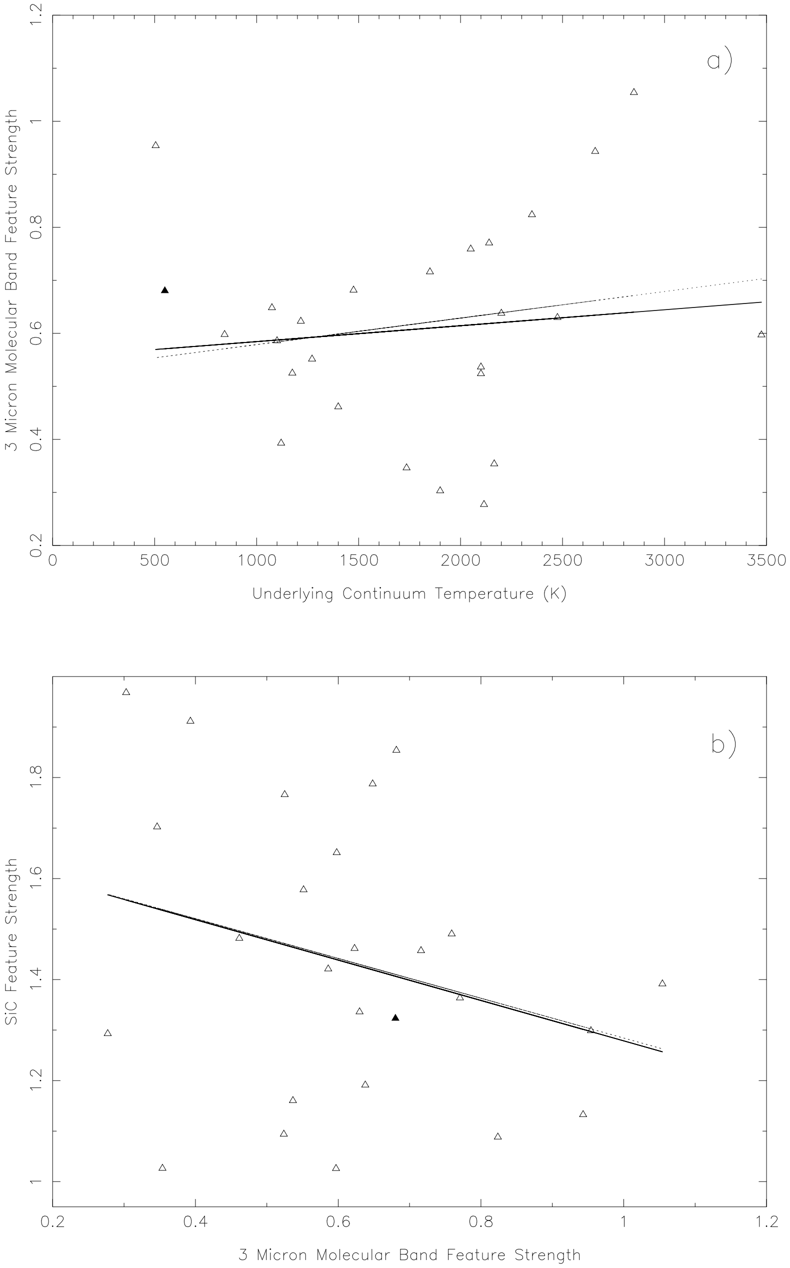

Figure 5.7: Molecular bands in continuum-divided spectra. a) T_{cont} vs. HCN 3 μm band strength; b) HCN 3 μm band strength vs. SiC feature strength; c) ΔT vs. HCN 3 μm band strength; d) T_{cont} vs. C_2H_2 13.7 μm band strength; e) C_2H_2 13.7 μm band strength vs. SiC feature strength; f) ΔT vs. C_2H_2 13.7 μm band strength; g) T_{cont} vs. C_2H_2/HCN/CS 7-8 μm molecular band strength; h) C_2H_2/HCN/CS 7-8 μm molecular band strength vs. SiC feature strength; i) ΔT vs. C_2H_2/HCN/CS 7-8 μm molecular band strength; *ISO* SWS points = open triangle; *ISO* SWS IRC+10°216 point = filled triangle; Correlation line including IRC+10°216 = solid line; Correlation line not including IRC+10°216 = dotted line; *ISO* SWS correlations = black lines.

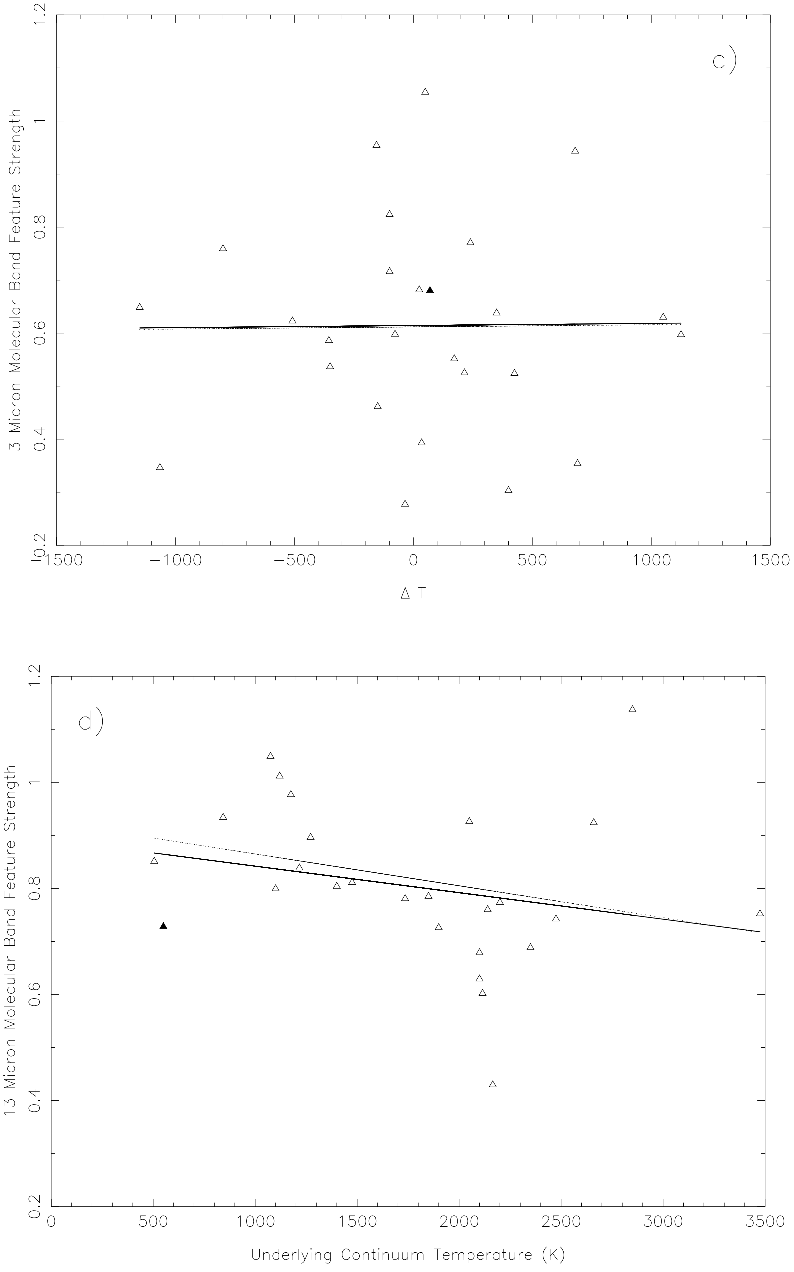

Figure 5.7: Molecular bands in continuum-divided spectra continued.

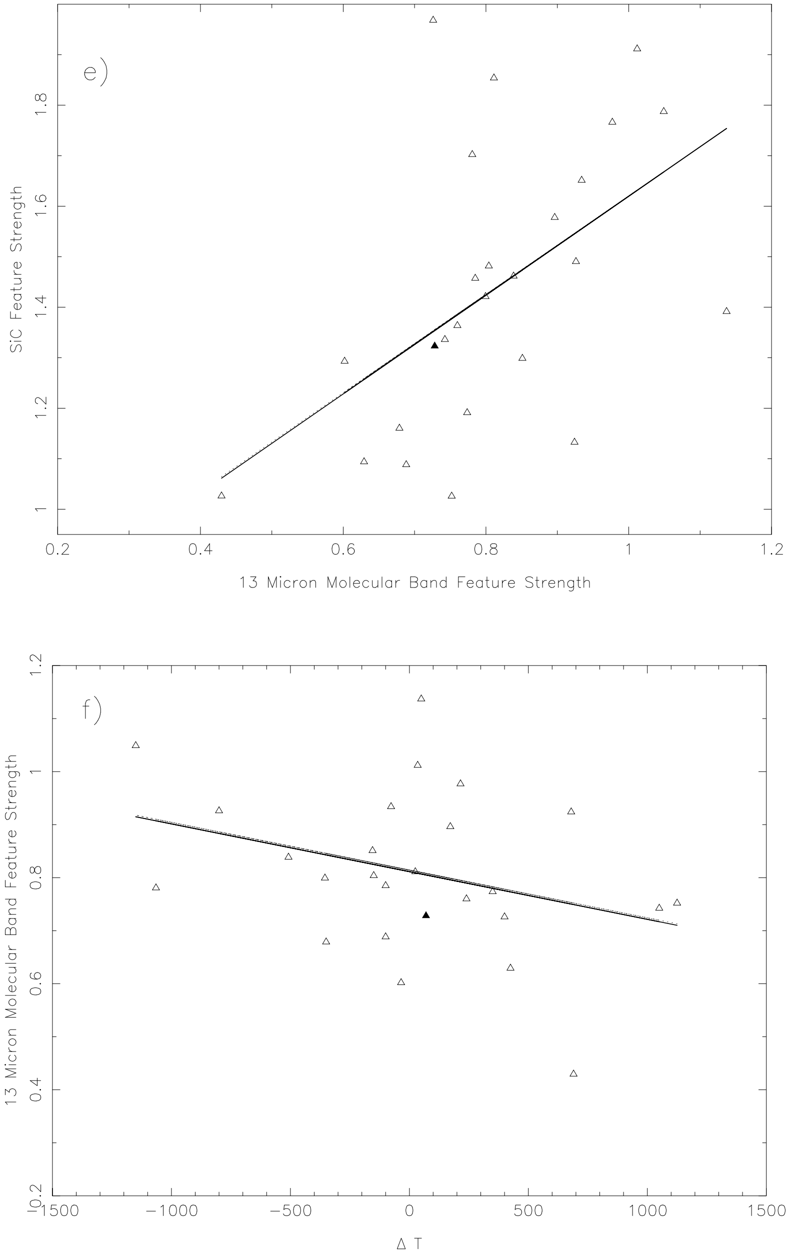

Figure 5.7: Molecular bands in continuum-divided spectra continued.

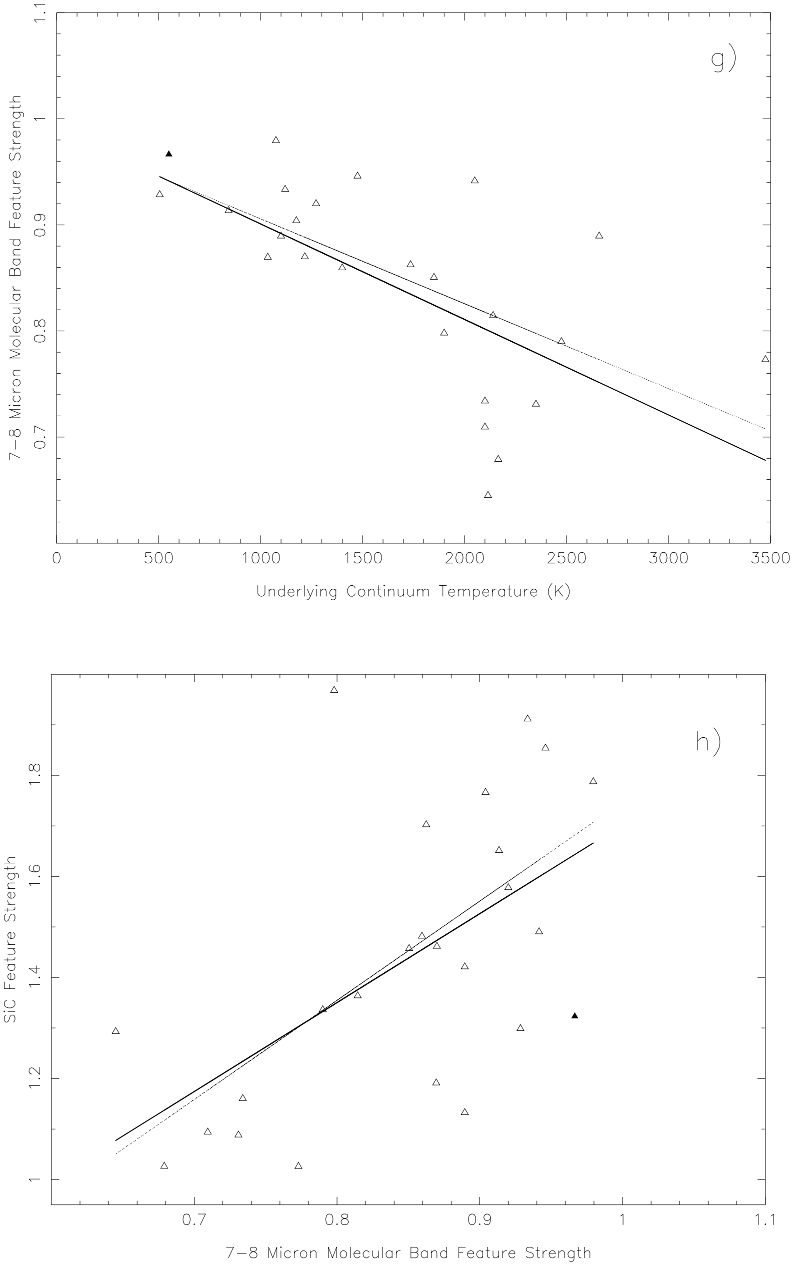

Figure 5.7: Molecular bands in continuum-divided spectra continued.

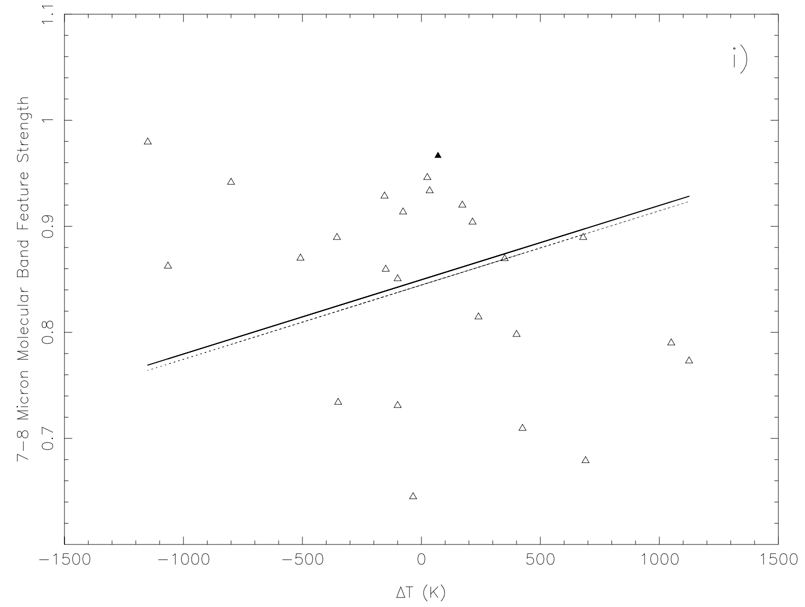

Figure 5.7: Molecular bands in continuum-divided spectra continued.

were obtained for SiC strength vs. T_{cont} in the continuum-subtracted data. This is the only trend that is agreed upon by all previous studies.

5.5 Modeling

In addition to analyzing observational data, we performed one dimensional radiative transfer modeling using DUSTY (Ivezic & Elitzur, 1995; Nenkova et al., 2000, also see the discussion in section 3.3.1), which allowed us to determine theoretically how the emerging spectrum should change as a function of various dust shell parameters. In this case, the parameters examined were the effective temperature of the star, inner dust shell temperature, optical depth, and dust composition. In all cases the dust was entirely composed of a mixture of SiC and amorphous carbon, but the relative abundances of these constituents varied. The optical constants for SiC came from Pègourié (1988), while those for amorphous carbon came from Hanner (1988).

For simplicity we assumed spherical dust grains, though DUSTY has the capability of processing non-spherical shapes. In addition, we assumed a radial dust density distribution of $1/r^2$, which was shown by Rowan-Robinson & Harris (1982, 1983b,a) to reproduce the IR spectrum of AGB stars. Finally, we assumed an MRN grain size distribution (i.e., $n(a)$ proportional to a^{-q}, where n is the number of grains in the size interval $(a, a + da)$ and $q = 3.5$; $a_{min} = 0.005\mu$m and $a_{max} = 0.25$ μm; Mathis et al., 1977).

Spectra were produced by varying the chosen parameters until a complete grid of models was produced (See table 5.5.). For each of these spectra, we fitted a blackbody continuum to the mid-infrared region, which was then used to produce continuum-divided spectra (in an identical manner to the technique used in section 5.3 for observational spectra.). This allowed us to determine the $\sim$11 μm feature strength and position. We were then able to repeat the search for correlations between different spectral parameters, this time for model spectra.

Table 5.5: The parameters and their value ranges for the 1-D radiative transfer modeling.

Parameter	Minimum Value	Maximum Value	Interval
Stellar Temperature	2000 K	4000 K	1000 K
Dust Temperature	500 K	1500 K	500 K
Optical Depth of Dust	0.1	1	1 dex
SiC concentration	0%	30%	5%

Figure 5.8 shows the fitted continuum temperature versus the $\sim$11 μm feature peak strength. Here it is clear that there is no discernible correlation between these parameters. Similar results were obtained in all pairings of parameters, with one exception. Figure 5.9 shows the relative abundance of SiC versus the peak strength of the $\sim$11 μm feature. As one may expect, the maximum peak strength increases with an increase of SiC abundance (relative to amorphous carbon). However, this is not a

correlation *per se* because it is impossible to determine the SiC abundance from the peak strength alone.

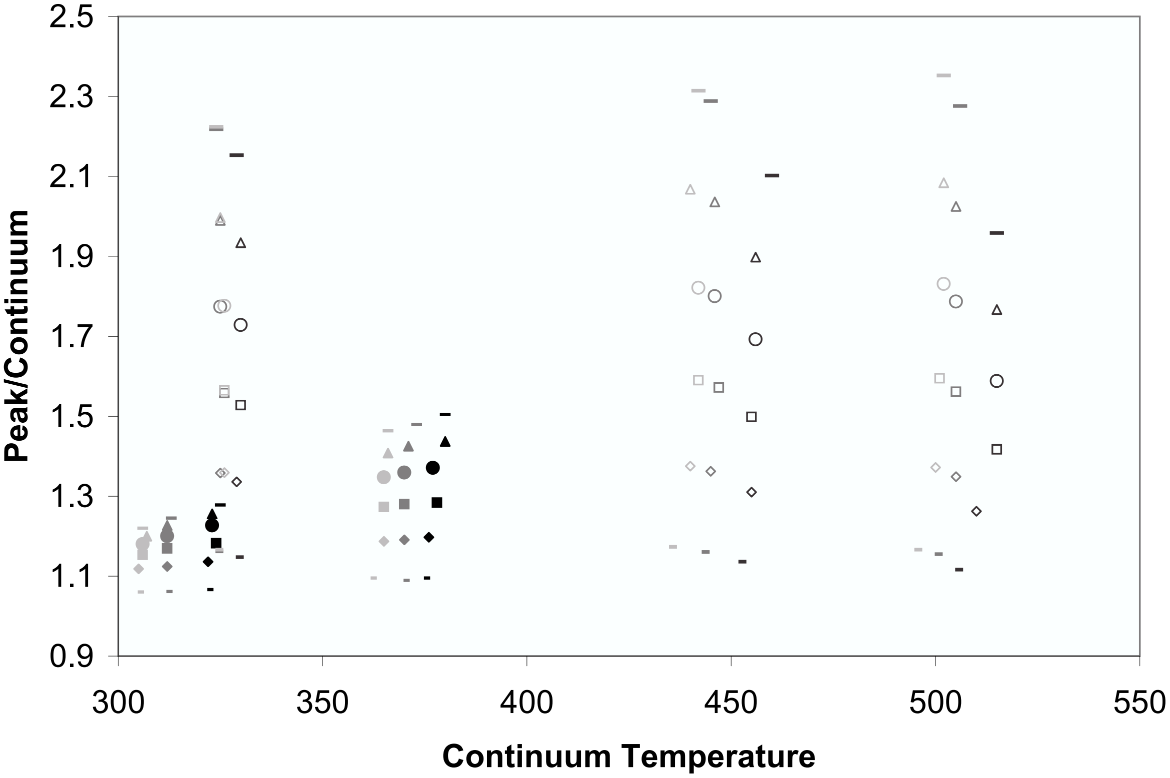

Figure 5.8: Radiative transfer model results: T_{cont} vs. peak strength. Model parameters are denoted as follows: star effective temperature is denoted by color (black = 2000K, dark grey = 3000K, light grey = 4000K); composition of dust is denoted by shape (short bar = 5% SiC/95% amorphous carbon, diamond = 10%SiC/90% amorphous carbon, square = 15%SiC/85% amorphous carbon, circle = 20%SiC/80% amorphous carbon,, triangle = 25%SiC/75% amorphous carbon, long bar = 30%SiC/70% amorphous carbon,); and optical depth is denoted by fill (hollow = $\tau_{10\mu m}$ of 0.1 [except for the long and short bars, which are slightly longer in this case]; filled = $\tau_{10\mu m}$ of 1).

For low SiC abundance, the ∼11 μm feature is always weak. Higher SiC abundances can yield SiC features which are stronger, but also yield features that are weak, depending on the details of the other parameters of the models. Thus, a strong feature necessitates a certain minimum SiC abundance, whereas a weak feature is not very diagnostic of the relative abundance of SiC.

Our radiative transfer modeling results are in good agreement with our observa-

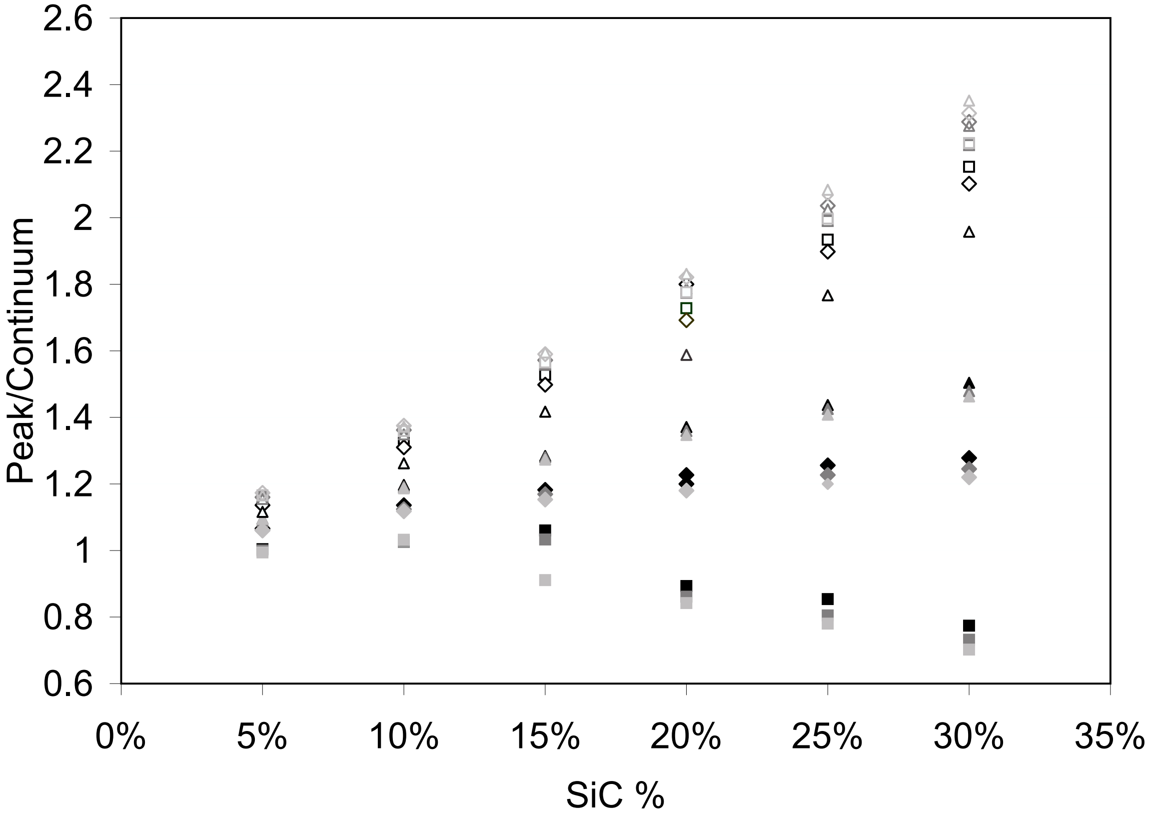

Figure 5.9: Radiative transfer model results: composition vs. feature strength. Model parameters are denoted as follows: star effective temperature is denoted by color (black = 2000K, dark grey = 3000K, light grey = 4000K); inner dust shell temperature is denoted by shape (square = 500K, diamond = 1000K, triangle = 1500K); and optical depth is denoted by fill (hollow = $\tau_{10\mu\mathrm{m}}$ of 0.1, filled = $\tau_{10\mu\mathrm{m}}$ of 1).

tional studies, and suggests that we should not expect to find correlations between pairings of spectral parameters. This is due to the large degeneracy present in these systems; as an example, weak feature strength could be due to low optical depth, low SiC concentration, or low inner dust shell temperature (or a combination of these). This makes it impossible to use the SiC ∼11 μm feature to determine specific information about the dust shell without first limiting the parameter space. As can be seen in figure 5.9, for a given stellar temperature, inner dust temperature and optical depth, the ∼11 μm feature increases in strength as the fraction of SiC increases. However, once a realistic range of these parameters is adopted, we can no longer see such a simple trend. Since optical depth, dust shell composition and dust temperature parameters are intimately linked to each other and with the C/O ratio, N-abundance, metallicity, mass-loss rate, outflow velocities etc., there is obviously a large free parameter space. This precludes the determination of dust shell parameters from the infrared spectrum alone.

Our dust models have a maximum optical depth at 10 μm of 1, and thus do not exhibit self-absorption behavior in the 11 μm feature. However, including the effect of self-absorption of the ∼11 μm feature into our analysis would further obfuscate any trends. The effect would be to lower the probability of getting the strongest possible feature for a given composition. Therefore our modeling results err towards the possibility of finding trends in the spectra.

5.6 Discussion

Previous analyses have determined apparent patterns in the mid-IR spectral features of carbon stars which have been explained in terms of condensation sequences.

The current study suggests that there are no simple patterns in the mid-IR spectral features of carbon stars and, thus, no single condensation sequence can explain the nature and evolution of circumstellar dust around carbon stars. The disparity between the current and previous studies arises predominantly from the mis-identification of the continuum level in the *IRAS* spectra. This is exacerbated by the many different approached to normalization of spectra (continuum-subtraction vs continuum division; $T_{\rm cont}$ = dust continuum or stellar continuum etc). There is no simple relationship between the 3, 7–8, and 13.7 μm band strengths, however, simply being aware of the locations of the molecular absorption bands yield better continuum estimations for the *IRAS* data. Application to the larger IRAS dataset (>100 carbon star spectra) should not change the results presented here, but will facilitate sub-division of the sample according to other parameters (see below).

We have modeled the effect of various dust shell parameters using DUSTY (see section 5.5), where optical depth and dust shell density distribution act as proxies for gas pressure, and the C/O ratio is represented by different dust compositions (i.e. ratio of SiC/carbon). Our radiative transfer models show that, for the range of optical depths, stellar and dust temperatures and compositions expected in carbon stars, it should be impossible to discern trends such as those discussed above. Therefore our results should have been expected.

In order to discern trends in the spectral features, and thus determine a condensation sequence it will be necessary to classify stars into subgroups according to, for example, C/O ratio, N-abundance, mass-loss rate, galactic latitude, metallicity, stellar variability, etc.

In addition, as these stars evolve the Si-abundance remains more or less constant, while the C/O increases. Therefore dust far from the star (formed in an earlier mass-loss episode) may have a different nature (composition, structure, size) to that close to the star - further complicating the interpretation of the spectra.

Speck et al. (2005) showed that simply changing the grain size from the inner to the outer shell can affect the spectra, since the optical properties change. In addition, Speck et al. (2005) suggested that the emergence of the 9 μm feature is associated with the decrease in Si/C ratio, leading to more carbon impurities in SiC grains. This argument has also been used to explain the 21 μm feature seen in C-rich post-AGB stars in terms of C-doped SiC grains (Speck & Hofmeister, 2004; Speck et al., 2005). However, we showed in section 5.4.1 that the apparent $\sim 9\mu$m feature is probably not real.

With all these complexities feeding into the physical nature of the dust formation zones around carbon stars, it is not entirely surprising that we do not find any trends indicative of a single dust condensation sequence. The true situation is even more complex and has more possibilities than accounted for in our modeling. In order to extract the condensation sequence(s), and to test theoretical models, we must separate a large sample of carbon stars according to various parameters (e.g. C/O; metallicity; mass-loss rate; variability type; phase of light curves; etc.) and again hunt for trends in the spectral features. We cannot sub-divide the present sample according to these criteria and still obtain statistically meaningful results. Therefore, we must apply the knowledge gleaned from the present study to determine continua for the larger IRAS dataset. This dataset should be sufficiently large for subdivision into groups which still yield statistically meaningful results.

Furthermore, as expressed in equation 3.49, it is necessary to determine the dust shell parameters through radiative transfer modeling rather than through such simplistic approaches as presented here.

Moreover, we need to use radiative transfer codes that can accommodate changing dust parameters with distance from the star (and possibly changing dust shell geometries.)

5.7 Conclusion

Previous studies of the evolution of IR dust features based on *IRAS* have yielded contradictory results. In order to assess the problems/complications of previous studies, we have re-evaluated 26 *IRAS* spectra and compared them to their respective *ISO* spectra. Inaccurate estimates of continuum levels in carbon star spectra are due largely to the difficulty in assessing the impact of molecular absorptions in low resolution spectra such as *IRAS* LRS. This effect is exacerbated by the relatively narrow wavelength range. This has led to inaccurate spectra used to analyze trends in the shape, strength, and position of mid-IR features. The higher resolution of the *ISO* data and their broader wavelength coverage allow a more accurate fitting of the underlying continuum. We have therefore reassessed the trends in shape, strength, and position of the $\sim$11 μm SiC feature, and the apparent emergence of the $\sim 9\mu$m feature and find that there does not appear to be any correlation of these feature parameters with the temperature of the underlying continuum, all of which is in accordance with 1-D radiative transfer modeling. In addition to looking for correlations between the continuum temperature, feature strength, and feature peak position, we also investigated whether any of these parameters correlate with the strength of the molecular bands. In all cases, only very weak correlations were found at best.

These null results are due in part to the large number of factors that feed into determining the emerging spectrum from a star (e.g. the stellar effective temperature, C/O ratio, mass-loss rates, metallicity, etc). In order to determine the true carbon dust condensation sequence(s) and thus test theoretical predictions, we must divide our dataset into subsets according to such parameters and seek stronger correlations within these subsets. Furthermore, as suggested by equation 3.49, the only realistic way to extract the spectral parameters accurately is through radiative transfer modeling, which in turn requires a broader wavelength coverage than provided by *IRAS* to provide unique results.

Chapter 6

The Carbon Star V Cyg

"I cannot without great astonishment - I might say without great insult to my intelligence - hear it attributed as a prime perfection and nobility of the natural and integral bodies of the universe that they are invariant, immutable, inalterable, etc., while on the other hand it is called a great imperfection to be alterable, generable, mutable, etc. For my part I consider the earth very noble and admirable precisely because of the diverse alterations, changes, generations, etc. that occur in it incessantly." - Galileo Galilei

6.1 Introduction

In chapter 5 we examined a large collection of dust shells around carbon stars to look for general trends. Now we will investigate the dust shell around a single carbon star, V Cyg, in greater detail in order to see how the shell has changed with time, in addition to attempting to observe the spatial structure of the shell through the use of long-slit spectroscopy.

6.1.1 V Cyg

V Cyg is a relatively bright Mira variable, with a visual magnitude varying between about 7.7 and 13.9 over a period of about 421 days (Kholopov et al., 1998) and it has been recognized as a carbon star for at least sixty years (Lee et al., 1943). Forrest et al. (1975) detected significant emission from a circumstellar shell around V Cyg. More recently, V Cyg has been included in several studies of circumstellar shells because of its brightness and the fact that it has been observed with both IRAS and ISO. LeVan & Sloan (1989) compared two observations five years apart for a sample of 8 stars, including V Cyg, in an attempt to observe variations in spectral features over that time. For the carbon stars in their sample, including V Cyg, they saw no variation in the width of the ∼11μm feature over this period, however, the temperature of the continuum for V Cyg underwent a variation which correlated with the magnitude of the star. Speck et al. (1997) performed a survey of 32 carbon stars, including V Cyg. This study used a $\chi 2$ spectral fitting technique in order to determine the composition and continuum temperatures for their sample. Interestingly in the case of V Cyg (in addition to three other stars) this technique failed, and the blackbody-continuum divided spectrum had to be used in order for the minimization routine to produce acceptable fits for this star. Speck et al. (1997) found that V Cyg has one of the strongest ∼11 μm SiC features, significantly stronger than all but one other sample star. This apparent high feature strength may be an artifact of missing the molecular absorption bands either side of the SiC feature, and thus underestimating the continuum level. Furthermore, they found that the shape and strength of the SiC feature was consistent with pure emission; no self-absorption of the feature was apparent. In addition, the ∼9 μm feature is evident, if weak, in their spectrum (see section 5.1.2 for a discussion of this feature). Sloan et al. (1998) developed a spectral classification system for carbon stars, using a large sample (96) of carbon stars observed by IRAS and including V Cyg. They classified V Cyg as a SiC star, indicating a weak-to-moderate ∼9 μm feature, and implying that V Cyg has progressed somewhat along its evolutionary track. Yang et al. (2004) concurred with Sloan et al. (1998) in the assessment of the evolutionary status, classifying V Cyg in their group B. This indicates that V Cyg has a higher C/O ratio than a younger AGB star and its shell is optically thicker than for a new-born carbon star.

Bieging et al (2001) used millimeter CO observations of V Cygs circumstellar shell and concluded that the mass-loss rate has decreased by a factor of 2-3 over the past few hundred years. Meanwhile Groenewegen et al. (2002) selected V Cyg as part of their millimeter survey investigating the mass-loss rate and expansion velocities of IR carbon stars. [expand on this] Thompson et al. (2006) investigated the SiC feature of V Cyg as part of their analysis of 26 carbon stars, looking for correlations between various spectral parameters, including molecular bands. No correlations were found, and this was attributed to the large degeneracy space implicit in circumstellar parameters. In their investigation of carbon stars in the Magellanic Clouds, Matsuura et al. (2002, 2005) used V Cyg as a Galactic comparison star, because its molecular bands seem similar to the Magellanic Cloud samples they studied (i.e. strong). They hypothesize that the unusually strong molecular absorption bands seen in the Magellanic Cloud carbon stars are due to a high C/O ratio, which implies that V Cyg could have an above-average high C/O ratio for a Galactic carbon star.

6.2 Observations

The data presented here include 5 observations spread over one of V Cyg's pulsation cycles, obtained by the ISO SWS instrument. The distribution of observations dates provides data for investigation of temporal changes in the spectrum of this carbon star.

In addition, new observations from Gemini MICHELLE also provide data for analysis of the spatial structure of the dust shell at a single epoch. Below we divide the detailed description of the acquisition and processing of the spectra into spatially-resolved and time-resolved datasets.

6.2.1 Spatially resolved spectra

In an attempt to observe any structure in V Cyg's dust shell, we performed long-slit spectroscopy using the Michelle mid-infrared imager/spectrometer attached to the Gemini North Observatory's 8.1 m telescope at Mauna Kea, Hawaii. As this is not always a familiar use of a spectrometer, we will briefly discuss it below.

6.2.1.1 Long-slit spectroscopy

Imagine a simple spectrometer, consisting of an entrance slit, a grating, and an exit slit (though for this discussion we will ignore the exit slit). The width of the entrance slit is one of the factors that determines the resolution of the spectrum; to see why, consider the spectrometer obtaining a line spectrum. The spectrometer images the entrance slit on the detector, so the width of the lines will be the width of the image of the slit (which is controlled by the slit width). The wider the slit, and therefore the lines, the harder it is to get the precise location of the line; in addition, lines that are near each other could overlap and become difficult or impossible to resolve. However, a narrower slit lets in less light, which requires more time from the instrument to obtain the same signal, and instrument time is very precious in astronomy. So the choice of slit width is an important decision to make when planning an observation.

The slit width is not the only dimension the slit has, however; it also has a length. This is often ignored during basic treatments of spectroscopy, but we will examine it here because spatially-resolved spectra can be generated by exploiting this dimension of the slit. Because the spectrometer images the slit on the detector, the whole length of the slit is projected onto this surface; if the detector is large enough, it can record data from all points of the slit's length in addition to the spectral information governed by its width. But because different parts of the slit's length are covering different areas of the sky (and the object being observed), this means the detector is getting spectral information from those areas on different parts of its own surface, and so can resolve this spatial data as well. A schematic diagram illustrating this method of observation is given in figure 6.1.

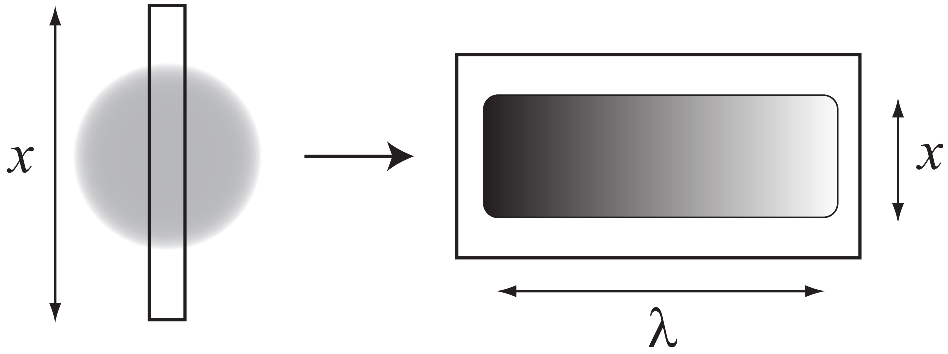

Figure 6.1: A schematic diagram illustrating the technique of long slit spectroscopy. On the left, the entrance slit to the spectrometer is placed over an extended source. The length of the slit determines how much of the source will be observed. On the right, the resulting spectrum on the observing device (typically a CCD) is shown. The horizontal axis gives the spectral information, the vertical axis is the spatial dependence of the spectrum.

6.2.1.2 Data processing

The raw data was reduced in the standard manner using the Gemini IRAF package. For imaging the raw frames were stacked and the images were calibrated using the observation of the photometric standard star to convert from ADU to Jansky or from ADU to Jansky per square arc-second as appropriate. The expected fluxes of the standard star were taken from Cohen et al. (1999). For spectroscopy the telluric correction and absolute calibration were carried out by taking the ratio of the object spectrum to the standard star spectrum, with a small wavelength shift and scaling for airmass as required to remove the atmospheric bands, and then multiplying through by the expected spectrum of the standard star, again taken from the spectrophotometic templates of Cohen et al. (1999). Then, the 2-d spectrum was sliced (that is, the 2-d data was reduced to a series of 1-d spectra corresponding to positions in the shell). Ten of these slices were produced, each [0.4] in width. The two outermost slices were discarded from further analysis due to their very low signal-to-noise ratio. These spectra are presented in figure 6.2

6.2.2 Time resolved spectra

The time-resolved spectral sample comprises seven observations stretching from 1993 to 2007. The spectra presented here were collected using ISO SWS and were acquired from the ISO database. This comprises 5 observations between February 1996 and October 1997. For the raw ISO data we used pipeline version OLP 10.1 from the ISO data archive. Individual spectral sub-bands were cleaned from glitches (caused by cosmic ray particles) and other bad data sections. Next they were flat-fielded, sigma-clipped (using the default value $\sigma = 3$) and rebinned, the final spectral resolution ($R = \frac{\lambda}{\Delta\lambda}$), which ranged from 200-700, depending on the scanning speed of the SWS grating during the observation (Leech et al. 2003). All these spectra can be seen in figure 6.3.

In order to interpret the variations in spectra over time, we accessed the American Association of Variable Star Observers (AAVSO) database and extracted the visual lightcurve data for V Cyg (see figure 6.4).

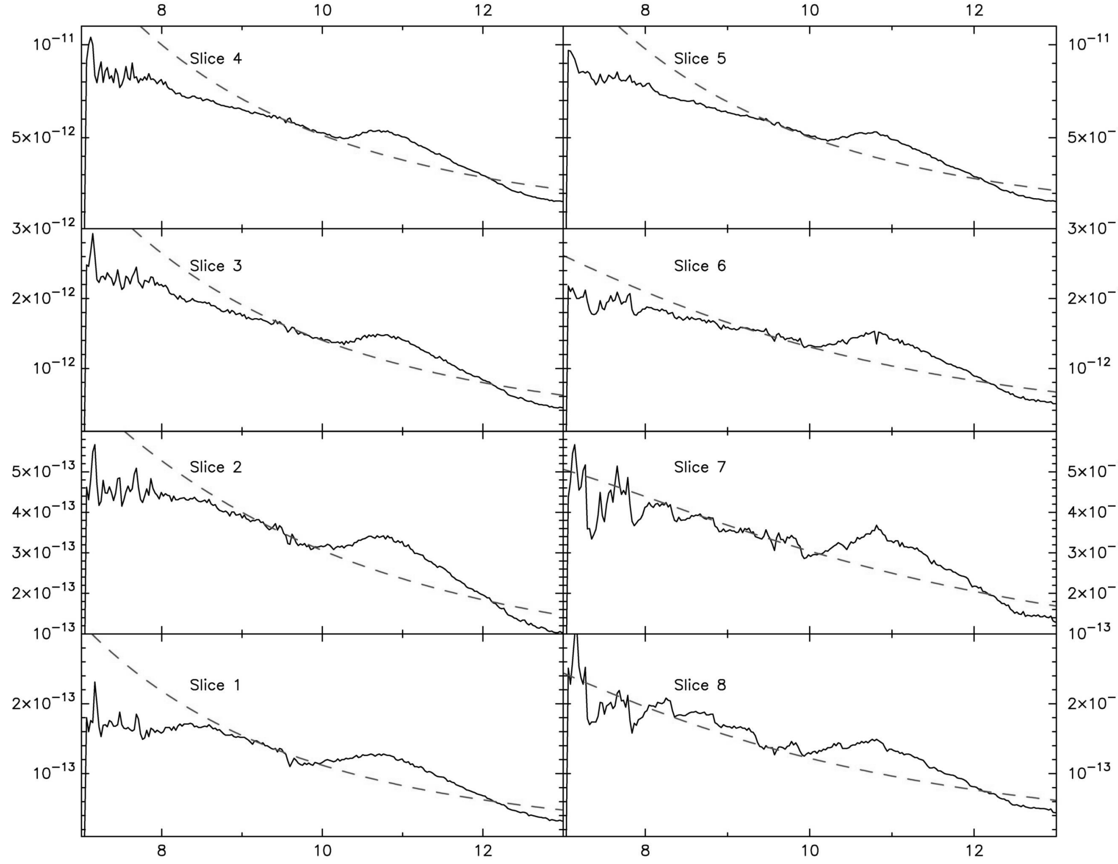

Figure 6.2: Spectra of the dust shell around V Cyg showing the SiC feature at different positions. Each spectrum corresponds to one of the slices referred to in section refslices. The dashed line represents the fitted blackbody to each spectrum. The x-axis is wavelength in μm, y-axis is normalized flux in $W \cdot m^{-2} \cdot \mu m^{-1}$

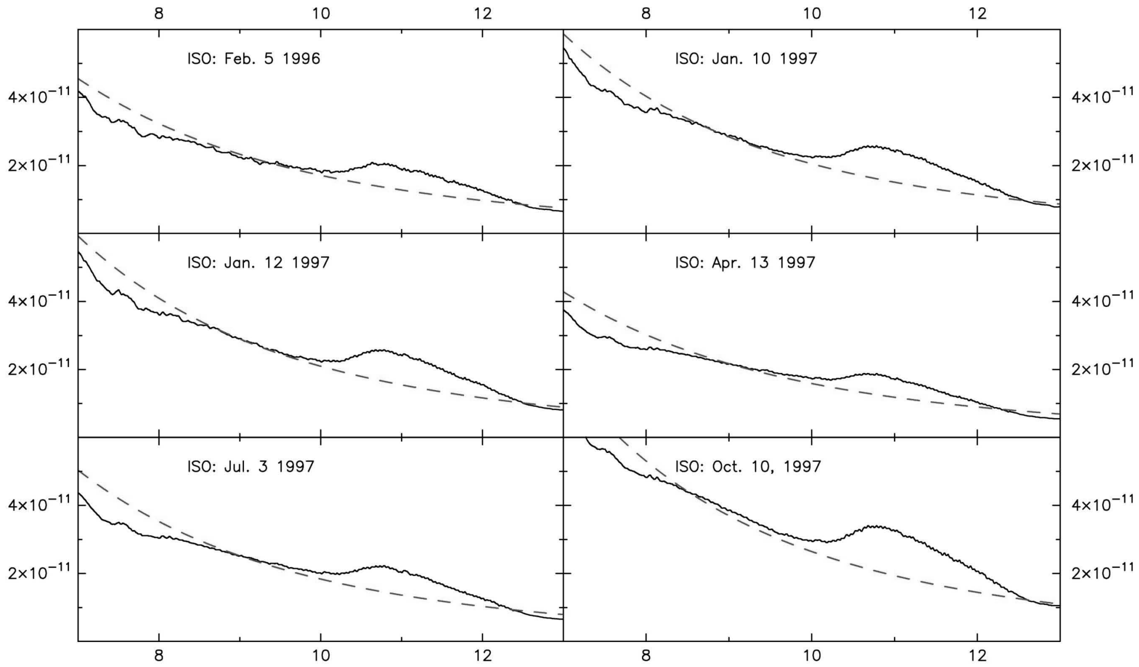

Figure 6.3: Spectra of the dust shell around V Cyg showing the SiC feature at different times. Each spectrum corresponds to one of the observations referred to in section reftime. The dashed line represents the fitted blackbody to each spectrum. The x-axis is wavelength in μm, y-axis is normalized flux in $W \cdot m^{-2} \cdot \mu m^{-1}$

6.3 Analysis

Both spatially and time-resolved spectra were first analyzed by manually fitting a blackbody continuum to each spectrum. This process was complicated, however, by the presence of strong molecular bands throughout the spectral range of the observations. Molecular absorption bands (particularly broad, shallow ones) were not recognized in early, low-resolution spectroscopic studies of carbon stars. When not recognized, these molecular bands can lead to misinterpretation of the continuum level, which gives rise to apparent emission features (Thompson et al. 2006; Speck et al. 2006; see also chapter 5). Consequently the strong molecular absorptions in the spectra of V Cyg make continuum fitting difficult. They can obscure the true position of the continuum. In particular, automatic fitting routines and chi-squared analyses of the

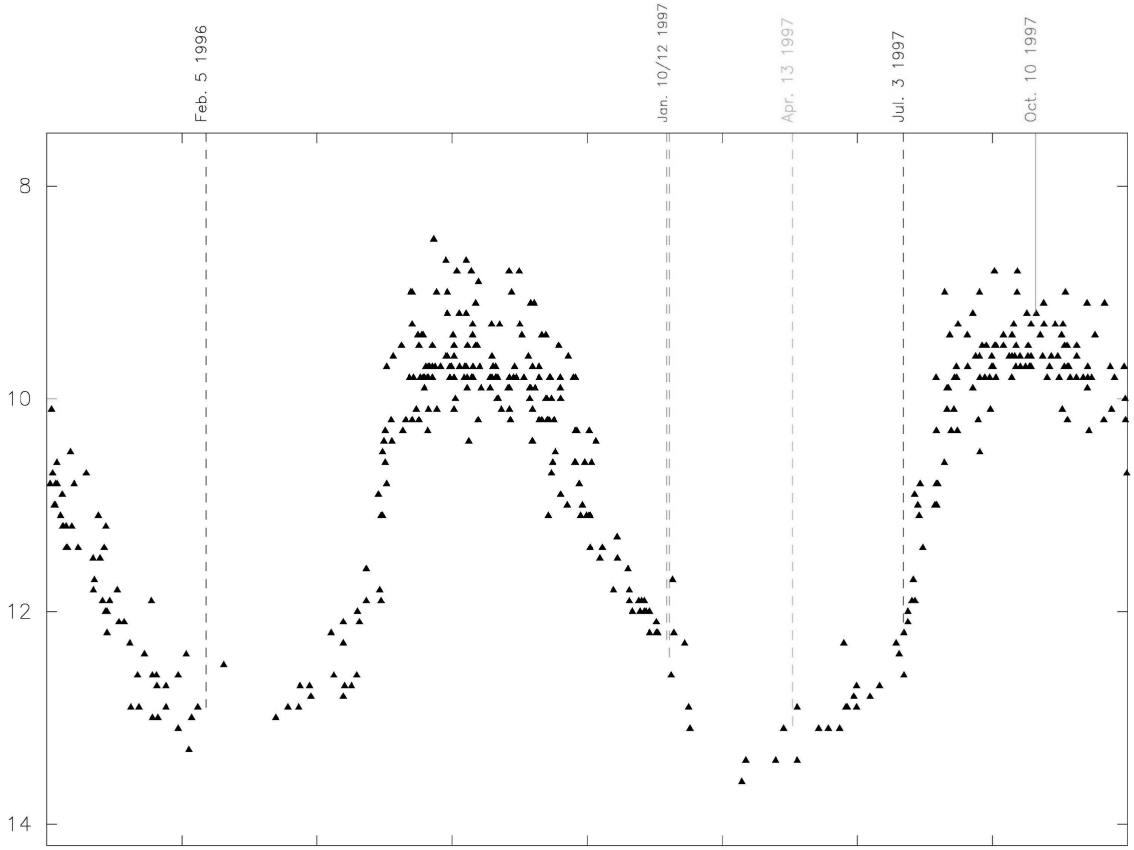

Figure 6.4: The light curve of V Cyg over the period of observation. The x-axis is time in Julian days with the dates of observation denoted by the dashed lines, and the y-axis is the visual magnitude. Because of the way the magnitude scale functions, a smaller magnitude means a brighter object. This data was kindly provided by the American Association of Variable Star Observers, www.aavso.org .

quality of fits are precluded by the problem of limited true continuum in these spectra. In order to ameliorate these fitting issues, we determined the wavelengths at which the continuum is not compromised by molecular absorptions, which enabled us to fit a single blackbody continuum to each of these observational spectra. We then divided each spectrum by its corresponding blackbody continuum. The fitted continua are shown in figures 6.2 and 6.3. Using the continuum-divided data the following parameters for the 11m SiC feature were determined: the peak-to-continuum ratio, the peak wavelength position, and the full width half maximum (FWHM). A further parameter, the FWHM multiplied by the peak-to-continuum ratio, was calculated as a proxy for the feature strength (equivalent width). These spectral parameters were compiled along with the previously determined blackbody continuum temperature (see tables 6.1 and 6.2). For time resolved spectra, the visual magnitude at the time of observation was extracted from the AAVSO data and compiled with the spectral parameters.

Observation Date	Apparent Magnitude During Observation	Fitted Blackbody Temp. (K)	Peak to Continuum Ratio	Peak Position (μm)	FWHM	Feature Strength
Feb 05, 1996	12.6	895	1.53	11.2	1.61	2.47
Jan 10 ,1997	12.5	1040	1.62	11.3	1.62	2.63
Jan 12 ,1997	12.6	1010	1.61	11.1	1.64	2.63
Apr 13, 1997	13.3	920	1.49	10.8	1.37	2.05
Jul 3, 1997	12.2	950	1.55	11	1.53	2.37
Oct 10, 1997	9.2	1125	1.70	10.9	1.69	2.87

Table 6.1: Parameters of the ISO SWS time-resolved spectra and fitted blackbodies. FWHM refers to the Full Width Half Maximum of the SiC feature; feature strength refers to the FWHM multiplied by the peak to continuum ratio.

Slice Number	Fitted Blackbody Temp. (K)	Peak to Continuum Ratio	Peak Position (μm)	FWHM	Feature Strength
1	1000	1.45	10.9	1.3	1.89
2	700	1.39	10.9	1.19	1.65
3	900	1.36	10.9	1.19	1.62
4	1000	1.34	10.8	1.14	1.53
5	1000	1.35	10.8	1.10	1.49
6	600	1.42	10.8	1.19	1.69
7	500	1.42	10.8	0.98	1.39
8	600	1.48	10.8	1.13	1.67

Table 6.2: Parameters of the Gemini Michelle sliced spectra and fitted blackbodies. FWHM refers to the Full Width Half Maximum of the SiC feature; feature strength refers to the FWHM multiplied by the peak to continuum ratio.

6.3.1 Correlations

In order to determine whether changes in spectral feature could be correlated with either position in the dust shell (in the case of the spatially-resolved spectra) or with the dust shells variations in time as a result of pulsations cycles (the time-resolved spectra) we then sought least-square fits correlations between all possible sets of parameters. The results of this analysis can be seen below, where the R^2 values of the best-fits are listed in tables 6.3 and 6.4 respectively, followed by plots of the data points and the best-fit lines.

	Apparent Magnitude	Blackbody Temp.	Peak to Continuum Ratio	Peak Position	FWHM	Feature Strength
Feature Strength	0.0033	0.1135	0.2551	0.7353	0.6275	
FWHM	0.3907	0.4289	0.6897	0.2768		
Peak Position	0.0592	0.0004	0.0202			
Peak to Continuum Ratio	0.6869	0.9284				
Blackbody Temp.	0.6411					

Table 6.3: Correlations in the time-resolved spectra of V Cyg. R^2 is the linear correlation coefficient for the given correlation.

6.4 Discussion

Inspection of table 5.4.2 reveals several correlations between the measured parameters in the time-resolved spectra. The strong correlation between the peak to continuum ratio and the blackbody temperature occurs because the dust emits more strongly

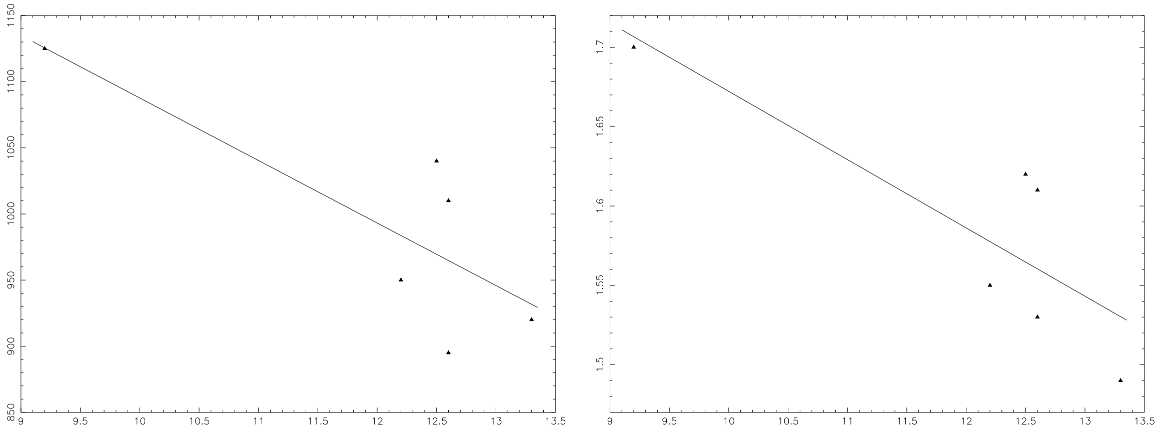

(a) Visual magnitude vs. fitted blackbody temperature.

(b) Visual magnitude vs. peak to continuum ratio.

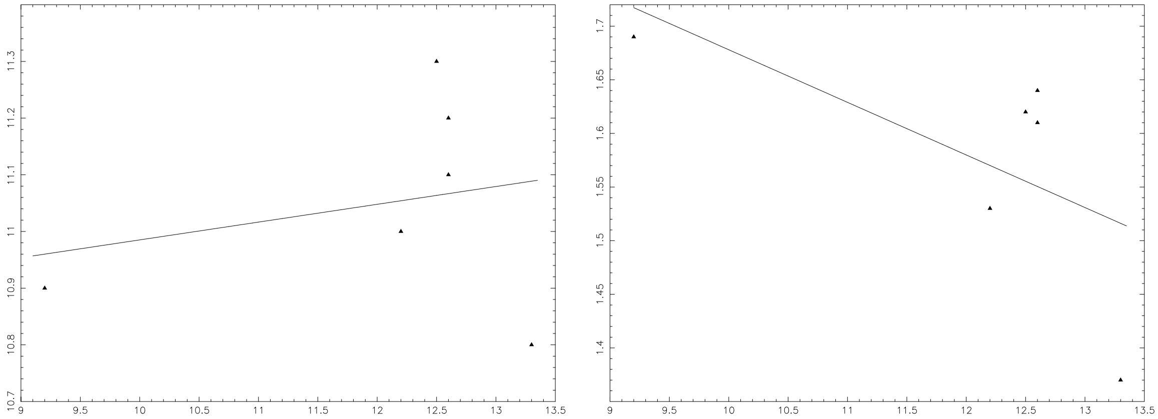

(c) Visual magnitude vs. peak position.

(d) Visual magnitude vs. FWHM

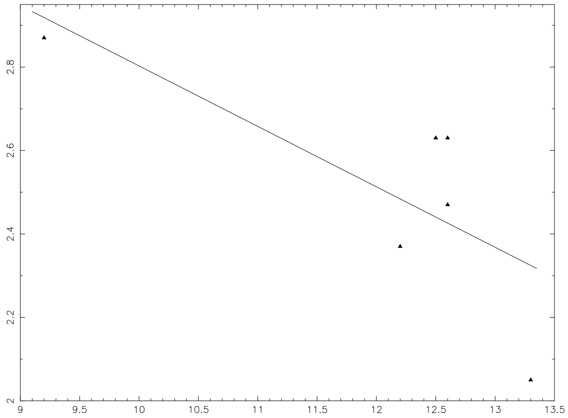

(e) Visual magnitude vs. feature strength.

Figure 6.5: Correlations in the time-resolved spectra of V Cyg, with the visual magnitude as the x-axis in all figures.

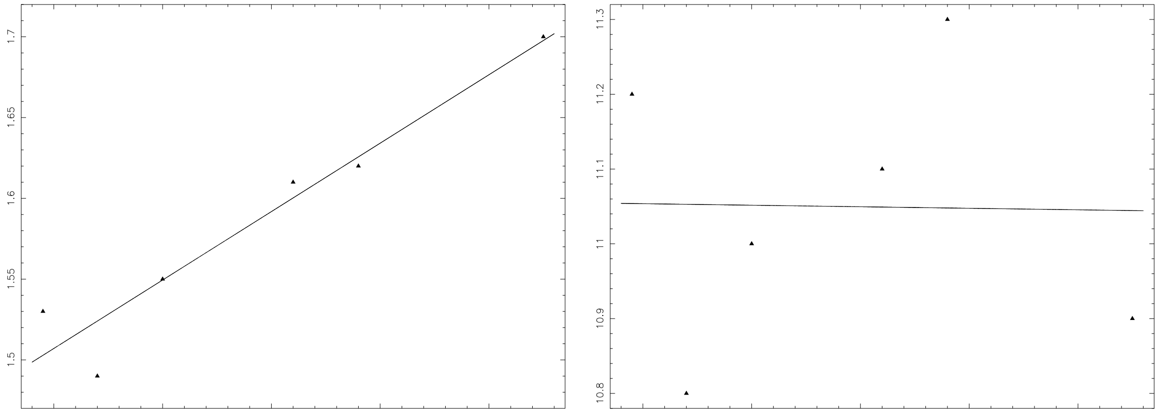

(a) Fitted blackbody temperature vs. peak to continuum ratio.

(b) Fitted blackbody temperature vs. peak position.

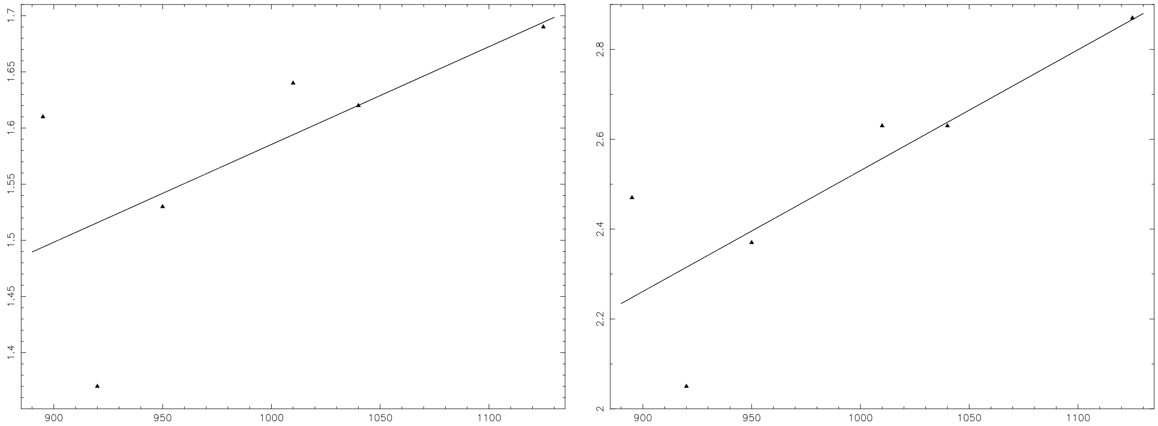

(c) Fitted blackbody temperature vs. FWHM.

(d) Visual magnitude vs. feature strength.

Figure 6.6: Correlations in the time-resolved spectra of V Cyg, with the fitted blackbody temperature as the x-axis in all figures.

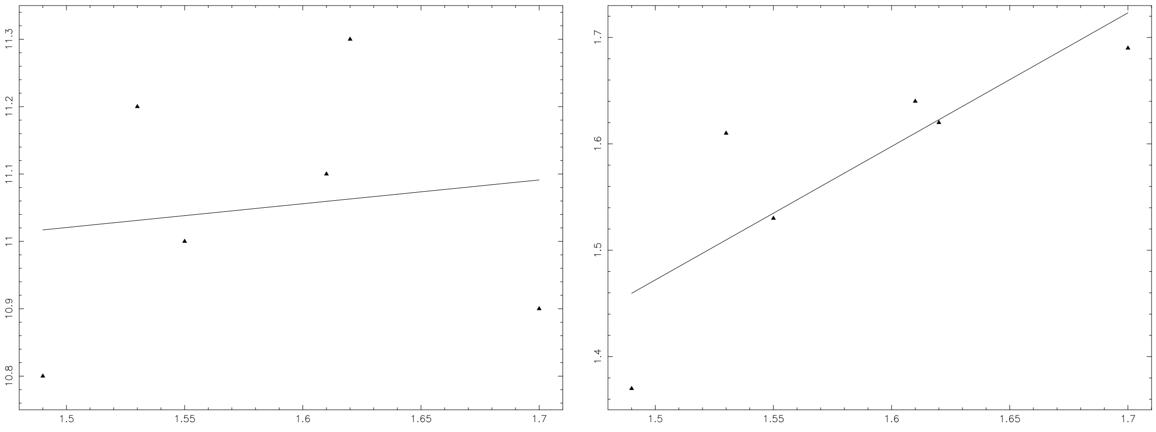

(a) Peak to continuum ratio vs. peak position. (b) Peak to continuum ratio vs. FWHM.

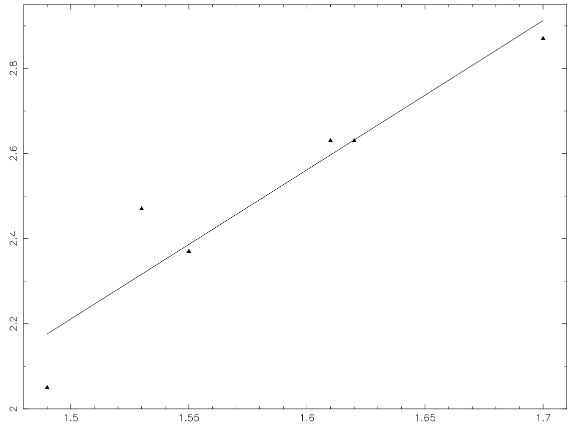

(c) Peak to continuum ratio vs. feature strength.

Figure 6.7: Correlations in the time-resolved of V Cyg, with the peak to continuum ratio as the x-axis in all figures.

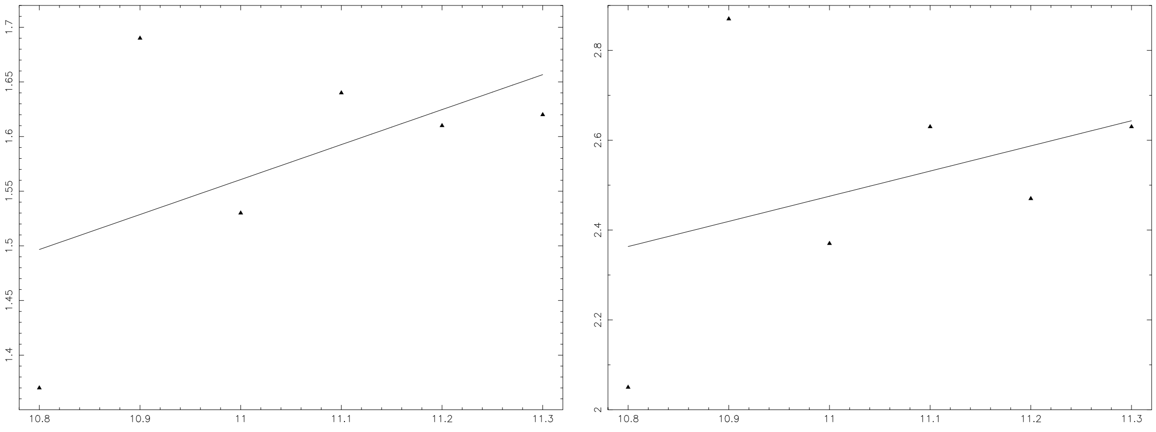

(a) Peak position vs. FWHM. (b) Peak position vs. feature strength.

Figure 6.8: Correlations in the time-resolved spectra of V Cyg, with the peak position as the x-axis in all figures.

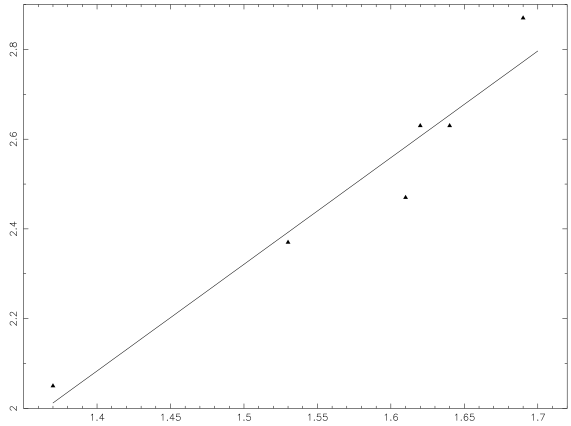

Figure 6.9: Correlations in the time-resolved spectra of V Cyg, with the FWHM as the x-axis and feature strength as the y-axis.

	Blackbody Temp.	Peak to Continuum Ratio	Peak Position	FWHM	Feature Strength
Feature Strength	0.0543	0.2420	0.3250	0.8628	
FWHM	0.2331	0.0185	0.4464		
Peak Position	0.0974	0.0004			
Peak to Continuum Ratio	0.3094				

Table 6.4: Correlations in the spatially resolved spectra of V Cyg. R^2 is the linear correlation coefficient for the given correlation.

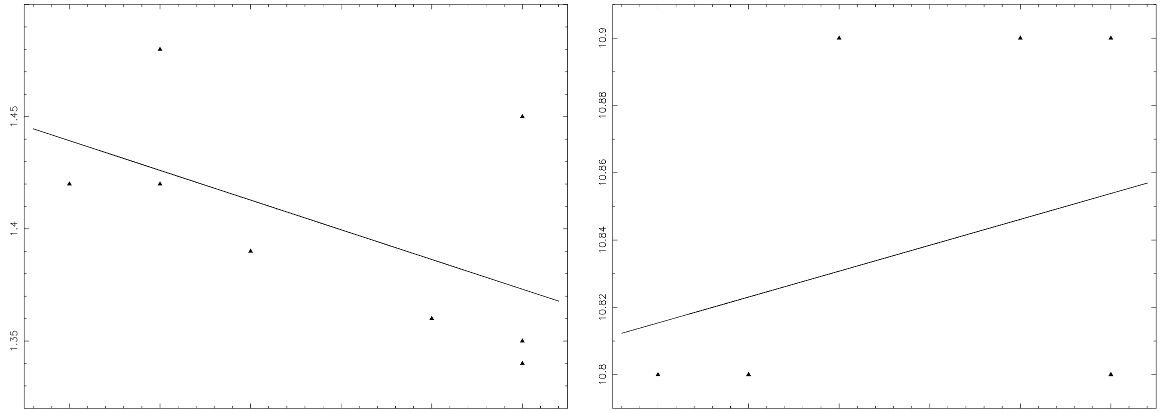

(a) Fitted blackbody temperature vs. peak to continuum ratio.

(b) Fitted blackbody temperature vs. peak position.

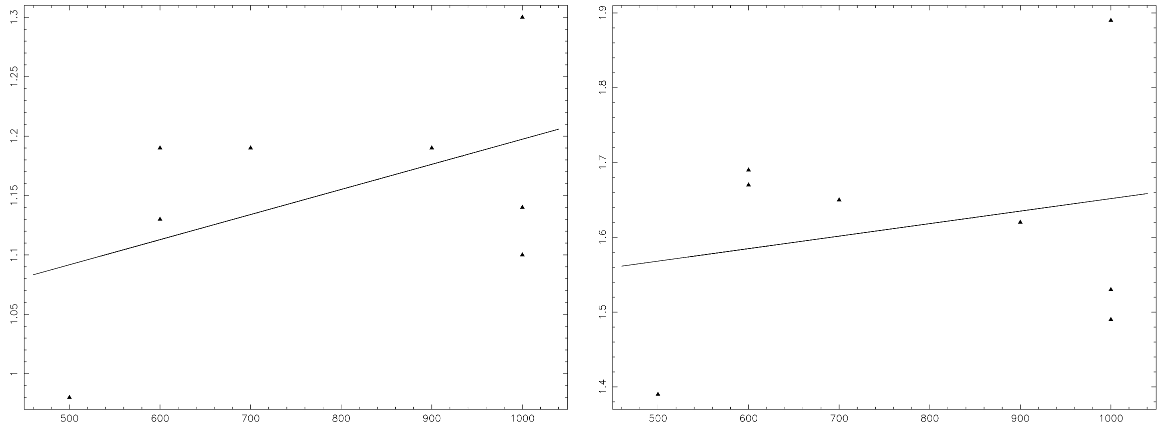

(c) Fitted blackbody temperature vs. FWHM.

(d) Visual magnitude vs. feature strength.

Figure 6.10: Correlations in the spatially-resolved spectra of V Cyg, with the fitted blackbody temperature as the x-axis in all figures.

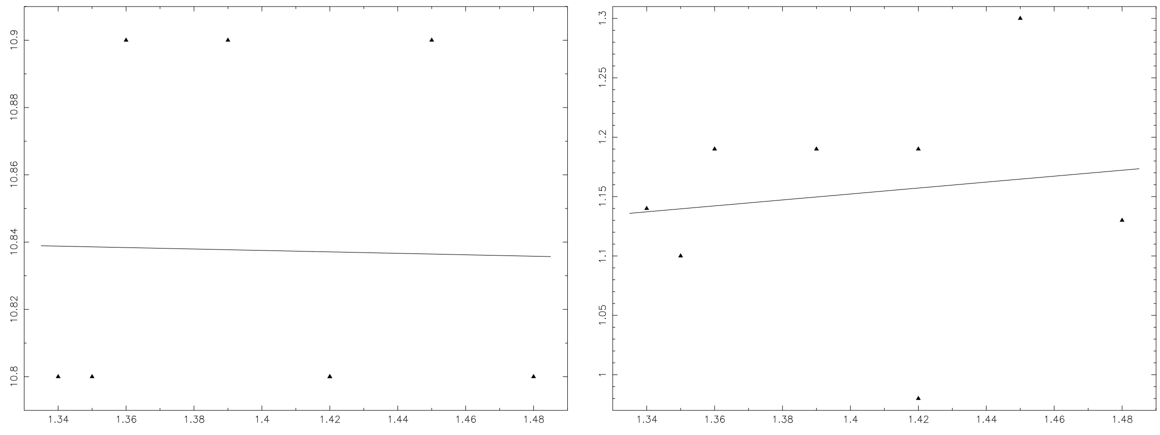

(a) Peak to continuum ratio vs. peak position. (b) Peak to continuum ratio vs. FWHM.

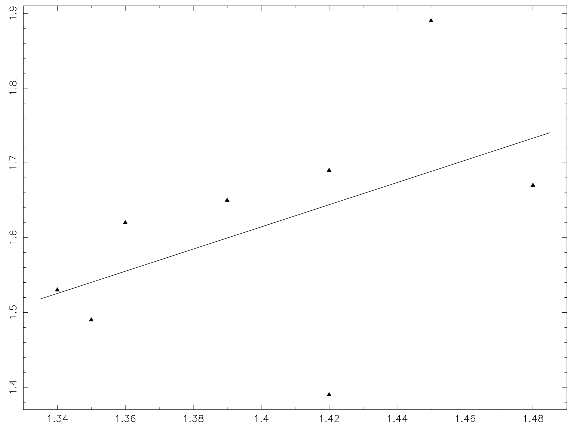

(c) Peak to continuum ratio vs. feature strength.

Figure 6.11: Correlations in the spatially-resolved spectra of V Cyg, with the peak to continuum ratio as the x-axis in all figures.

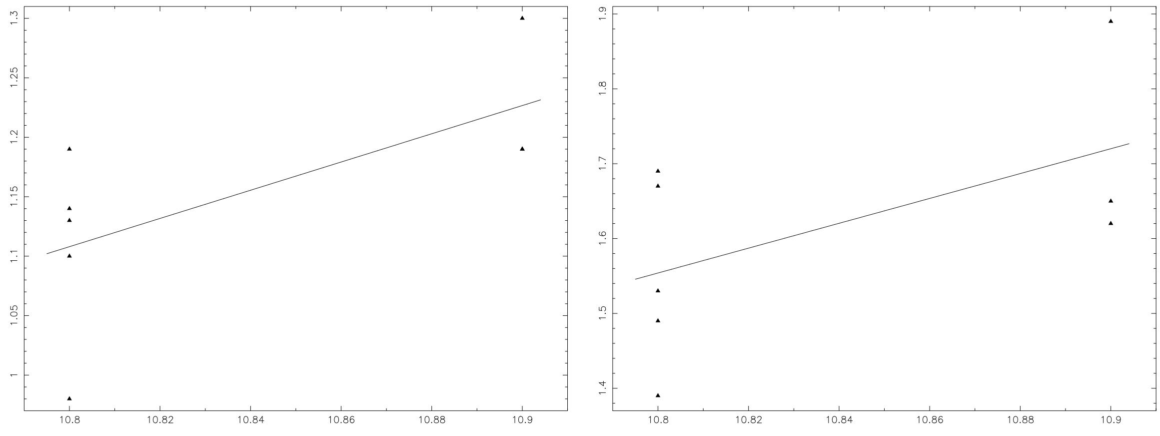

(a) Peak position vs. FWHM. (b) Peak position vs. feature strength.

Figure 6.12: Correlations in the spatially-resolved spectra of V Cyg, with the peak position as the x-axis in all figures.

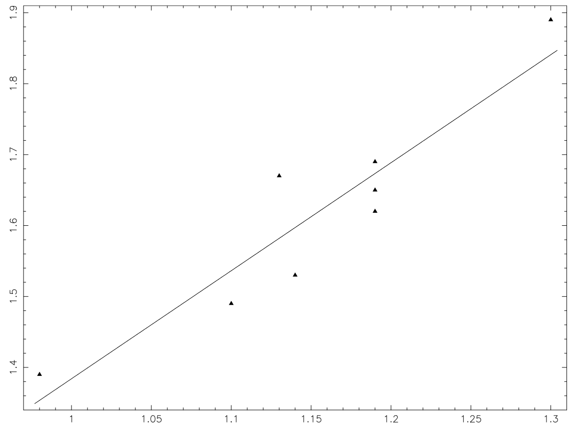

Figure 6.13: Correlations in the spatially-resolved spectra of V Cy, with the FWHM as the x-axis and feature strength as the y-axis.

as it is heated; the correlation between the apparent magnitude and the blackbody temperature is also reasonable, because we expect the dust to warm when the star is bright. To explain the other two correlations, we must recall section 7.1.2, where we discussed the SiC absorption feature around extreme carbon stars. Because those stars are totally obscured by their dust shells, we saw an absorption feature that resulted from the cooler SiC grains towards the outside of the shell absorbing light emitted by the warm grains nearer the star. Though V Cyg has a much lower optical depth and essentially the whole shell is being illuminated and heated by the star (which is the explanation for the correlation between the apparent magnitude and the blackbody temperature), the outer layers are still relatively cooler than the inner layers, and so it is not unreasonable that we would observe some self-absorption of the SiC feature. Another more speculative possibility is that there is possibly a grain shape effect which is influencing the exact position on the emission feature where the self-absorption is taking place; as we shall see in chapter 9, theoretical models involving different grain shapes show differing absorption features. This would be influencing the correlation between peak position and the feature strength. the More work would need to be done on this data though before a firmer conclusion could be reached.

The lack of correlations in the spatially-resolved spectra (except for the single one between the feature strength and the FWHM, which isn't meaningful) is somewhat strange, because we were so successful finding them in the time-resolved spectra. One possibility is that the difficulty in determining the continuum for the short wavelength range available for these spectra has introduced enough uncertainty in the fits to mask correlations. Another factor that may be preventing us from discovering correlations is that the pulsation scale (the distance between two pulsations as they drift away from the star) is much smaller than our spatial resolution. This would tend to smear out any dependence the SiC feature may have on the structure of the dust shell. A schematic diagram illustrating this is seen in figure 6.14.

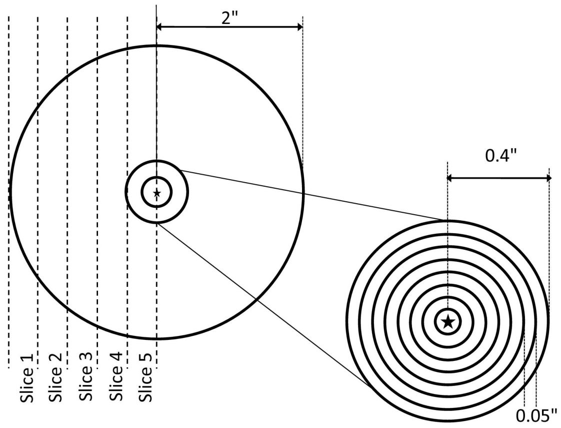

Figure 6.14: A schematic diagram illustrating the slices over the dust shell and the finer structure present in the shell. The slice numbers in this figure are only for illustrative purposes; they do not correspond to the actual position of the slices discussed in section refslices.

In order to observe the fine structure of the dust shell believed to be present, it would be necessary to obtain spectra of much higher spatial/angular resolution.

6.5 Summary and conclusions

Using a series of data sets taken over one of V Cyg's pulsation cycles, we generated blackbody fits and determined several parameters of the SiC emission feature visible in this star's spectrum. Then we investigated these parameters, looking for correlations; several were found, which seem to support the idea that V Cyg's dust shell is quite optically thin, and suggests that the SiC emission feature may be undergoing slight self-absorption. There is also the tentative possibility that a grain shape effect is altering the SiC feature.

The spatially-resolved spectra did not possess any significant correlations, which probably indicates that our spatial-resolution is much to low to observe structure and so any positional dependence on the SiC feature is averaged out and lost. It is also possible that the difficulty in obtaining a precise blackbody fit to the observational data over so short a wavelength range is influencing this result.

Chapter 7

Extreme Carbon Stars

"We can only see a short distance ahead, but we can see plenty there that needs to be done." - *Alan Turing*

7.1 Introduction

In section 2.2.5.2 we introduced the concept of a carbon star, and the dust shells that form around these stars; in chapter 5 we examined this concept in more detail through an investigation of a collection of these stars and their dust shells. The dust shells in that collection had relatively low optical depth; now we turn our attention to stars who have a dust shell so optically thick that only the infrared emission from the shell can be seen; the star itself is hidden from view.

This research was previously published in Speck et al. (2009), for which this author was a co-author.

7.1.1 Extreme Carbon Stars

As carbon stars evolve, mass loss is expected to increase. Consequently, their circumstellar shells become progressively more optically thick, and eventually the central star is obscured. Volk et al. (1992, 2000) christened such stars "extreme carbon stars". These stars have also been dubbed "infrared carbon stars" (Groenewegen, 1994), and "very cold carbon stars" (Omont et al., 1993). Extreme carbon stars are expected represent that small subset of carbon-rich AGB stars which are in the superwind phase, which is a period of intense mass loss just prior to leaving the AGB. The existence of the superwind has been inferred from observations, but the mechanism behind it is uncertain; possibly it is a result of particularly efficient dust-driven gas loss.

Because the superwind phase is short-lived compared to the AGB phase the number of extreme carbon stars is intrinsically small. Consequently, few of these objects are known. At present there are ∼30 known extreme carbon stars in the Galaxy (Volk et al., 1992) compared to ∼30,000 known visible carbon stars (Skrutskie et al., 2001).

van der Veen & Habing (1988) attempted to define a way to distinguish between oxygen-rich and carbon-rich AGB stars using IRAS color-color space, which was divided into subsections according to the properties of the dusty shells are these stars (see table 1 of van der Veen & Habing, 1988). This was further refined by Omont et al. (1993) who identified a population of very cold carbon stars using HCN and CO observations, and showed that the regions originally designated as extremely dusty O-rich AGB stars also contain a significant fraction of C-rich stars.

The refinement of the van der Veen & Habing (1988) color-color diagram by Omont et al. (1993) defined subdivisions of the seven zones in color-color space (see figure 1 in Omont et al., 1993). Cool carbon stars with high mass-loss rates (and little or no SiC emission) fall into regions III and IV, which had previously been assumed to define OH-IR stars (i.e. the oxygen-rich counterparts to extreme carbon stars). The numbered regions have been subdivided into smaller regions denoted by IIIa1, IIIa2, IIIb1 etc.

A subset of the color-color space, covering parts of regions IIIa1c, IIIb2, IIIb2 and VIb is reproduced in figure 7.1 and includes our sample stars.

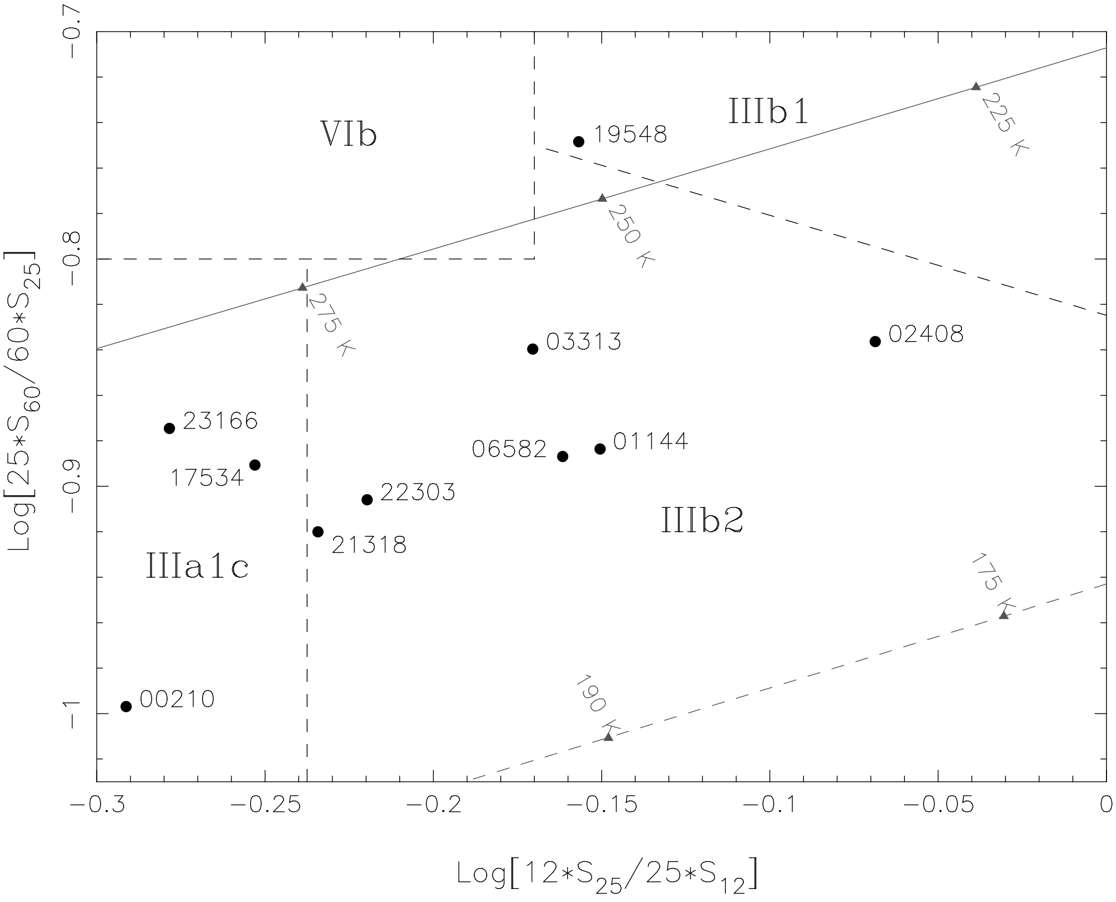

Figure 7.1: Regions in the IRAS color-color diagram populated by extreme carbon stars; see text for details. The black body curve is indicated by the solid grey line. The modified blackbody $[B(T, \lambda) * \lambda^{-1}]$ is indicated by the dashed grey line

7.1.2 SiC absorption features

A few extreme carbon stars have been shown to have an absorption feature at $\sim 11\mu$m which has been tentatively attributed to SiC. This feature was discovered in the "prototype" extreme carbon star AFGL 3068 (hereafter referred to as IRAS 23166+1655; Jones et al., 1978), and was re-examined by Speck et al. (1997), which also identified three additional extreme carbon stars with this feature. Clément et al. (2003) examined the absorption features of two of these extreme carbon stars (IRAS 23166+1655 and IRAS 02408+5458), and showed that their 11μm absorption features are consistent with β-SiC.

The broad absorption features of IRAS 19548+3035 and IRAS 21318+5631 (also discovered by Speck et al., 1997) were attributed to SiC absorption with an interstellar silicate absorption contribution (see also Groenewegen et al., 1996). This will be discussed further in section 7.4.6.

The absorption features in the spectra of IRAS 19548+3035 and IRAS 21318+5631 were revisited by Clément et al. (2005) who suggested Si_3N_4 grains as the carrier. However, this hypothesis has been shown to be erroneous (Pitman et al., 2006).

The failure of the Si_3N_4 hypothesis led Speck et al. (2005) to suggest that amorphous SiC grains may be able to account for the breadth, structure and barycentric position of the observed broad 10-13μm feature in IRAS 19548+3035 and IRAS 21318+5631. However, the dearth of amorphous presolar SiC grains seems to preclude this hypothesis (see section 7.1.4).

An alternative explanation for this feature is molecular line absorption, however, currently available line lists are not sufficient to properly assess this hypothesis (see Speck et al., 2006, and references therein). One molecular candidate which has transitions in the correct wavelength range is C_3 (e.g. Zijlstra et al., 2006; Jørgensen et al., 2000), but the line lists are not readily available. Furthermore, C_3 is expected to be photospheric, rather than circumstellar, which probably precludes its detection in optically obscured stars. Moreover, the theoretical spectrum of C_3 from Jørgensen et al. (2000) shows a strong absorption close to the $\sim 5\mu$m CO line, which is stronger than the $\sim 11\mu$m feature. As will be seen in section 7.4.4, the spectrum of IRAS 17534−3030 does not show the 5μm absorption band and provides evidence that the observed absorption feature is not molecular in origin.

Though previous research has included the effects of SiC self-absorption (shown to be crucial to produce accurate models Volk et al., 1992; Speck et al., 1997, 2005), no work has been done to directly fit the apparent SiC absorption feature in radiative transfer models of extreme carbon stars.

7.1.3 Previous Radiative Transfer Models of Extreme Carbon Stars

Volk et al. (1992) performed radiative transfer modeling in order to match the Infrared Astronomical Satellite (*IRAS*; Neugebauer et al., 1984) Low Resolution Spectrometer (LRS) data for several of extreme carbon stars. They determined that the exact star temperature entered into the model was not important for the emerging spectra due to the very thick dust shells around extreme carbon stars (c.f. DePew et al., 2006; Speck et al., 2000). Their models used a fixed composition (a mixture of graphite and SiC), and a fixed dust condensation temperature. Groenewegen (1994) also performed radiative transfer modeling on a larger set of extreme carbon stars, but these models varied the dust condensation temperature. Again this was based on *IRAS* LRS data. Following up on this, Groenewegen (1995) modeled a large sample of carbon stars using amorphous carbon optical constants (Rouleau & Martin, 1991), and assumed low dust condensation temperature in a fairly narrow range (650–900 K for the extreme carbon stars). Consequently the inner dust radius is larger than expected. Moreover the resulting models all have relatively low optical depths ($\tau_{11.3\mu\mathrm{m}} < 2$). The optical depth for their IRAS 23166+1655 model was found to be $\tau_{11.3\mu\mathrm{m}} < 1$, even though this star has an absorption feature at 11μm. Groenewegen et al. (1998) remodeled these stars, again assuming relatively low dust condensation temperatures, with similar results.

Finally, Volk et al. (2000) used the improved spectral resolution of the the Infrared Space Observatory (*ISO*; Kessler et al., 1996) Short Wavelength Spectrometer (SWS; de Graauw et al., 1996) to examine five extreme carbon stars. In their modeling study, Volk et al. (2000) allowed the optical depth and radial dust density distribution to vary; the resulting optical depths were relatively high (1.4-4.5 at 11.3μm), and the density of the dust shell was found to increase rapidly towards the center. This increase was interpreted as evidence of an increasing mass-loss rate within the last few thousand years, consistent with the identification of extreme carbon stars as the final stage of AGB star evolution. While these models did include SiC opacity data, the 11μm absorption feature was not recognized and consequently no attempt was made to fit this feature in these models.

A summary of the parameters of previous models for extreme carbon stars with 11μm absorption features in our sample can be found in table 7.1.

Interestingly, all previous models assume relatively low inner dust temperatures. This will be discussed further in section 7.3.4.1. Furthermore, the modeled dust density distributions suggest a relatively slow increase in mass-loss rates ($1/r^x$, where $x \approx$ 2.25—3.0).

In reality, dust shells are expected to have heterogeneities and anisotropies in their density structure as a result of pulsation-driven dust formation and the ensuing hydrodynamic turbulent effects (e.g. Woitke, 2006). These dust formation models suggest that carbon star mass-loss is expected to be modulated on several timescales, especially that of the pulsation cycle.

Furthermore Woitke (2006) has suggested that the dynamics in the dust-forming zones around carbon stars lead to inhomogeneous dust formation, producing fine scale

Table 7.1: Previous models of extreme carbon stars with 11μm absorption features

Star	composition† (SiC%)	Grain-size (μm)	$\tau_{11.3\mu m}$	drop-off	R$^*_{in}$ ($\times10^{-4}$ pc)	T$_{in}$ (K)	$\dot{M}^*$ M$_\odot$ yr^{-1}	REF
00210+6221	0	0.1	4.5	3.00	0.362/D	1000	$12\times10^{-5}/D$	2
01144+6658	8	0.1	4.84			1000	9.50×10^{-7}	4
06582-1507	0	...	5.15			1000	1.08×10^{-4}	1
	0	0.1	2.1	2.25	1.23	1000	2.59×10^{-4}	2
17534−3030	0	0.1	4.4	2.50	1.39	1000	8.20×10^{-4}	2
19548+3035	0	0.1	2.5	2.50	1.17	1000	3.89×10^{-4}	2
21318+5631	0	...	1.36			700	1.10×10^{-4}	3
23166+1655	0	0.1	1.12			650	5.50×10^{-7}	4
	30	...	7.85			1000	3.30×10^{-5}	1
	0	...	1.19			650	1.00×10^{-4}	3

References 1: Volk et al. (1992); 2: Volk et al. (2000); 3: Groenewegen (1995); 4: Groenewegen et al. (1998)

$*$ originally quoted as a function of distance. Value quoted here assume distances from Groenewegen et al. (2002), listed in table 7.5

† composition assumes remainder dust is carbon. In all but Volk et al. (1992) the carbon is amorphous; Volk et al. (1992) uses graphitic carbon.

Neither Volk et al. (1992) nor Groenewegen (1995) specify the grains sizes used in their models

structure in the density of¿ the dust envelope. In addition, while pulsation shocks are predicted to have a strong effect on local conditions (e.g. Cherchneff, 2006), this is not reflected in temporal changes in the IR spectra of carbon stars (see chapter 6). As will be seen in section 7.4, the spatial scale of the heterogeneities is small and the timescale for pulsations is short compared to the timescales associated with even the thinnest dust shells. Moreover, the inhomogeneities are expected to be wiped out over time by the hydrodynamic interactions (Villaver et al., 2002b,a). Consequently, we do not consider these small scale structures in our models.

7.1.4 Meteoritic evidence for non-SiC grain types

In section 4.3.1 we discussed the properties of presolar grains of SiC discovered in meteorites. SiC, is not, however, the only kind of presolar grain that has been observed, and at this point it is useful to discuss two kinds of these grains.

7.1.4.1 Presolar "graphite"

In addition to SiC presolar grains, carbon grains are also relatively abundant and well studied (see Bernatowicz et al., 2005, and references therein). Presolar carbon grains are usually referred to as "graphite" grains, but their structures are more complex than this name infers. Presolar graphite is found in two types of spherules classified according to their external morphologies as "onion-like" and "cauliflower-like". In general the graphite spherules follow a similar size distribution to the SiC grains. However, the high-density grains ($\rho \approx 2.15 - 2.20\,\mathrm{g}\,cm^3$) associated with AGB stars have a mean size of 2μm. In addition, the AGB presolar graphite spherules span a larger range of isotopic compositions than the SiC grains, possibly suggesting that they form at a wider range of times during the AGB phase.

While the presolar SiC grains tend to be single crystals, the graphite grains regularly contain carbide grains. These carbides are enriched in *s*-process elements, indicative of formation around late-stage AGB stars.

Many of the "onion-like" graphite grains have a core mantle structure in which the core contains disordered agglomerations of graphene[1] sheets and PAH[2]-like products, while the mantle is composed of well-ordered graphitic concentric shells. The graphene particles have a typical size of 3-4nm.

---

[1] Graphene is basically a single sheet of graphitic material. If it is disordered, there are some heptagons and pentagons in place of the regular hexagonal carbon structure. Graphite is the 3-d structure.

[2] polycyclic aromatic hydrocarbon

The “cauliflower-like” graphite grains also have a concentric shell structure, but it is less well ordered, and is composed primarily of the disordered graphene.

Whether “onion” and “cauliflower” graphites are formed in the same outflows is not known. Both types of grain contain the refractory carbides and both span the same range of isotopic compositions.

7.1.4.2 Other presolar carbides

As discussed in chapter 4 and section 7.1.4.1, refractory carbides are found inside “graphite” grains but not in SiC grains. Furthermore, SiC is not one of the carbides found in “graphite” grains. The refractory carbides (TiC, ZrC, MoC and RuC) provide more constraints on the dust formation processes around carbon stars. In particular, the formation of “graphite” spherules with TiC nuclei limits the range of C/O ratios in which these grains could form to $1 \approx C/O \approx 1.2$. Meanwhile, the ZrC can form nuclei at higher C/O, but the value still needs to be less than two. This is consistent with the measured C/O ratios of Galactic carbon stars, which have an average of 1.15 and a maximum of 1.8 (Lambert et al., 1986)

7.1.5 Investigation

In the present work, we investigate a subset of extreme carbon stars, those which exhibit the 11μm absorption feature. Through radiative transfer modeling, we investigate the nature of these dust shells. We use theoretical models and meteoritic data to limit the parameter space and thus reduce the degeneracy within the model results. In addition, we look for correlations between observed parameters, such as those that define the 11μm feature (strength, position, etc) as well as mass-loss rates and expansion velocities associated with the dust shells. Finally, we determine timescales associated with the dust shells.

7.2 Observations and Data Processing

We investigated 10 extreme carbon stars observed spectroscopically by the ISO SWS all of which show evidence for an $\sim 11\mu$m absorption feature (see table 7.2 and figures 7.2, 7.3,7.4 and 7.5).

Table 7.2: Target list

IRAS Number	Other Names	R.A. [a] (J2000)	Decl. (J2000)	TDT number	Date of Observation
00210+6221	CGCS 6006	00 23 51.2	+62 38 16.4	40401901	1996 Dec 24
01144+6658	V829 Cas, AFGL 190, CGCS 6017	01 17 51.6	+67 13 55.4	68800128	1997 Oct 03
02408+5458		02 44 25.2	+55 11 15	80002504	1998 Jan 24
03313+6058	CGCS 6061	03 35 30.7	+61 08 47.2	62301907	1997 Jul 31
06582+1507	CGCS 6193	07 01 08.44	+15 03 39.8	71002102	1997 Oct 26
17534−3030	AFGL 5416, CGCS 6690	17 56 33.1	−30 30 47.1	12102004	1996 Mar 17
19548+3035	AFGL 2477, CGCS 6851	21 50 45.0	+53 15 28.0	56100849	1997 May 30
21318+5631	AFGL 5625S, CGCS 6888	21 33 22.98	+56 44 35.0	11101103	1997 Mar 7
22303+5950	CGCS 6906	22 32 12.8	+60 06 04.1	77900836	1998 Jan 02
23166+1655	LL Peg, AFGL 3068, CGCS 6913	23 19 12.39	+17 11 35.4	37900867	1996 Nov 29

---

[a] Note: Units of right ascension are given in hours, minutes and seconds; units of declination are degrees, arcminutes and arcseconds.

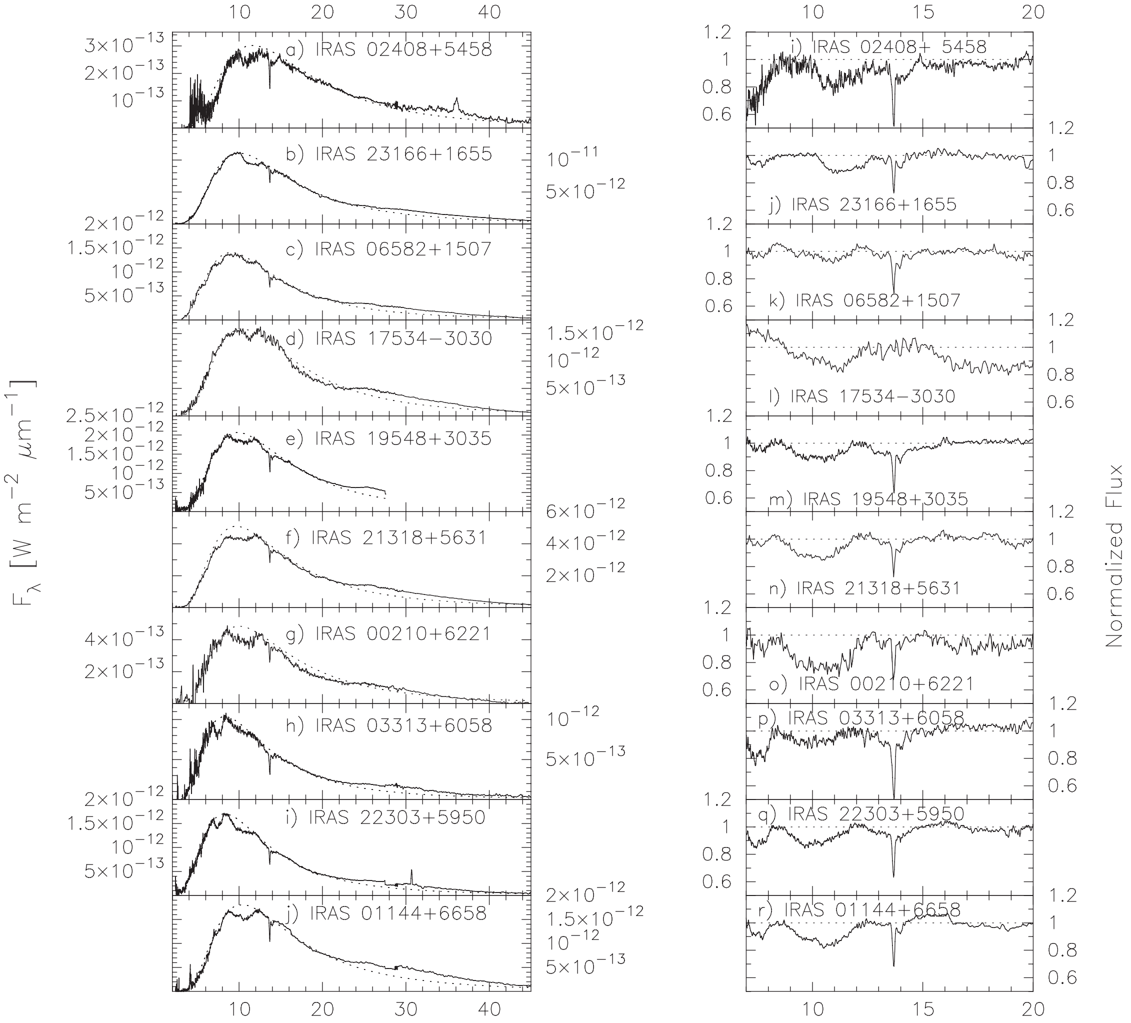

Figure 7.2: *ISO* SWS spectra of ten extreme C-stars. *Left Panel*: Flux-calibrated spectra and fitted blackbody continua. Solid line = *ISO* spectrum; dashed line = best-fitting blackbody continuum; The y-axis is the flux (F_λ) in $W\,m^{-2}\,\mu m^{-1}$; the x-axis is wavelength in μm. *Right Panel*: Continuum-divided spectra. Table 7.3 lists the blackbody temperatures used in each case to produce the continuum and the continuum-divided spectra.

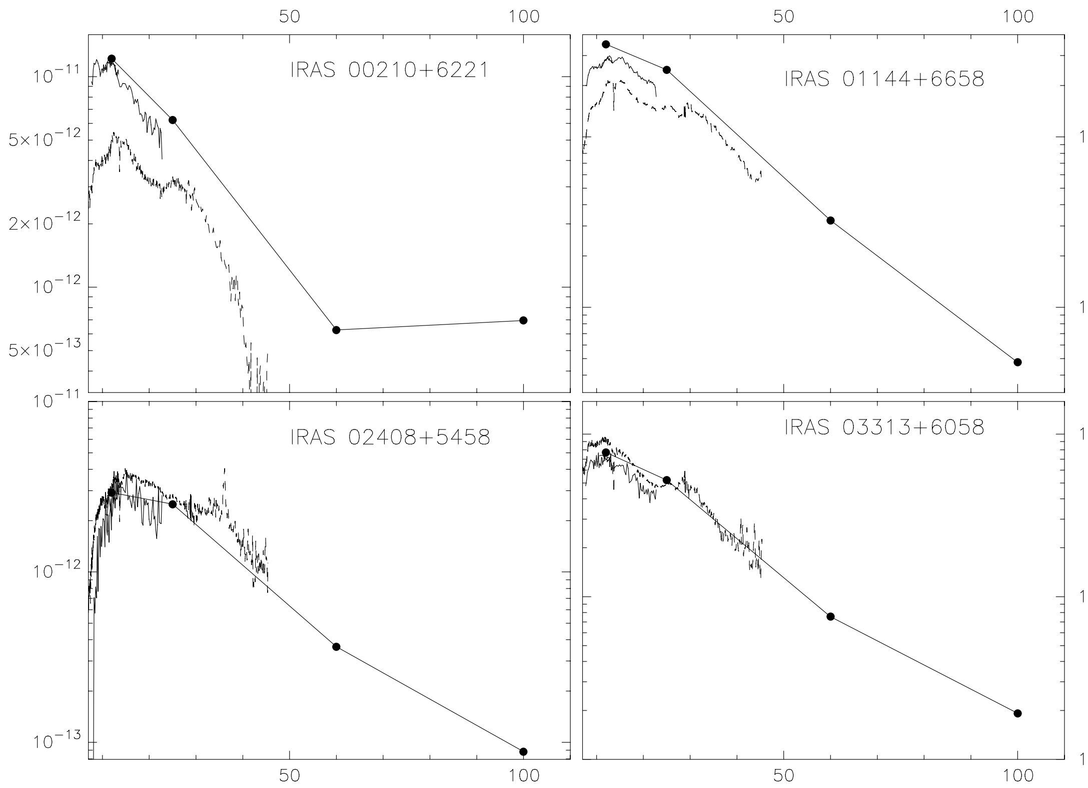

Figure 7.3: *ISO* SWS spectra of sample extreme C-stars together with *IRAS* 12, 25, 60 and 100μm photometry points and *IRAS* LRS spectra. Solid line = *IRAS* spectrum; points = *IRAS* photometry points; dashed line = *ISO* SWS spectrum. The y-axis is the flux (λF_λ) in W m^{-2}; the x-axis is wavelength in μm.

These sources were chosen by searching the ISO archive for spectra of extreme carbon stars listed in Volk et al. (1992) and selecting those with an apparent 11μm absorption feature. In addition, we used the color-color classification of “very cold” carbon stars by Omont et al. (1993) to identify further potential sources. Unfortunately most of the potential sources found in the color-color space (e.g. IRAS 17583-2291) were not observed by ISO SWS, and the IRAS LRS spectra are too low resolution and/or too noisy to be used in the present study.

Four of our sources (IRAS 02408+5458, IRAS 19548+3035, IRAS 21318+5631, and IRAS 23166 +1655) were previously studied using ground-based observations and were

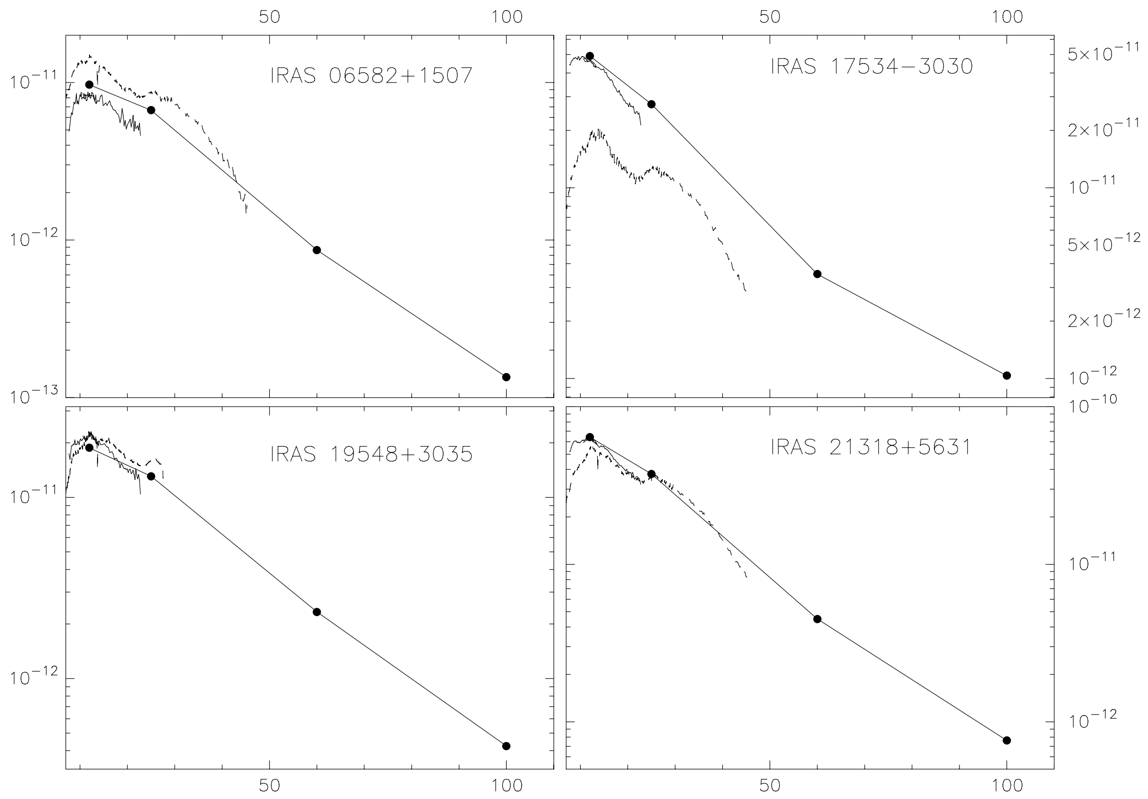

Figure 7.4: *ISO* SWS spectra of sample extreme C-stars together with *IRAS* 12, 25, 60 and 100μm photometry points and *IRAS* LRS spectra (part 2). Solid line = *IRAS* spectrum; points = *IRAS* photometry points; dashed line = *ISO* SWS spectrum. The y-axis is the flux (λF_λ) in W m^{-2}; the x-axis is wavelength in μm.

found to be consistent with a self-absorbed SiC feature (Speck et al., 1997). Two of these sources needed an extra absorption component at ~10μm, which were attributed to interstellar absorption. As discussed in section 7.1.2, these have since been the source of some controversy (Clément et al., 2005; Pitman et al., 2006).

Following the modeling efforts of Volk et al. (2000), Speck et al. (2005) identified IRAS 00210+6221, IRAS 06582+1507, and IRAS 17534−3030 as exhibiting an SiC absorption feature. The modeling of Volk et al. (2000) did not include SiC and did not attempt to fit the 11μm absorption. Thus, division of the observed spectra by their respective RT model spectra revealed the 11μm absorption feature.

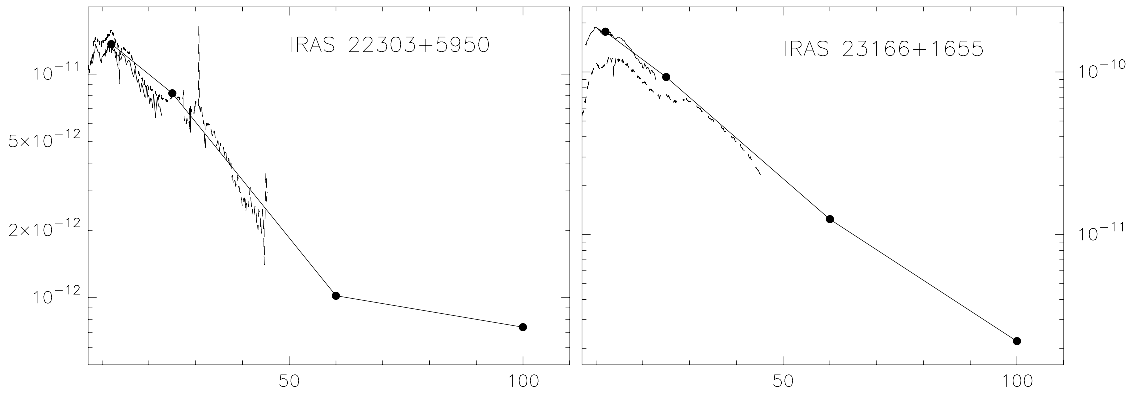

Figure 7.5: *ISO* SWS spectra of sample extreme C-stars together with *IRAS* 12, 25, 60 and 100μm photometry points and *IRAS* LRS spectra (part 3). Solid line = *IRAS* spectrum; points = *IRAS* photometry points; dashed line = *ISO* SWS spectrum. The y-axis is the flux (λF_λ) in W m^{-2}; the x-axis is wavelength in μm.

Three new, potential SiC absorption features in ISO SWS spectra (IRAS 01144+6658, IRAS 03313+6058, and IRAS 22303+5950) were discovered by searching the ISO archive for any extreme or "very cold" carbon stars as determined by their location in the IRAS color-color space. Those sources that fall within region III without OH maser emission were examined.

The locations of the stars in our sample in *IRAS* color-color space (van der Veen & Habing, 1988; Omont et al., 1993) are plotted in figure 7.1. Interestingly, all sources except IRAS 19548+3035 plot along a line parallel to and between the blackbody emission and the $B(T, \lambda, T) \times \lambda^{-1}$ emission lines.

The raw ISO data were extracted from the ISO data archive, and we used the Off-Line Processing (OLP) pipeline, version 10.1. Individual spectral sub-bands were cleaned of glitches (caused by cosmic ray particles) and other bad data sections. Next, they were flat-fielded, sigma-clipped (using the default values $\sigma = 3$) and rebinned to the final spectral resolution ($R = \Delta\lambda/\lambda$), which ranged from 200 to 700, depending on the scanning speed of the SWS grating during the observation (Leech, 2003).

Table 7.3: Observed parameters of the target sources

IRAS Number	$T_{\rm BB}$ (K)	Feature Barycenter	Feature[1] Strength	FWHM	Equivalent Width	9.7μm[2] Strength	11.3μm[3] Strength	SiC[4] position
00210+6221	290K	10.45	0.73	2.28	0.60	0.76	0.77	11.3
01144+6658	280K	10.51	0.82	2.32	0.35	0.88	0.87	11.3
02408+5458	250K	11.28	0.73	2.20	0.30	—	0.83	11.3
03313+6058	350K	10.12	0.87	1.72	0.17	0.90	0.97	10.8
06582+1507	320K	10.25	0.91	0.70	0.1	0.97	0.94	11.0
17534−3030	280K	10.59	0.87	0.80	0.30	0.92	0.83	11.3
19548+3035	295K	10.24	0.87	2.39	0.25	0.88	0.93	11.0
21318+5631	300K	10.20	0.84	2.90	0.37	0.88	0.93	11.0
22303+5950	350K	10.25	0.84	1.70	0.25	0.86	0.94	11.0
23166+1655	290K	11.42	0.86	2.00	0.21	—	0.88	11.4

[1] Feature strength is the “peak”-to-continuum ratio and is measured and the barycentric position.

[2] The 9.7μm strength is the feature-to-continuum ratio measured at 9.7μm.

[3] The 11.3μm strength is the feature-to-continuum ratio measured at 11.3μm.

[4] The SiC position, the the approximate barycentric position that the SiC feature would have if the short wavelength side of the absorption were due to silicate 9.7μm absorption.

The final spectra are presented in figure 7.2, which also shows the best-fitting[3] blackbody continuum for each spectrum and the resulting continuum-divided spectra. The blackbody temperatures of the continua at listed in table 7.3.

The continuum-divided spectra clearly show an absorption feature in the 10-13μm region, the basic parameters of which (barycentric position, peak-to-continuum ratio, full width half maximum; FWHM) are listed in table 7.3. The excellent match between the overall spectrum and a single temperature blackbody suggests that we are seeing an isothermal surface within the dust shell. This represents the depth at which the shell becomes optically thick. The lack of extra emission at longer wavelengths suggests that any outlying dust is low enough in density to have an insignificant contribution to the overall emission.

In addition to the *ISO* SWS spectra, Fig 7.3, 7.4 and 7.5 shows the *IRAS* LRS spectra and the *IRAS* 12, 25, 60 and 100μm photometry measurements. The difference in the flux levels between the *IRAS* and *ISO* data is not unexpected, since these stars are variable. However, the shape of the spectrum does not change significantly

---

[3] Best fits are achieved by eye and proceed by examination of the continuum-divided spectra.

between the two observations, suggesting that changes in the stellar luminosity do not significantly impact the structure and composition of the dust shells.

In order to determine the cause of the 10-13μm feature and the factors that govern its strength, width and position we have tabulated the barycentric position, feature-to-continuum ratio and equivalent width of the feature (table 7.3). In addition, we have also tabulated where the barycenter of the SiC feature would be if the short wavelength side of the absorption is due to silicate (as has been postulated, see section 7.1.2). This, along with the feature-to-continuum ratio measured at 9.7 and 11.3μm, can be found in table 7.3.

7.2.1 The "30μm" feature

Another prominent spectral feature exhibited by our sample of extreme carbon stars is the so-called "30μm" feature. This feature is relatively common amongst carbon-rich AGB stars, PPNe and PNe and was first discovered in Kuiper Airborne Observatory (*KAO*) spectra of carbon stars and PNe (Forrest et al., 1981). It has been widely attributed to magnesium sulfide (MgS; e.g. Goebel & Moseley, 1985; Nuth et al., 1985; Omont et al., 1995; Begemann et al., 1994; Hony et al., 2002). Modeling this feature is beyond the scope of the present work, but will be investigated in follow-up modeling. Our models make no attempt to fit the "30μm" feature.

7.3 Radiative Transfer Modeling

Radiative transfer modeling has been particularly useful in investigating extreme carbon stars (see section 7.1.3; Volk et al., 1992; Groenewegen, 1995; Volk et al., 2000). We used the 1-D radiative transfer program DUSTY (Ivezic & Elitzur, 1995; Nenkova et al., 2000), to determine the effect of dust shell parameters on the emerging spectra from carbon stars. In all cases, the central star was assumed to be at 3000 K (typical for an AGB star). Speck et al. (2000) and DePew et al. (2006) showed that changing this temperature by ±1000 K did not significantly change the radiative transfer model's spectra (c.f. Volk et al., 2000). For simplicity, dust grains are assumed to be spherical. While DUSTY can include other grain shapes, this expands parameter space to create more degeneracy between models and is beyond the scope of the present work.

7.3.1 Radial dust density distribution

We assume a radial dust density distribution of $1/r^2$ which would reflect a constant mass-loss rate. This choice is somewhat controversial and certainly needs justifying. Current dust formation models suggest that carbon star mass-loss is expected to be modulated on several timescales, especially that of the pulsation cycle (Woitke, 2006, and references therein). Furthermore Woitke (2006) has suggested that the dynamics in the dust-forming zones around carbon stars lead to inhomogeneous dust formation, producing fine scale structure in the density of the dust envelope. While pulsation shocks are predicted to have a strong effect on local conditions (e.g. Cherchneff, 2006), this is not reflected in temporal changes in the IR spectra of carbon stars (see chapter 6). Previous models of extreme carbon stars have included steeper a density drop-off (see table 7.1; Volk et al., 1992, 2000; Groenewegen, 1995; Groenewegen et al., 1998), which is meant to represent the increasing mass-loss rate associated with the onset of the superwind phase. However, Villaver et al. (2002b,a) showed that the hydrodynamics in the circumstellar shell wipe out density structure and leave a shell with a

$1/r^2$ density distribution. In addition Rowan-Robinson & Harris (1983a) showed that carbon star spectra can be well-fitted using such a density distribution.

In our models we assume that modulations in density have been wiped out or are unimportant in determining the spectrum at these high optical depths, as we are clearly seeing an outer dust shell surface. We also assume we are only detecting the dust that has formed since the onset of the superwind. We assume that there was a sudden increase in mass loss at some time in the last ~10000 years and that this mass-loss rate is now approximately constant, with small scale fluctuations being unimportant for dust properties. Consequently, the $1/r^2$ density distribution suffices. As will be seen in section 7.4, the impact of assuming a steeper the density distribution is to remove dependence on shell size, and thus remove the ability to out limits on timescales. If we were to adopt a $1/r^3$ density distribution, all the dust would effectively be contained close to the star and would reflect the total mass lost over only a relatively short period.

7.3.2 Modeling grain-size distributions

The issue of choosing a grain size distribution is interesting and certainly requires more discussion. Our initial modeling studies used an MRN distribution (i.e., $n(a)$ proportional to a^{-q}, where n is the number of the grains in the size interval $(a, a+da)$ and $q = 3.5$;$a_{min} = 0.005\mu$m; and $a_{max} = 0.25\mu$m; Mathis et al., 1977). This was chosen because as will become evident below, we do not actually know the grain size distribution and MRN is as plausible as any other. However, the MRN distribution was developed for interstellar dust where the balance of formation and destruction is different from AGB circumstellar environments. Dominik et al. (1989) suggested that the grain-size distribution created in the circumstellar environments of AGB stars has a steeper power law (i.e. a^5), while Kim et al. (1994, KMH) modified the MRN distribution to include an exponential fall-off term.

We should also consider the "observational" evidence for range and distribution of grain sizes in carbon star outflows. Meteoritic presolar SiC grains from carbon stars have a huge grain-size distribution, ranging for 1.5nm up to 26μm, with the majority of grains ($\sim$70%) falling in the 0.3–0.7μm range (see Daulton et al., 2003; Bernatowicz et al., 2006; Clayton & Nittler, 2004). Half the mass of the presolar SiC found in the Murchison meteorite is in grains larger than 0.6μm (Virag et al., 1992). Carbon presolar grains follow a similar grain size distribution to SiC (Bernatowicz et al., 2005). However, the sample may be biased in favor of large grains, which may be more apt to survive the journey through the ISM and incorporation into a solar system body.

Conventional theories of grain growth cannot produce the largest grains. Since AGB stars typically have mass-loss rates $< 10^{-5}$ $M_\odot\,yr^{-1}$ there should be an upper limit to the grain sizes of $\sim 0.1\mu$m. However, this assumes an isotropic distribution of material. The existence of meteoritic titanium carbide (TiC) within presolar carbon grains necessitates density inhomogeneities in the gas outflows (c.f., inhomogeneities caused by turbulence in hydrodynamic models of carbon-rich dust formation regions; Woitke, 2006). In addition, the grains must be $\approx 1\mu$m to produce the 11μm feature, implying that there is a large population of small grains (but not necessarily precluding large grains). Constraints on grain size were also discussed by Martin & Rogers (1987) who found an upper limit to the grain size of $\sim$0.1μm based on polarization measurements of the famous carbon star, IRC+10216. On the other hand, Groenewegen et al. (1997) used polarization measurements to limit the grain size to 0.1 = a = 0.35μm and suggested that very small grains (<80 nm) may not exist around carbon stars (however, smaller SiC grains are found in meteorites). Meanwhile, Jura (1994) argued the case for grains larger than 1μm in the circumstellar shells of IRC+10216.

Towards the end of the AGB the onset of the superwind may lead to mass-loss rates as high as a few $\times 10^{-4}$ M$_\odot$ yr^{-1} (e.g. Hony et al., 2003) which could translate into larger grains (see e.g. Bernatowicz et al., 2005, and references therein). However, the relationship between the evolution of carbon stars and the consequent evolution of grain sizes in their circumstellar shells was discussed by Speck et al. (2005). They argued that the increased mass-loss rates at the end of the AGB phase lead to smaller, rather than larger grains as suggested by meteoritic evidence. Even the highest observed mass-loss rates cannot account for formation of titanium carbide (TiC) grains unless the distribution of material is not spherically symmetric and density enhancements exist (Bernatowicz et al., 2005). Such a distribution of material makes the concept of grain size distributions even more complex.

The range of grain sizes used in previous radiative transfer modeling attempts varies hugely. The IRC+10216 models of Griffin (1990) required grain sizes limited to $5 \leq a \leq 50$nm. Similarly Bagnulo et al. (1995) required grains smaller than 50nm. Groenewegen et al. (1997) also modeled IRC+10216 and found that the spectrum was best fit using a single grain size of 0.16μm (rather than a distribution of grain sizes). The single-grain size approach was also adopted by Volk et al. (2000) who assume a single grain size of 0.1μm. This is supported by the success of the early carbon star models of Rowan-Robinson & Harris (1983a) who also used a single grain size (0.1μm). However, since extreme carbon stars are expected to be the direct precursors for post-AGB objects, it may be more appropriate to consider the models of post-AGB stars. Such modeling efforts have found they need grains up to millimeter- or even centimeter-in size (e.g. Jura et al., 2000; Meixner et al., 2002). Meixner et al. (2002) used a KMH-like distribution with an effective maximum grain size of 200μm (hereafter referred to as KMH200). Meanwhile, Szczerba et al. (1997) modeled a carbon-rich post-AGB object with a power-law distribution of grains in the range 0.01–1μm.

Given the range of possible grain sizes and distributions, it is difficult to know how best to model the dust. Groenewegen (1995) argued that the specific grain-size is not important as long as the grains are small enough that the absorption and scattering properties are independent of grain size. However, given the arguments for a population of large grains, limiting grains to smaller than 0.1μm is unrealistic.

In order to determine the effect of the choice of grain sizes on the model spectra we have generated models using five additional grains size distributions: 1) MRN-like with a steeper power law, i.e. $a_{min} = 0.005\mu$m, $a_{max} = 0.25\mu$m; $q = 5$ (as suggested by Dominik et al., 1989); 2) only 0.1μm-sized grains (as used or suggested by Volk et al., 2000; Rowan-Robinson & Harris, 1983a; Groenewegen, 1995; Martin & Rogers, 1987); 3) the dominant meteoritic grain sizes, i.e. 0.1–1μm only; 4) the standard KMH distribution (i.e. $n(a) \propto a^{-q}e^{a/a_0}$, $a_{min} = 0.005\mu$m, $a_0 = 0.2\mu$m; $q = 3.5$); and finally 5) KMH200: KMH with $a_0 = 200\mu$m. The results of this study are shown in figure 7.6, which shows the effect of changing the grain size distribution while keeping all other parameters constant.

If we examine the differences in the spectra generated by changing the grain-size distributions, this can be understood in terms of the absorption efficiency of the grains and breadth of the grain size distribution. Changing from our default grain size distribution (MRN) to a modified MRN-like distribution with a steeper power law drop off ($q = 5$) as suggested by Dominik et al. (1989) makes very little difference to the model spectral energy distribution (SED). Likewise, switching from MRN to KMH has little effect on the overall shape of the SED. That the MRN, $q = 5$ and the KMH models are so similar is because they are basically weighted towards the same small grains. While the weighting is different, the same-sized small grains dominate

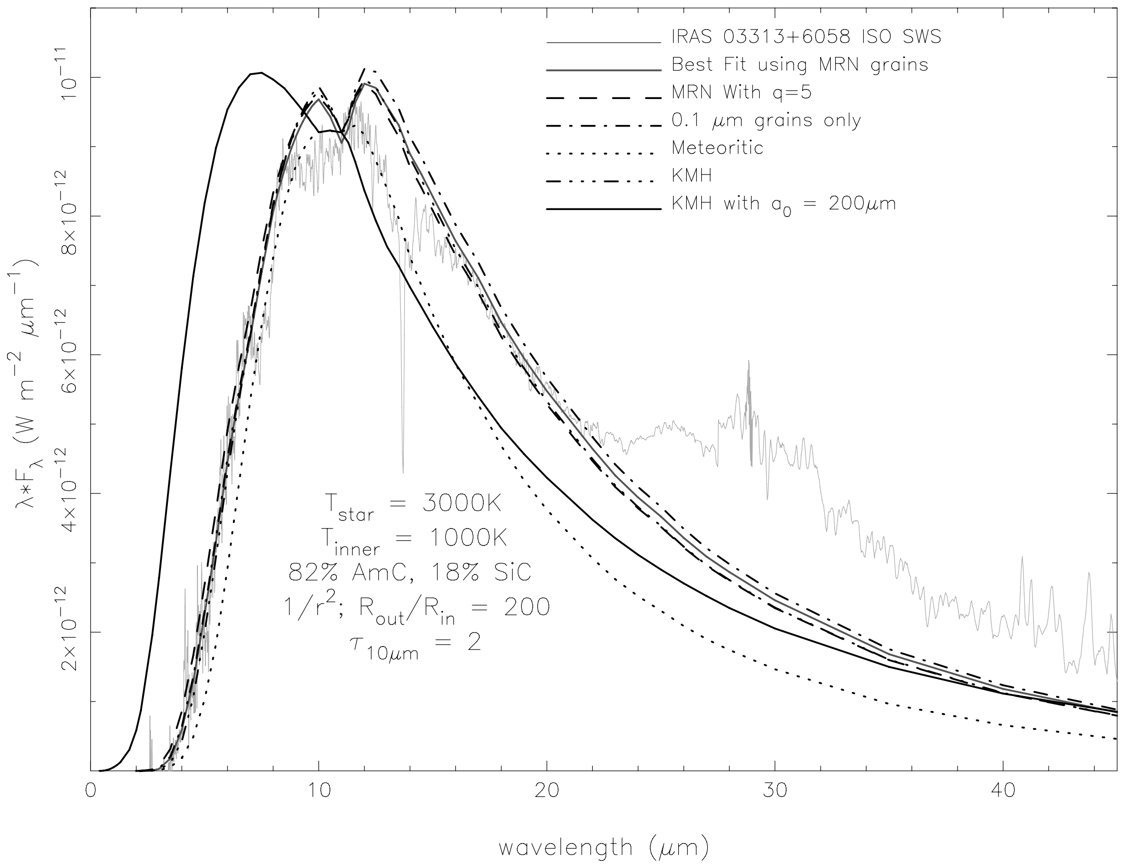

Figure 7.6: The effect of grain-size distributions on the model spectral energy distribution. In all cases the model parameters are identical except for the grain-size distribution; see section 7.3.2 for detailed description of the grain-size distributions. The grey line shows the ISO-SWS spectrum of IRAS 03313+6058 for comparison.

the SED. However, changing the size distribution to include larger dust grains as used in models of post-AGB stars (e.g. Meixner et al., 2002) has an major effect. The SED shifts to peak at much shorter wavelengths. This is because of the reduction in the number of small grains in order to include larger grains. The proportion of larger grains is small, but the removal of the smaller grains makes it possible for the stellar photons to penetrate deeper into the dust shell and provides a large population of warmer grains, resulting in a warmer SED. In both the KMH200 and 0.1μm cases there is a lack of very small grains which absorb a lot of stellar photons and change the temperature distribution (i.e. after the first layer of dust the temperature is lower, but if there are no small grains the stellar photons penetrate further.) Since size distributions similar to KMH200 are typically associated with long-lived dust disks, this particular distribution is not considered further.

For the meteoritic grain size distribution, the short wavelength side of the SED is similar to the default (MRN) model, but now the SED is much narrower. This can be explained by the very narrow range of grain sizes. There are no very small grains that can be easily heated and thus the shorter wavelength emission seen in KMH200 does not occur, but the lack of small grains also allows deeper penetration of stellar photon leading to a narrower temperature distribution.

This grain size study suggests that for most adopted grain-size distributions, the resulting SEDs will be equivalent and we assume the MRN distribution as "generic". However, the meteoritic grain-size distribution can narrow the overall SED. For this reason, our modeling efforts concentrate on the generic (MRN) and "meteoritic" grain size distributions, where the "meteoritic" is taken to be an extreme amongst the range of reasonable grain-size assumptions. The impact of choosing different grain size distributions and the implications of these differences for the potential errors in our models will be discussed in section 7.4. However, essentially, most grain-size distributions will yield the same results except for "meteoritic" and KMH200. In both cases changes in optical depth, inner dust temperature and/or relative geometrical shell thickness can be manipulated to fit the spectrum. There is a degeneracy in model fits due to the relationship between these three parameters that will be discussed in the next section. As will be seen in the section 7.4, the grain size effects cannot be ignored. In one source the need for "meteoritic" grain-size distribution is clear.

7.3.3 Parameter space investigated

In addition to grain sizes and radial density distribution, the variables investigated with DUSTY are the inner dust shell temperature ($\mathrm{T_{inner}}$), optical depth (specified at 10μm; $\tau_{10\mu\mathrm{m}}$), dust composition, and the geometrical thickness of the dust shell, $\xi = R_{\mathrm{out}}/\mathrm{R_{in}}$, where $\mathrm{R_{in}}$ and $\mathrm{R_{out}}$ are the inner and outer radii of the dust shell, respectively. The optical constants for the dust components came from Pègouriè (1988); Hanner (1988) and Draine & Lee (1984) for SiC, amorphous carbon and graphite, respectively. In nearly all cases it was possible to generate more than one model to fit the spectra, consequently we also investigate this degeneracy in parameter space and look for realistic ways to restrict it.

7.3.3.1 Degeneracies in radiative transfer modeling

There is a clear degeneracy in the models because of the relationship between certain parameters, e.g. optical depth and geometric shell thickness, or optical depth and the temperature at the inner edge of the dust shell. Ivezic & Elitzur (1997) discussed these degeneracies and the relationship between the different input parameters in radiative transfer models, but we need to understand these relationship if we are to understand what our models mean.

The wavelength-dependent optical depth, τ_λ is defined by:

$$d\tau_\lambda = \rho(r)\kappa_\lambda dr \tag{7.1}$$

where $\rho(r)$ is the density of the absorbing/scattering particles (i.e. the dust grains) and κ_λ is the wavelength dependent opacity of the assemblage of particles along the line of sight.

$$\tau_\lambda = \int_{R_{\rm in}}^{R_{\rm out}} \rho(r)\kappa_\lambda dr$$

where $R_{\rm in}$ is the inner dust shell radius and $R_{\rm out}$ is the outer dust shell radius. While κ_λ is dependent on the density distribution of the grains, maintaining the size, shape and composition (and crystal structure) of the grains means that κ_λ will not change significantly. For simplicity we assume κ_λ remains constant. In our models we assume the density of the dust shell drops off as $1/r^2$ from the central star. In addition, our models specify the relative geometrical thickness of the dust shell as $\xi = R_{\rm out}/R_{\rm in}$. Thus we get:

$$\tau_\lambda = \kappa_\lambda \left[\frac{\xi - 1}{\xi R_{\rm in}}\right] \tag{7.2}$$

The value of $R_{\rm in}$ is set by the values we input for the star's effective temperature and the inner dust radius (or condensation temperature, $T_{\rm inner}$). If we know the temperature and luminosity of the star, we can use a $T(r) \propto r^{-\frac{1}{2}}$ temperature distribution to determine the relationship between $T_{\rm inner}$ and $R_{\rm in}$ and substituting into equation 7.2 we get:

$$\tau_\lambda = \sqrt{\frac{16\pi\sigma}{L_\star}}\ \kappa_\lambda T^2_{\rm inner} \left[\frac{\xi - 1}{\xi}\right] \tag{7.3}$$

Here we assume that the grains are blackbodies because they are largely carbon. Including the albedo would allow for a more accurate calculation, but this would depend on detailed dust parameters (like crystal structure), and the error incurred by our assumption is small (i.e. significantly less than an order of magnitude).

Therefore, according the equation 7.3, for a dust shell with constant relative shell thickness (ξ) the optical depth should increase with the square of the inner dust temperature. Alternatively, if the inner dust temperature is fixed, then increasing the relative shell thickness should decrease optical depth a little (as $(\xi - 1)/\xi$). This latter effect becomes negligible for large geometric sizes.

7.3.4 Determining the Dust Condensation Temperature

7.3.4.1 Theoretical dust condensation models

As seen in the previous section, the value of the dust condensation temperature is a source of degeneracy on radiative transfer modeling. In order to reduce this degeneracy we turn to dust condensation theory to determine a theoretical dust condensation temperature (i.e. $T_{\rm inner}$) that is appropriate for our stars.

As discussed in section 7.1.4, many presolar grains can be attributed to carbon stars and are valuable resources for investigation of dust formation regions. For example, in presolar grains titanium carbide (TiC) is found in the center of carbon (C) grains from AGB stars, but only one SiC grain has been found coated in carbon (Clayton & Nittler, 2004; Bernatowicz et al., 2005). Consequently there have been many studies of the theoretical condensation sequence in Galactic carbon stars in attempts to constrain the physical parameters of the dust condensation regions. These studies showed how the condensation sequence of C, TiC and SiC is dependent on various parameters, most notably C/O ratio and gas pressure[4] (Lodders & Fegley, 1995; Sharp & Wasserburg, 1995).

Sharp & Wasserburg (1995) argued that if carbon forms at a higher condensation temperature, closer to the star than SiC, there is a significant decrease in the amount of carbon available in the gas, and thus SiC and C do not form simultaneously, resulting in naked SiC grains. Therefore, for Galactic sources, the condensation sequence in

---

[4] Gas pressure is a measure of the mass-loss rate ($\dot{M}$) convolved with the photospheric temperature ($T_\star$) and outflow velocity ($v_{\rm exp}$).

the majority of carbon stars should be TiC — C — SiC, in order to produce the coated TiC grains and uncoated (naked) SiC grains seen in the meteoritic presolar grains samples. Observational evidence for naked SiC grains is discussed by Speck et al. (2005). Sharp & Wasserburg (1995) argued that from kinetic and stellar model considerations, dust grains should form in the pressure range $2 \times 10^{-7} < P < 4 \times 10^{-5}$ bars[5].

Lodders & Fegley (1995) also modeled the effect of C/O and pressure on the condensation sequence in carbon stars, as well as the effect of *s*-process and nitrogen abundances. They also briefly discuss the effect of metallicity. The general trends in condensation temperatures are: (1) all condensation temperatures decrease as the gas pressure decreases; and (2) At C/O > 1 the condensation temperature of graphite increases with C/O (for a given pressure and otherwise constant composition).

Figure 7.7 shows how the condensation temperature of carbon and SiC vary with the gas pressure in the dust condensation zone.

For the range plotted carbon always forms first from a cooling gas. Very high pressures are required for SiC to form before carbon. For solar metallicity and C/O = 1.05, SiC forms before carbon for $P \geq 3.4 \times 10^{-5}$ bars. As C/O increases, the minimum pressure required to form SiC first increases. Above C/O ∼1.5 carbon always forms before SiC. The exact C/O ratio at which the carbon forms before SiC depends on pressure. Therefore, in order to account for observations of SiC features in the Galaxy, and the presolar grain record, we can restrict the P–C/O space such that, for low C/O the gas pressure must remain low, but for higher C/O the pressure can be higher. This can be used to constrain the dust forming environment around Galactic carbon stars.

Studies of carbon star spectra in the Galaxy and the Magellanic Clouds have lead to different interpretations with respect to the condensation sequence. Lagadec et al.

---

[5] The expected range of gas pressures in the dust formation zone for O-rich AGB stars in the LMC is 10^{-7} bars $\approx P \approx 10^{-4}$ bars (Dijkstra et al., 2005)

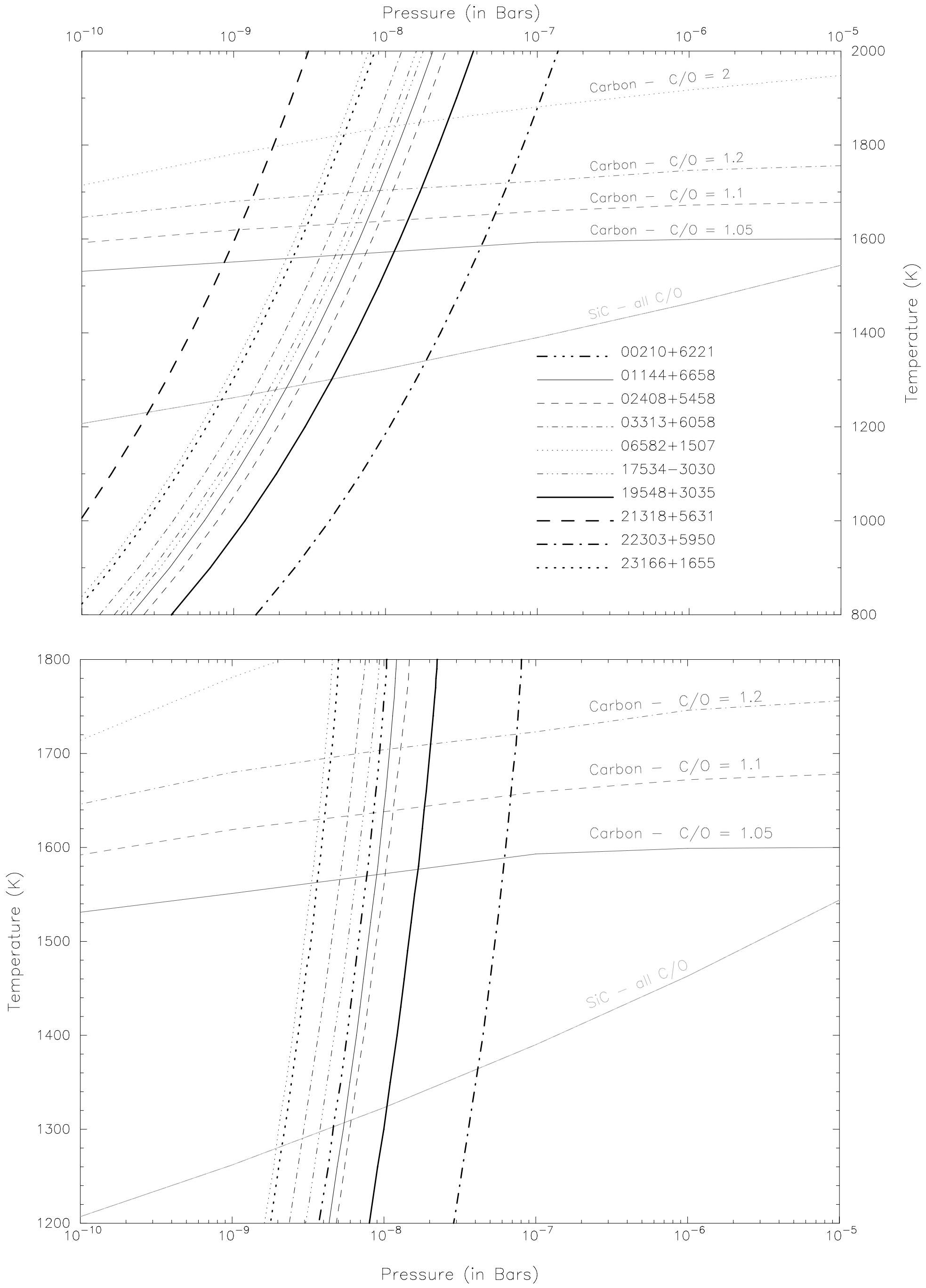

Figure 7.7: Pressure-Temperature space for the dust condensation region around extreme carbon stars (assumes solar metallicity). Grey lines indicate the condensation temperature for a given pressure as calculated by Lodders & Fegley (1995). Black lines indicate the P–T paths for the otuflowing gas from our sample stars; (*top*) as calculated from the published CO mass-loss rates and expansion velocities (see section 7.3.4.2 for details); and (*bottom*) as calculated from the modeled dust temperature radial profile.

(2007) argued for a sequence in which SiC forms before C in the Galaxy, whereas SiC and C form together in the Large Magellanic Cloud (LMC) and the sequence is reversed (C, then SiC) in the Small Magellanic Cloud (SMC). However, they also suggest that the change in the strength of the features is due to the lower number of Si atoms available for SiC formation. The proposed Galactic condensation sequence is at odds with both the models and the meteoritic evidence. Leisenring et al. (2008) support the condensation sequence in which C forms before SiC for the Galactic carbon stars, while finding that the Magellanic Clouds tended to form SiC first, followed by simultaneous condensation of SiC and C. Speck et al. (2006) used the Lodders & Fegley (1995) model to explain an unusual LMC carbon star spectrum, which suggests that the condensation sequence is sensitive to both metallicity and mass-loss rate.

7.3.4.2 P-T space in the condensation zone around extreme carbon stars

In order to constrain the input parameters to our model we need to be able to determine the pressure-temperature space in the dust condensation zone. For a mass-losing star with a mass-loss rate $\dot{M}$ and an expansion velocity of $v_{\rm exp}$, the density ρ of the circumstellar shell at a radius r is given by:

$$\rho = \frac{\dot{M}}{4\pi r^2 v_{\rm exp}}$$

If we know the temperature and luminosity of the star and the composition of the outflowing material we can combine this information with the Ideal Gas Law and a $T(r) \propto 1/\sqrt{r}$ temperature distribution to determine the gas pressure at the condensation radius, where the condensation radius is the distance from the star where the gas has the condensation temperature ($T_{\rm cond}$).

For simplicity, the solid and gas phases are assume to be at the same temperature.

While this is clearly a simplification (e.g. Chigai & Yamamoto, 2003), the temperature difference is small compared to the difference needed to significantly affect dust formation. We assume that most of the outflowing material is atomic hydrogen. In fact it will probably be a mixture of atomic and molecular hydrogen (H_2) since H_2 forms around 2000 K and the temperature in the outflow is decreasing from the stellar surface temperature of $\sim$3000 K to the dust condensation temperature in the 1000–1800 K range. An entirely molecular hydrogen gas would halve the gas pressure compared to the the atomic gas. However, we also assume published CO outflow velocities, which reflect the speed of the outflowing material after radiation pressure acceleration. Adopting the pre-dust-formation outflow speed ($\approx$ 5km/s), would increase the pressure. Thus using published values for our sample stars' luminosities, mass-loss rates and expansion velocities, we can estimate where their dust condensation zones fall in P–T space.

7.3.4.3 Comparison of P–T space for dust condensation models and sample stars

Figure 7.7 shows how the P–T space for the dust condensation zone for our target stars compares to condensation models in P–T space. It is clear the pressure is never high enough for SiC to form before carbon. Since our sample stars are expected to be the carbon stars with the highest mass-loss rates, it implies that this NEVER happens in Galactic carbon stars. This agrees with the meteoritic evidence which suggests that SiC does not get coated in carbon and supported the idea that variations in the strength of the SiC feature are related to self-absorption.

The dust condensation temperature is dependent on the pressure in the gas from which the dust forms. In addition, the P–T space occupied by the target sources suggests that carbon grains will form at temperatures $\approx$ 1600 K. If the C/O is very high, then graphite could form as high as $\sim$1800 K. However, Galactic carbon stars for which the C/O ratios have been measured show that it is in the range 1 to 1.8, with a mean C/O ratio of ∼1.15 (Lambert et al., 1986; Olofsson et al., 1993a,b). The precise C/O for our sample is not known, but even low C/O stars yield $T_{\rm cond} \approx 1550\,{\rm K}$ (see figure 7.7). Previous models of carbon stars have assumed much lower inner dust temperatures. The pressures and temperatures in the gas around these stars meet the criteria for forming carbon dust at $T_{\rm cond} \approx 1600\,{\rm K}$, (precise temperature depends on the C/O ratio). Therefore it should form at these high temperatures.

Once dust starts to form, the radial temperature profile will change due to absorption of starlight by dust grains. Therefore, we use the comparison above only to determine the inner dust radius. Using radial temperature profiles from our models we show that the temperature drops significantly more rapidly than $1/\sqrt{r}$ (see figure 7.7), which suggests that the next condensate (SiC) forms fairly close to the inner dust radius and thus mitigates the problem with DUSTY that the grains are assumed to be co-spatial. Indeed the models show that the temperature in the dust shell drops to the SiC formation temperature at $\sim 1.3{\rm R}_{\rm in}$ for all cases, which is small compared to the shell thickness, even for the thinnest shells.

7.3.5 Constraining Dust Composition

Since our stars are carbon-rich, we limit the models to only including carbonaceous species such as graphite, amorphous carbon and silicon carbide. The choice of carbon grains is equivocal. We do not know whether the grains composed mostly of carbon are glassy, poly-nanocrystalline or well-ordered. The meteoritic presolar "graphite" grains suggest that circumstellar dust can contain either well-ordered graphite or poly-nanocrystalline-graphene grains. It should be noted, however, that even the disordered graphene sheets are considered to be more graphitic than amorphous.

Amorphous carbon essentially consists of a mixture of sp^2 (graphite-like) and sp^3 (diamond-like) carbon bonds. On heating, sp^3 bonds tend to convert to sp^2 bonds, thus graphitizing the amorphous carbon, but it will remain dense like the amorphous phase (2.8 g/cm^3 Comelli et al., 1988; Saada, 2000; Kelires, 1993). At ∼1300 K the fraction of graphitic bonds is ∼90%. Comparison of the gas pressure in the circumstellar outflows to graphite formation temperature in section 7.3.4.3 shows that graphite should be able to form at temperatures significantly above 1300 K. Even if solid state carbon forms as a chaotic solid, at these temperatures it will quickly anneal to a graphitic form. Consequently, we argue that graphite is the better choice of carbonaceous material for modeling extreme carbon star dust shells.

The limitations of the use of the Pègouriè (1988) data are discussed in chapter 8; this research was conducted before the new optical constants presented in that chapter were available. Clearly, this data cannot produce the broad absorption feature seen in the observations. However, we can use the relative changes in composition from star to star as a guide to understanding why these stars have the features we see.

7.4 Radiative Transfer Modeling Results

The results of the radiative transfer modeling can be seen in figures 7.8, 7.9 and 7.10. The parameters used in each case can be seen in table 7.4. For each source, we have produced models using both MRN (generic) and “meteoritic” (extreme) grain size distributions.

Table 7.4: Model and derived parameters

IRAS Number	$T_\star$	$T_{\rm inner}$	$R_{\rm out}/R_{\rm in}$	$\tau_{10\mu{\rm m}}$	Composition SiC%	Graphite %
MRN grain size distribution						
00210+6221	3000	1800	10	6	10	90
01144+6658	3000	1800	15	6.5	10	90
02408+5458	3000	1800	20	12	3	97
03313+6058	3000	1800	15	4	10	90
06582+1507	3000	1800	10	6	5	95
17534-3030	3000	1800				
19548+3035	3000	1800	15	6.5	5	95
21318+5631	3000	1800	10	8	3	97
22303+5950	3000	1800	15	4	10	90
23166+1655	3000	1800	15	7.5	3	97
Meteoritic grain size distribution						
00210+6221	3000	1800	10	6	30	70
01144+6658	3000	1800	10	7.5	30	70
02408+5458	3000	1800	100	8.5	12	88
03313+6058	3000	1800	500	3.25	40	60
06582+1507	3000	1800	10	6	20	80
17534-3030	3000	1800	20	5	35	65
19548+3035	3000	1800	100*	4.75	25	75
21318+5631	3000	1800	100	5	20	80
22303+5950	3000	1800	500	3.25	40	60
23166+1655	3000	1800	50	5	25	75

$*$ Models with $R_{\rm out}/R_{\rm in} > 100$ can be accommodated because the data beyond 26μm is poor and ignored, but based on the similarity of this source to IRAS 21318+5631, we assume this is a good upper limit.

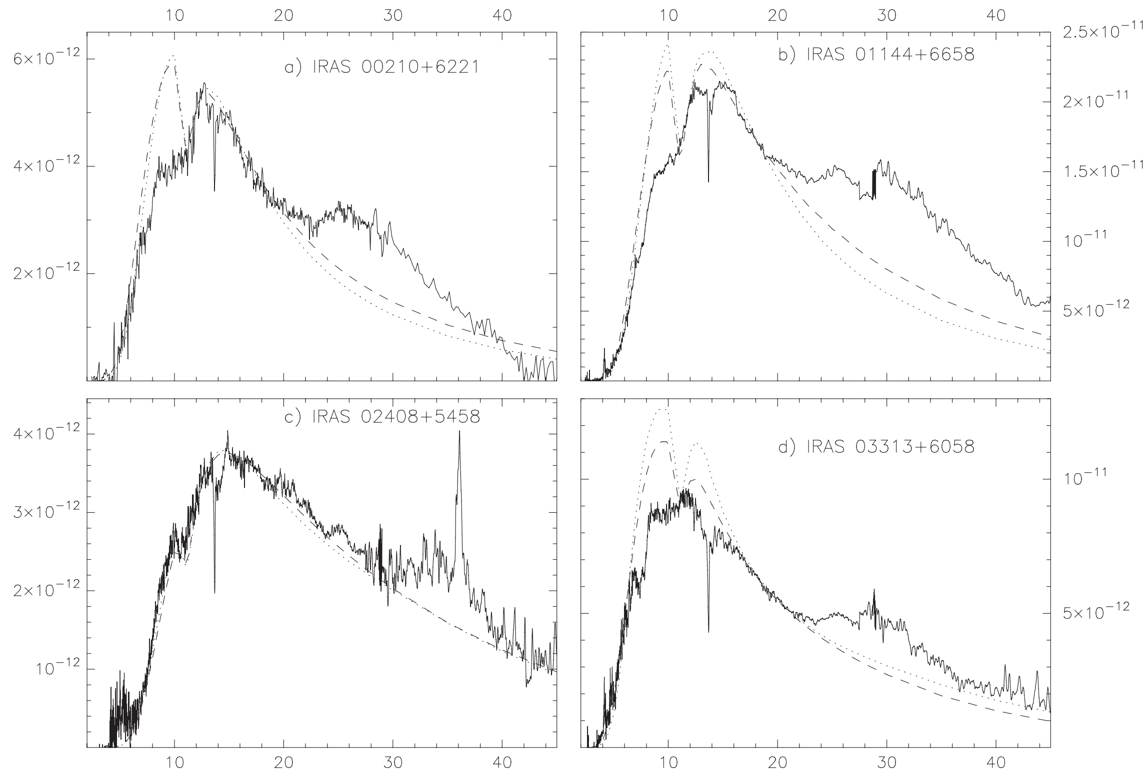

Figure 7.8: Extreme C-star best fit models (Part 1). solid line = ISO-SWS spectrum; dashed line = best fit model using MRN grain-size distribution; dotted line = best fit model using "meteoritic" grain-size distribution; X-axis is wavelength (μm); y-axis is flux (λF_λ) in W m^{-2}. In all cases, $T_\star$=3000 K and $T_{\rm inner}$=1800 K. Model parameters are listed in table 7.4

7.4.1 The effect of grain-size distribution

Table 7.4 shows the model input parameters for both grainsize distributions. In all cases switching from MRN to "meteoritic" grainsizes leads to the need for increased SiC component (compared to graphite), typically requiring a three- or fourfold increase in the SiC fraction.

There are other general trends including the need for decreased optical depths ($\tau_{10\mu{\rm m}}$) and increased geometric shell thickness. However, these trends do not hold for all objects. In the cases of IRAS 00210+6221 and IRAS 06582+1507, the only difference in parameters between the different grain size models is the fraction of SiC.

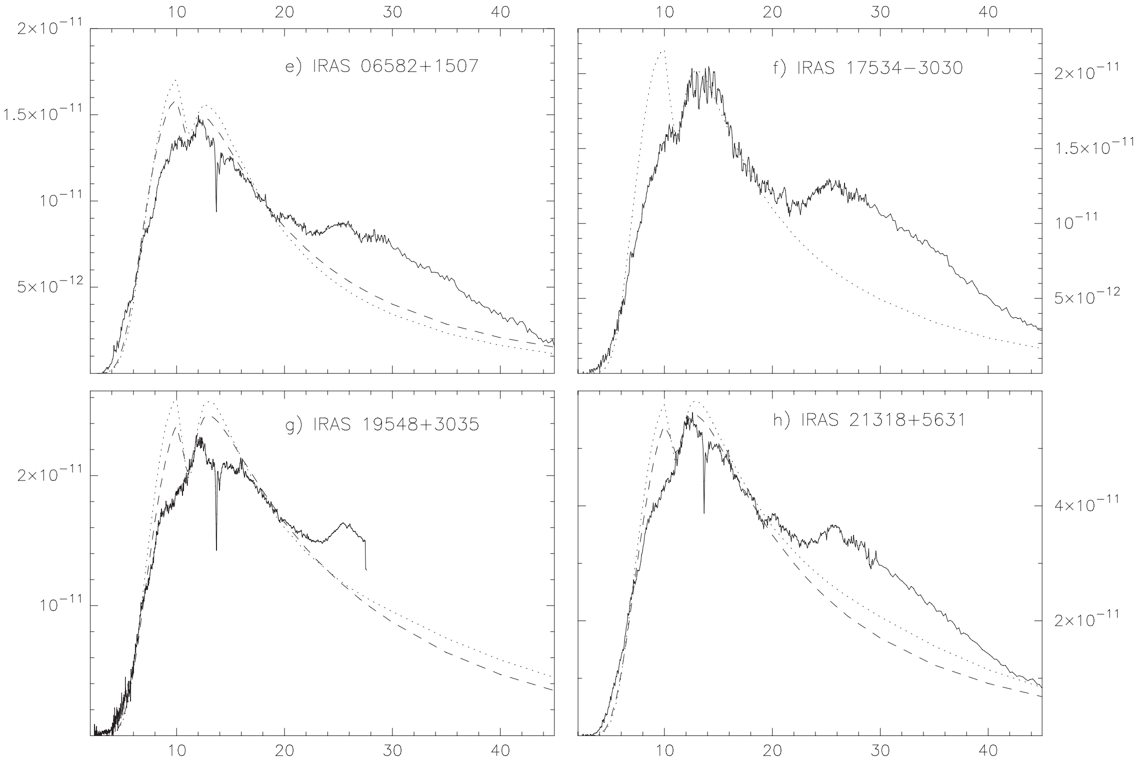

Figure 7.9: Extreme C-star best fit models (Part 2). solid line = ISO-SWS spectrum; dashed line = best fit model x-axis is wavelength (μm); y-axis is flux (λF_λ) in W m^{-2}. In all cases, $T_\star$=3000 K and $T_{\rm inner}$=1800 K. Model parameters are listed in table 7.4

IRAS 01144+6658 is the only source for which optical depth was increased and shell thickness was decreased in the "meteoritic" model.

7.4.2 Dust Shell Thicknesses

As discussed in section 7.3.3.1, there is a degeneracy between relative shell thickness, inner dust temperature and optical depth. The inner dust temperature variability has been limited to 1550–1800 K by theoretical considerations (see section 7.3.4.1). It is possible to tweak parameters such as shell thickness, inner dust temperature and optical depth and get almost identical models. figure 7.11 shows two almost identical model spectra for IRAS 23166+1655 with different inner dust temperatures, optical

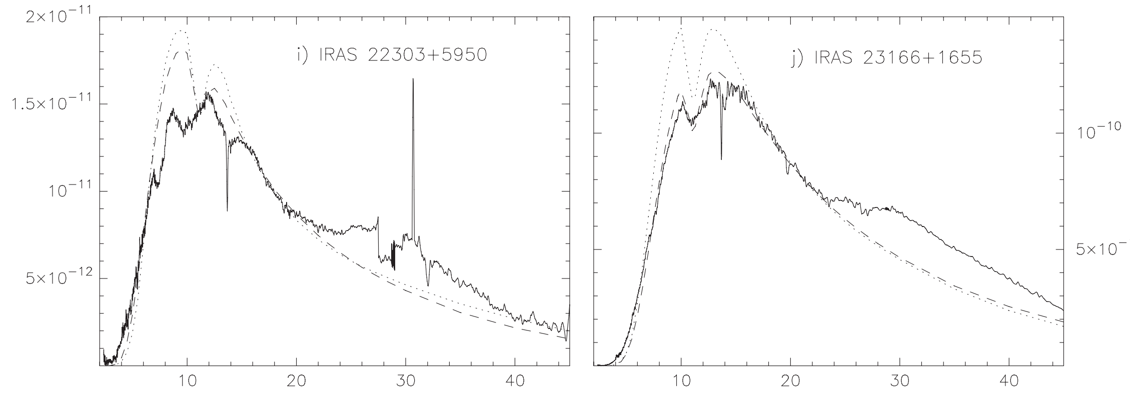

Figure 7.10: Extreme C-star best fit models (Part 3). solid line = ISO-SWS spectrum; dashed line = best fit model x-axis is wavelength (μm); y-axis is flux (λF_λ) in $\mathrm{W\,m^{-2}}$. In all cases, $T_\star$=3000 K and $T_{\rm inner}$=1800 K. other parameters are indicated in the legend. Parameters of these models are also listed in table 7.4

depths and shell thicknesses. However, reducing the inner dust temperature merely requires reduction of the optical depth.

While increasingly geometrically large dust shells can be accommodated by decreasing optical depth (see equation 7.3), at some point, this also breaks down, as it leads to a significant population of colder grains which emit too much at long wavelengths. In this way we can use the models to place to an *upper limit to the shell thickness*. Table 7.5 lists the published expansion velocities for our extreme carbon stars.

From the model parameters, the physical value for $R_{\rm out}$ can be calculated, which gives the physical size of the dust shell. Since the models give an upper limit to the shell thickness, this upper limit to $R_{\rm out}$ together with the expansion velocity ($v_{\rm exp}$) was used to calculate the time since the outermost edge of the shell was ejected from the star. The resulting ages of the dust shells are listed in table 7.6.

As can be seen in figure 7.6, it is possible to accommodate thick shells, if we assume a much lower $T_{\rm inner}$ (1000 K), and assume that the dust grain are composed of amorphous rather than graphitic carbon, but these parameter values are precluded

Table 7.5: Compilation of CO mass-loss rates and expansion velocities, together with distances and luminosities of sample stars.

Source Name	$v_{\rm exp}$ km/s	D kpc	$\dot{M}_{\rm gas}$ $M_\odot\,{\rm yr}^{-1}$	$\dot{M}_{\rm dust}$ $M_\odot\,{\rm yr}^{-1}$	$L_\star$ $L_\odot$
00210+6221*	16.7	3.97	3.02×10^{-5}	—	1×10^{4}
01144+6658	18	2.78	6.38×10^{-5}	1.51×10^{-7}	1.69×10^{4}
02408+5458*	11	5.3	1.60×10^{-5}	$3.5\ \times10^{-7}$	5.70×10^{3}
03313+6058	13.9	5.24	2.37×10^{-5}	1.14×10^{-7}	1.31×10^{4}
06582+1507	13.7	4.7	1.43×10^{-5}	1.07×10^{-7}	1.32×10^{4}
17534−3030	19	2	3.76×10^{-5}	1.06×10^{-7}	1.21×10^{4}
19548+3035	22.3	3.38	1.14×10^{-4}	2.15×10^{-7}	1.32×10^{4}
21318+5631	19.6	1.77	7.69×10^{-6}	1.18×10^{-7}	1.24×10^{4}
22303+5950	18.3	3.86	3.19×10^{-4}	1.09×10^{-7}	1.25×10^{4}
23166+1655	15.1	1	1.44×10^{-5}	8.27×10^{-8}	1.10×10^{4}

All data are from Groenewegen et al. (2002) except those marked with $*$. IRAS 02408+5458 data come from Groenewegen et al. (1999). IRAS 00210+6221 data are compiled from Volk et al. (2000) ($\dot{M}$, which also convolves the distance from Groenewegen et al., 2002); and Volk et al. (1992) ($v_{\rm exp}$).

Table 7.6: Size and age of the extreme C-star dust shells

	MRN size distribution			Meteoritic size distribution		
IRAS Number	$R_{\rm in}$ (10^{14}cm)	$R_{\rm out}$ (10^{14}cm)	Age (yrs)	$R_{\rm in}$ (10^{14}cm)	$R_{\rm out}$ (10^{14}cm)	Age (yrs)
00210	2.68	26.8	50.9	2.78	2.78	52.8
01144	2.74	41.1	72.4	3.08	30.8	54.2
02408	4.11	82.2	236.8	2.99	299	861.3
03313	2.17	32.6	74.2	2.10	1050	2393.7
06582	2.73	27.3	63.1	2.72	27.2	62.9
17534	2.51	50.2	83.7	2.51	50.2	83.7
19548	2.78	41.7	59.3	2.38	238	338.2
21318	3.18	31.8	51.4	2.41	241	389.6
22303	2.24	33.6	58.2	2.10	1050	1818.2
23166	2.88	43.2	90.7	2.45	123	257.1

Calculation of $R_{\rm out}$ is based on the model parameters listed in table 7.4. $R_{\rm in}$ comes from the model output. The calculation of the age of the dust shells is then done using these data and the observed expansion velocities listed in table 7.5

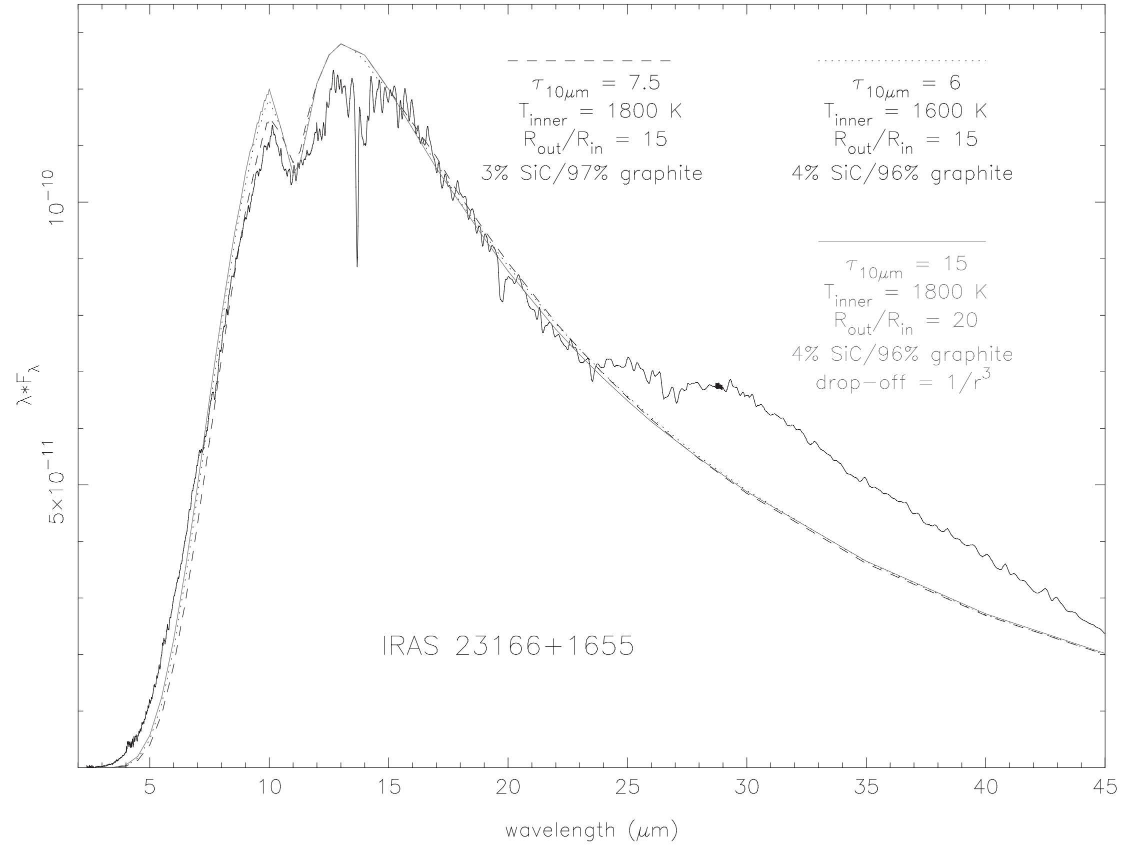

Figure 7.11: Degeneracy in the best fit models for IRAS 23166+1655. solid line = ISO-SWS spectrum; dashed line = best fit model with $T_{\rm inner}$=1800 K dotted line = best fit model with $T_{\rm inner}$=1600 K X-axis is wavelength (μm); y-axis is flux (λF_λ) in W m^{-2}. In both cases, $T_\star$=3000 K other parameters are indicated in the legend.

by the theoretical constraints on $T_{\rm inner}$ and composition/crystal structure discussed above. Clearly, since our constraints are theoretical, they may change as hypotheses are refined.

The timescales for increased mass-loss are model dependent. As can be seen in table 7.4 using a “meteoritic” grain size distribution generally requires a geometrically thicker shell, as well as lower values for $\tau_{10\mu m}$ and higher percentages of SiC. However, timescales associated with our dust shells are always very short (less than a few thousand years) regardless of grain-size distribution. Moreover, our timescales are consistent with those derived for the "superwind" seen in post-AGB objects (e.g. Skinner et al., 1997; Meixner et al., 2004). These timescales are too short to be associated with the theoretical superwind (e.g. Vassiliadis & Wood, 1993), which is expected to last up to ∼10% of the duration of the thermally-pulsing AGB phase. However, if we compare the number of extreme carbon stars to the total number of carbon stars in the Galaxy, we find that extreme carbon stars constitute only ∼0.1% of the total C-star population. The thermally pulsing AGB phase is expected to last $\sim 10^6$ years, and the time a star spends as a C-stars is even shorter (e.g. Lagadec et al., 2007). Consequently, we might expect the dust-obscured phase to only last $\sim 10^3$ years. This is consistent with the model timescales, although the MRN-models still appear to have very short timescales. Lagadec & Zijlstra (2008) suggested that the trigger for the superwind is a combination of luminosity and carbon abundance. Although the duration of the C-star phase maybe be $\sim 3 \times 10^5$ years, for much of this time, a C-star will be below the critical carbon abundance required to drive the superwind and obscure the star.

How does the extreme carbon star phase fit into the broader C-star evolution? Many, if not most, carbon-rich post-AGB stars showed marked axisymmetric morphologies (Meixner et al., 1999; Waelkens & Waters, 1999; Sahai, 2004; Soker & Subag, 2005). The extreme carbon stars are expected to be the direct precursors of these objects (e.g. Skinner et al., 1998), but presently show little evidence for axisymmetry[6]. The cause and timing of this axisymmetric structure is not known, but is believed to occur at the very end of the AGB phase. Dijkstra & Speck (2006) showed that significant axisymmetry is not expected to develop until the last few tens or hundreds of years of the superwind phase. The onset of axisymmetry also leads to an optically thicker toroid of dust, as the circumstellar shell becomes equatorially enhanced. We

---

[6] one would expect to see more near-IR emission in the spectrum of strongly axisymmetric objects due to scattering of starlight escaping in the bipolar axis direction.

suggest that the very short timescales associated with our model results may indicate that the extreme AGB stars are in the process of developing axisymmetry, but that this has not developed to the point of allowing large amounts of NIR scattered light into the spectrum.

7.4.3 Dust Shell Density Distribution

In section 7.3 we argued the case for maintaining a dust density distribution that follows a $1/r^2$ law. However, it has been argued that the increasing stellar luminosity and the onset of the superwind phase should give rise to a steeper density drop-off.

Following the same arguments as shown in section 7.3.3.1, giving rise to equation 7.3 we can derive an equation in which the exponent of the density power law is a variable. This gives us the relationship between the optical depth (τ_λ), inner dust temperature (T_{inner}), relative shell thicks (ξ) and the exponent of the density power law (x):

$$\tau_\lambda = \kappa_\lambda \left[\frac{\xi^{x-1} - 1}{(x-1)\xi^{x-1}} \right] \left(\sqrt{\frac{16\pi\sigma}{L_\star}} T_{\mathrm{inner}}^2 \right)^{x-1} \tag{7.4}$$

where κ_λ is the wavelength dependent opacity of the assemblage of particles along the line of sight; $L_\star$ is the luminosity of the star; and σ is the Stefan-Boltzmann constant.

As an example of the effect this, we assume the exponent, $x = 3$ (which is the highest value in the previous models). In this case, the relative shell thickness dependence dwindles, and the optical depth is essential strongly dependent on the inner dust temperature only. Since the previous models have severely underestimated the inner dust temperature, they have also underestimated the optical depth (which may explain Groenewegen, 1995).

The lack of dependence on shell thickness at $x > 2$ leads to a situation where most of the dust is essentially confined to a region close to the star and the outer dust becomes negligible, and so this confinement to the inner region is effectively the same as our assumption that there was a sudden increase in mass loss in the recent past. However, we attempted to model our sources with a $1/r^3$ radial density distribution and found that we cannot match the shape of the SED without restricting the geometrical shell thickness. Using the $1/r^3$ radial density distribution with the MRN grain-size distribution and $R_{\rm out}/R_{\rm in} \approx 20$ produces a SED that has too much emission longwards of $\sim 20\mu$m. Therefore, even if the radial density distribution is indicative of a steep increase in mass-loss rate the shells still need to be geometrically thin, and the shell thickness and percentage of SiC needed are essentially the same as for the $1/r^2$ models (see figure 7.11 for an example.) If the "meteoritic" grain-size distribution is used in conjunction with a $1/r^3$ drop-off, the observed SED cannot be matched. The model SED becomes too narrow, and increasing the outer dust-shell radius does not help.

7.4.4 IRAS 17534−3030

IRAS 17534−3030 is exceptional amongst the present sample of extreme carbon stars, and certainly requires more discussion. As can be seen in the flux-calibrated and continuum-divided spectra in figure 7.2, IRAS 17534−3030 does not exhibit the usual molecular absorption bands around 13.7μm (due the C_2H_2) and shortwards of $\sim 8\mu$m (due to both C_2H_2 and HCN), which are present in the other sample sources. Its 11–13μm feature is intermediate between the narrow feature exemplified by IRAS 23166+1655 and the broad feature exemplified by IRAS 19548+3035, indicating that at least some of whatever substance causes the broadening is present around IRAS 17534−3030. One of the suggested carriers for the short wavelength broadening of the 10-13μm absorption feature is C_3 (Zijlstra et al., 2006). However, C_3 is expected to be photospheric, rather than circumstellar, which probably precludes its detection in optically obscured stars. Moreover, the theoretical spectrum of C_3 from Jørgensen et al. (2000) shows a strong absorption close to the $\sim 5\mu$m CO line, which is stronger than the $\sim 11\mu$m feature. The spectrum of IRAS 17534−3030 does not show this 5μm absorption band. This, together with the lack of other molecular absorption feature provides evidence that the broadening of the 10-13μm feature is not molecular in origin.

In addition to the lack of molecular absorption in its spectrum, IRAS 17534−3030 is unique is another way: it cannot be modeled with the MRN grain-size distribution. Modeling of this source requires the "meteoritic" grain-size distribution because of its narrow SED. Whereas our other sources can be fitted with either MRN or "meteoritic" grains, IRAS 17534−3030 cannot.

7.4.5 Impact of the dust condensation temperature

The increase in the inner dust temperature from ≈ 1000 K in previous models up to ≈ 1600 K decreases the inner dust radius significantly. Consequently the flux of energy from the star hitting the inner dust radius is increased, leading to a greater acceleration and consequently a more effectively dust-driven wind. If graphite is formed by annealing of amorphous carbon, the grain density should remain high (with ρ=2.8g/cm^3) and the increased acceleration is entirely due to increases flux of stellar photons. However, if graphite forms directly, rather than by annealing of amorphous carbon, the radiation pressure effect is further enhanced, because graphite grains generally have a lower density than amorphous carbon. Assuming 0.1μm-sized grains, the acceleration felt by graphite grains (with ρ=2.2g/cm^3; c.f. meteoritic presolar grains; see section 7.1.4.1) at $T_{\rm inner} = 1800$ K is 13 times greater than the acceleration felt by amorphous carbon grains (with ρ=2.8g/cm^3) at $T_{\rm inner} = 1000$ K.

7.4.6 Correlations between observed and model parameters

In the course of this investigation we have compiled a large number of parameters for these stars. For instance, table 7.3 lists the peak position, peak strength, FWHM and equivalent width of the $\sim 11\mu$m absorption feature. Table 7.5 lists the published mass-loss rates, luminosities and expansion velocities for our sample stars.

In order to understand the physical conditions that give rise to the observed 11μm absorption feature, we have sought correlations between various parameters associated with the sample stars (as found in tables 7.3, 7.5, 7.4). We have looked for correlations between each of the following:

- Mass-loss rate (from CO observations);
- Expansion velocity (from CO observations);
- Stellar luminosity;
- Strength of the observed absorption;
- FWHM of the absorption;
- Barycentric position of the absorption;
- Equivalent width of the absorption;
- Model parameters.

Loup et al. (1993) showed that, for low mass loss rates there is a simple relationship between the [25]-[12] color and mass-loss rates. This breaks down at mass-loss rates $\approx 10^{-5}\,\mathrm{M}_{\odot}\mathrm{yr}^{-1}$. It has been suggested that such high mass-loss rate stars at CO-emission deficient due to either saturation effects, low kinetic temperatures or possibly dramatic recent increases in mass-loss. If we extrapolate the trends from low mass-loss rates to determine mass-loss rates from the [25]-[12] color we find that these objects should have a mass-loss rate in excess of $10^{-4}\,\mathrm{M}_{\odot}\mathrm{yr}^{-1}$, consistent with the high modeled optical depths. Because of this relationship, we sought correlations between the various observed and modeled parameters and the [25]-[12] and [60]-[25] colors. This search yielded only one correlation: between the [60]-[25] colors and the dust mass-loss rate from previous models. It is possible that a better correlation may be found using the *Manchester Method* i.e. the [6]-[9] color (e.g. Sloan et al., 2006; Zijlstra et al., 2006), however, we suspect that the lack of correlation arises because of the intrinsic degeneracy in the modeling.

In section 7.1.2 and section 7.2 we discussed the possibility that the broadening of the 10–13μm feature might be due to silicate dust. With this in mind, we re-measured the position and strength of the 11μm feature assuming that the short wavelength wing is due to silicate. This involved measuring the feature-to-continuum strength at 9.7 and 11.3μm. These data are presented in table 7.3 and were also included in the investigation of correlations between parameters.

One pair of parameters that yielded a correlation were the best-fit blackbody temperature and the model optical depth, which is demonstrated in figure 7.12. This correlation occurs whether we assume MRN or “meteoritic” grainsizes.

Since there is a relationship between the optical depth and shell thickness, this correlation seems to support models validity.

In addition to this relationship between the modeled optical depth and the best-fit blackbody temperature, we found two other parameters that the optical depth correlates with: modeled percentage of SiC in the dust shell; and the calculated timescale of the obscuring dust. In both cases, these correlations only hold for the generic (MRN) grain-sze distribution models. (shown in figure 7.13).

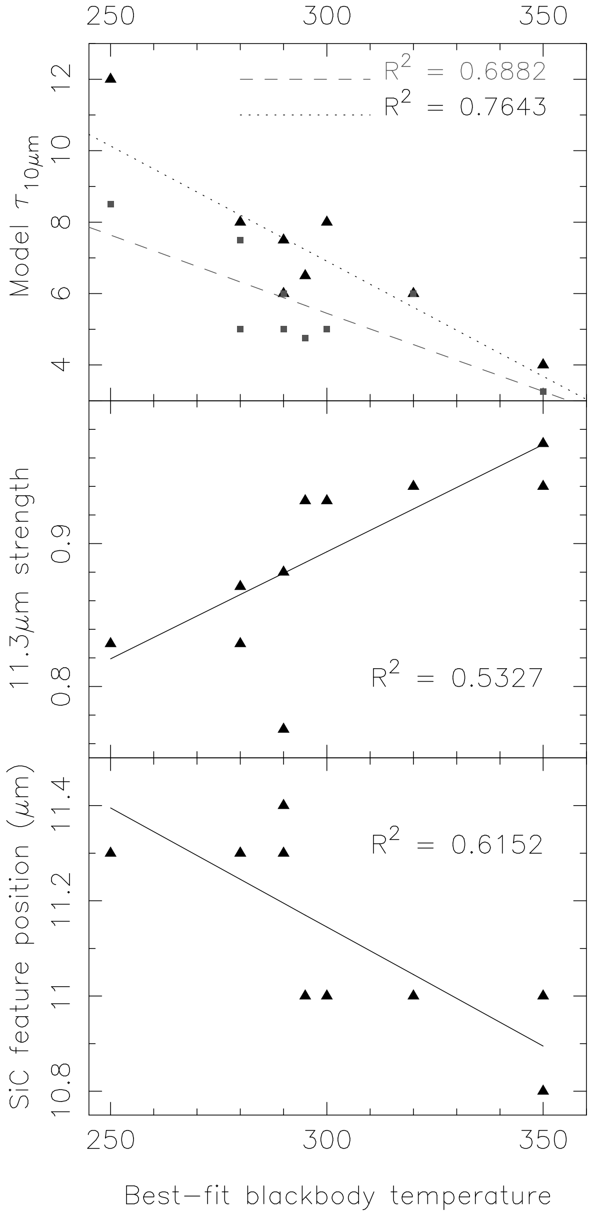

Figure 7.12: Correlations between the best-fit blackbody temperature and (*top*) modeled optical depth; (*middle*) 11.3μm feature-to-continuum ratio; and (*bottom*) SiC feature position. Solid lines represent the linear regression fit through the points. In the top figure, the dotted line represents the linear regression for model fits with MRN grainsize distributions. Grey points are for meteoritic grainsize models, and grey dashed line is the linear regression fit through the points.

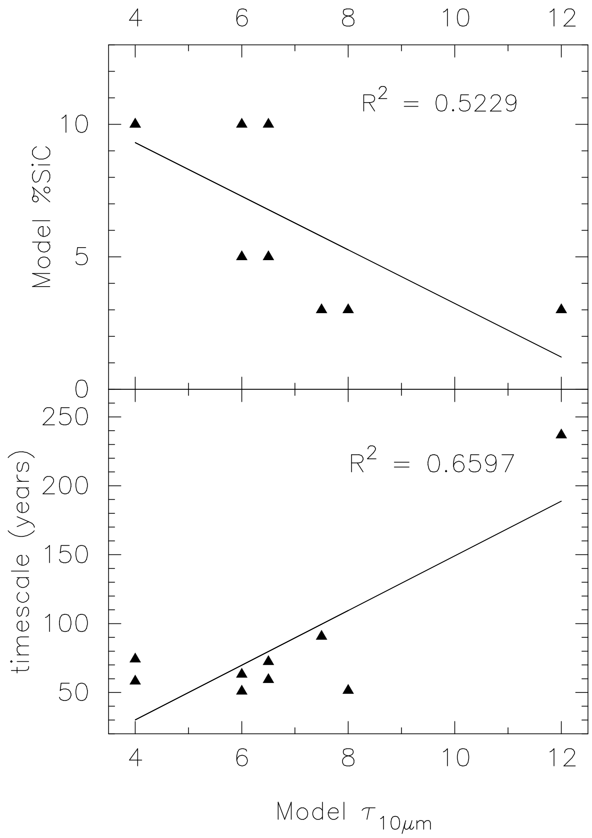

Figure 7.13: Correlations between the modeled optical depth and (*top*) the modeled %age SiC (*bottom*) the calculated superwind timescale from table 7.6 Solid lines represent the linear regression fit through the points.

The correlation between optical depth and percentage SiC is such that lower optical depths require more SiC. This in turn suggests that as mass-loss rates increase, the SiC component dwindles. This can be interpreted in two ways: (1) at these high mass-loss rates SiC gets coated by carbon; and (2) increased mass-loss rates are associated with higher C/O ratios; carbon is enriched but not silicon, and thus more carbon grains can be made, but not more SiC grains. The first option seems unlikely in light of meteoritic evidence (section 7.1.4) and theoretical condensation models (section 7.3.4.1). However, it is possible that there is a metallicity effect in play. The presolar grains were formed prior to the formation of the solar system, and thus their source stars may have had lower metallicities. Speck et al. (2006); Leisenring et al. (2008) argued that coating of SiC grains is more likely in lower metallicity environments, and thus it is difficult to see how the higher metallicity objects we are now witnessing could have carbon-coated SiC grains. However, Leisenring et al. (2008) argued that SiC grains form the nucleation seed for MgS, which may explain this correlation. The second option may be logical if outflows are dust driven. If more carbon grains can form, the radiation pressure driving the outflow is more effective.

The second optical depth correlation is with the calculated timescale (also shown in figure 7.13 and again, only for the MRN grain-size distribution). In this case, the timescale for the dust shell increases with optical depth. The oldest shells have the highest optical depth. This may simply be due to the path length dependence of optical depth (see equation 7.1), since τ depends on the geometric size of the dust shell the oldest shells should have the largest optical depth. However, this should also lead to a correlation between model dust shell thickness and optical depth. No such correlation exists. Another interpretation is that older stars have higher mass-loss rates, and thus denser dust shells and higher optical depths. However, this assumes the stars all had the same initial mass. This apparent correlation is not strong, and does not holds for “meteoritic” grains. Consequently, we will not attempt to place too much importance on it.

There is no correlation between the strength of the 9.7μm absorption and that at 11.3μm, implying that the carriers of these features may not be related. Furthermore, there is no correlation between the 9.7μm strength and distance to the object, which leads us to suggest that the cause is not interstellar. Obviously there is a strong correlation between the strength of the 9.7μm absorption and the barycentric position of the feature, indicating that this is the cause of the broadening.

The most interesting correlations are between the “isolated” 11.3μm feature (i.e. the residual feature after taking silicate absorption into account) and the fitted blackbody temperature. There is a correlation both between the SiC barycentric position and the blackbody temperature and between the 11.3μm feature-to-continuum ratio (i.e. SiC feature strength) and the blackbody temperature (both shown in figure 7.12).

The position of the SiC absorption feature moves to shorter wavelengths for higher blackbody temperatures while also becoming weaker. This can be understood as being the result of more absorption occurring when the surface we see is at a lower temperature, which is associated with longer wavelength absorption.

We can interpret this result in terms of the self-absorption scheme described by Speck et al. (2005). The shifts in wavelength were attributed to a changes in grain size. However, the weaker absorption and warmer blackbody temperatures associated with the shortest wavelength peaks is the opposite trend to that described by Speck et al. (2005). Following their scheme, this would imply that the weakest absorption is associated with the largest SiC grain. The problem with interpreting this observation is that we do not know the C/O ratios for these stars. While C/O does not affect the SiC condensation temperature, it will affect the graphite condensation temperature. As seen in Fig 7.11, we can reduce the inner dust temperature and compensate by decreasing both the optical depth and the shell thickness. This would also change the depth into the shell at which the SiC forms. It is also possible that the shift in position is due to incomplete subtraction of the silicate contribution. Further studies are ongoing, but are beyond the scope of the present work.

The assumption that there is a silicate contribution to the spectrum raises several questions. Identifying the source of the 9.7μm contribution to the absorption feature remains beyond the scope of the present work, but, needless to say, if it is silicate, the specter of dual chemistry would require seriously rethinking our current models of dust formation around carbon stars. Lodders & Fegley (1999) suggested that silicates could form around carbon stars, and indeed silicate carbon stars exist. It is possible that the feature may be attributable to some form of hydrogenated amorphous carbon, which has been postulated as the source of an $\sim 9\mu$m emission feature in optical thin carbon star spectra; see chapter 5.

No additional correlations were found. The lack of correlation between most of the observable or modeled parameters echoes the results of chapter 5, where we found that there are no trends in the parameters associated with 11μm emission feature in visibly observable carbon stars. This suggests that even amongst the extreme carbon stars, variations in C/O, *s*-process and nitrogen enhancements make discernment of the physical properties associated with the 11μm feature very difficult.

7.5 Conclusions

We have presented three previously unrecognized SiC absorption features in the spectra of extreme carbon stars. Together with the seven known SiC absorption stars, this brings the total of known extreme carbon stars with SiC absorption features to ten.

Previous radiative transfer models of extreme carbon stars utilized relatively low condensation temperatures. Here, theoretical condensation models have been used to justify much higher condensation temperatures. In addition, our models use graphite instead of amorphous carbon, because of the preferential formation of graphite at higher temperature and the meteoritic evidence. Both the higher condensation temperature (through a decrease in the inner radius of the dust shell) and to a smaller extent the use of graphite will greatly increase the acceleration felt by the dust grains in the shell relative to parameters used in previous research.

We have shown that grain-size issues cannot be ignored in the production of models that accurately fit the observed spectra of extreme carbon stars. The size distribution that is needed is not clearly defined because of the inherent degeneracy in radiative transfer modeling. Meteoritic grain-size distributions are as valid as other size distributions with the advantage of being model independent. However, they may underestimate the contribution from small grains.

With the exception of IRAS 17534−3030, all sample stars could be modeled with either the generic (MRN) or "meteoritic grain-size distribution IRAS 17534−3030's narrow SED required the use of the "meteoric" distribution. Furthermore, there is no evidence for any molecular absorption in its spectrum. Because the 11μm feature is still present in the absence of the other molecular features, it supports the attribution of this feature to a solid state carrier.

The various parameters compiled in the course of this research (both through radiative transfer modeling and from observations) have been compared in order to identify any correlations, with the result that the cause of differences is the spectra cannot be attributed to mass-loss rate or gas pressure in the dust condensation zone. In fact the paucity of correlations between parameters echoes the results of chapter 5 and suggests that even amongst the extreme carbon stars, variations in C/O, *s*-process and nitrogen enhancements make 11μm a poor probe of the details of dust shell parameters.

The timescales associated with the heavy mass-loss experienced by these extreme carbon stars are very short (tens to hundred of years) and are not consistent with timescales for the superwind. This indicates that the heavy mass-loss phase of carbon stars is not a direct result of thermal pulse (although thermal pulses may be the root cause).

Chapter 8

New Silicon Carbide Optical Constants

"It is one thing to show a man that he is in error, and another to put him in possession of the truth." - John Locke

8.1 Introduction

As was mentioned in chapter 4, previous measurements of the optical properties of SiC all have various limitations (discussed below in section 8.1.1). In order to improve this situation, new SiC optical constants were measured that eliminate the limitations in previous data sets.

This research was previously published in Pitman et al. (2008), for which this author was a co-author.

8.1.1 Limitations of previously obtained optical properties of SiC

The limitations of the previous data can be summarized as follows:

1. Most of the obtained optical constants (the complex refractive indices) were calculated through measurements of α-SiC (which is easily available commercially) rather than the β-SiC believed to be more common in astronomical environments.

2. The previously obtained data was mostly acquired by absorbance studies of powdered SiC rather than bulk samples. SiC powder tends to clump and produce grain clusters, which can strongly influence the optical properties of the sample (Huffman, 1988). Additionally, the matrix in which the powder is dispersed also modifies the optical properties (Mutschke et al., 1999).

3. SiC samples produced through laser pyrolysis are believed to produce particles that resemble those in stellar environments (Willacy & Cherchneff, 1998; Mutschke et al., 1999); however, these samples are not appropriate for determining the bulk (grain size independent) optical constants because the crystals present in the samples are not large enough for polarized IR reflectance data (Hofmeister et al., 2003). Basically, because the optical constants obtained through analysis of these samples depend on the specific grain size and shape distributions used during the measurement, it is inappropriate to use these constants with any other size or shape distributions; the bulk optical constants however are size and shape independent and so can be used in a wider verity of situations.

4. The KBr matrix correction (essentially this correction attempts to remove the effect of the potassium bromide matrix in which particles are dispersed; see

Friedemann et al., 1981) has been applied to some laboratory spectra of submicron diameter SiC grains dispersed in single-crystal matrices; studies of thin films and isolated nanoparticles of β-SiC have shown that this correction is unnecessary when measurements are carefully made (Speck et al., 1999; Clément et al., 2003). In fact, use of this correction produced a discrepancy between spectra of SiC found in meteorites and SiC around C stars (Speck et al., 1999). Because the most widely used SiC optical constants were produced before this was discovered, the KBr matrix correction was used by Bohren & Huffman (1983, for spherical grains) and Pègourié (1988). Laor & Draine (1993) used these two data sets to produce their own values for the optical constants, so the KBr matrix correction affects their data as well.

8.1.2 Implications of these limitations on previous research

Because most radiative transfer models of the dust shells around C stars have used constants affected by the limitations mentioned in 8.1.1 (Martin & Rogers, 1987; Lorenz-Martins & Lefevre, 1993, 1994; Lorenz-Martins et al., 2001; Groenewegen, 1995; Groenewegen et al., 1998; Griffin, 1990, 1993; Bagnulo et al., 1995, 1997, 1998, and others) in order to place limits on the SiC abundance, those abundances are probably incorrect. Additionally, models other than those of C stars have used these optical constants; examples are LMC stars (Speck et al., 2006, LMC stands for Large Magellanic Cloud, a small companion galaxy to our own), protoplanetary nebulae (Clube & Gledhill, 2004; Jiang et al., 2005), and planetary nebulae (Hoare, 1990). At least some of the conclusions drawn from these models are now suspect.

Because the SiC laboratory data obtained by Borghesi et al. (1985), later used by both Pègourié (1988) and Laor & Draine (1993), used particles of SiC instead of a bulk sample, these data sets are only appropriate (even ignoring the other limitations) for modeling SiC particles with exactly the same size and shape distributions as the original sample (this was previously mentioned in 8.1.1; in this case the particles fit a narrow size distribution of $\sim r^{-2.1}$, with $r = 0.004\mu$m as a typical size). However, this data has in fact been used in attempts to analyze grain size effects on the spectrum of SiC (for example, Bagnulo et al., 1995, see Speck et al. 2005), which is inappropriate.

8.2 Experimental methods

8.2.1 Sample characteristics

Grain properties and manufacturers' information for the SiC samples studied here are presented in table 8.1. We verified sample polytype by optical microscopy and by the spectroscopic results below. Some samples were highly pure (table 8.1). Though we cannot rule out small departures from non-stoichiometry (e.g., Kimura et al. 2006), impurities at the few per cent level would be required to affect band positions in the mid- to far-IR. The colors of the α-SiC samples are associated with impurities which should not affect the main spectral band. Under magnification of x50, the samples are homogeneous in color and, thus, in estimated impurities. The samples lack inclusions but present crystal growth sectors (i.e. planes parallel to $\vec{c}$).

Hexagonal polymorphs of SiC grow as plates perpendicular to the crystal plane (001). This orientation was confirmed using sample morphology and optical microscopy. For α-SiC, we created $\vec{a}$-$\vec{a}$ plates and $\vec{a}$-$\vec{c}$ plates by grinding and polishing parallel or perpendicular to the large faces of our samples, respectively. Because SiC is an extremely hard mineral (9.1–9.5 on the Mohs scale at 20° C), with layering and growth sectors, mirror surfaces were difficult to attain. Thus, the measured reflectance will be lower than the true, absolute reflectance.

8.2.2 Laboratory IR spectroscopic measurements

Room temperature (18–19°C) IR specular reflectance spectra were acquired at near-normal incidence (i.e., the beam passes through the microscope at an angle of $= 90 \pm 10°$) using a Spectra-Tech Fourier transform infrared (FT-IR) spectrometer[1] microscope in an evacuated Bomem DA 3.02 Fourier transform spectrometer[2]. Resolutions of 1 cm^{-1} (mostly for the mid-IR) or 2 cm^{-1} resolution (far-IR) suffice to separate peaks for solid samples at room temperature. Instrumental accuracy is ~ 0.01 cm^{-1}. For the $\vec{E} \| \vec{c}$ polarization of 6H only, we used a specular reflection device instead of the microscope, wherein the incident beam strikes the center of the sample at 30° to the normal. We used the “S” polarization, where the direction of the electric field is parallel to the line defined by the two mirror planes. The beam size was 600 μm in the microscope and ~ 1 mm in the specular reflectance device. A Si-bolometer and a coated mylar beamsplitter were used for the far-IR, ~ 50 to 650 cm^{-1} ($\sim$ 200–15.0 μm). A KBr beamsplitter and a liquid-nitrogen-cooled HgCdTe detector were used for the mid-IR, 450–4000 cm^{-1} ($\sim$ 22–2.5 μm). A gold mirror (100% reflection assumed; 98% average reflection measured) was used as the reference. 2000 scans yielded a reasonable noise level.

The laboratory reflectance spectra in figure 8.1 and figure 8.2 have been merged, corrected for artifacts and rescaled from the raw spectra. Where reflectance spectra were available for both wavelength regions, mid- and far-IR reflectance intensities were scaled to match in the region of overlap and merged. Because back reflections

---

[1] Spectra-Tech Inc. (Thermo Electron Corp.), Stamford, CT, USA.

[2] Bomem Inc., Quebec, Canada.

(e.g. from growth sectors, Hofmeister et al., 2003) increase apparent reflectance, the segment with the lowest reflectance above 1000 cm^{-1} was presumed to be correct. For the $\vec{a}$-$\vec{a}$ sections, we collected spectra from several areas and present the spectrum with the highest reflectance at the peak center (i.e., best polished surface). For our α-SiC, the maximum absolute reflectance measured is low ($R = 0.72$) due to surface imperfections. We estimate the effect of errors in R on our data analysis and compare peak shapes by scaling all reflectance spectra to 92–99% maximum reflectance (cf. Spitzer et al., 1959b; Il'in et al., 1972; Zorba, 1996; Goncharenko et al., 1996). Our (blue-gray) α-SiC hopper crystal sample was large enough to provide good data from the $\vec{a}$-$\vec{c}$ section, but its structure of intergrown, stacked crystals caused artifacts in the reflectance spectrum. The $\vec{a}$-$\vec{a}$ plates we studied were too thin to allow us to collect data from the $\vec{a}$-$\vec{c}$ edges. The size of our mossanite sample was marginally large enough for a $\vec{a}$-$\vec{c}$ sample but is comparable in size to the beam diameter and thus our apparatus may not have sampled the same areas from the reference mirror and the moissanite sample.

8.2.3 IR Data Analysis

To avoid presenting results that are affected back reflections, we compared reflectance R_ν in the limit that $k \to 0$ at visible wavelengths,

$$R_\nu \approx \frac{(n_\nu - 1)^2}{(n_\nu + 1)^2}. \tag{8.1}$$

with literature values of the index of refraction determined through microscopy in white or yellow light (either $n(\lambda = 467\text{ nm})$ or $n(\nu = 22\,000\text{ cm}^{-1})$ ($\lambda = 467$ nm or $\nu = 22\,000$ cm^{-1}, respectively, table 8.1). If the reflectance at $\nu = 4000$ cm^{-1} was less than R_{white} by a few percent, then back reflections did not affect the data.

We used Kramers-Kronig analyses (Fahrenfort, 1961; Roessler, 1965) to determine starting estimates of peak positions and widths and followed up with classical dispersion analyses to provide robust $n(\nu)$ and $k(\nu)$ values. β-SiC has poorly resolved peaks; this is problematic for a Kramers-Kronig calculation, but not for classical dispersion analysis (e.g. Giesting & Hofmeister, 2002). Values of n and k from our best fits are presented in figures 8.3b-8.7b.

We constructed synthetic reflectance spectra from three parameters: (1) the TO peak positions (ν_i) determined from the maxima in $\epsilon_2(\nu)$, the full width at half-maximum (FWHM$_i$) of each peak in $\epsilon_2(\nu)$, and the oscillator strength $f_i = 2\ \mathrm{FWHM}_i \sigma_{max}/\nu_i^2$, where the conductivity $\sigma(\nu) = \nu\epsilon_2(\nu)/2$. The light angle of incidence Φ is accounted for after Jackson (1975):

$$r_{s\Phi} = \sqrt{R_{meas}} = \frac{cos\Phi - \sqrt{n^2 - k^2 + 2ink - sin^2\Phi}}{cos\Phi + \sqrt{n^2 - k^2 + 2ink - sin^2\Phi}}. \tag{8.2}$$

The equations for the components of the dielectric function for m oscillators using the damping coefficient $\Gamma_i = 2\pi\mathrm{FWHM}_i$ are

$$\epsilon_1 = \epsilon_\infty + \sum_{j=1}^{m} \frac{4\pi^2 f_j(\nu_j^2 - \nu^2)}{4\pi^2(\nu_j^2 - \nu^2)^2 + \Gamma_j^2\nu^2}, \tag{8.3}$$

where ϵ_∞ is n^2 in the visible, and

$$\epsilon_2 = \sum_{j=1}^{m} \frac{2\pi f_j \nu_j^2 \Gamma_j \nu}{4\pi^2(\nu_j^2 - \nu^2)^2 + \Gamma_j^2\nu^2}. \tag{8.4}$$

The absorption coefficient A is calculated from

$$A(\nu) = \frac{2\pi\nu\epsilon_2(\nu)}{n(\nu)} = 4\pi\nu k(\nu). \tag{8.5}$$

We note that Mutschke et al. (1999) have calculated spectral absorption and emis-

Table 8.1: Experimental samples: Manufacturer information and references

Polytype	Mineral Name	Grain Size	Manufacturer	Refractive Index	Comments
α-SiC	synthetic moissanite	diam. = 6.5 mm	Charles & Colvard, Ltd^{TM}	$n_o = 2.654$[a] $n_e = 2.967$	round brilliant cut gem
α-SiC	6H-SiC (gray, amber)	2 μm powder; surf. area = 9–11 m^2 g^{-1}	Alfa/Aesar (Lot # C19H06)	$n_o = 2.55$, $n_e = 2.59$ (IR) $n_o = 2.5531+(3.34\cdot10^4)\cdot\lambda^{-2}$, $n_e = 2.5852+(3.68\cdot10^4)\cdot\lambda^{-2}$ [b]	hexagonal plates purity: 99.8% metals basis
α-SiC	6H-SiC (blue-gray); synthetic carborundum	several mm per crystal	unknown	$n_o = 2.654$[a] $n_e = 2.967$	Hopper crystal; (i.e., intergrown crystals)
α-SiC	6H-SiC (green, yellow)	4–8 mm wide, 0.25–1.20 Car. each	Morion Co.	$n_o = 2.654$[a] $n_e = 2.967$	green: layered, hexagonal, flat yellow: single crystal
β-SiC	3C-SiC wafer (fcc cubic)	diam= 5 μm	Rohm & Haas, Advanced Materials (Grade SC-001)	$n_{o,e} = 2.55$[b] $n_{o,e} = 2.55378+(3.417\cdot10^4)\cdot\lambda^{-2}$ [c]	CVD wafer purity: $\geq$ 99.9995%
β-SiC	3C-SiC gray (fcc cubic)	diam. $\sim$ 2.5–25 μm	Superior Graphite	$n_{o,e} = 2.55$[b] $n_{o,e} = 2.55378+(3.417\cdot10^4)\cdot\lambda^{-2}$ [c]	equant (spherical) chips

[a] Indices of refraction for the O-ray (n_o) and E-ray (n_e) given for white light (Gaines et al., 1997) or IR λ (Goldberg et al., 2001).

[b] Values for visible light (467 nm $< \lambda <$ 691 nm at T = 300 K; Schaffer & Naum (1969); Shaffer (1971). Formulae assume λ in nanometers.

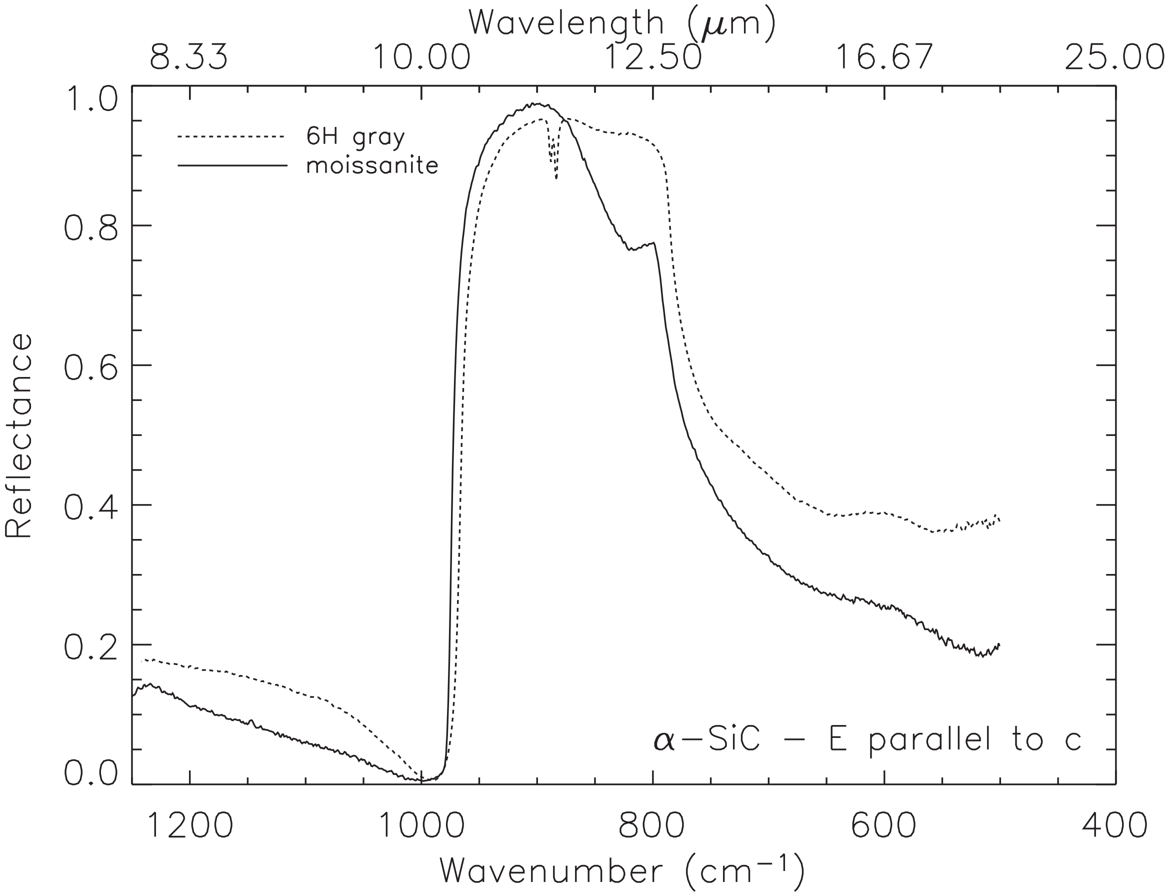

Figure 8.1: Mid- and mid+far-IR laboratory specular reflectance as a function of wavenumber (wavelength) for $\vec{E}\|\vec{c}$ faces of α-SiC: moissanite (dash-dot line) and gray 6H (dashed line). Laboratory values scaled to 95% maximum reflectance from 35% (moissanite) and 45% (gray 6H).

sion cross-sections for different particle shapes using ad hoc damping coefficients γ for 6H-SiC. Mutschke et al. (1999) provide a simplified version of Eq. 7 that is appropriate for spectra arising from one oscillator (their eq. 1) and further relate the strength of a single oscillator to $\nu_{LO}^2 - \nu_{TO}^2$ (their eq. 2). Because multiple oscillators occur for certain polarizations of SiC and are seen in all of our samples, we instead use equations (8.3) through (8.5) to constrain peak widths and oscillator strengths.

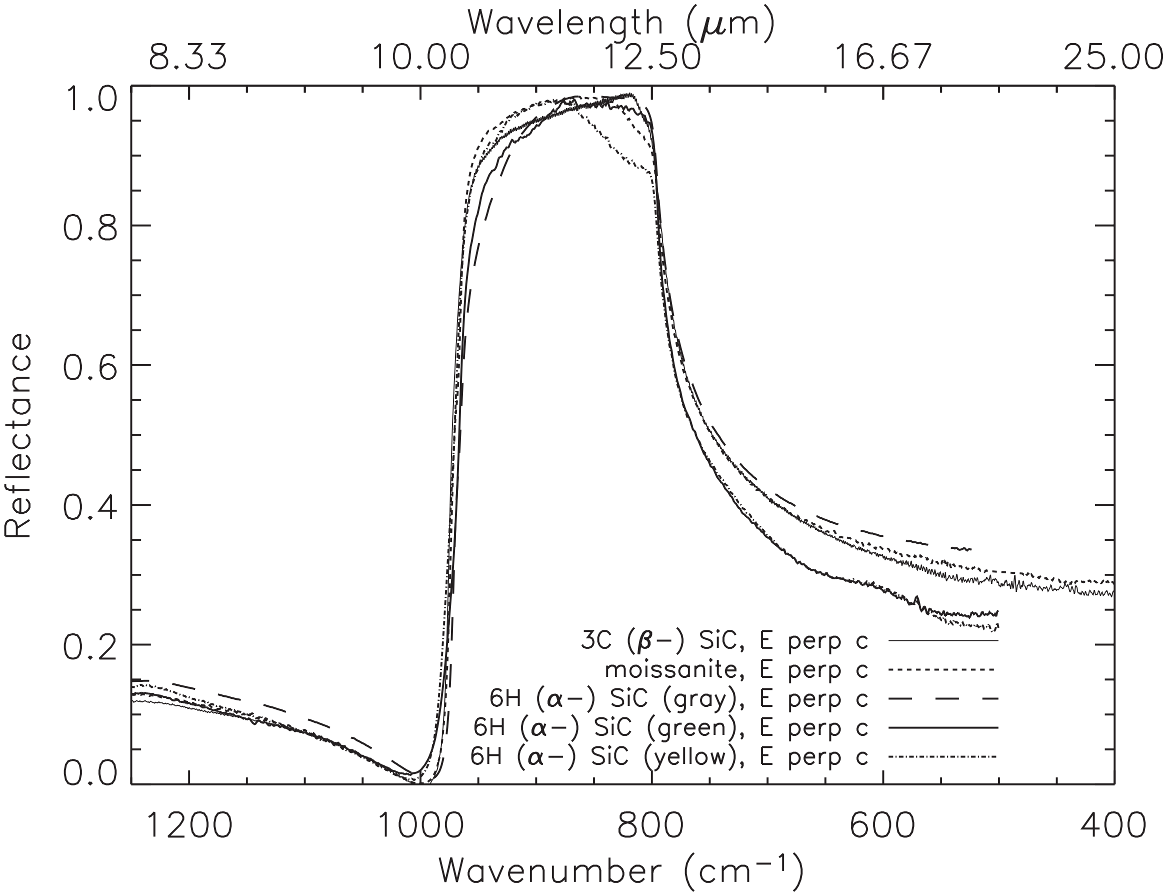

Figure 8.2: Mid- and mid+far-IR laboratory specular reflectance for $\vec{E}\perp\vec{c}$ faces of β-SiC (dashed line), and two α-SiC samples: moissanite (solid line) and gray 6H (dash-dot line). A mode occurs at $\sim$ 965 cm^{-1}; polish effects account for the differences in shape of the main peak. Values scaled from 72% (β-SiC), 95% (moissanite), 84% (gray 6H), 76% (green 6H) and 84% (yellow 6H) to 98% maximum reflectance.

8.3 Results

8.3.1 Laboratory reflectance spectra

Laboratory reflectance spectra of α- and β-SiC are presented in figures 8.1–8.2; peak positions are given in cm^{-1} wavenumber, or $10^4/(\lambda \text{ in } \mu\mathrm{m})$. Reflectance spectra of β-SiC show a large, broad feature extending from the TO position near 797.5 cm^{-1} to a LO mode near 973 cm^{-1}, consistent with Raman frequencies measured by Feldman et al. (1968). Because the sum of transverse and longitudinal acoustic modes at $\nu_{TA} + \nu_{LA} = 876$ cm^{-1} falls between the LO and TO modes of β-SiC, a resonance is possible near that position. For α-SiC, from zone folding and Raman measurements of the dispersion, IR modes for $\vec{E}\|\vec{c}$ could also occur at 965, 940, 889, and 836 cm^{-1} and in $\vec{E}\perp\vec{c}$ at 797, 789, 772, and 767 cm^{-1}. As in β-SiC, the strong TO mode in α-SiC occurs near 797 cm^{-1} in $\vec{E}\perp\vec{c}$ and at $\sim$ 789 cm^{-1} for $\vec{E}\|\vec{c}$ in α-SiC. Modes at lower frequencies are not apparent, i.e. these are too weak for resolution in reflectivity data, if they exist.

We fitted the laboratory reflectance spectra via classical dispersion analysis to characterize the position, FWHM, and oscillator strength parameters of the main peak and also to resolve the structure near the TO and LO positions in both SiC polytypes. This structure does not occur near the expected peak positions and appears to be due to physical optics effects, as discussed in section 8.3.2. The suspect features may be described as a divot in the reflectance spectrum near the TO mode for both polarizations of the α-SiC (moissanite and 6H gray) samples, in $\vec{E}\perp\vec{c}$ polarization only for the yellow α-SiC sample, and also in the β-SiC wafer sample. In $\vec{E}\perp\vec{c}$ for the 6H gray and, to some extent, the green α-SiC reflectance spectra, the slope near the LO mode is more shallow than that of the yellow α-SiC and moissanite reflectance spectra and may also be a spectral artifact.

8.3.2 Optical constants: $n(\nu)$, $k(\nu)$

We fitted our laboratory reflectance data to various numbers of oscillators via classical dispersion analysis to determine if the derived optical constants and absorption coefficients are strongly affected by both weak features predicted from symmetry analyses and by spectral artifacts induced by layering or small sample size. Figures 8.3-8.7 show the resulting optical functions and the corresponding fitting parameters. By comparing and contrasting these fits, we determine whether multiple oscillators or a single oscillator best represents the behavior of α- and β-SiC. The n and k values obtained from single-crystal spectra samples are not dependent on grain size.

For β-SiC, a classical dispersion analysis fit using one oscillator matches the peak sites and the sloping top of the main reflectance peak well, but to fit the corner dip and the slight sway on the top of the peak, three oscillators are required (figures 8.7, 8.10a). The LO mode is at $\nu = 973$ cm^{-1}. The large breadth and the position of the 875 cm^{-1} feature is consistent with assignment as an acoustic overtone. Its presence is within the uncertainty of the measurements. From figure 8.10a, n and k are slightly affected by the number of oscillators used. Using three oscillators instead of one makes the peak in k more narrow and causes the maximum k value to increase by 25%. The total area under the peak for k is not affected by the number of oscillators. Similarly, n differs little when the number of oscillators is varied. Because no extra oscillators are expected at 802 cm^{-1} for β-SiC, we suspect the appearance of a peak at that location is associated with back reflections for this very thin wafer. For the purpose of modeling the spectrum, the single oscillator fit ($\nu = 797.5$ cm^{-1}, FWHM $= 6.0$ cm^{-1}, and $f = 3.5$ with $\nu_{LO} = 975$ cm^{-1}) suffices and agrees with symmetry analysis.

Fitting the moissanite $\vec{E} \perp \vec{c}$ reflectance spectrum with one oscillator shows that there is structure on the main band near both 800 and 950 cm^{-1} (figure 8.6). Also, the divot makes it difficult to constrain the TO position. A one oscillator fit with peak wavenumber at 797.5 cm^{-1}, FWHM = 4.5 cm^{-1}, and $f = 3.45$ is equally good (not shown). Two additional oscillators are needed to characterize the structure near 800 cm^{-1}, and one additional oscillator is needed to account for the structure near 970 cm^{-1} (figure 8.6). The best fit for two oscillators is $\nu_1 = 797.5$ cm^{-1}, FWHM$_1$ = 4.1 cm^{-1}, $f_1 = 3.45$ and $\nu_2 = 970.0$ cm^{-1}, FWHM$_2$ = 11.0 cm^{-1}, and $f_2 = 0.0010$. The presence of a peak at 970 cm^{-1} is in agreement with zone folding and Raman data. Addition of the 970 cm^{-1} makes very little difference to n and k (figure 8.10).

For the 6H gray α-SiC sample ($\vec{E}\perp\vec{c}$), a one oscillator fit does not match the slope at high frequency (figure 8.4). n and k differ very little between the fits, though multiple oscillators appear to make k more narrow and peak at a higher value (figure 8.10). The main peak parameters differ very little among various fits to different numbers of oscillators for this reflectance spectrum. The green and yellow α-SiC samples ($\vec{E}\perp\vec{c}$) were fitted with a single oscillator (not shown). For the green α-SiC, the best fitting parameters are a peak position of 797.5 cm^{-1}, FWHM = 6.0 cm^{-1} and $f = 3.3$; n.b., this does not fit the slope at high frequency well. For the yellow α-SiC, the best fitting parameters are a peak position at 798.0 cm^{-1}, FWHM = 5.5 cm^{-1} and $f = 3.5$. This TO position is not well constrained due to the presence of the divot.

Regarding possible spectral artifacts, Spitzer et al. (1959b) also observed a divot in their reflectance spectrum for a polished SiC surface and a slope for an oxidized surface; they obtained their best data for a grown surface. Data on α-SiC, $\vec{E}\perp\vec{c}$ from figure 9.6 in Bohren & Huffman (1983) resemble the results of Spitzer et al. (1959b) for the grown surface. No divot exists, but the slope is greater than we observed for moissanite. We note that the green and 6H gray α-SiC samples both have thin layers perpendicular to $\vec{c}$ and high slopes at high ν. The 6H gray α-SiC sample has a slightly stronger slope, but not much (figure 8.2). The yellow α-SiC and moissanite samples lack the slope but have the divot at low ν. These samples are single crystals; however, the yellow α-SiC is the thinnest sample and its spectrum has the deepest divot. The moissanite is not thin but has growth sectors (on the order of 0.5 mm thick). We conclude that the divot is connected with back reflections, not surface polish, because the green and yellow α-SiC and moissanite samples are all polished by the manufacturers and have smooth surfaces. Given how difficult this divot was to fit via classical dispersion analysis, it cannot be a vibrational mode and is probably associated with a physical optics effect and the high reflectivity of the sample. We also conclude that the slope at high frequency is associated with the thin layers and is also a problem of physical optics. Neither the slope nor the divot are intrinsic to the samples. Samples larger than 5 mm in diameter without growth sectors are needed to provide the best possible data for SiC.

For moissanite ($\vec{E}\|\vec{c}$), the main reflectance peak has a very large divot, which is an artifact, as in the $\vec{E}\perp\vec{c}$ polarization (figure 8.5). Because of the divot, the TO peak position is difficult to constrain. The best classical dispersion fit provides a high value of ν (802 cm^{-1}) that is uncertain. The data do not reveal the presence of any of the folded modes or of acoustic overtone/combination bands. The 6H gray ($\vec{E}\|\vec{c}$) sample can be fitted with one oscillator at $\nu = 787.8$ cm^{-1} with a FWHM $= 5.5$ cm^{-1} and $f = 4.45$ (figure 8.3). The peak position is hard to constrain, but clearly it is lower than the TO peak for $\vec{E}\perp\vec{c}$. The corresponding LO position is at $\nu_{LO} = 966.9$ cm^{-1}. The divot at low frequency is different, being comprised of one broad mode near 830 cm^{-1} and having reduced intensity near the TO position, like the other samples (figure 8.1). The latter fact should not impact the TO position of the main peak. We attempted fits with various numbers of peaks. The 4 oscillator fit in figure 8.3 confirms the low frequency TO position near 787 cm^{-1} for 6H gray α-SiC ($\vec{E}\|\vec{c}$). The presence of two modes near 888 cm^{-1} are consistent with zone folding and possible involvement of resonance with the acoustic modes. However, the narrow widths for these bands indicate that these are fundamentals, not overtones. The broad feature near 835 cm^{-1} appears to be a folded mode; its position is consistent with Raman spectra, although its breadth suggests it is an overtone/combination band. In contrast, the reduced intensity near the TO position was difficult to fit, which is the hallmark of a spectral artifact and consistent with the problems incurred in the other samples. The strong layering in the 6H gray α-SiC sample could contribute to the artifacts. The fit parameters that should represent the intrinsic behavior of this particular sample is ν = 787.8 cm^{-1} (FWHM = 5.5 cm^{-1}, f = 4.35), 836.0 cm^{-1} (FWHM = 30.0 cm^{-1}, f = 0.10), 883.7 cm^{-1} (FWHM = 2.5 cm^{-1}, f = 0.0041) and 888.5 cm^{-1} (FWHM = 3.3 cm^{-1}, f = 0.0033). The intense LO mode occurs at 968.9 cm^{-1}, consistent with Raman measurements. We suggest that the sample has impurities connected with the strength of the folded modes. These weak modes add structure to the n and k spectra but do not change the peak maximum.

8.3.3 Calculated absorbance

Absorbances calculated via classical dispersion analyses are cross-checked through comparison with measured absorbance of the α- and β-SiC samples (figure 8.8,8.9). In contrast to the calculated $A(\nu)$, laboratory absorbances (a_{SCM}) are dependent on grain size via

$$a_{SCM} = \frac{A(\nu)d}{2.3026} - 2\log_{10}(1-R). \tag{8.6}$$

a_{SCM} is converted for direct comparison to $A(\nu)$ in the figures. For α-SiC, a weighted average,

$$a_{avg} = (2a_{\perp} + a_{\parallel})/3, \tag{8.7}$$

is used in the comparison of figure 8.8. Averaging provides one main peak and a shoulder for α-SiC. The position of the main peak matches that of β-SiC (figure 8.9), but the shoulder is at lower frequency. Real, measured spectra have strongly rounded peaks due to light leakage between cracks in thin-film samples or around the particulates in dispersions. In measured spectra, the α-SiC peak occurs at a lower frequency than for β-SiC, consistent with our calculations. Because of the light leakage, the two peaks for α-SiC are blended into one band. In figure 8.8, the measured spectrum of α-SiC fits into the envelope. Some of the differences between the calculated and measured absorbances are due to reflectivity not being subtracted from the raw data; in these diamond anvil cell measurements, the spectral baseline involves both the reflectivity of the diamonds and of the sample, and it is not clear how best to proceed with the subtraction. In dispersions, the spectral baselines are uncontrolled, consisting of sample and medium properties. For β-SiC, the measured peaks are much more rounded than in the calculations, and more rounded than the peaks measured for α-SiC (cf. figures 8.8,8.9). Because the β-SiC chips are harder, it is more difficult to make a thin film; this results in a more rounded profile. The nano-β-SiC samples are softer and form a better thin film, producing a peak very close to the ideal, and also a large shoulder at the LO position. The prominence of the LO mode is expected for the β-SiC absorbance spectrum which consists of a doubly degenerate TO mode and a single LO mode. Hence absorbance peaks round and shift to high frequency in measurements as compared to classical dispersion analysis calculations (figure 8.9). For the hexagonal samples, symmetry suggests something much different: a degenerate planar optic mode near the cubic TO position and 1 axial optic mode near the

LO position. That is, the TO and LO modes that are strongly coupled in the cubic structure are decoupled in the hexagonal structure. For $\vec{E} \perp \vec{c}$ in α-SiC, the TO and LO modes are like those in β-SiC. The behavior of the absorbance spectrum for α-SiC ($\vec{E} \| \vec{c}$) is confusing because several criteria must be met that seem to be contradictory. One is that the TO mode must be lower in frequency than the LO mode, despite the fact that symmetry suggests a main mode occurs near $\nu = 970$ cm^{-1} for the axial configuration. Another is that the same dipoles exist, so the stretching frequency cannot be much different. The end result is that the LO position is preserved and the TO position is derived from a zone-folded mode. It seems that more strength is shifted to the TO position in the process. But it is also expected that the hexagonal particles are preferentially oriented and that the measured absorption is skewed to the TO position. These effects combined indicate that less energy goes toward the LO position in α-SiC than in β-SiC, consistent with the rounding of the peaks and the lower frequency of the α-SiC peak maximum.

8.4 Discussion

Past studies are divided on whether the crystal structure of SiC can be determined from IR spectra (in favor: Borghesi et al. 1985; Speck et al. 1999; opposed: Spitzer et al. 1959a,b; Papoular et al. 1998; Andersen et al. 1999a,b; Mutschke et al. 1999). Section 8.3 shows that spectroscopic differences exist between certain orientations of α- and β-SiC. This section compares β-SiC to α-SiC from the laboratory perspective and discusses implications for astronomers.

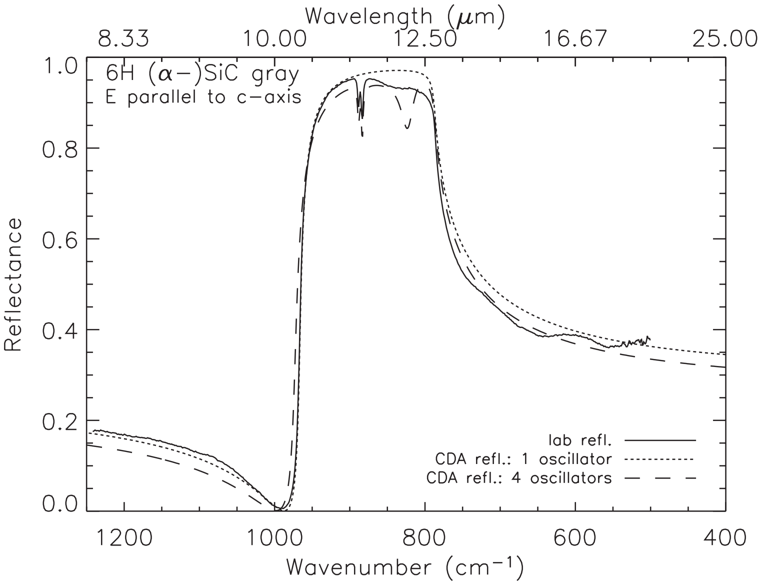

(a)

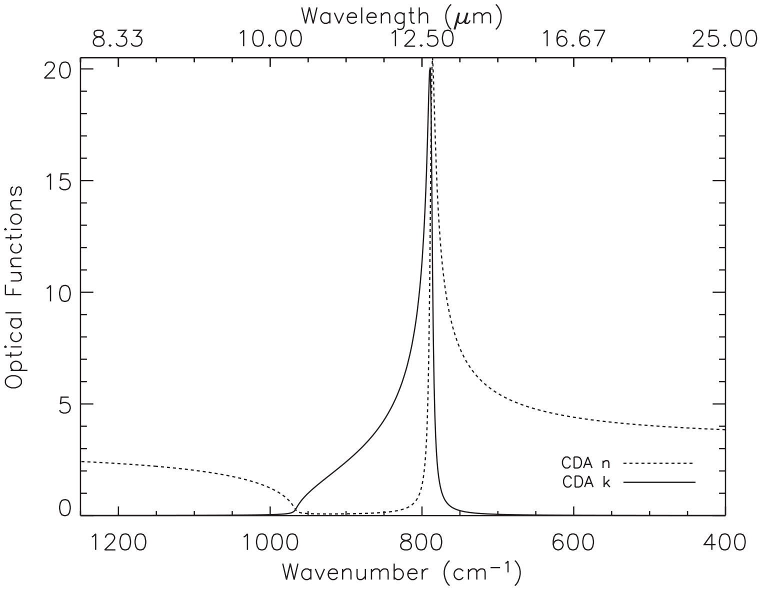

(b)

Figure 8.3: Reflectivity at near-normal incidence of 6H gray α-SiC ($\vec{E}\|\vec{c}$ orientation) and derived functions from classical dispersion analysis. (a) Laboratory reflectivity spectrum (solid line, scaled to 95% maximum reflectance), calculated reflectivity fitted by 1 oscillator (ν_1 = 787.5 cm^{-1}, FWHM$_1$ = 5.50 cm^{-1}, oscillator strength f_1 = 4.45) (long dashed line), and fitted by 4 oscillators (ν_1 =787.5 cm^{-1}, FWHM$_1$ = 6.60 cm^{-1}, f_1 = 3.57; ν_2 = 825.0 cm^{-1}, FWHM$_2$ = 20.0 cm^{-1}, f_2 = 0.3; ν_3 = 883.7 cm^{-1}, FWHM$_3$ = 2.5 cm^{-1}, f_3 = 0.00475; ν_4 = 888.5 cm^{-1}, FWHM$_4$ = 3.3 cm^{-1}, f_4 = 0.00425) (short dashed line). (b) Real and imaginary parts of the complex index of refraction for the 1 oscillator fit: n (solid line) and k (dashed line).

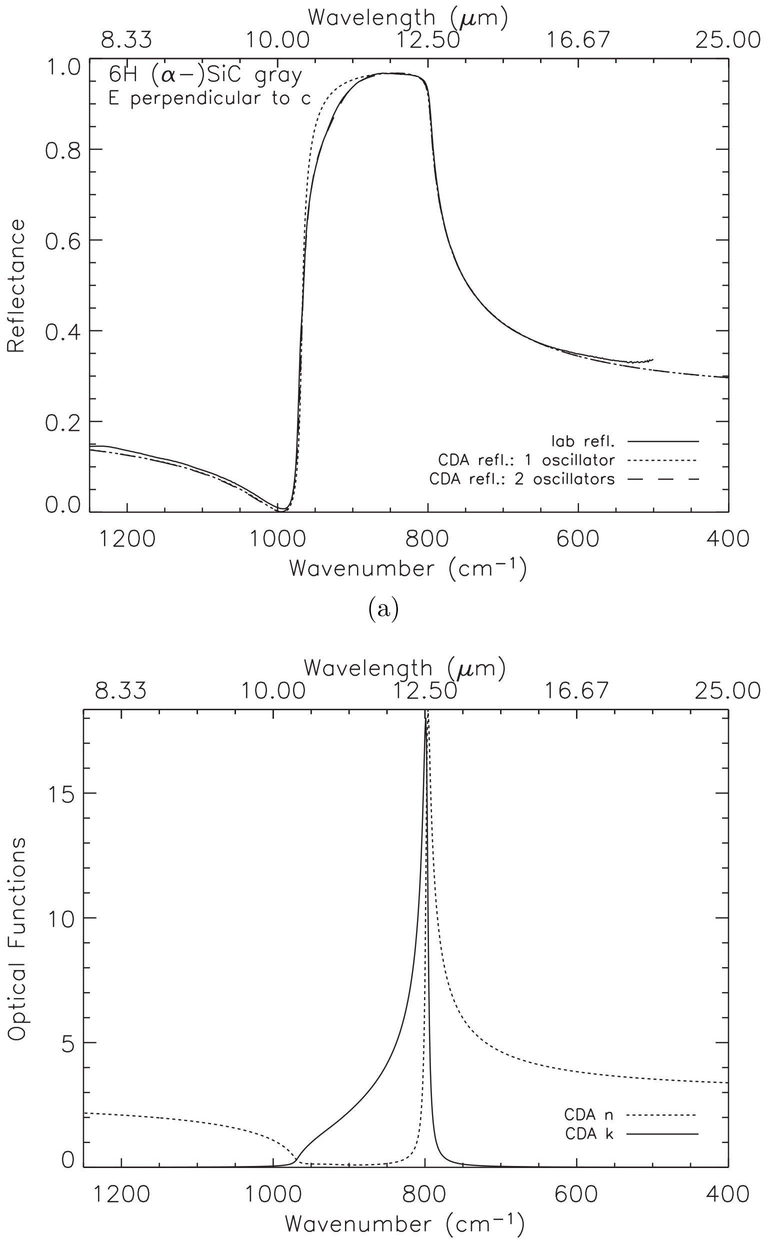

(a)

(b)

Figure 8.4: Reflectivity at near-normal incidence of 6H gray α-SiC ($\vec{E}\perp\vec{c}$ orientation) and derived n and k. (a) Laboratory reflectivity spectrum (solid line, scaled to 97% maximum reflectance), calculated reflectivity fitted by 1 oscillator (ν = 797.5 cm^{-1}, FWHM = 5.30 cm^{-1}, f = 3.33) (long dashed line), and by 2 oscillators (ν_1 = 797.5 cm^{-1}, FWHM$_1$ = 5.20 cm^{-1}, f_1 = 3.32; ν_2 = 928.0 cm^{-1}, FWHM$_2$ = 65.0 cm^{-1}, f_2 = 0.013) (short dashed line). (b) n (solid line) and k (dashed line) for the 2 oscillator fit.

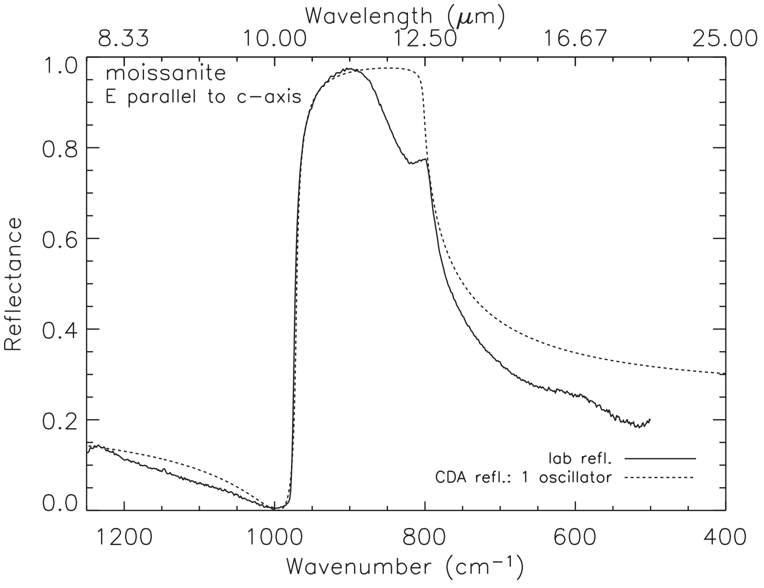

(a)

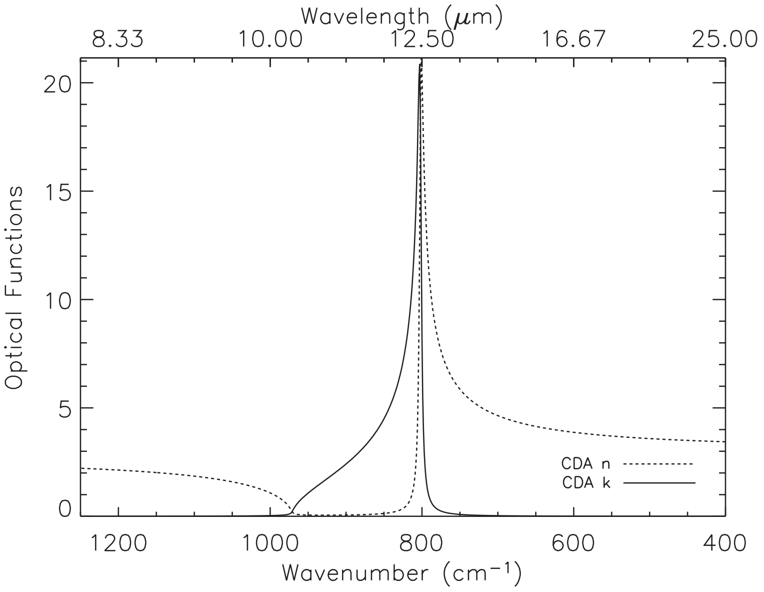

(b)

Figure 8.5: Reflectivity at near-normal incidence of moissanite (α-SiC, $\vec{E} \| \vec{c}$ orientation) and derived n and k fitted by 1 oscillator ($\nu = 802.0$ cm^{-1}, FWHM = 4.0 cm^{-1}, $f = 3.4$). (a) Laboratory reflectivity spectrum (solid line, scaled to 97% maximum reflectance) and calculated reflectivity (dashed line). (b) n (solid line) and k (dashed line).

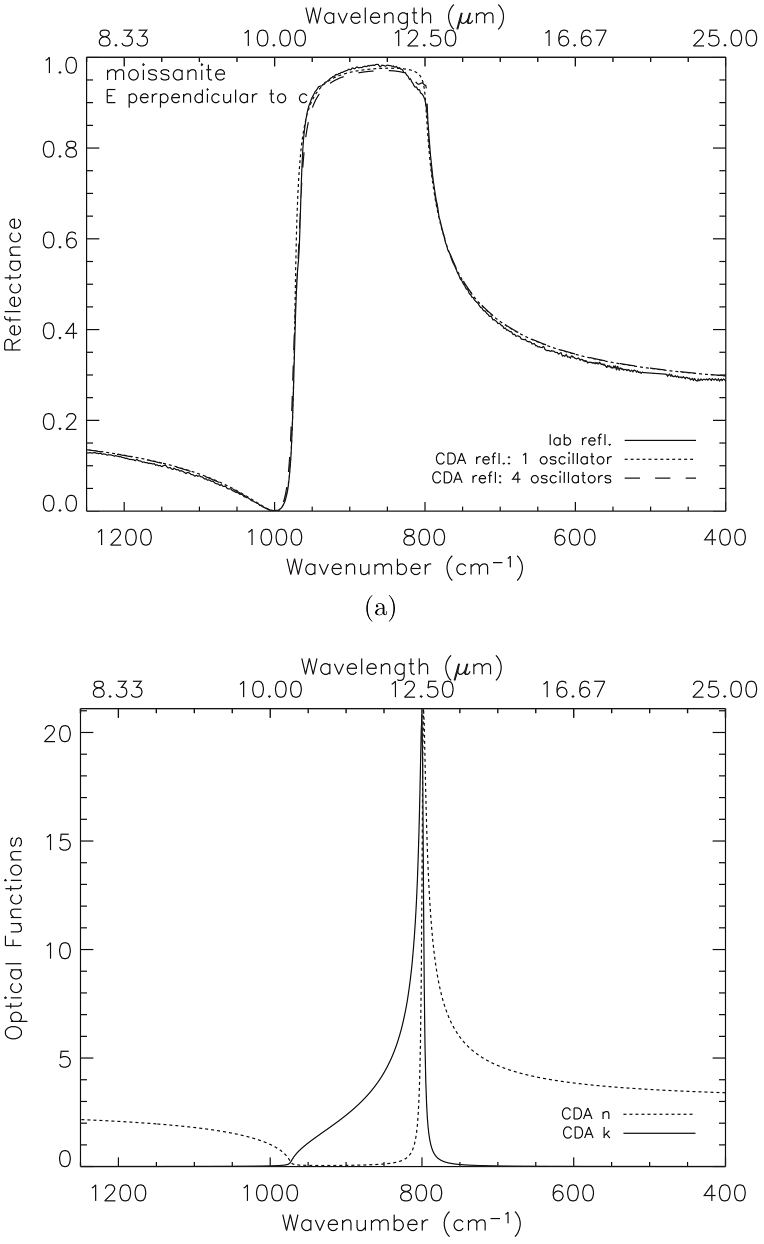

(a)

(b)

Figure 8.6: Reflectivity at near-normal incidence of moissanite (α-SiC, $\vec{E}\perp\vec{c}$ orientation) and derived n and k. (a) Laboratory reflectivity spectrum (solid line, scaled to 97% maximum reflectance), calculated reflectivity fitted by 1 oscillator (ν = 799.0 cm^{-1}, FWHM = 4.0 cm^{-1}, f = 3.4) (long dashed line), and by 4 oscillators (ν_1 = 797.5 cm^{-1}, FWHM$_1$ = 1.75 cm^{-1}, f_1 = 2.04; ν_2 = 799.0 cm^{-1}, FWHM$_2$ = 7.0 cm^{-1}, f_2 = 1.10; ν_3 = 808.0 cm^{-1}, FWHM$_3$ = 14.0 cm^{-1}, f_3 = 0.28; ν_4 = 970.0 cm^{-1}, FWHM$_4$ = 12.5 cm^{-1}, f_4 = 0.0010) (short dashed line). (b) n (solid line) and k (dashed line) for the 1 oscillator fit.

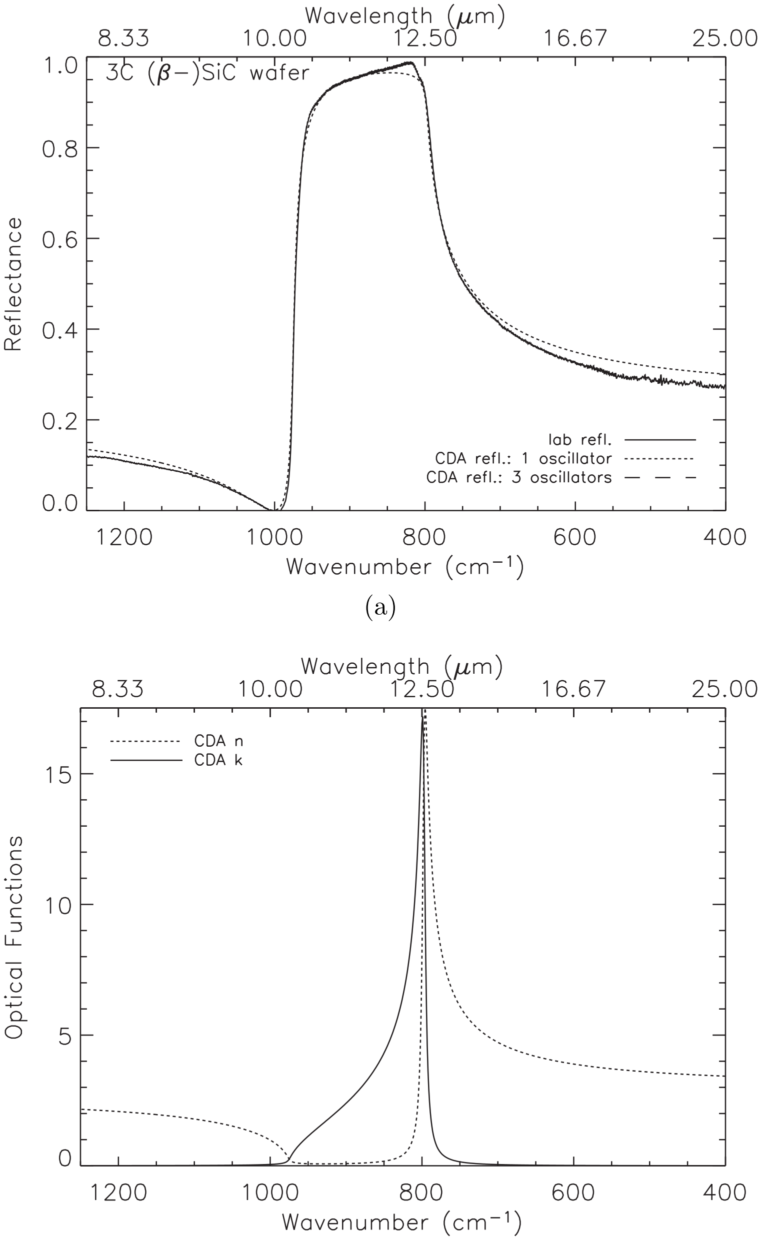

(b)

Figure 8.7: Reflectivity at near-normal incidence of β-SiC and derived n, k. (a) Laboratory reflectivity spectrum (solid line, scaled to 98% maximum reflectance), calculated reflectivity for 1 oscillator (long dashed line: ν = 797.5 cm^{-1}, FWHM = 6.0 cm^{-1}, f = 3.5) and 3 oscillators (short dashed line: nu_1 = 797.5 cm^{-1}, FWHM$_1$ = 2.66 cm^{-1}, f_1 = 2.7, nu_2 = 802 cm^{-1}, FWHM$_2$ = 7.0 cm^{-1}, f_2 = 0.68, nu_3 = 875 cm^{-1}, FWHM$_3$ = 7.0 cm^{-1}, f_3 = 0.03). An LO mode occurs at ν = 975 cm^{-1}. (b) n (solid line) and k (dashed line) for the 1 oscillator fit.

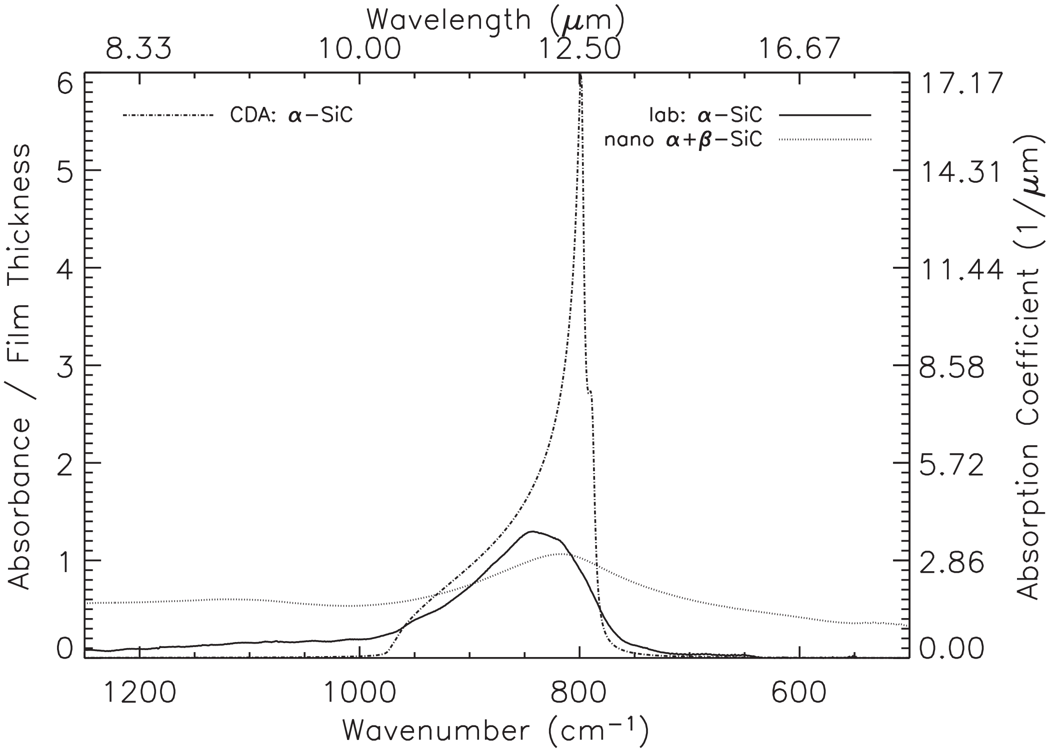

Figure 8.8: Laboratory thin film absorbances (Speck et al. 1999; Speck et al. 2005) divided by estimated sample thicknesses ($d \sim 0.5$ μm) compared to calculated classical dispersion analysis absorbance coefficients for α-SiC. Calculated absorbance coefficients for the remaining α-SiC samples are indistinguishable.

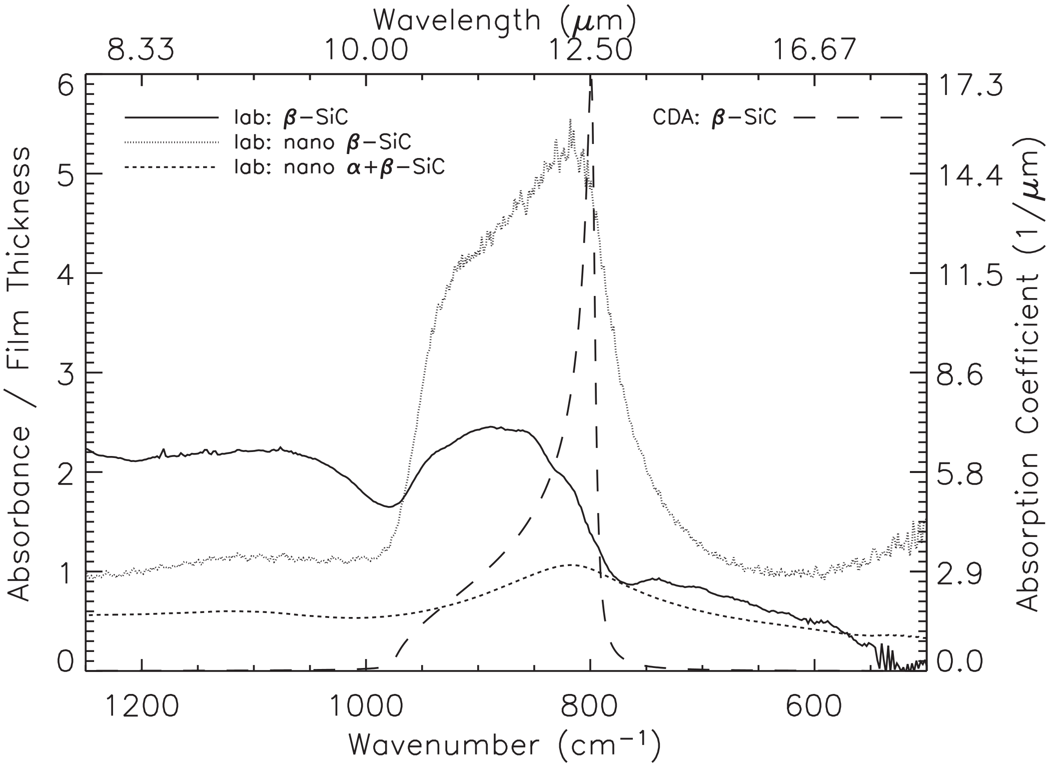

Figure 8.9: Laboratory thin film absorbances (Speck et al., 1999, 2005) divided by estimated sample thicknesses ($d \sim 0.15$ μm for β-SiC, 0.5 μm for nano samples) compared to calculated classical dispersion analysis absorbance coefficients for a 1 oscillator fit to β-SiC (figure 8.7). Given the uncertainty in estimated sample thicknesses, laboratory values can be scaled by factors of 3-5.

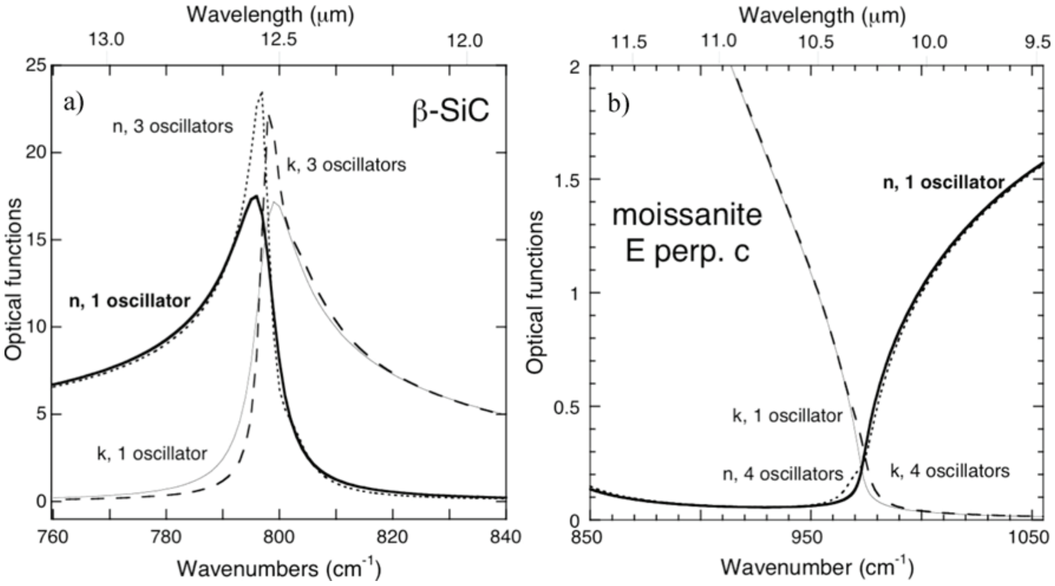

Figure 8.10: Comparison of n and k values calculated via classical dispersion for single and multiple oscillator fits: (a) β-SiC (figure 8.7, section 8.3.2), and (b) α-SiC (moissanite $\vec{E}\perp\vec{c}$, figure 8.6b). In (a), peak heights for n and k increase if more oscillators are used in the fit. In (b), adding oscillators to account for structure at $\nu \sim 800$, 970 cm^{-1} improves the fit to the laboratory reflectance spectrum, but the difference to n and k is small.

8.4.1 Comparisons to previous works

Spitzer et al. (1959a) obtained reflectivity data from a thin (0.06 μm) film of β-SiC that was vapor-deposited on a Si surface ($\nu_{TO} = 793.6$ cm^{-1}, $\Gamma = 8.4$ cm^{-1}, $f = 3.30$). The film was slightly irregular in appearance and thin enough to transmit light at all frequencies (their figure 3). Because the TO mode dominates those spectra, the TO peak position should be as accurate as their spectrometer could provide. However, the width of 8.5 cm^{-1} is large compared to that from 6H crystals, which probably stems from the LO mode being disproportionately large in the thin-film spectra. This effect occurs commonly due to non-normal beam incidence, wedging of the film, or irregular film thickness (Berreman, 1963). The LO value obtained from the parameters of Spitzer et al. (1959a) will be influenced by the large Γ value.

The α-SiC $\vec{E}\perp\vec{c}$ data shown in figure 9.6 of Bohren & Huffman (1983) is historically important because it was used in the widely cited work by Laor & Draine (1993). Because Bohren & Huffman (1983) only provide reflectance data for $\vec{E}\perp\vec{c}$ and did not provide experimental details, such as which type of α-SiC was used, direct comparison between our 6H-SiC data and past studies is weighted more heavily toward results of the Spitzer et al. (1959b) study, which provides data for both polarizations of 6H single-crystals.

Our results suggest that the $n(\lambda)$ and $k(\lambda)$ for $\nu = 797.5$ cm^{-1}, FWHM = 4.0–6.0 cm^{-1} and $f = 3.3$–3.45 best represents α-SiC $\vec{E}\perp\vec{c}$. These values are quite similar to the $\vec{E}\perp\vec{c}$ results of Spitzer et al. (1959b) for 6H-SiC ($\nu_{TO} = 793.9$ cm^{-1}, FWHM $= 4.8$ cm^{-1}, $f = 3.30$) and Bohren & Huffman (1983) for α-SiC ($\nu_{LO} = 969.2$ cm^{-1}, $\nu_{TO} = 793$ cm^{-1}, $\Gamma = 4.7$ cm^{-1}). Thus, we confirm past findings that f is high and that the FWHM of the main SiC peak is of the order of 5 cm^{-1}. For dispersive instruments such as the ones used by Spitzer et al. (1959b) and presumably Bohren & Huffman (1983), resolutions depend on the slits used and vary with wavelength.

Low resolution is suggested by the spacing of data points in previous figures by these authors. High resolution is needed to properly depict profiles of sharp, steeply rising peaks (cf. Bowey et al., 2001), such as the reflectance peaks for SiC. The few cm^{-1} difference for the reported TO positions may either be due to resolution difference or to older, dispersive instruments lacking internal calibration that exists in modern FT-IR spectrometers. Peak positions obtained from our high resolution reflectance measurements agree closely with Raman studies; because Raman peaks are narrower than IR reflectance or absorbance peaks and have FWHM values similar to those of the TO modes in the dielectric functions, the TO values presented in this study can be considered more accurate than the lower values previously reported. Spectral artifacts observed by Spitzer et al. (1959b) exist for our samples as well and are consistent with the presence of back reflections from internal surfaces. This deduction is based on the different thicknesses of the internal reflection surfaces in our various samples. In contrast to the Bohren & Huffman (1983) α-SiC data and Spitzer et al. (1959b) data for the 6H-SiC grown surface, we see a new divot in our 6H-SiC spectra. The slope of the spectral profiles in past studies is greater than what we observed for moissanite. The weak oscillator seen in our 6H-SiC data at ν = 970 cm^{-1}, FWHM = 11.0 cm^{-1} and f = 0.001 is real, but its presence barely alters n and k and will not affect RT models.

For $\vec{E}\|\vec{c}$, Spitzer et al. (1959b) observed one weak band near 883 cm^{-1}. We observed a doublet due to use of higher resolution. Their peak parameters of $\nu = 785.9$ cm^{-1}, FWHM = 5.5 cm^{-1}, and f = 3.3 for a single oscillator fit (with a LO mode at 966.9 cm^{-1}) are quite similar to ours and within the experimental uncertainty, given the results for various samples. Their TO positions for both polarizations are low, consistent with the resolution or calibration. We conclude that the best representation of $\vec{E}\|\vec{c}$ for essentially pure α-SiC is the 1 oscillator fit for our 6H gray sample.

There exists precedent in the SiC literature to average spectral parameters from many laboratory studies to obtain TO frequency positions, LO frequency positions or oscillator strengths, and FWHM values for SiC. For example, Mutschke et al. (1999) give the following frequencies, averaged from experimental studies from the 1960's to 1990's (their table 1): (for 3C-SiC) $E_{1T} = A_{1T} = 795.9$ cm^{-1}, $E_{1L} = A_{1L} = 972.3$ cm^{-1}, and (for 6H-SiC) $E_{1T} = 797.0$ cm^{-1}, $A_{1T} = 788.1$ cm^{-1}, $E_{1L} = 969.9$ cm^{-1}, $A_{1L} = 965.3$ cm^{-1}. The frequency positions presented in this work seem at first glance to be farther from values based on Raman measurements (from Hofmann et al. 1994, 3C-SiC: $E_{1T} = A_{1T} = 795.7$ cm^{-1}, $E_{1L} = A_{1L} = 979.0$ cm^{-1}; 6H-SiC: $E_{1T} = 797.0$ cm^{-1}, $A_{1T} = 788.1$ cm^{-1}, $E_{1L} = 969.9$ cm^{-1}, $A_{1L} = 965.3$ cm^{-1}); however, if the data by Spitzer et al. (1959a,b) had been included in the averages, the mean values reported by Mutschke et al. (1999) would be shifted by an amount up to 0.4 cm^{-1}.

We have discussed our data in context with some of the major past laboratory studies and compilations of experimental data on SiC. To determine which spectral parameters are most representative of SiC, we strongly encourage readers to assess individual datasets on a case-by-case basis. This is because a single set of extremely precise data may be as accurate or more so than values obtained by averaging several sets of moderately precise data (McKenna & Hodges, 1988; Kohn & Spear, 1991). Averaging datasets also presumes that all errors in each dataset are random. If, instead, systematic errors arise either in data collection or analysis, then averaging will not provide the true values (e.g. Bevington, 1969). Systematic errors exist in previously published SiC reflectance data, e.g., the differences between the instrumental resolutions of dispersive and FT-IR spectrometers can contribute up to factors of a few cm^{-1} difference in the reported positions of peaks. For these reasons, we discourage readers from directly combining our (or any FT-IR) SiC data with older results.

8.4.2 Differences between β- and α-SiC; implications for 2H

By obtaining reflectivity spectra from different samples and polytypes, we have constrained the peak parameters of the main SiC features and the optical functions below UV frequencies where metal-anion charge transfer exists. Peak parameters for β and $\vec{E}\perp\vec{c}$ of 6H α SiC were virtually indistinguishable (ν = 797.5 cm^{-1}, FWHM = 5–6 cm^{-1}, $f \sim 3.5$). The parameters for $\vec{E}\|\vec{c}$ of 6H α-SiC were also similar but the peaks occurred at slightly lower frequencies. This behavior is consistent with symmetry analysis and Raman data, indicating that peak positions from past IR studies err by several cm^{-1}. Additional weak modes exist (acoustic for β-SiC, zone-folded for 6H α-SiC), but most of these are too weak and broad to affect $n(\lambda)$ and $k(\lambda)$. For samples with impurities (excess C), zone-folded modes near 880 cm^{-1} are relatively strong and sharp. The presence of these modes in $\vec{E}\|\vec{c}$ alters $n(\lambda)$ and $k(\lambda)$ in a minor way by shifting the main peak ν down by < 2 cm^{-1}. Thus, we believe that the 1 oscillator fit should be used for β-SiC or for "pure" SiC. The doublet in α-SiC ($\vec{E}\|\vec{c}$) is real and should be accounted for; we recommend use of a 3 oscillator fit for that or for SiC with carbon excess or stacking anomalies.

The peak parameters for 6H α-SiC can also be used for 2H α-SiC. Symmetry analysis and Raman data indicate that the IR peak parameters for $\vec{E}\perp\vec{c}$ of 2H should be similar to those for 6H, i.e., our data on moissanite represent 2H for $\vec{E}\|\vec{c}$. For $\vec{E}\|\vec{c}$ of 2H α-SiC, a weak mode should occur near 838 cm^{-1} and the strong mode is downshifted in frequency to about 965 cm^{-1}. Although folded modes are not expected near 888 cm^{-1}, a broad feature is seen in this region for 3C SiC. We suggest that 2H α-SiC ($\vec{E}\|\vec{c}$) is represented by the parameters found for the main peak and 838 cm^{-1} mode of 6H SiC, with the broad oscillator near 881 cm^{-1} from β-SiC.

8.4.3 Recommendations for radiative transfer modelers

The purpose of this research is to provide accurate optical data for the polytype of SiC most commonly found in astronomical environments (β-SiC) and the most commonly manufactured SiC polytype (α-SiC), so that we and others may construct improved radiative transfer (RT) models. The advantages to modelers in using this dataset are:

1. We measured β-SiC and α-SiC in all orientations in the same laboratory;
2. We have used the full classical dispersion equations to arrive at $n(\lambda)$ and $k(\lambda)$;
3. Our n and k data are not dependent on grain shape or size.

The electronic files for n and k have been prepared assuming that these will be inputs to the RT code DUSTY (see section 5.5). The original n and k data files we generated contained over 4000 points; we have regridded these data to a smaller number of points as required for DUSTY, maintaining high λ resolution where needed (i.e., where the slope of the data is steep) and using low λ resolution where the slope is shallow or flat. We provide the regridded n and k data electronically; readers may contact the author for the 4000 point high resolution files. If using DUSTY, the default wavelength grid is too coarse and must be altered to provide sufficient spectral resolution at 10–13 μm where SiC has its strong resonance feature. The spectral resolution in this region is 0.005 μm. DUSTY and many other RT models invoke Mie theory to calculate absorption and scattering cross-sections when a user supplies n and k. This implicitly assumes spherical grains. As discussed below, spherical grains are probably inappropriate in most astrophysical environments. Thus, we recommend supplying absorption and scattering coefficients for non-spherical grains calculated from our n and k instead of directly supplying n and k to DUSTY.

The intrinsic shape for circumstellar SiC grains remains unknown. Some recent works have modeled SiC grains as spheres (cf. Gauba & Parthasarathy, 2004; Thompson et al., 2006; Lunttila & Juvela, 2007). Jiang et al. (2005) argue that spheres are adequate for μm- or sub-μm-sized SiC grains at $\lambda > 11$ μm because the broadening of the 11.3 and 21 μm features (expected if one assumes that the grains are a continuous distribution of ellipsoids) is not likely to differ in the Rayleigh regime. Rayleigh scattering suffices when particles are small. However, the strength of the absorption as well as particle size is required to ascertain which scattering regime pertains (Lynch & Mazuk, 1999). Because SiC has high absorption and nearly perfect reflection at peak center and the SiC particle sizes expected in astronomical environments are close to the sizes where Rayleigh scattering no longer applies, other shapes should be considered. It is clear that distributions of more complex shapes (e.g., Continuous Distribution of Ellipsoids, CDE, Bohren & Huffman 1983; Distribution of Hollow Spheres, DHS, Min et al. 2003 ; aggregates, Andersen et al. 2006 and references therein; CDE and DHS grain shape distributions will be discussed in more detail in chapter 9) should be used in rigorous parameter space explorations of SiC grains. Most of the standard non-spherical grain shape distributions give rise to a feature at the relevant wavelength and with the broader observed feature width.

There is no clear consensus on what the grain size distribution for SiC grains should be. We expect SiC grains to deviate from the MRN grain size distribution (i.e., $m_d(a) \propto a^{-q}$, where m_d is the number of grains in the size interval $(a, a + da)$ and $q = 3.5$ $a_{min} = 0.005$ μm and $a_{max} = 0.25$ μm; Mathis et al. 1977), used in works cited in section 8.1 and the default grain size distribution in DUSTY. The MRN distribution is based on UV and visible data and gives no information for IR wavelengths. In addition, SiC dust is generally found in circumstellar, not interstellar, dust; circumstellar dust is known not to be MRN in size or composition. Some previously published n and

k data are based on specific samples and are only relevant to the grain sizes used in the lab experiments which provided the raw data. In both Pègouriè (1988) and Laor & Draine (1993), the data originates from SiC-600 (ground and sedimented) sample from Borghesi et al. (1985). The Borghesi et al. (1985) sample is 99.3% pure 6H α-SiC, with a typical grain size of 0.04μm and a large grain size tail which goes as $\propto a^{-2.1}$ ($a_{max} \sim 0.5$ μm). From the IR spectrum, one infers that the grains are ellipsoidal rather than spherical or irregular (even though the unground grains are clearly irregular in morphology). n and k derived from the Borghesi et al. (1985) data should thus only be applied to the grains in a similar grain size/shape regime. The n and k values presented here offer an advantage over past datasets in that the new values may be used for extended grain size distributions such as MRN or KMH (Kim et al., 1994, this is discussed in further detail in section 9.1.5 below).

Several recent papers have discussed the occurrence of a mid-IR absorption feature in the spectra of a few carbon stars (e.g. Clément et al., 2003, 2005; Speck et al., 2005, 2006; Pitman et al., 2006). Whilst this feature has been attributed to SiC, it tends to occur at a shorter wavelength. Investigating grain size and shape effects with the new optical constants may allow us not only to fit this mid-IR feature, but also to determine what physical parameters differ in the stars that exhibit this absorption feature. In addition, past studies of grain size and shape based on the optical constants of Pègouriè (1988) and Laor & Draine (1993) should be revisited.

8.5 Conclusions

1. Previously reported laboratory reflectivity data are for α-SiC, whereas SiC dust surrounding astronomical objects is β-SiC; the optical functions $n(\lambda)$ and $k(\lambda)$ for these differ slightly. We have provided electronic table values for optical

functions $n(\lambda)$ and $k(\lambda)$ at $\lambda = 0.05$–2000 μm derived via classical dispersion analysis from room temperature, near-normal incidence laboratory specular reflectance spectra of several samples of both 3C (β-) and 6H (α-) SiC. These n and k values are independent of grain size, do not change with scaling of the raw reflectance spectra, and may be used when modeling optically thin conditions.

2. We have investigated whether fitting SiC IR spectra with one or more oscillators makes a difference to n and k. We suggest that a one oscillator fit best represents pure SiC. A three oscillator fit best represents impure SiC (due to carbon excess or layer stacking). β-SiC and α-SiC $\vec{E}\perp\vec{c}$ are best fitted using one oscillator with peak parameters $\nu = 797.5$ cm^{-1}, FWHM $= 4.0$–6.0 cm^{-1}, and $f = 3.5$. Adding a peak at $\nu = 970$ cm^{-1} makes little difference to n and k. For pure α-SiC $\vec{E}\|\vec{c}$, 1 oscillator works well; as impurities increase, 3 oscillators are needed. Strong layering of the sample contributes spectral artifacts to the reflectance spectra of α-SiC when $\vec{E}\|\vec{c}$; thus, the fit parameters for that orientation carry more uncertainty. The main difference between n and k for the different orientations of 6H α-SiC is that the TO peak position for $\vec{E}\|\vec{c}$ is lower than that of $\vec{E}\perp\vec{c}$. Because the fit parameters for 6H α-SiC ($\vec{E}\perp\vec{c}$) are similar to those of β-SiC, this is also the main difference between α-SiC and β-SiC. Peak parameters for the moissanite sample may also be used for meteoritic 2H α-SiC.

3. Peak positions in our SiC reflectance spectra are in agreement with Raman determinations of peak positions for SiC, which should be highly accurate due to the narrow widths, instrument calibrations, and large number of measurements made. Our calculated peak widths and strengths for 6H-SiC are in agreement with published Raman and reflectance studies. Past data for β-SiC were collected from a thin film and give information on the TO mode, but the presence of

the LO mode may affect those results. Differences in peak positions between this and past works are due to calibration, instrumental resolution, or a combination of both effects. Apart from the fact that past n and k datasets were compiled from several studies, older n and k values are not appropriate for dust that is optically thin at all frequencies, nor are these values appropriate for all grain sizes; thus, n and k data from past studies should be used carefully. Comparing and contrasting results of more sophisticated radiative transfer models that use these new n and k values as inputs will allow the community to test competing hypotheses on grain size and shape effects in astronomical environments in future work.

Chapter 9

Size and Shape Dependent Optical Properties

"Software and cathedrals are much the same - first we build them, then we pray." - Samuel Redwine

9.1 Introduction

The previous chapter illustrated how one advantage of the new optical constants is the freedom to set the size and shape of dust particles over a wide range. To exploit this freedom, the size and shape independent complex refractive index must first be converted to the size and shape dependent absorption and scattering efficiencies (for a given size and shape distribution). A program, absscat[1], was developed to calculate these values. Before a discussion of this program can begin, however, it is first necessary to understand the theoretical background behind absorption and scattering that was used to generate the code.

---

[1] The source code for this program may be found in Appendix A starting on page 271.

9.1.1 Theoretical background

The following analysis assumes that the particles under investigation are small compared to the wavelength of the incident light (i.e. the Rayleigh limit). That is, $\frac{2\pi r}{\lambda} = kr \ll 1$, where for non-spherical particles r represents the radius of the sphere of equivalent volume; this will be the convention used for the rest of this chapter. An additional requirement is that $kr|m| \ll 1$, where m is the complex refractive index of the particles. The second requirement comes from the fact that Rayleigh approximations become increasingly inaccurate as $|m|$ increases relative to kr (Kerker et al., 1978; Bohren & Huffman, 1983). Finally, we will only examine smooth particles, the most general form of which is the ellipsoid.[2]

If these criterion are met, it is possible to write the absorption and scattering cross section of an ellipsoid averaged over all orientations as (Bohren & Huffman, 1983)

$$C_{abs} = k\,\mathrm{Im}(\frac{1}{3}P_1 + \frac{1}{3}P_2 + \frac{1}{3}P_3) \tag{9.1}$$

$$C_{sca} = \frac{k^4}{6\pi}(\frac{1}{3}|P_1|^2 + \frac{1}{3}|P_2|^2 + \frac{1}{3}|P_3|^2) \tag{9.2}$$

where P_1, P_2, and P_3 are the polarizabilities of the particle in each orientation. In the case of the isotropic ellipsoids we will be discussing,

$$P_i = 4\pi r^3 \frac{\varepsilon - \varepsilon_m}{3\varepsilon_m + 3L_i(\varepsilon - \varepsilon_m)} \tag{9.3}$$

where ε and ε_m are the complex dielectric functions of the particle and the surrounding medium, respectively. L_i are geometric factors given by

$$L_1 = \frac{abc}{2}\int_0^\infty \frac{dq}{(a^2+q)f(q)} \tag{9.4}$$

---

[2] An ellipsoid is a particle bound by the surface $\frac{x^2}{a^2} + \frac{y^2}{b^2} + \frac{z^2}{c^2}$.

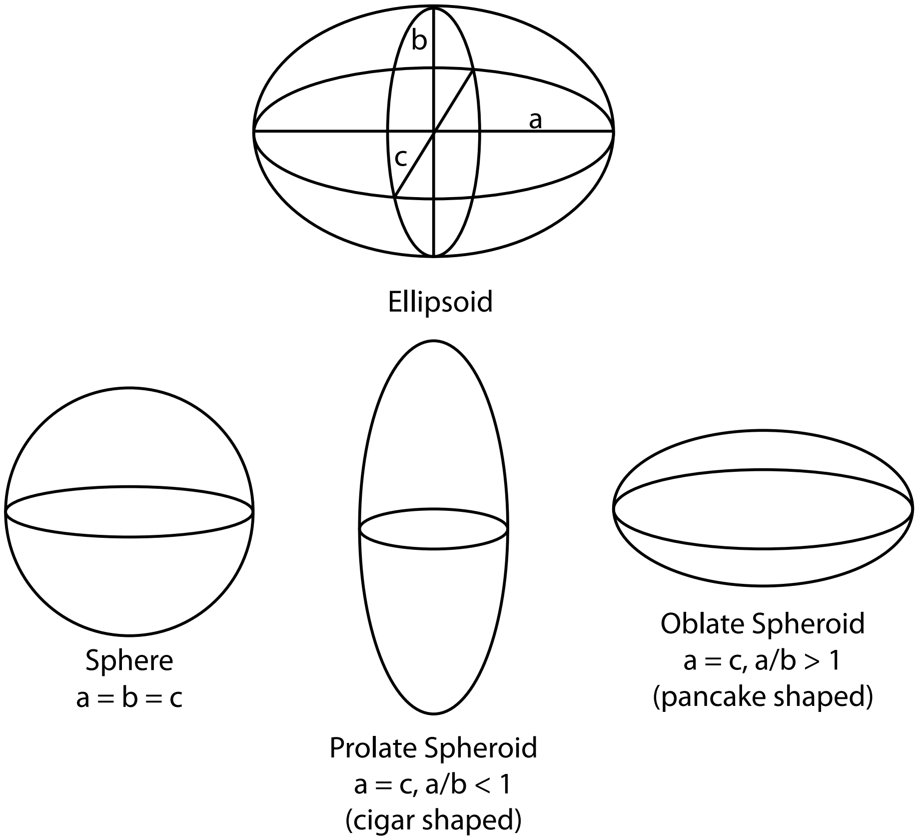

Figure 9.1: Smooth particle shapes

$$L_2 = \frac{abc}{2} \int_0^\infty \frac{dq}{(b^2+q)f(q)} \tag{9.5}$$

$$L_3 = \frac{abc}{2} \int_0^\infty \frac{dq}{(c^2+q)f(q)} \tag{9.6}$$

where $f(q)$ is given by $f(q) = [(q+a^2)(q+b^2)(q+c^2)]^{\frac{1}{2}}$.

If the factor of $4\pi r^3$ in each P_i is removed, and we assume the surrounding medium is vacuum (i.e. $\varepsilon_m = 1$; a reasonable assumption for dust particles in space!) we obtain

$$C_{abs} = kV\,\mathrm{Im}(\alpha_1 + \alpha_2 + \alpha_3) \tag{9.7}$$

$$C_{sca} = \frac{k^4 V^2}{2\pi}(|\alpha_1|^2 + |\alpha_2|^2 + |\alpha_3|^2) \tag{9.8}$$

where

$$\alpha_i = \frac{m^2 - 1}{3 + 3L_i(m^2 - 1)} \tag{9.9}$$

are the polarizabilities of the particle per unit volume, with m as the complex refractive index of the particle, obtained from the relationship $\varepsilon = m^2$. It is at this point that Min et al. (2003) begin their analysis of the absorption and scattering efficiencies for several particle shape distributions; the following discussion will closely follow that work and use identical notation.

9.1.2 Spherical particles

In the case of a homogeneous spherical particle, $a = b = c = r$ which gives us

$$L_1 = L_2 = L_3 = \frac{r^3}{2} \int_0^\infty \frac{dq}{(r^2 + q)^{\frac{5}{2}}} = \frac{r^3}{3(r^2 + q)^{\frac{3}{2}}} \Big|_0^\infty = \frac{1}{3} \tag{9.10}$$

Applying this to (9.9) gives

$$\alpha_1 = \alpha_2 = \alpha_3 = \alpha_{sph} = \frac{m^2 - 1}{m^2 + 2} \tag{9.11}$$

which can then be applied to (9.7) and (9.8) to produce

$$\begin{aligned} C_{abs} &= 3kV \, \mathrm{Im}(\alpha_{sph}) \\ &= 3kV \, \mathrm{Im}\Big(\frac{m^2 - 1}{m^2 + 2}\Big) \end{aligned} \tag{9.12}$$

$$\begin{aligned} C_{sca} &= \frac{3k^4V^2}{2\pi}|\alpha_{sph}|^2 \\ &= \frac{3k^4V^2}{2\pi}\left|\frac{m^2-1}{m^2+2}\right|^2 \end{aligned} \tag{9.13}$$

The remainder of this section deals with distributions of particles, but in the case of spheres a 'distribution' is simply a collection of identical spheres of volume V. The situation where there is a distribution of spheres of varying volume will be considered in 9.1.5.

9.1.3 Distributions of non-spherical particles

For non-spherical particles the situation is more complex, because a distribution of particles of the same volume will be a collection of particles of varying dimensions and therefore different absorption and scattering cross sections. For the absorption cross section, the average value over the distribution can be obtained by averaging the polarizabilities per unit volume, but the non-linear nature of the scattering cross section makes this impossible. However, Min et al. (2003) showed that it is possible to obtain a relationship between the absorption and scattering coefficients that can be used to eliminate this difficulty. First, observe

$$\operatorname{Im}(z) = -|z|^2 \operatorname{Im}(z^{-1}) \quad \forall z \in \mathbb{C} \tag{9.14}$$

Following Min et al., the proof of this is as follows:

Proof.

$$\forall z \in \mathbb{C}, z = |z|e^{i\phi} \Rightarrow z^{-1} = |z^{-1}|e^{-i\phi}. \text{ Thus,}$$

$$\mathrm{Im}(z) = |z|\sin(\phi), \quad \mathrm{Im}(z^{-1}) = -|z^{-1}|sin(\phi)$$

$$\frac{\mathrm{Im}(z)}{|z|} = -\frac{\mathrm{Im}(z^{-1})}{|z|^{-1}}$$

$$\mathrm{Im}(z) = -|z|^2\mathrm{Im}(z^{-1}) \qquad \square$$

Applying this to (9.9) gives

$$\mathrm{Im}(\alpha_i) = -|\alpha_i|^2\,\mathrm{Im}(\alpha_i^{-1}) = -|\alpha_i|\,\mathrm{Im}(\frac{3+3L_i(m^2-1)}{(m^2-1)})$$

$$= -|\alpha_i|^2\cdot\,\mathrm{Im}(\frac{3}{(m^2-1)})\cdot\,\mathrm{Im}(3L_i) \tag{9.15}$$

Because the L_i are real numbers, this becomes

$$\mathrm{Im}(\alpha_i) = -3|\alpha_i|^2\,\mathrm{Im}(\frac{1}{(m^2-1)}) \tag{9.16}$$

Using (9.14) again gives

$$\mathrm{Im}(\frac{1}{(m^2-1)}) = -\Big|\frac{1}{(m^2-1)}\Big|^2\,\mathrm{Im}(m^2-1) = -\frac{\mathrm{Im}(m^2)}{|m^2-1|^2} \tag{9.17}$$

Substituting this into (9.16), we obtain

$$\mathrm{Im}(\alpha_i) = \frac{3|\alpha_i|^2\mathrm{Im}(m^2)}{|m^2-1|^2} \tag{9.18}$$

Rewriting this to get $|\alpha_i|^2$,

$$|\alpha_i|^2 = \frac{|m^2-1|^2\,\mathrm{Im}(\alpha_i)}{3\,\mathrm{Im}(m^2)} \tag{9.19}$$

Now that we have an equation relating $\mathrm{Im}(\alpha_i)$ and $|\alpha_i|^2$, we can substitute it into (9.8)

$$\begin{aligned} C_{sca} &= \frac{k^4V^2}{2\pi}\Big(\frac{|m^2-1|^2\,\mathrm{Im}(\alpha_1)}{3\,\mathrm{Im}(m^2)} + \frac{|m^2-1|^2\,\mathrm{Im}(\alpha_2)}{3\,\mathrm{Im}(m^2)} + \frac{|m^2-1|^2\,\mathrm{Im}(\alpha_3)}{3\,\mathrm{Im}(m^2)}\Big) \\ &= \frac{k^4V^2|m^2-1|}{6\pi\,\mathrm{Im}(m^2)}(\mathrm{Im}(\alpha_1) + \mathrm{Im}(\alpha_2) + \mathrm{Im}(\alpha_3)) \\ &= \frac{k^4V^2|m^2-1|}{6\pi\,\mathrm{Im}(m^2)}\,\mathrm{Im}(\alpha_1+\alpha_2+\alpha_3) \qquad (9.20) \end{aligned}$$

Inspection of this along with (9.7) immediately gives us the final relationship,

$$C_{sca} = \frac{C_{abs}}{\sigma} \qquad (9.21)$$

where

$$\sigma = \frac{6\pi\,\mathrm{Im}(m^2)}{k^3V|m^2-1|^2} \qquad (9.22)$$

using the same notation as Min et al.. Now we are ready to progress to specific distributions of non-spherical particles.

9.1.3.1 Continuous distribution of ellipsoids

If a distribution of ellipsoids contains particles of the same volume, it is possible to normalize the L_i terms in (9.4), (9.5), and (9.6) so that for all the particles

$$L_1 + L_2 + L_3 = 1 \qquad (9.23)$$

This allows us to reduce the number of independent terms to two (setting $L_3 =$

$1 - L_1 - L_2$). With this, we can write the average value of the absorption cross section over a normalized shape probability function $\mathcal{P}(L_1, L_2)$ as (Bohren & Huffman, 1983; Min et al., 2003)

$$\begin{aligned}\langle C_{abs} \rangle &= kV \int_0^1 \mathrm{d}L_1 \int_0^{1-L_1} \mathrm{d}L_2 \, \mathrm{Im}(\alpha_1 + \alpha_2 + \alpha_3) \mathcal{P}(L_1, L_2) \\ &= kV \, \mathrm{Im}(\bar{\alpha}) \qquad (9.24)\end{aligned}$$

where $\bar{\alpha}$ represents the averaged polarizability per unit volume over the distribution $\mathcal{P}$. Because σ is shape independent, from (9.21) we obtain

$$\langle C_{sca} \rangle = \frac{\langle C_{abs} \rangle}{\sigma} \qquad (9.25)$$

If we consider a shape distribution where all possible ellipsoidal shapes with a given volume are equally probable - a continuous distribution of ellipsoids, or CDE - the shape probability function is simply $\mathcal{P} = 2$ (Bohren & Huffman, 1983; Min et al., 2003). It may seem odd that $\mathcal{P} = 2$ instead of 1, particularly as $\mathcal{P}$ is normalized! However, the factor of 2 is in fact a result of that normalization (due to the L_i terms having 2 degrees of freedom). Consider the normalization condition

$$\int_0^1 \mathrm{d}L_1 \int_0^{1-L_1} \mathcal{P}(L_1, L_2) \mathrm{d}L_2 = 1.$$

If we assume a constant $\mathcal{P}$, this becomes

$$1 = \mathcal{P} \int_0^1 \mathrm{d}L_1 \int_0^{1-L_1} \mathrm{d}L_2 = \mathcal{P} \int_0^1 \mathrm{d}L_1 (1 - L_1) = \mathcal{P}(\frac{1}{2})$$

Thus $\mathcal{P} = 2$ in the case of a continuous distribution of ellipsoids.

Using this, we can now determine $\bar{\alpha}$, as the α_i terms are the only ones in (9.24) that are functions of L_1 and L_2

$$\begin{aligned}\bar{\alpha} &= 2\int_0^1 \mathrm{d}L_1 \int_0^{1-L_1} (\alpha_1+\alpha_2+\alpha_3)\mathrm{d}L_2 \qquad (9.26)\\ &= 2\Big(\int_0^1 \mathrm{d}L_1 \int_0^{1-L_1} \alpha_1\,\mathrm{d}L_2 + \int_0^1 \mathrm{d}L_1 \int_0^{1-L_1} \alpha_2\,\mathrm{d}L_2 + \int_0^1 \mathrm{d}L_1 \int_0^{1-L_1} \alpha_3\,\mathrm{d}L_2\Big)\end{aligned}$$

It is most convenient to take each of these terms separately. Starting with the first term, we have

$$\begin{aligned}&\int_0^1 \mathrm{d}L_1 \int_0^{1-L_1} \frac{m^2-1}{3+3L_1(m^2-1)}\mathrm{d}L_2\\ &= \frac{m^2-1}{3}\int_0^1 \mathrm{d}L_1 \int_0^{1-L_1} \frac{1}{1+(m^2-1)L_1}\mathrm{d}L_2\\ &= \frac{m^2-1}{3}\int_0^1 \frac{1-L_1}{1+L_1(m^2-1)}\mathrm{d}L_1\\ &= \frac{m^2-1}{3}\Big(\frac{m^2\ln m^2 - m^2 - 1}{(m^2-1)^2}\Big)\\ &= \frac{m^2\ln m^2}{3(m^2-1)} - \frac{1}{3} \qquad (9.27)\end{aligned}$$

Moving on to the second term, we obtain

$$
\begin{aligned}
&\int_0^1 \mathrm{d}L_1 \int_0^{1-L_1} \Big(\frac{(m^2-1)}{3+3L_2(m^2-1)}\Big)\mathrm{d}L_2 \\
&= \frac{m^2-1}{3}\int_0^1 \mathrm{d}L_1 \int_0^{1-L_1} \frac{1}{1+(m^2-1)L_2}\mathrm{d}L_2 \\
&= \frac{m^2-1}{3}\int_0^1 \frac{\ln\left(m^2-(m^2-1)L_1\right)}{m^2-1}\mathrm{d}L_1 \\
&= \frac{m^2\ln m^2}{3(m^2-1)} - \frac{1}{3} \qquad (9.28)
\end{aligned}
$$

And finally, the third term

$$
\begin{aligned}
&\int_0^1 \mathrm{d}L_1 \int_0^{1-L_1} \Big(\frac{m^2-1}{3+3(1-L_1-L_2)(m^2-1)}\Big)\mathrm{d}L_2 \\
&= \frac{m^2-1}{3}\int_0^1 \mathrm{d}L_1 \int_0^{1-L_1} \frac{1}{(m^2-m^2L_1+L_1)-(m^2-1)L_2}\mathrm{d}L_2 \\
&= \frac{m^2-1}{3}\int_0^1 \frac{\ln\left(m^2-(m^2-1)L_1\right)}{(m^2-1)}\mathrm{d}L_1 \\
&= \frac{m^2\ln m^2}{3(m^2-1)} - \frac{1}{3} \qquad (9.29)
\end{aligned}
$$

And so we can see that in fact all three integrals evaluate to the same expression. Combining these expressions with the additional factor of two in (9.26) gives us

$$
\bar{\alpha} = \frac{2m^2\ln m^2}{m^2-1} - 2 \qquad (9.30)
$$

Precisely the same equation obtained by Min et al.. If we now use this value for $\bar{\alpha}$ to evaluate (9.24) and (9.25), we obtain

$$\begin{aligned}\langle C_{abs}\rangle &= 2kV\,\mathrm{Im}(\frac{m^2\ln m^2}{m^2-1}-1)\\ &= 2kV\,\mathrm{Im}(\frac{m^2\ln m^2}{m^2-1}) \qquad (9.31)\end{aligned}$$

and

$$\langle C_{sca}\rangle = \frac{\langle C_{abs}\rangle}{\sigma} \qquad (9.32)$$

9.1.3.2 Continuous distribution of spheroids

Having considered the most general case where the relationship between the axes of the particles is arbitrary, we now turn to a special case where two of the axes are the same length. This kind of shape is called a spheroid (see Figure 9.1). If we examine (9.4), (9.5), and (9.6) under the condition that $a = c$, it can immediately be seen that $L_1 = L_3 = \frac{1-L_2}{2}$, thus reducing the degrees of freedom of the L_i terms to only one; L_2. Following Min et al., we will therefore simply refer to L, where $L = L_2$.

If we imagine a continuous distribution of such particles, and re-examine (9.24) this time only allowing L a single degree of freedom[3], $\bar{\alpha}$ will be

---

[3] Thus, $\mathcal{P}(L) = 1$

$$
\begin{aligned}
\bar{\alpha} &= \int_0^1 (2\alpha_1 + \alpha_2)\mathrm{d}L \\
&= \frac{m^2-1}{3}\int_0^1 \Big(\frac{2}{1+(m^2-1)(\frac{1-L}{2})} + \frac{1}{1+(m^2-1)L}\Big)\mathrm{d}L \\
&= \frac{m^2-1}{3}\Bigg(\int_0^1 \frac{4}{(m^2+1)-(m^2-1)L}\mathrm{d}L + \int_0^1 \frac{1}{1+(m^2-1)L}\mathrm{d}L\Bigg) \\
&= \frac{m^2-1}{3}\Big(4\frac{\ln(\frac{m^2-1}{2})}{m^2-1} + \frac{\ln m^2}{m^2-1}\Big) \\
&= \frac{4}{3}\ln(\frac{m^2-1}{2}) + \frac{1}{2}\ln m^2 \qquad (9.33)
\end{aligned}
$$

which is again the same result obtained by Min et al.. Substituting this into (9.24) and (9.25), we get

$$\langle C_{abs}\rangle = kV\,\mathrm{Im}(\frac{4}{3}\ln(\frac{m^2-1}{2}) + \frac{1}{2}\ln m^2) \qquad (9.34)$$

and

$$\langle C_{sca}\rangle = \frac{\langle C_{abs}\rangle}{\sigma} \qquad (9.35)$$

9.1.4 Non-homogeneous particles

9.1.4.1 Distribution of hollow spheres

Up to this point we have only considered homogeneous particles, but the presence of 'fluffy' agglomerations of dust grains and their role in light extinction has been a matter of some debate in the literature (for example, Mathis, 1996; Li, 2005). As can be expected, actually calculating the absorption and scattering efficiencies of such agglomerations is much more difficult than the simple homogeneous grains we have previously considered[4]. Fortunately for our purposes, though, it has been shown that the much simpler case of a hollow sphere (that is, a sphere with a centered, spherical void containing vacuum) can give a good approximation to the absorption and scattering properties of agglomerations (at least in the infrared; see Jones, 1988; Iatì et al., 2001; Min et al., 2003). This is very advantageous, because (9.7)[5] reduces to simply

$$C_{abs} = kV\,\mathrm{Im}(3\alpha) \tag{9.36}$$

due to the perfect symmetry of the hollow sphere. Actually calculating α for this case is more complex than the examples we have considered so far, but it has been shown that the α of such a sphere is (van de Hulst, 1957; Min et al., 2003)

$$\alpha = \frac{(m^2-1)(2m^2+1)}{(m^2+2)(2m^2+1) - 2(m^2-1)^2 f} \tag{9.37}$$

where f is the fraction of the sphere's volume containing void.

At this point, we should pause and consider what the volume of such a sphere really represents. In all the previous examples the meaning of volume has been unambiguous, but for a hollow sphere one can speak of both the total volume of the sphere ($\frac{4}{3}\pi r^3$) and the material volume of the sphere (that is, the volume of the matter it contains, $\frac{4}{3}\pi r^3(1-f)$). For our purposes, we will consider volume to refer only to the latter

---

[4] Several workers have examined this problem, though in practice their results are rather too complex to be used here; see for example Borghese et al. (1992, 1994) and the brief discussion in the appendix of Iatì et al. (2001).

[5] This equation is still valid for a non-homogeneous particle; as discussed by Bohren & Huffman (1983), this equation holds for any particle whose dielectric anisotropy can be diagonalized (that is, expressed entirely in terms of separate $\alpha_1, \alpha_2, \alpha_3$), and so certainly in the case of a perfectly isotropic hollow sphere.

meaning; the α given in (9.37) in fact is the polarizability per unit material volume, instead of total volume as we have considered before. If we apply (9.37) to (9.36), we can obtain the scattering cross section of a single hollow sphere, but we wish to examine a collection of such hollow spheres just as we considered distributions of the previous particle shapes. As before, all the particles in our distribution will have the same volume, so the only parameter that can vary over the distribution is f. Thus, in order to calculate the average $\bar{\alpha}$ needed for (9.24) we must perform an integration over all possible values of f

$$\begin{aligned}\bar{\alpha} &= \int_0^1 (3\alpha)\mathrm{d}f \\ &= \frac{6m^2+3}{2m^2-2}\ln\left(\frac{(2m^2+1)(m^2+2)}{9m^2}\right)\end{aligned} \tag{9.38}$$

Unfortunately, as pointed out by Min et al. (2003), we cannot use equation (9.21) to determine the scattering cross section as we did before, because the derivation of the relationship between C_{abs} and C_{sca} depended on the equations for α_i (and thus L_i) which were only valid for homogeneous ellipsoids. Therefore a numerical integration of $|\alpha|^2$ over f will be required; the technique for this will be discussed when we deal with the actual algorithms used in absscat.

9.1.5 Size distributions and cross-sections

So far we have dealt with only distributions of particle shapes, where the particles all have the same material volume. Realistically, however, we would expect the particles to not only vary in shape, but in volume as well, so we wish to extend these results to include the effects of a distribution of particle volumes.

First, in order to simplify notation, we will speak of a particle's 'size' and refer to this size by using the radius r of the equivalent volume sphere discussed earlier. It is important to remember, though, that what is really changing is the material volume of the particles; for the DHS distribution, in particular, the exterior radius of the particles follows a distribution of $r_{ext} = (\frac{3V}{4\pi(1-f)})^{\frac{1}{3}}$, where f is continuous from 0 to 1.

Second, we should consider that what we have derived so far are the absorption and scattering cross sections for our particle distributions, where 'cross section' again refers to the cross sectional area of the volume equivalent sphere. Now that we are going to apply specific distributions of volumes to the particles, it is most convenient to eliminate the cross sectional dependence entirely and obtain the absorption and scattering efficiencies (Q_{abs} and Q_{sca}) of the particle distributions. This will be done by including a factor of $\frac{1}{\pi r^2}$ when we apply the size distributions to our absorption and scattering cross sections.

If we examine equation (9.7), we can see that it is possible to split this equation into three parts; a part that depends on the complex index of refraction of the particles, a part that depends on the volume (and thus the volume equivalent radius) of the particles, and a part that depends on the wavelength, in the following way

$$\begin{aligned} C_{abs} &= (k) \cdot (V) \cdot \mathrm{Im}(\alpha_1 + \alpha_2 + \alpha_3) \\ &= (k) \cdot (\frac{4}{3}\pi r^3) \cdot \mathrm{Im}(\alpha_1 + \alpha_2 + \alpha_3) \\ &= (\frac{4k\pi}{3}) \cdot (r^3) \cdot \mathrm{Im}(\alpha_1 + \alpha_2 + \alpha_3) \qquad (9.39) \end{aligned}$$

and so we can see that it will only be necessary to examine how the r^3 term changes when the size distribution is applied, as none of the other terms depend on the size (the L_i terms in α_i depend only on the shape of the particle, not its volume). This kind of separation is both convenient for the current analysis, and will be convenient later when we apply these equations to the program. We can perform the same analysis on the scattering cross section (9.8)

$$\begin{aligned}C_{sca} &= \frac{k^4V^2}{2\pi}(|\alpha_1|^2 + |\alpha_2|^2 + |\alpha_3|^2)\\ &= (\frac{k^4}{2\pi}) \cdot (\frac{16}{9\pi}r^6) \cdot (|\alpha_1|^2 + |\alpha_2|^2 + |\alpha_3|^2)\\ &= (\frac{8k^4}{3\pi^2}) \cdot (r^6) \cdot (|\alpha_1|^2 + |\alpha_2|^2 + |\alpha_3|^2) \qquad (9.40)\end{aligned}$$

so this time only the r^6 term will be changed when we apply the size distribution.

Now, we must consider specifically how to apply the size distributions. All the distributions we will examine can be expressed by the function $n(r)$, which represents the probability that a randomly chosen particle in the distribution has volume equivalent radius r. Because the total probability over all r must be 1, we are required to normalize the distributions by dividing by a normalization constant

$$C = \int_{r_{min}}^{r_{max}} n(r)\mathrm{d}r \qquad (9.41)$$

If we apply $n(r)$ and the normalization constant to the r-dependent term in equations (9.39) and (9.40), also including the $\frac{1}{2\pi r^2}$ term mentioned earlier to eliminate the cross sectional dependence, we will obtain the general form for the absorption and scattering efficiencies

$$
\begin{aligned}
Q_{abs} &= \frac{(\text{non r terms})}{C} \cdot \int_{r_{min}}^{r_{max}} \frac{r^3}{\pi r^2} n(r) \mathrm{d}r \\
&= \frac{(\text{non r terms})}{C\pi} \int_{r_{min}}^{r_{max}} r n(r) \mathrm{d}r
\end{aligned}
\tag{9.42}
$$

$$
\begin{aligned}
Q_{sca} &= \frac{(\text{non r terms})}{C} \cdot \int_{r_{min}}^{r_{max}} \frac{r^6}{\pi r^2} n(r) \mathrm{d}r \\
&= \frac{(\text{non r terms})}{C\pi} \int_{r_{min}}^{r_{max}} r^4 n(r) \mathrm{d}r
\end{aligned}
\tag{9.43}
$$

9.1.5.1 Single grain size

In this simple case $n(r) = 1$ and $C_{single} = 1$, and no integration is required.

9.1.5.2 MRN

A very commonly used grain size distribution for astronomical purposes was developed by Mathis, Rumpl, & Nordsieck (1977) (hence, it is referred to as the 'MRN' distribution). This distribution takes the form (this distribution and the one which follows were also discussed in section 8.4.3 above)

$$
n(r) \propto r^{-q}\,,\ r_{min} \leq r \leq r_{max} \tag{9.44}
$$

where q is a specified exponential falloff term. The original parameters used in the MRN distribution (for non-graphite grains) were $r_{min} = 0.005\mu$m, $r_{max} = 0.25\mu$m, and $q = 3.5$, but they are often varied depending on the usage. Applying this to equations (9.42) and (9.43), we obtain

$$
\begin{aligned}
Q_{abs} &= \frac{1}{\pi C_{MRN}} \int_{r_{min}}^{r_{max}} r^{-q+1} \mathrm{d}r \\
&= \frac{1}{\pi C_{MRN}(-q+2)} (r_{max}^{(-q+2)} - r_{min}^{(-q+2)})
\end{aligned} \tag{9.45}
$$

$$
\begin{aligned}
Q_{sca} &= \frac{1}{\pi C_{MRN}} \int_{r_{min}}^{r_{max}} r^{-q+4} \mathrm{d}r \\
&= \frac{1}{\pi C_{MRN}(-q+5)} (r_{max}^{(-q+5)} - r_{min}^{(-q+5)})
\end{aligned} \tag{9.46}
$$

where C_{MRN} is a given by

$$
\begin{aligned}
C_{MRN} &= \int_{r_{min}}^{r_{max}} r^{-q} \mathrm{d}r \\
&= \frac{1}{(-q+1)} (r_{max}^{(-q+1)} - r_{min}^{(-q+1)})
\end{aligned} \tag{9.47}
$$

9.1.5.3 KMH

The MRN distribution was later modified by Kim, Martin, & Hendry (1994) (hence, 'KMH' distribution) to include an exponential falloff instead of a maximum grain size. This distribution takes the form

$$
n(r) \propto r^{-q} e^{-r/r_0}\,,\ r_{min} \leq r \tag{9.48}
$$

where r_0 represents the 'falloff' point where the exponential term begins to significantly affect the distribution. If we apply this distribution to (9.42) and (9.43), we get

$$Q_{abs} = \frac{1}{\pi C_{KMH}} \int_{r_{min}}^{\infty} r^{-q+1} e^{-r/r_0} \mathrm{d}r \tag{9.49}$$

$$Q_{sca} = \frac{1}{\pi C_{KMH}} \int_{r_{min}}^{\infty} r^{-q+4} e^{-r/r_0} \mathrm{d}r \tag{9.50}$$

where C_{KMH} is given by

$$C_{KMH} = \int_{r_{min}}^{\infty} r^{-q} e^{-r/r_0} \mathrm{d}r \tag{9.51}$$

Unfortunately, unlike the MRN case, these integrals do not have closed-form solutions for arbitrary values of the parameters (the integration results in the incomplete gamma function). Therefore, it will be necessary to perform numerical integrations in order to evaluate these integrals for practical use.

9.2 Implementation

Now that we have fully derived the absorption and scattering efficiencies for all the cases we wish to examine, we can begin to investigate how to implement these equations into code. We will do so by looking at a program developed by the author, absscat. The source code for this program is available in Appendix A starting on page 271, and is also included in the CD supplement to this text.

9.2.1 Overview of absscat

absscat is written in Java, which is the programming language the author is most familiar with. However, though it may seem like an odd choice for a scientific code, it also has other advantages for this purpose. It is easily expandable and maintainable, and relatively easy to read even for someone not familiar with the language. Additionally, though it is commonly considered to be slow, it has become increasingly more efficient over time and for some high-performance uses it can approach the speed of Fortran (Amedro et al., 2008). It is certainly fast enough for the kind of calculations presented here.

The general usage of absscat is as follows. The user supplies a configuration file which contains a list of data files, containing the n and k data for any number of grain species (the same data file can be use repeatedly if different configurations of grains with the same n and k values are desired in a single ensemble of grains). For each of these files, the configuration file also contains details about the parameters of the desired grains; the grain shape distribution, size distribution, and the parameters of the size distribution. A weighting factor is also supplied which allows multiple different kinds of grains to be combined (for example, one could have 10% of one kind of grain, and 90% of another). Additionally, if desired, the data files can be interpolated to a supplied wavelength grid. This allows data files based on differing wavelength grids to be combined, but it also allows the output to be tuned to whatever is optimum for the desired purpose of the absorption and scattering efficiencies. Example configuration files can be found in section A.2.2 of the appendix and the CD supplement.

When called, absscat requires a command line argument (-inputfile) which specifies which file it should look at for the configuration information. There are several other command line arguments available; information about the others is available in the readme file given in section A.2.1 of the appendix or on the CD. absscat will then input the configuration file using the methods found in the FileInput class, and parse the file for the configuration parameters using the Parser class. Once the file is parsed, absscat then begins to open (again using FileInput) the specified n and k data files for each set in the configuration file; these files are then parsed by Parser and the data is stored in arrays for further processing.

If interpolation has been requested in the configuration file, absscat then opens the supplied wavelength grid, and performs a linear interpolation to match the data sets to that grid (and also a linear extrapolation if the wavelength grid extends beyond some part of a data set).

The calculations are then straightforward (except for the numerical integration, which we will examine below), but because Java contains no native methods to manipulate complex numbers it was necessary to create a new class, Complex, that could handle the required operations on complex numbers. The equations themselves are implemented in the Calculations class, which calls on the SizeIntegrator class to handle the r-dependent parts of the equations. As seen in section 9.1.5, the 'integration' involved for everything except the KMH size distribution is simply the evaluation of an equation, but for the KMH distribution SizeIntegrator calls on the IterativeSimpsons class to perform the required numerical integrations (see section 9.2.1.1 below). Additionally, for the DHS distribution's scattering efficiency, Calculations directly calls on the IterativeSimpsons class to perform the numerical integration. After all the calculations are complete, absscat uses the FileOutput class to write the absorption and scattering efficiencies to a file, and then exits.

9.2.1.1 Numerical integration

An adaptive Simpson's method was chosen for the technique of numerical integration; though there are more complicated methods which are more efficient, it has the double benefit of being conceptually easy to understand and also easy to code. Any adaptive Simpson's method starts from Simpson's Rule, which states (derivations can be found in many sources; one example is Thomas & Finney (1996))

$$\int_a^b f(x)\mathrm{d}x \approx \frac{b-a}{6}\big(f(a) + 4f\Big(\frac{a+b}{2}\Big) + f(b)\big) \tag{9.52}$$

where the error in the approximation is given by

$$|E| \leq \frac{(b-a)^5}{2880}M \tag{9.53}$$

with M as an upper bound for $|f^4|$ over $[a,b]$.

Inspection of this error term immediately shows that the error in approximation very rapidly decreases as the interval between a and b decreases, and so Simpson's method gives improved results by subdividing the integral at the midpoint between a and b. In other words, since

$$\int_a^b f(x)\mathrm{d}x = \int_a^{\frac{a+b}{2}} f(x)\mathrm{d}x + \int_{\frac{a+b}{2}}^b f(x)\mathrm{d}x \tag{9.54}$$

one can obtain an improved result by using Simpson's Rule twice over the interval (once for each of the integrals on the right hand side of equation (9.54)) instead of once over the interval. This process of subdivision can be continued as deeply as desired. It is possible to write an algorithm that will subdivide an integral in this way and repeatedly apply Simpson's Rule to each subdivision until the error bound is met, but in practice this is inefficient because some areas of the function may need a finer degree of subdivision than other areas, and applying the finest subdivision to the entire function can lead to many unneeded evaluations. Instead, it is better to produce a routine that can adaptively change the degree of subdivision to different areas of the integral based on how well that area is converging, and such a routine is called an adaptive Simpson's method.

The general way an adaptive Simpson's method works is as follows (this derivation also can be found in many sources; one example is Mathews & Fink (1999)). Simpson's Rule (denoted by S in the rest of this discussion) is first used over the entire interval, and then the interval is split in half (as in (9.54)) and Simpson's Rule is applied to each of those subintervals. The result of Simpson's Rule over the full interval is then compared to the sum of the results of Simpson's Rule over the subintervals, and evaluated according to the criterion

$$\left|S\big(a, \frac{a+b}{2}\big) + S\big(\frac{a+b}{2}, b\big) - S(a,b)\right| \leq \frac{\epsilon}{15} \tag{9.55}$$

where ϵ is the desired error bound for the integration. If the inequality is met, then the method has completed and the approximation to the integration is given by

$$\int_a^b f(x)\mathrm{d}x \approx S\big(a, \frac{a+b}{2}\big) + S\big(\frac{a+b}{2}, b\big) + \frac{\left|S\big(a, \frac{a+b}{2}\big) + S\big(\frac{a+b}{2}, b\big) - S(a,b)\right|}{15} \tag{9.56}$$

If it is not met, then the method continues by treating each of the subdivisions $(a, \frac{a+b}{2})$ and $(\frac{a+b}{2}, b)$ as a full interval, and then repeating the process in (9.55) and (9.56). The only difference is that the error bound for the two new inequalities is now given by $\frac{\epsilon}{30}$, because the eventual summation must have combined error under $\frac{\epsilon}{15}$ (and the error bound for each new subinterval gets divided by 2 every time an interval is split, for the same reason). This process repeats until a set of subdivisions meets the inequality in (9.55), at which point the approximate value over that subdivision is obtained using (9.56), and the value is added to the total value of the integral over the entire interval. Then any parts of the interval that have not yet met the inequality are processed.

This method has the advantage that any particular subinterval is only processed long enough to meet the inequality in (9.55); some subintervals may very rapidly satisfy the inequality, while others take more subintervals, but in all cases only the minimum number of subintervals needed to meet the error bound are used.

This is the basic theory; the exact details of how this method was implemented in absscat can be seen in the source code for IterativeSimpsons, located in section A.1.9 starting on page 359 of the appendix, but it is useful to examine the outline of the algorithm here. First, the program makes a stack in which it will store each subsection of the interval as it subdivides; each element in the stack consists of the beginning and endpoint of the subdivision, the result of Simpson's Rule as applied to this interval (which would have been calculated in the previous step of the algorithm), and the error bound to be used to evaluate the inequality in (9.55) (recall that the error bound is divided by a factor of two each time an interval is subdivided). As the algorithm progresses, when it subdivides an interval each of those subintervals is added to the stack (this is referred to as 'pushing' an element onto the stack), and every time it loops it removes the topmost element from the stack for evaluation against (9.55) (removing an element from a stack is referred to as 'popping' that element). This process continues until all the needed subdivisions have been calculated, which results in the stack becoming empty and the algorithm ends. More formally,

Algorithm 1 Adaptive Simpson's method using iteration

```
$T \leftarrow 0$
$PUSH(a, b, S(a, b), \epsilon)$
while $POP(MIN, MAX, S_{OLD}, \epsilon_{OLD})$ do
    $MID \leftarrow (MAX + MIN)/2$
    $LEFT \leftarrow S(MIN, MID)$
    $RIGHT \leftarrow S(MID, MAX)$
    $DIFFERENCE \leftarrow LEFT + RIGHT - S_{OLD}$
    if $|DIFFERENCE| < \epsilon_{OLD}/15$ then
        $T \leftarrow LEFT + RIGHT + (DIFFERENCE)/15$
    else
        $PUSH(MIN, MID, LEFT, \epsilon_{OLD}/2)$
        $PUSH(MID, MAX, RIGHT, \epsilon_{OLD}/2)$
    end if
end while
return $T$
```

9.3 Application to newly derived SiC optical properties

In order to more fully investigate the optical properties of SiC discussed in 8, absscat was used to generate the absorption and scattering efficiencies for each of the sets of new optical constants (α-SiC and β-SiC) and for one set of older optical constants (the SiC constants generated by Pègouriè (1988)). Because of the way the Pégourié data was obtained (as discussed in Chapter 8), it is not really appropriate to obtain the absorption and scattering efficiencies using shape and size distributions different than the size and shape distribution found in the original sample (which is not available). However, as long as we keep that in mind, it is useful to apply the shape and size distributions we derived to this data set, both because it provides an illustrative example which can be compared to the α and β-SiC data, and also because the Pégourié data is often wrongly treated as being size and shape independent (and thus appropriate for this kind of analysis).

For each of these sets of optical constants, absorption and scattering efficiencies were obtained for all four of the shape distributions discussed in 9.1.1. The three size distributions discussed in 9.1.5 were applied to each of these shape distributions, resulting in twelve sets of absorption and scattering data for each optical constant set. The parameters used for the size distributions are given in table 9.1.

Distribution	Parameters
Single	$r = 0.1\mu$m
MRN	$r_{min} = 0.005\mu$m, $r_{max} = 0.25\mu$m, $q = 3.5$
KMH	$r_{min} = 0.005\mu$m, $r_0 = 0.25\mu$m, $q = 3.5$

Table 9.1: The grain size distribution parameters used to investigate the newly derived SiC optical properties.

Radiative transfer models were then produced using these absorption and scattering efficiencies; the parameters used for those models and the models themselves may be found in section 9.3.2 below.

9.3.1 Absorption and scattering efficiencies of SiC

The absorption and scattering efficiencies generated by absscat are presented in the following figures. For each set of newly derived SiC optical constants, there is one figure for each grain size distribution, containing the four grain shape distributions discussed in 9.1.1. Additionally, the absorption and scattering efficiencies calculated for the SiC optical properties presented by Pègourié (1988) that correspond to the grain size distribution for a paticular figure are also presented on that figure for comparison.

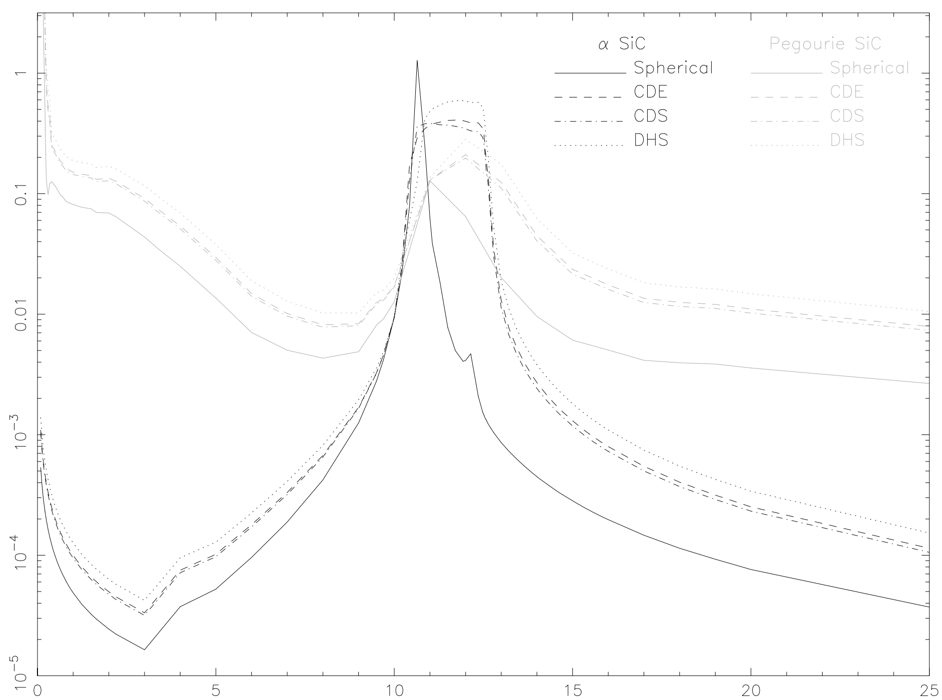

(a) Absorption efficiencies

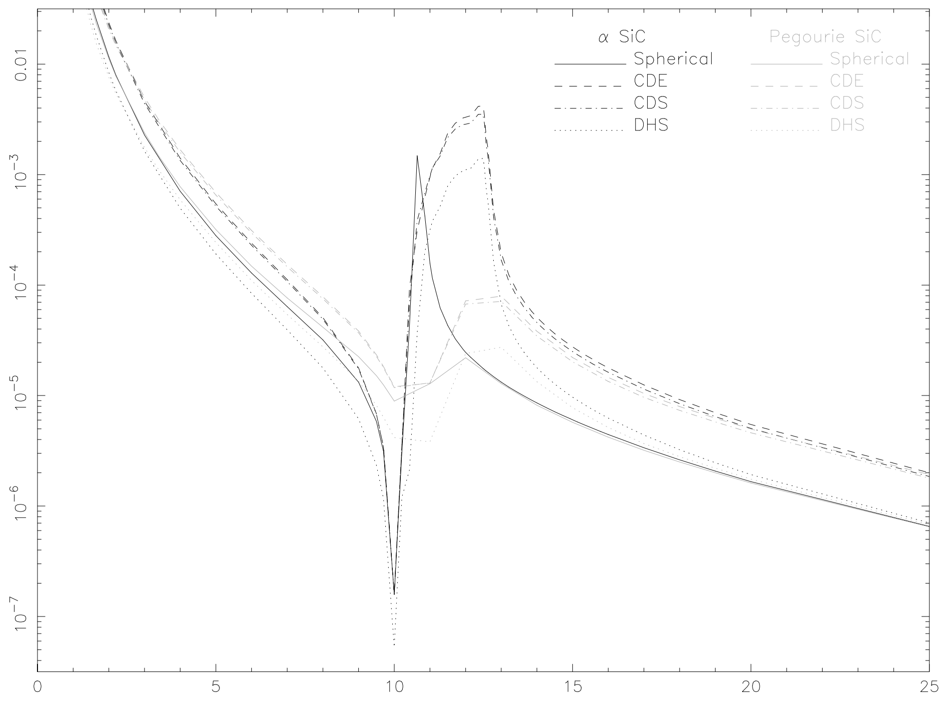

(b) Scattering efficiencies

Figure 9.2: Absorption and scattering efficiencies of α-SiC compared to Pegourie SiC, 0.1 μm single size grains; the x-axis is wavelength in μm, the y-axis is the logarithm of the absorption or scattering efficiency.

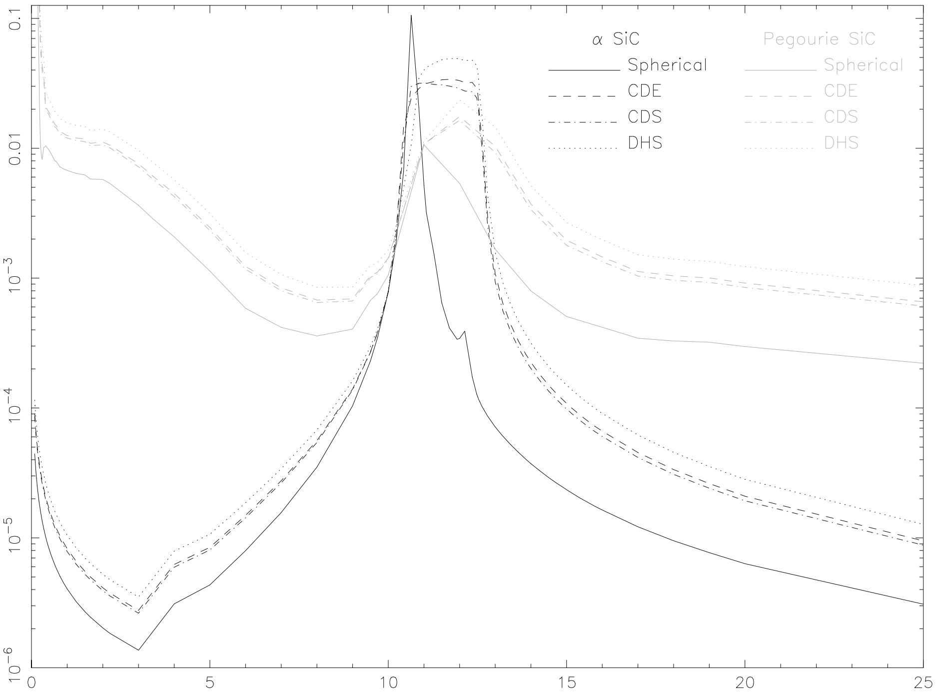

(a) Absorption efficiencies

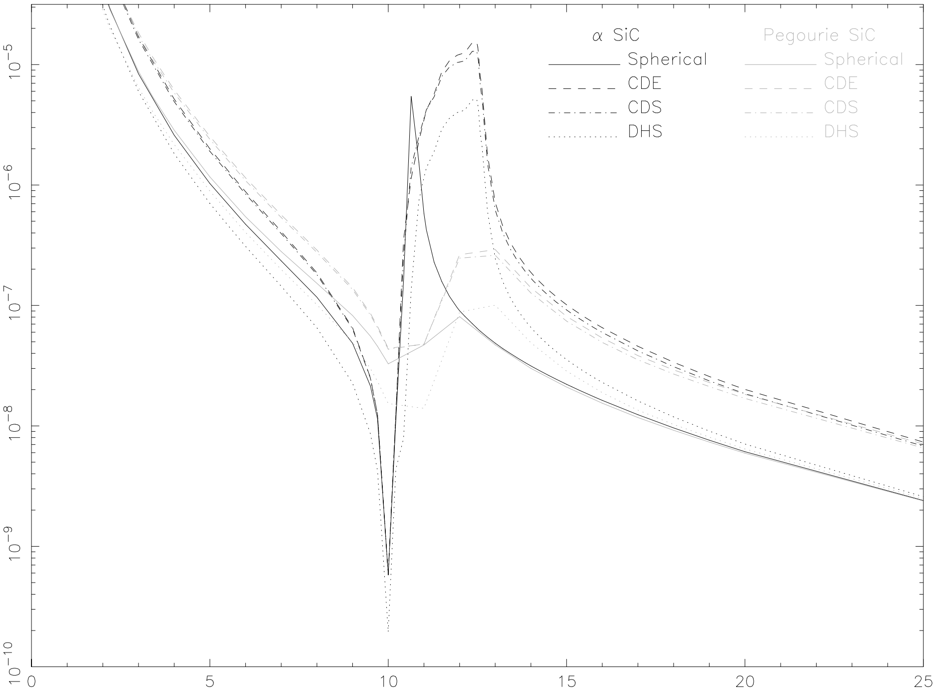

(b) Scattering efficiencies

Figure 9.3: Absorption and scattering efficiencies of α-SiC compared to Pegourie SiC, MRN grain size distribution; the x-axis is wavelength in μm, the y-axis is the logarithm of the absorption or scattering efficiency.

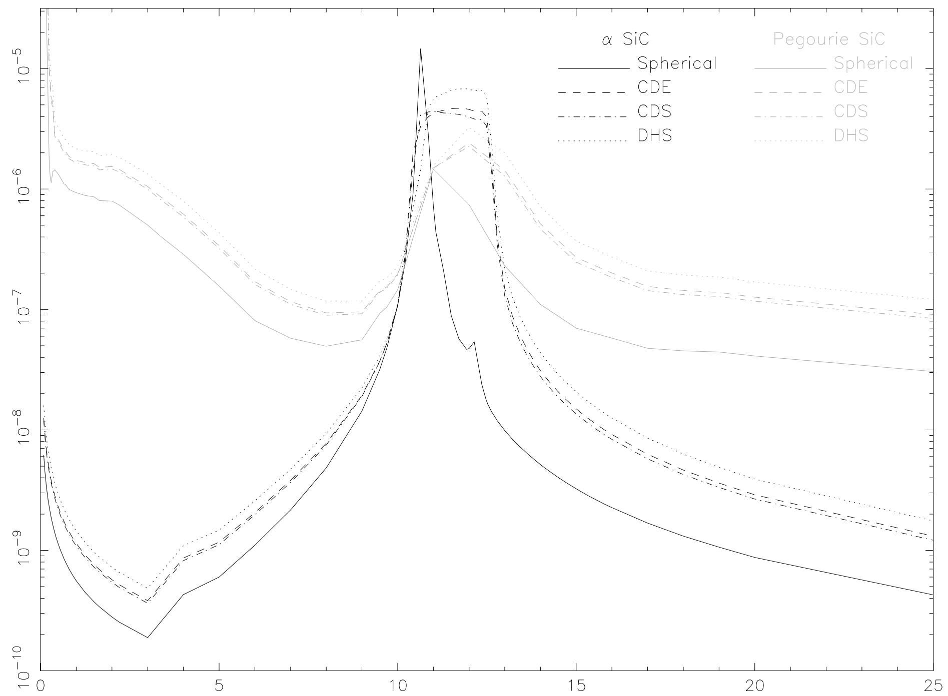

(a) Absorption efficiencies

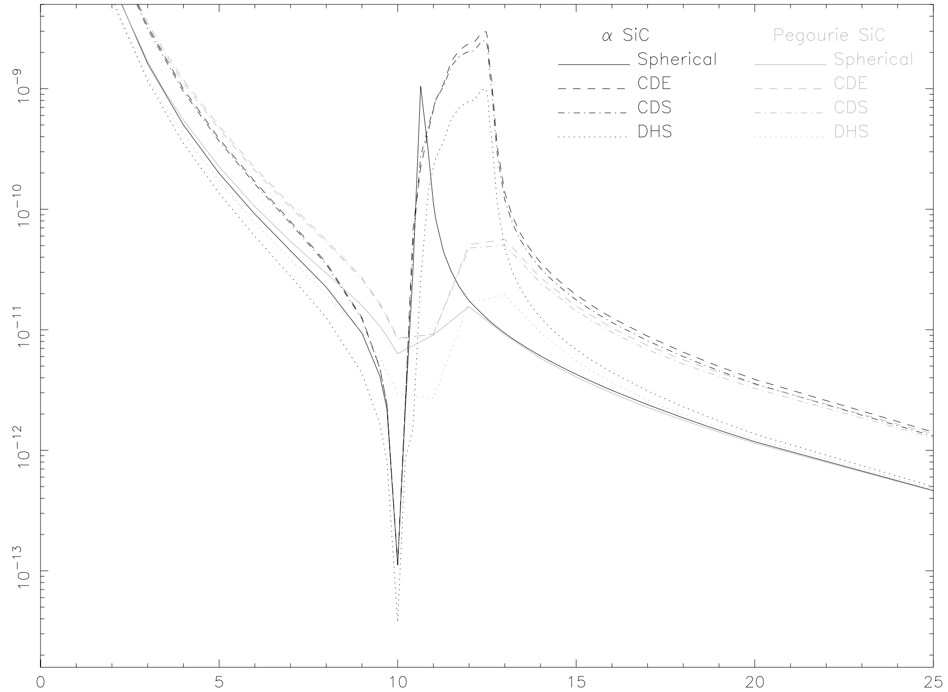

(b) Scattering efficiencies

Figure 9.4: Absorption and scattering efficiencies of α-SiC compared to Pegourie SiC, KMH grain size distribution; the x-axis is wavelength in μm, the y-axis is the logarithm of the absorption or scattering efficiency.

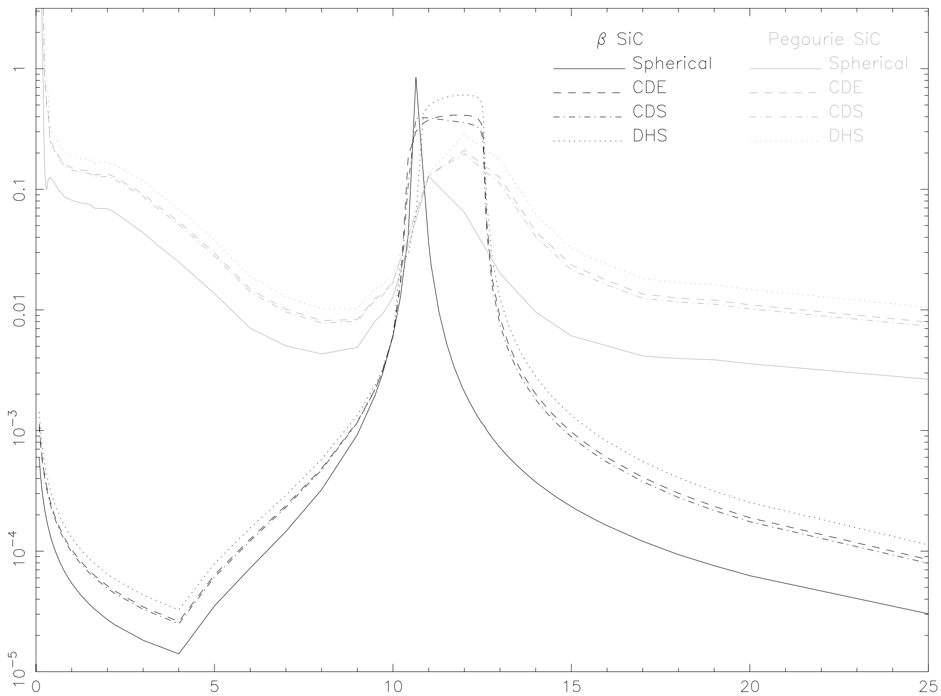

(a) Absorption efficiencies

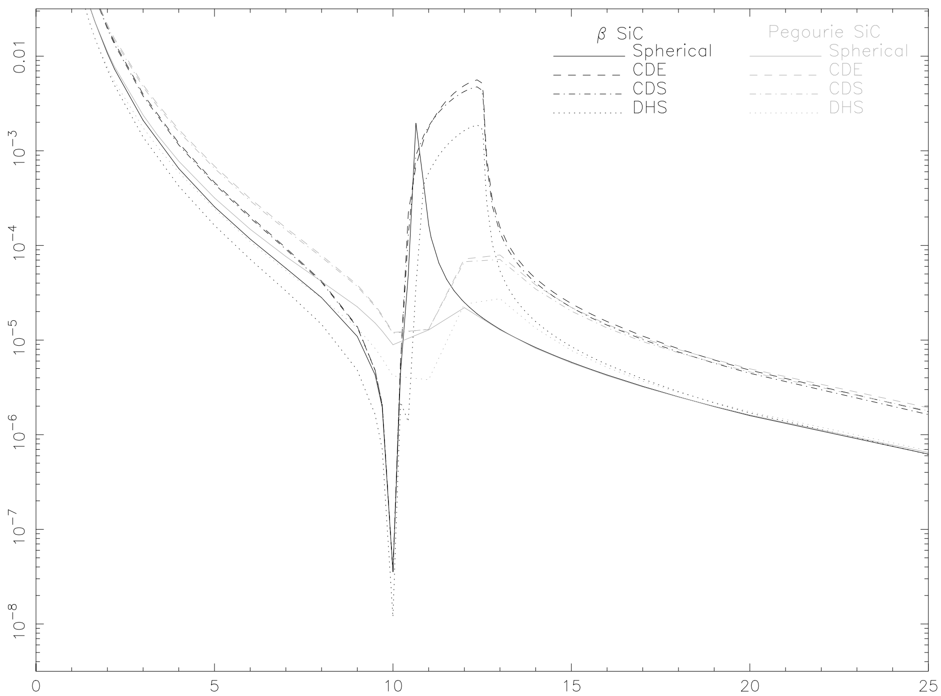

(b) Scattering efficiencies

Figure 9.5: Absorption and scattering efficiencies of β-SiC compared to Pegourie SiC, 0.1 μm single size grains; the x-axis is wavelength in μm, the y-axis is the logarithm of the absorption or scattering efficiency.

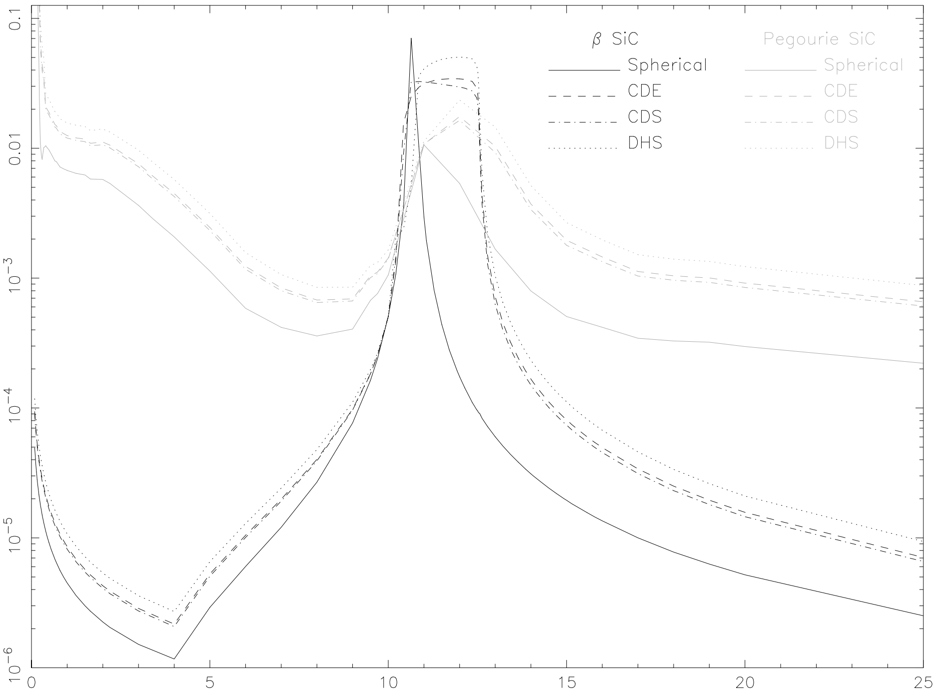

(a) Absorption efficiencies

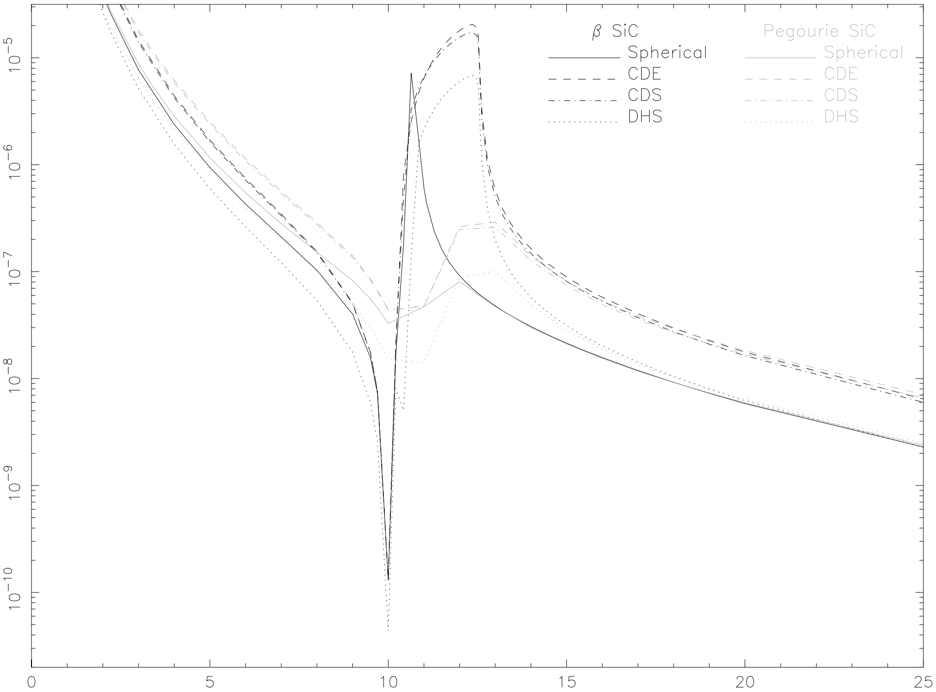

(b) Scattering efficiencies

Figure 9.6: Absorption and scattering efficiencies of β-SiC compared to Pegourie SiC, MRN grain size distribution; the x-axis is wavelength in μm, the y-axis is the logarithm of the absorption or scattering efficiency.

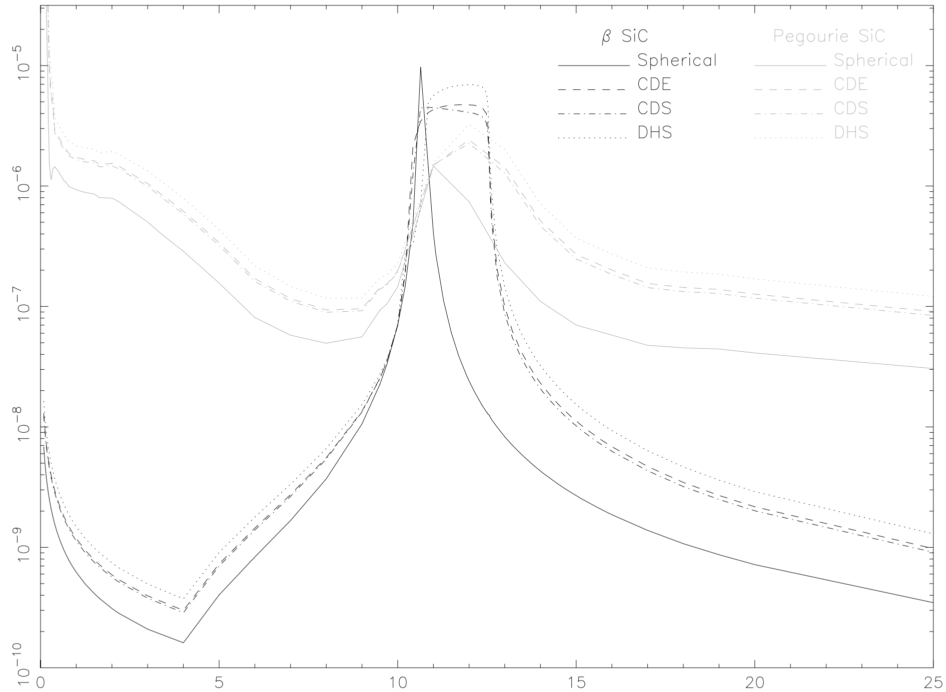

(a) Absorption efficiencies

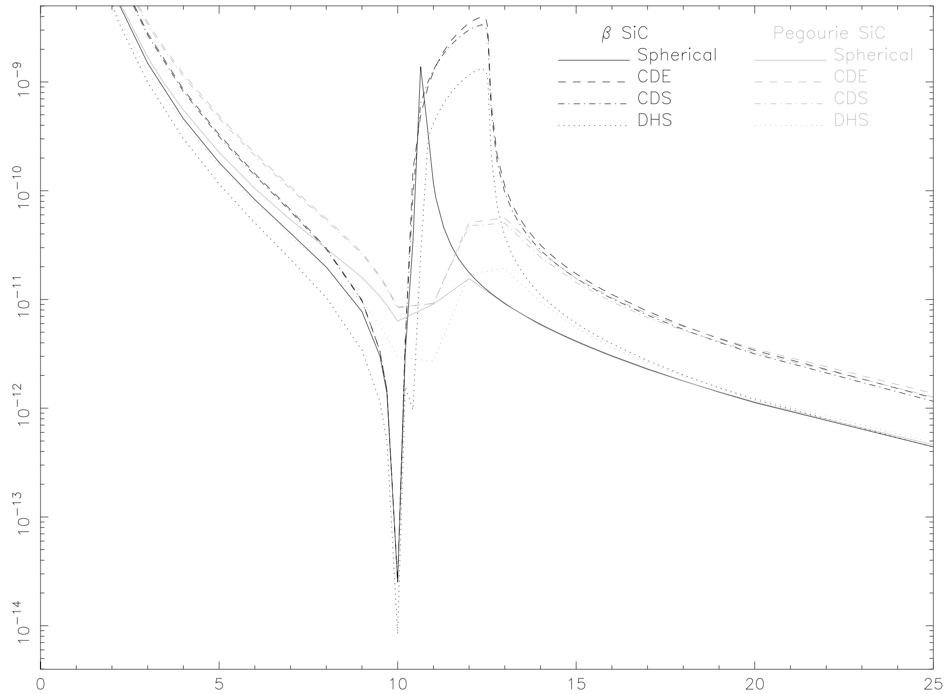

(b) Scattering efficiencies

Figure 9.7: Absorption and scattering efficiencies of β-SiC compared to Pegourie SiC, KMH grain size distribution; the x-axis is wavelength in μm, the y-axis is the logarithm of the absorption or scattering efficiency.

9.3.1.1 Discussion

An examination of these figures immediately shows that spherical grains have absorption and scattering efficiencies quite different than the other grain shape distributions (though the effect is less pronounced for the Pégourié data). For both the absorption and scattering efficiencies, the spherical grains produce a sharp peak, where the other grain shape distributions produce a broader feature. Additionally, the center of the feature is at a longer wavelength for the non-spherical grains; the peak produced by the spherical grains is at the short-wavelength end of the broader feature. Finally, in the case of α-SiC, a smaller peak is present at about 12 μm in the case of spherical grains, but not in the other grain shape distributions (this small feature is not present in the β-SiC or the Pégourié data for any grain shape distribution).

We can explain the difference between the homogeneous spheres and the other shape distributions by considering that a perfect mathematical sphere should be expected to have strong resonances due to the symmetry. In addition, since all orientations of a sphere are absolutely identical, there is no possibility that one orientation could produce a spectral feature that another orientation did not (which would 'dilute' that feature, making it less intense, and possibly shift the peak wavelength of that feature as well). This is not the case with the other shape distributions. If we think of a single grain, we would expect that due to the anisotropy of the elliptical shape (we will consider hollow spheres in a moment) the main spectral feature would shift in position and intensity depending on how the grain was orientated relative to the incident light. To put it another way, the anisotropy in the dielectric function of the grain depends on the way it is oriented. This dependence would grow larger as the grain shape became less spherical, and smaller the closer its shape was to that of a sphere. Returning to a collection of ellipsoids, we have shapes ranging from nearly spherical (and thus having absorption and scattering efficiencies close to that of perfect spheres) to extreme elliptical shapes, and the absorption and scattering efficiencies of the collection would be a mixture of all of the individual absorption and scattering efficiencies. The individual resonances of the particles thus tend to get 'smeared out' when large numbers of them are combined. In fact, Min et al. (2003) was able to show that as increasingly elliptical shapes are added to a collection of particles, the central peak of the absorption cross section of a Lorentz oscillator (in this case, based on a model fit to fosterite [Mg_2SiO_4]) broadens and shifts towards longer wavelengths, which is precisely what we see for all our sets of SiC data. Though hollow spheres are isotropic, the inner void will certainly change the resonance of the particle; because the distribution of hollow spheres contains spheres with everything from tiny voids to ones nearly filling the sphere, we can expect this same sort of 'smearing' to occur.

In order to understand the small peak around 12 μm, it is necessary to examine the different orientations of the α-SiC separately (recall from Chapter 8 that the overall optical properties of a large collection of randomly oriented α-SiC grains is a weighted average of $\frac{(2\perp+\|)}{3}$). If we calculate the absorption efficiencies for the two orientations separately, as in Figure 9.8,

we can see that the small feature is a result of a resonance in the parallel orientation of the crystal. This actually provides a good example of the 'smearing' effect mentioned previously, because the mixture of parallel and perpendicular orientations diminishes the intensity of the small feature (and also some other structure in the parallel orientation between the small peak and the main peak, which is nearly completely eliminated).

Additionally, the figures show that the absorption and scattering efficiencies for the three kinds of non-spherical particles investigated here are quite similar in the infrared (this property of non-spherical grains was also noted by Min et al. (2003), though that conclusion was drawn from an examination of the absorption and scattering cross-

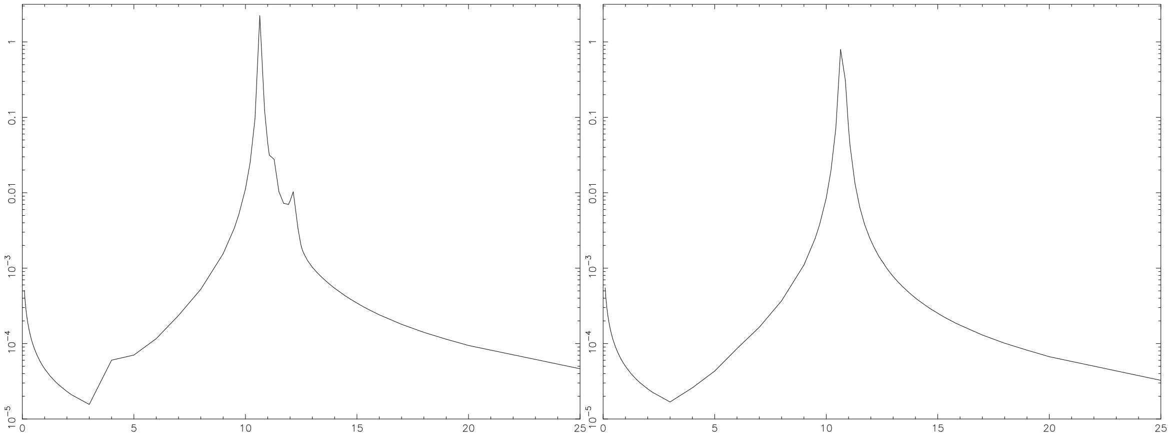

(a) Parallel orientation (b) Perpendicular orientation

Figure 9.8: Comparison of the absorption efficiencies of the parallel and perpendicular orientations of α-SiC. x-axis is wavelength in μm, y-axis is the logarithm of the absorption efficiency.

sections of fosterite). On one hand, this means that, at least in the infrared, any of these grain shape distributions is equally good (or bad) at modeling a particular distribution of grain shapes present in an astrophysical environment; on the other hand, however, it also means that the observed infrared spectra of dust grains alone doesn't provide enough information by which one can distinguish the actual shape distribution of astronomical grains, unless the grains are mostly spherical. Min et al. (2003) also points out though that this provides a strong justification for using the artificial distributions we have derived to model actual astrophysical grains, because if these different distributions all have quite similar absorption and scattering efficiencies, then it is reasonable to assume this approximates the actual irregular grain shapes we expect to see in space.

It is also interesting to look at the difference between the absorption and scattering efficiencies of α and β-SiC compared to those of the Pégourié data. First, as previously noted, the difference between spherical and non-spherical grains is less in the Pégourié data. This is not unexpected, because as discussed in Chapter 8 the sample used to obtain the Pégourié data was composed of particles of many different shapes and thus the 'smearing out' effect of non-spherical shapes would, to some extent, have already been included in the complex refractive index before the absorption and scattering efficiencies were calculated. Second, and more importantly, much finer structure is present in α and β-SiC. We will discuss this more fully when we examine synthetic spectra produced by these grains below (9.3.2.1), as the finer structure carries over to those spectra.

9.3.2 Radiative transfer modeling using shape and size dependent optical properties of SiC

DUSTY (previously discussed in 5.5) was used to produce synthetic spectra of dust shells containing SiC dust grains, using the absorption and scattering efficiencies produced in 9.3.1. The parameter space investigated for the models shown here can be found in 9.2.

Parameter	Value(s)
Star Temperature	3000 K
Inner Dust Shell Temperature	1000 K
Shell Relative Thickness (SRT)	10 and 1000 times the inner radius
Optical Depth at 10 μm	0.1 and 10

Table 9.2: The parameter space investigated by radiative transfer models using the generated absorption and scattering efficiencies.

Synthetic spectra were produced for each of the sets of absorption and scattering efficiencies located in 9.3.1; when combined with the parameter space investigated, a total of 68 models were generated. Therefore, only the models using the MRN grain size distribution and with 10 times the inner radius thickness will be presented here; all the essential properties we wish to examine are present in this subset of the models.

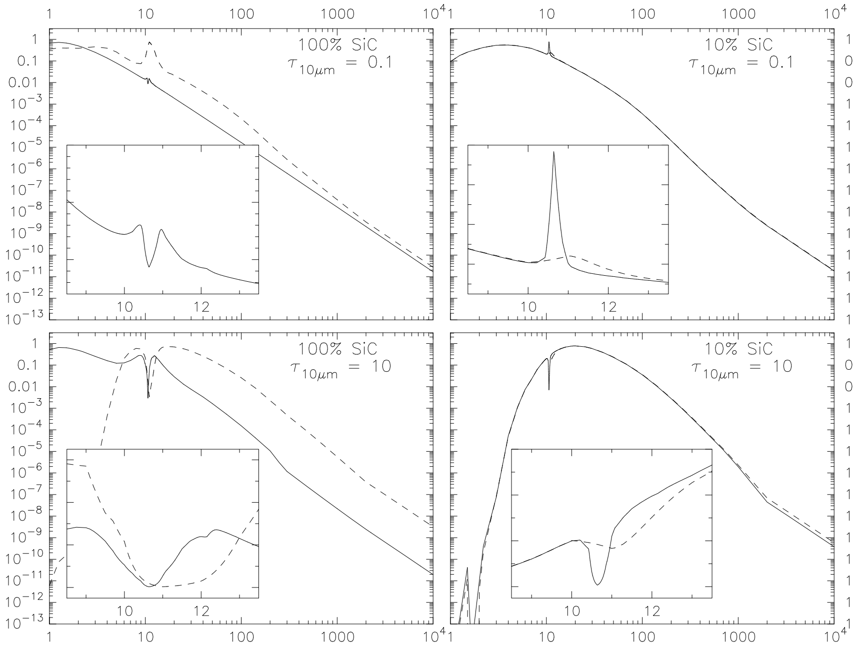

(a) Spherical grains.

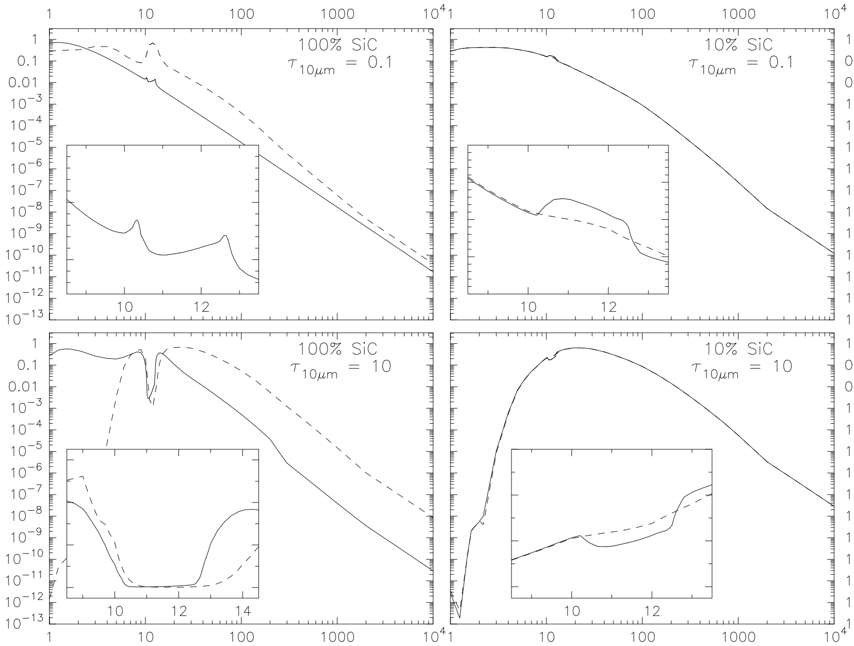

(b) CDE grain shape distribution.

Figure 9.9: Synthetic spectra generated using new α-SiC vs. Pégourié SiC, spherical and CDE grain shapes. Each large plot is log-log, with wavelength in μm on the x-axis and flux on the y-axis. The smaller insets are the same data as their respective large plots, but both axes are linear and the wavelength range is restricted from 8.5 μm to 13.5 μm. The upper left inset does not show the Pégourié spectrum, as it is much too large to fit into the smaller range. All spectra were generated using a MRN grain size distribution.

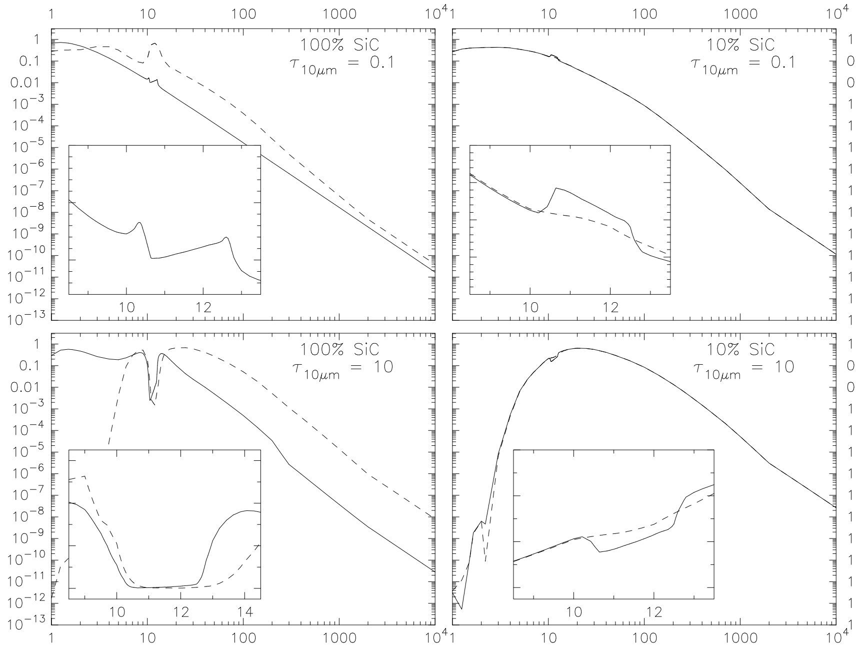

(a) CDS grain shape distribution.

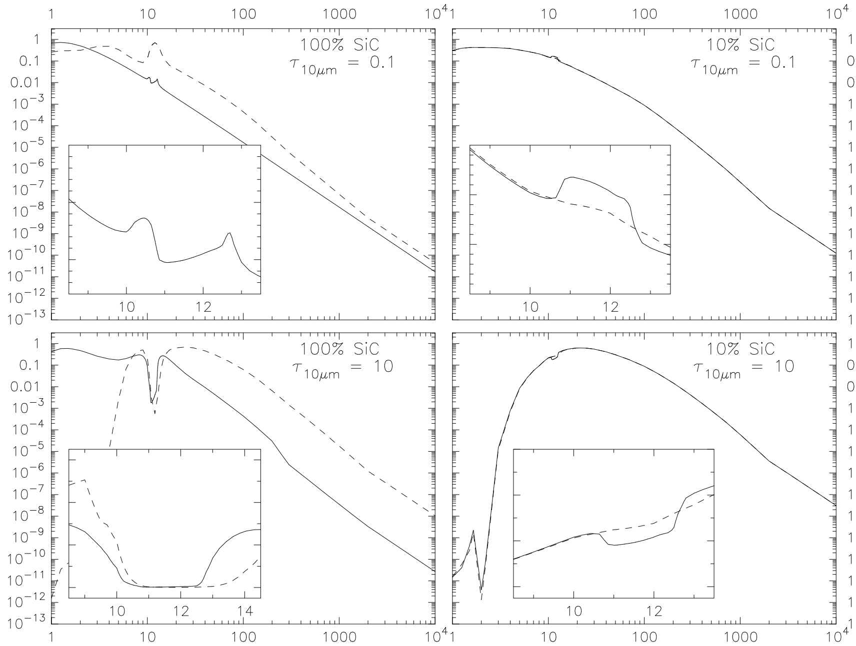

(b) DHS grain shape distribution.

Figure 9.10: Synthetic spectra generated using new α-SiC vs. Pégourié SiC, CDS and DHS grain shapes. Each large plot is log-log, with wavelength in μm on the x-axis and flux on the y-axis. The smaller insets are the same data as their respective large plots, but both axes are linear and the wavelength range is restricted from 8.5 μm to 13.5 μm. The upper left inset does not show the Pégourié spectrum, as it is much too large to fit into the smaller range. All spectra were generated using a MRN grain size distribution.

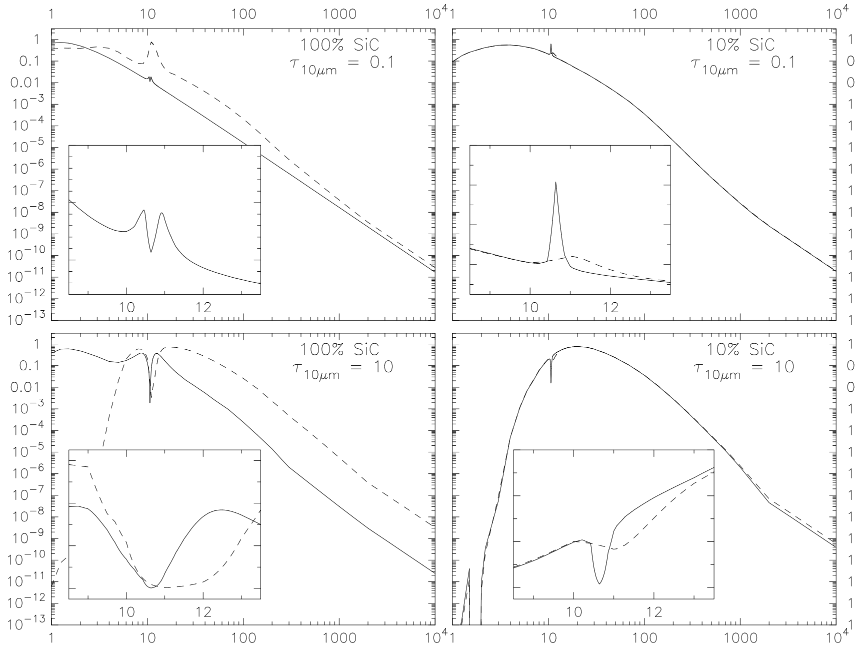

(a) Spherical grains.

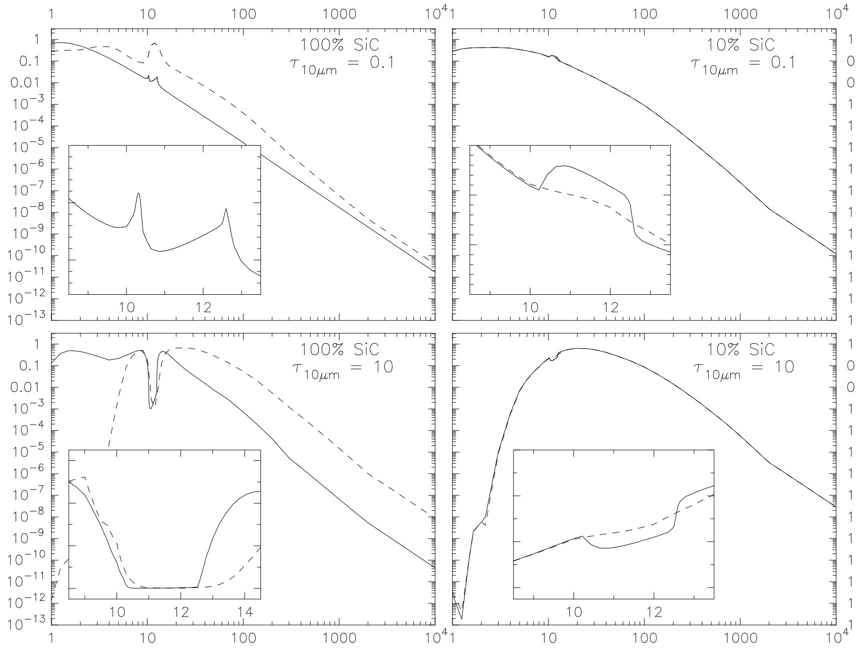

(b) CDE grain shape distribution.

Figure 9.11: Synthetic spectra generated using new β-SiC vs. Pégourié SiC, spherical and CDE grain shapes. Each large plot is log-log, with wavelength in μm on the x-axis and flux on the y-axis. The smaller insets are the same data as their respective large plots, but both axes are linear and the wavelength range is restricted from 8.5 μm to 13.5 μm. The upper left inset does not show the Pégourié spectrum, as it is much too large to fit into the smaller range. All spectra were generated using a MRN grain size distribution.

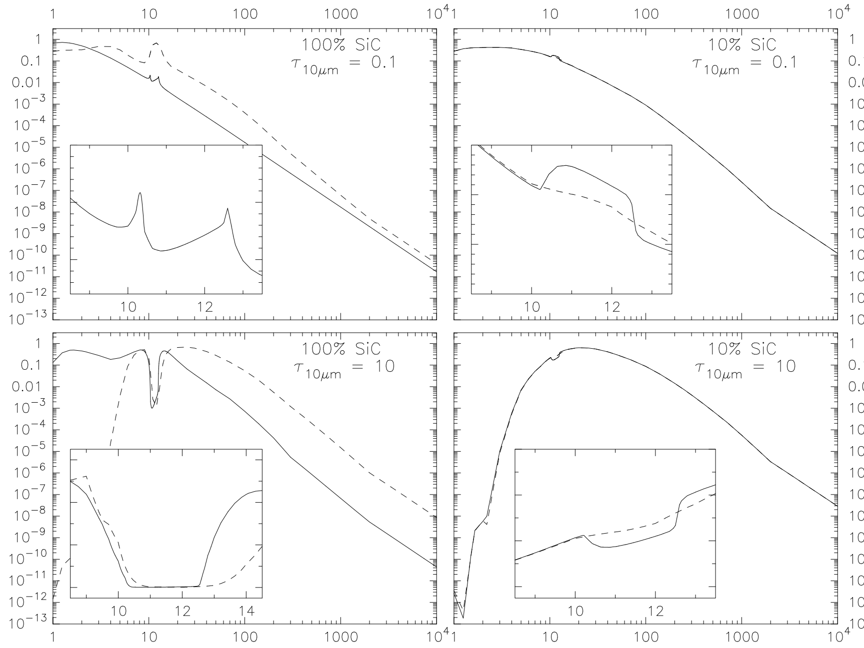

(a) CDS grain shape distribution.

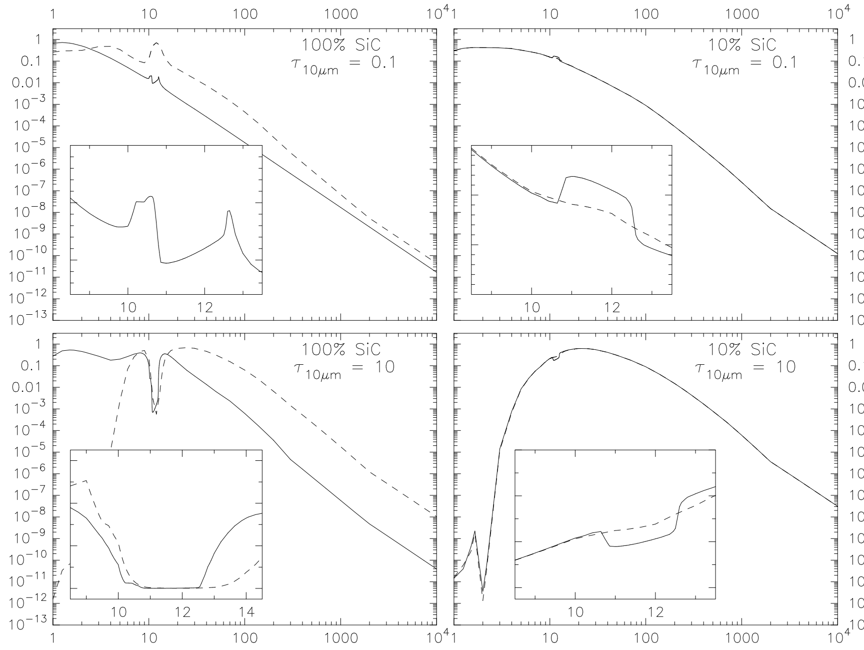

(b) DHS grain shape distribution.

Figure 9.12: Synthetic spectra generated using new β-SiC vs. Pégourié SiC, CDS and DHS grain shapes. Each large plot is log-log, with wavelength in μm on the x-axis and flux on the y-axis. The smaller insets are the same data as their respective large plots, but both axes are linear and the wavelength range is restricted from 8.5 μm to 13.5 μm. The upper left inset does not show the Pégourié spectrum, as it is much too large to fit into the smaller range. All spectra were generated using a MRN grain size distribution.

9.3.2.1 Discussion

A major difference revealed by an inspection of these synthetic spectra is that the new constatants in general emit and absorb much more strongly than was predicted by the older data. This is particularly obvious when looking at the 100% SiC, $\tau_{10\mu m} = 0.1$ spectra, where the Pégourié data produces a strong emission feature, but the new data is self absorbed in every grain size distribution. What appears to be happening is that, at least in the non-spherical cases, is that a large, broad emission feature is being self absorbed from roughly the center, and with this combination of parameters the self-absorption has reached just about to the continuum; this is what causes the two small peaks on either side. In fact, if we examine the 100% SiC, $\tau_{10\mu m} = 10$ spectra, we are probably seeing the continuation of this process; with a higher optical depth we expect more self-absorption (because the more of the outer layers of dust will be cool) and here we see the absorption continued to the point where it has widened and destroyed the two small peaks.

Another important difference visible in these spectra is that the spherical grains produce features that are narrower and at least in the self-absorbing cases more rounded, compared to the broader, flatter absorption features present in the other grain size distributions. This has the potential to be a diagnostic difference between the spherical and non-spherical grain shapes in observational spectra.

A somewhat unexpected result is the visible differences between the spectra generated by the non-spherical grain shape distributions. Of course, the absorption and scattering efficiencies are slightly different for each of the distributions, but the way the difference manifests in these spectra is interesting. For example, the difference between the DHS and CDS grain shape distributions; if we examine the 10% SiC, $\tau_{10\mu m}$ spectra, the self absorption is clearly wider in the case of the CDS shape distribution. This can also be seen in the 100% SiC, $\tau_{10\mu m} = 0.1$ cases, where the small 'peak' to the left of the absorption feature is thinner in the case of the CDS shape distribution; it appears that under the same conditions, a wider ‘chunk’ of the emission feature is being absorbed by this grain shape distribution.

There is a smaller difference between the α-SiC and β-SiC spectra, but differences are present; in all four of the 100% SiC, $\tau_{10\mu m} = 0.1$ spectra, the small peaks on each side of the absorption feature are taller relative to the absorption feature for β-SiC. In the other spectra, differences are visible but are more subtle, which means that identifying β-SiC in observational spectra - at least using this technique - might be difficult. A wider variety of test cases must be run however. It is possible that under certain conditions, such as the 100% SiC, $\tau_{10\mu m} = 0.1$ models, the differences become more pronounced and could possibly be visible in observational spectra of dust shells with similar parameters.

9.4 Summary and Conclusions

Starting with small particle absorption and scattering theory, we developed equations that allowed us to generate the absorption and scattering efficiencies for four different grain shape distributions; in addition, we incorporated the effects of different grain size distributions into our formulas. With this as a basis, we produced a code which applied the shape and size-dependent equations to the complex refractive index of the commonly used Pégourié SiC data, as well as to the new SiC refractive indices discussed in chapter 8. Using the absorption and scattering efficiencies output by the program, we then performed radiative transfer modeling over a test set of parameters, looking for differences in the resulting synthetic spectra.

The research presented here has only just begun to explore the possibilities that shape-dependent optical constants present. Many more synthetic spectra need to be produced in order to explore the properties of these shape distributions when applied to SiC; and there is no barrier from applying this theory to other grain species as well. It is clear, though, that spherical grains produce spectra different than any of the other grain shape distributions, and this is additional evidence that we should be wary before applying spherical grains to any model. The other shape distributions produce spectra that are similar but not exactly the same, leading to the tantalizing possibility that it may be possible to identify which grain shapes are contributing to a given SiC feature, and perhaps the features of other grain species as well.

Chapter 10

Summary and Future Work

"My undertaking is not difficult, essentially... I should only have to be immortal to carry it out." -

Jorge Luis Borges

10.1 Observations of carbon stars and the dust condensation sequence

In chapter 5, we examined a collection of carbon stars, examining their SiC features to attempt to identify any correlations between the feature parameters and other parameters of the star and dust shell. A major motivation for this research was the fact that previous similar studies of carbon stars have yielded contradictory results. Despite a careful analysis using *ISO* data to supplement the lower resolution *IRAS* datasets, we were unable to observe correlations. A possible cause for this is that there are many parameters that influence the spectrum we see when we observe these stars, and the parameter space is large enough that there is a degeneracy where different combinations of dust shell parameters could lead to similar spectral features. Theoretical radiative transfer models were produced that seem to support this conclusion.

10.1.1 Future work

If very accurate radiative transfer models were fit to these star's spectra, it might be possible to obtain more precise or additional dust shell parameters, which would either help strengthen our result or instead show a way past the degenerate parameter space. Additionally, it may be possible to subdivide our data set into smaller sets of stars based on common parameters; correlations within those smaller groups would be more likely as there would be less degeneracy.

10.2 Extreme carbon stars

In chapter 7 we investigated a collection of carbon stars whose dust shell has become so optically thick that we can no longer see the central star, only the infrared emission of the shell. These objects are called extreme carbon stars, and few are known; they probably represent a short period in a carbon star's life right before it leaves the AGB phase. Our investigation discovered three extreme carbon stars with a SiC absorption feature; this brought the total number of known extreme carbon stars with absorption features to ten. Additionally, we performed radiative transfer modeling in order to fit synthetic spectra to these star's spectra in an attempt to determine the parameters present in the dust shells; we discovered that we obtained the best fits when we used a higher dust condensation temperature than had been used by previous workers, and also that the use of graphite instead of amorphous carbon in our models improved our fit. One of the spectra we fitted required the use of a different grain size distribution in the radiative transfer models to produce an acceptable fit. In a similar situation to chapter 5, we were unable to discover correlations between the parameters of these star's dust shells.

10.2.1 Future work

With such a small number of extreme carbon stars currently known, and a particularly small number of extreme carbon stars with an absorption feature, the discovery of additional such objects could provide important new information about them. We have continued to investigate the dependence of radiative transfer models on the grain size and shape; in addition, we are continuing to investigate the use of graphite as opposed to amorphous carbon in the radiative transfer models of other stars. Finally, we are continuing to use the theoretical condensation models mentioned in this work, using them to constrain radiative transfer parameters in order to decrease the parameter space.

10.3 V Cyg

In chapter 6 we turned our focus onto a single carbon star. This star, V Cyg, had observational data available for several points over a pulsation cycle, and this data was processed and examined for correlations, several of which were found. Two of these correlations may indicate that a small amount of self-absorption is going on in the outer part of the dust shell around V Cyg; a more tentative and speculative possibility is that grain shape effects may partially explain these correlations. In addition, we used long-slit spectroscopy to obtain spatially resolved spectra of this star. No significant correlations were observed, which is possibly a result of the uncertainty in the blackbody fits, but could also be due to the low spatial resolution of our measurements relative to the structure expected to be present in the dust shell.

10.3.1 Future work

One feature in the spectrum of V Cyg that was not investigated for this work is a ~30 μm feature present in all the time-resolved data sets. An analysis of this feature is planned, and the parameters of this feature will be compared with both the other parameters of that feature and also the parameters of the SiC feature. Additional work will be done to try and make the spatially-resolved blackbody fits more precise. And though not directly related to V Cyg, spatially-resolved data for other carbon stars was obtained along with that of V Cyg, and it will undergo the same type of analysis.

10.4 New SiC optical constants

In chapter 8 we discussed limitations present in commonly used optical constants of SiC, and how these limitations make it inappropriate to use those constants for radiative transfer modeling without careful consideration. In order to obtain SiC optical constants that were not limited in the same way, we performed reflectance measurements on samples of α and β-SiC, and then used classical dispersion analysis to obtain the optical constants from those measurements.

10.4.1 Future work

An obvious extension of this kind of research is to obtain optical constants for additional mineral species; other optical constants suffer from the same kind of limitations that were addressed for SiC in this work. Also, we hope to raise awareness among other researchers that the origin and limitations of optical data should be understood and carefully considered before using them in radiative transfer models with possibly inappropriate parameters.

10.5 Size and shape dependent optical constants

In chapter 9, we investigated the scattering and absorption of light by different size and shape distributions of small particles. We began by using small particle absorption and scattering theory to develop equations which allowed us to convert shape and size-independent bulk optical properties into shape and size-dependent absorption and scattering efficiencies.

10.5.1 Future work

The absscat code presented in chapter 9.2 is already being used to investigate grain species other than SiC; the theory behind the equations holds for many different types of grain species.

Optical properties generated by this code will be used to generate additional radiative transfer model spectra, in order to try and fit observed spectra. This will not only test the reasonableness of our technique, but could perhaps also give us information about parameters of the dust grains that have been otherwise difficult to obtain, like the grain shape. It may also be possible to distinguish between α-SiC and β-SiC in some cases.

It is also interesting to consider shape distributions not currently incorporated into the absscat code. For example, the continuous distribution of spheroids described in section 9.1.3.2 contains spheroids of all shapes, with no bias towards any particular shape. A shape distribution that only included some types of spheroids (for example, only prolate or oblate) or the full distribution but biased towards certain shapes would be useful to represent preferential growth and destruction of SiC based on its crystal structure. The absorption and scattering equations for such particles would need to consider not only the shape of the grain, but also the orientation of the crystal structure in relation to that shape.

Appendix A

Source code for absscat

A.1 Package edu.missouri.stardust.absscat

A.1.1 Main.java

```
/*
 * class Main
 *
 * Version 2.3
 *
 * 01/30/10
 *
 */

package edu.missouri.stardust.absscat;
```

```
import java.util.LinkedList;

/**
 * The Main class connects all the other classes of this package and runs them
 * in the proper order to calculate a combined set of scattering and absorption
 * efficiencies when given given nk files, dust distributions, and the
 * percentage of the dust that each nk file represents.
 *
 * @author Adrian Corman
 * @version 2.3
 */
class Main {

    /* Indicates the desired level of console output. 0 indicates that
     * everything other than errors is suppressed, 1 is the standard output
     * wint starting and stopping messages, and 2 is the verbose option.
     */
    static int outputLevel = 1;

    /* Indicates the desired accuracy for the numerical integration of the
     * KMH grain size distribution.
     */
    static double epsilon = 1e-10;

    /* Indicates if the output file already exists, should it be overwritten. */
    static boolean overwrite = false;
```

```
/* Indicates if the interpolated nk data files are required to also be
 * outputted along with the final result.
 */
static boolean outputInterpolation = false;

/* Indicates if the interpolated nk data files only are required to be
 * outputted.
 */
static boolean onlyInterpolate = false;

static int precision = 3;

/* Holds the filename of the desired input file containing the parameters
 * for the calculations. This must be specified when the program is
 * called.
 */
static String inputFilename = null;

/* Holds the filename of the desired output file. If not specified on
 * the command line, this file name will be generated from the input
 * filename.
 */
static String outputFilename = null;

 /**
```

```
 * Calls and coordinates the other classes of package absscat.
 * The order is as follows; Main first calls the FileInput class, which
 * inputs the abscat.inp file in the default case, or the input file
 * specified by the user on the command line when the program is run
 * (in order to facilitate batch processing). This input file contains
 * the parameters needed to run the necessassary calculations.
 * It then passes this to the Parser class, which extracts
 * the parameters from the abscat.inp file, which Main then uses to
 * determine which data files it needs to open (again using FileInput),
 * and also if it needs to open the wavelengths.inp file for use in
 * interpolation. These files too are parsed using Parser, which gives
 * Main all the data needed to perform the calculations.
 *
 * If interpolation is required, Main passes this data to the Interpolator
 * class, which performs the requisite calculations. After this, or if
 * interpolation is not required, Main calls on the Calculations class
 * which generates the final output data.
 *
 * Finally, Main calls on the FileOutput class, which outputs the final
 * data to a file as specified in abscat.inp or the user supplied input
 * file.
 *
 * @param args the command line arguments.
 */
public static void main(String[] args) {
```

```
/* Gets the starting time for this run */
long startTime = System.nanoTime();

/* First, parse and check the arguments given to abscat on the command
 * line.
 */
Parser argsParser = new Parser(args);
argsParser.parseArguments();

/* If verbose mode is selected this will output a message that
 * absscat is beginning to work.
 */
ConsoleOutput.beginWorking();

/* Next use FileInput to open this file and obtain an array containing
 * each line of the file.
 */
FileInput parameterReader = new FileInput(inputFilename);
String[] unparsedParameters = parameterReader.lineReturner();

/* Pass this array to the Parser class to obtain an array containing
 * the individual parameters in the proper order. If verbose mode is
 * active, also output a message.
 */
ConsoleOutput.parsingParameters();
Parser parameterParser = new Parser(unparsedParameters);
```

```
String[] parsedParameters = parameterParser.parseParameters();

/* Now we extract the nk data files from the parameter array, open
 * them with FileInput, and store their data in one large array.
 * The first index of this array will indicate the internal
 * number of the nk data file (i.e. from 0 to the total number of
 * files − 1), the second will indicate the column of the data
 * file (0 = wavelength, 1 = n, 2 = k), and the third will hold the
 * line number of the data file.
 */
int numberOfNKFiles = Integer.parseInt(parsedParameters[0]);

/* Need to check and make sure that the total number of lines in the
 * input file corresponds with the number of nk files specified
 * on the first line. Because of the way Parser fills the
 * parsedParameters array, parsedParameters.length should equal
 * (numberOfNKFiles * 7) + 3.
 */
if (parsedParameters.length != (numberOfNKFiles * 7) + 3){

    /* Executes if the number of parameters doesn't correspond to
     * the given number of nk files. First calculate the number
     * of nk files the parameters do correspond to, then output
     * an error message and exit.
     */
    int correspondingNumber = ((parsedParameters.length − 3)/7);
```

```
        ConsoleOutput.wrongNumberOfNKFiles(numberOfNKFiles,
                correspondingNumber);
        System.exit(0); //Can't continue until this is fixed
    }

    /* Holds the parsed nk data before any further manipulation */
    double[][][] rawNK = new double[numberOfNKFiles][][];
    for (int i = 0; i < numberOfNKFiles; i++) {

        /* parsedParameters contains an nk data file name starting with
         * index 3 and then every 7th index after that. Also, output a
         * status message for each file that is read in, if verbose mode
         * is active.
         */
        ConsoleOutput.fileInputMessage(parsedParameters[(i*7) + 3]);
        FileInput nkInput = new FileInput(parsedParameters[(i * 7) + 3]);
        Parser nkParser = new Parser(nkInput.lineReturner());
        rawNK[i] = nkParser.parseNK();
    }

   /* Now we must perform interpolation if it was requested, and also
    * handle the case where interpolation was not requested, there are
    * more than two nk data files, and the wavelength grids of those
    * files are not identical (in which case we have to output an error
    * message and exit).
    */
```

```
/* Holds the final set of nk data to be used in the scattering and
 * absorption coefficient calculations.
 */
double[][][] finalNK = new double[numberOfNKFiles][][];

if (parsedParameters[1].equalsIgnoreCase(”yes”)) {

    /* If the verbose flag has been selected, this will output
     * a line indicating interpolation has begun.
     */
    ConsoleOutput.verboseInterpolating(parsedParameters[2]);

    /* Perform the interpolation. First input the wavelength grid
     * file and parse its data, then pass this along to the
     * Interpolator.
     */
    FileInput wavelengthInput = new FileInput(parsedParameters[2]);
    Parser wavelengthParser =
            new Parser(wavelengthInput.lineReturner());
    double[] wavelengthArray = wavelengthParser.parseWavelengths();

    for (int j = 0; j < numberOfNKFiles; j++) {

        /* Split rawNK up into the x and y values */
        double[] xArray = new double[rawNK[j].length];
```

```
double[] nArray = new double[rawNK[j].length];
double[] kArray = new double[rawNK[j].length];
for (int k = 0; k < rawNK[j].length; k++) {
    xArray[k] = rawNK[j][k][0];
    nArray[k] = rawNK[j][k][1];
    kArray[k] = rawNK[j][k][2];
}

/* Call the Interpolator and obtain the new, interpolated
 * values, then fill finalNK with this data.
 */
Interpolator nInterpolator = new Interpolator(xArray, nArray,
        wavelengthArray);
Interpolator kInterpolator = new Interpolator(xArray, kArray,
        wavelengthArray);
double[] finalN = nInterpolator.returnInterpolation();
double[] finalK = kInterpolator.returnInterpolation();
double[][] combinedArray =
        new double[wavelengthArray.length][3];
for (int m = 0; m < wavelengthArray.length; m++) {
    combinedArray[m][0] = wavelengthArray[m];
    combinedArray[m][1] = finalN[m];
    combinedArray[m][2] = finalK[m];
}
    finalNK[j] = combinedArray;
```

```
    }
} else if (numberOfNKFiles != 1 &&
        parsedParameters[1].equalsIgnoreCase(”no”)) {

    /* In this case, we need to check and make sure all the given
     * nk data files have the same wavelength grid (or else we
     * can’t continue because no interpolation was selected.
     */
    for (int n = 1; n < numberOfNKFiles; n++) {
        try {
            for (int p = 0; p < rawNK[n].length; p++) {
                if (rawNK[0][p][0] == rawNK[n][p][0]) {
                    continue; //Keep checking
                } else {

                    /* The nk data files use different wavelength grids
                     * so output an error message and exit.
                     */

                    ConsoleOutput.needsInterpolation();
                    System.exit(0);
                }
        }
        } catch(ArrayIndexOutOfBoundsException e) {
```

```
            /* If this block executes, it means that the wavelength
             * grids are not the same size and thus cannot be
             * the same.
             */
            ConsoleOutput.needsInterpolation();
            System.exit(0);
        }
    }

    /* If this is reached, it means that there is no problem with the
     * wavelength grids for the nk data sets.
     */
    finalNK = rawNK;

} else {
    finalNK = rawNK; //No manipulation needed in this case either
}

/* If either −outputinterpolation or −onlyinterpolation (or both) were
 * selected, output the interpolated nk data files now. If
 * −onlyinterpolate was selected, exit after this output.
 */
if (outputInterpolation || onlyInterpolate) {
    if (parsedParameters[1].equalsIgnoreCase(”yes”)){
        LinkedList <String>alreadyOutput = new LinkedList();
        for (int w = 0; w < numberOfNKFiles; w++){
```

```
          String interpFilename;
          String nkFilename = parsedParameters[(w * 7 + 3)];

          /* If the same nk data file is input more than once, the
           * program needs to check and see if the interpolated
           * version of that file has already been output. If it has,
           * then skip the second occurance and continue through
           * the rest of the files.
           */
          if (alreadyOutput.contains(nkFilename)) {
               continue; //Skip to the next nk data file
          }
          alreadyOutput.add(nkFilename);

          if (nkFilename.contains(".")) {

          /* If the nk data filename has a . extention, get rid of it
          * so the interpFilename doesn't have two of them.
          */
          String[] interpSplit = nkFilename.split("\\.");
          interpFilename = interpSplit[0] + "_interp.dat";
          } else {
          interpFilename = nkFilename + "_interp.dat";
          }
     FileOutput interpolatedOutput =
               new FileOutput(interpFilename,finalNK[w],overwrite);
```

```
        interpolatedOutput.output();
        }
        if (onlyInterpolate) {
            ConsoleOutput.onlyInterpolateExit();
            System.exit(0); //Processing is finished in this case
        } else {
            ConsoleOutput.outputInterpolationFinished();
        }
    } else {

        /* This block executes when the interpolation flag was set in
         * the input file as no, but output of the interpolated files
         * was requested on the command line. In this case, output
         * an error message and exit (because the program doesn't
         * know what it is supposed to do here).
         */
        ConsoleOutput.interpOptionsDontMatch();
        System.exit(0);
    }
}

/* Finally, all the data has been read in and prepared for processing.
 * Now we pass this data on to the Calculations class to calculate,
 * and additionally output a status message if verbose mode is
 * active.
 */
```

```
        ConsoleOutput.beginningCalculations();
        Calculations calculations = new Calculations(parsedParameters, finalNK);
        double[][] finalResult = calculations.returnResult();

        /* Output this result to a file */
        FileOutput fileOutput = new FileOutput(outputFilename, finalResult,
                overwrite);
        fileOutput.output();

        /* Get the estimated runtime for the program */
        long estimatedTime = System.nanoTime() - startTime;

        /* Print the finish message (will not output anything if the silent
         * flag was activated (and nonVerboseFinish will call on
         * verboseFinish if the verbose flag was activated).
         */
        ConsoleOutput.nonVerboseFinish(estimatedTime * 1E-9);

        /* End of absscat */
    }
}
```

A.1.2 FileInput.java

```
/*
 * FileInput
```

```
 *
 * Version 2.2
 *
 * 01/30/10
 *
 */

package edu.missouri.stardust.absscat;

import java.io.*;
import java.util.ArrayList;

/**
 * FileInput opens a file of a given filename and stores an array of Strings
 * corresponding to the individual lines of that file.
 *
 * @author Adrian Corman
 * @version 2.2
 */
class FileInput {

    /* The given input filename */
    private final String fileName;

    /* The file input stream */
    private BufferedReader bufferedFile;
```

```
/* The array holding each of the file's lines */
private String[] lineArray;

/*The only constructor for this class. Initalizes the class with a given
 * filename, then reads in each line of the file to an array.
 */
FileInput(String fileName) {

    this.fileName = fileName;
    this.openFile();
    this.lineReader();
    this.closeFile();

}

/* A simple class to open and return a file of the specified filename */
private void openFile() {

    try {
        bufferedFile = new BufferedReader(new FileReader(fileName));
    } catch (FileNotFoundException e) {
        System.out.println(fileName+ " " + "not found.");
        System.exit(0); //Exit because we need an input file to continue.
    }
}
```

```
/* A simple class to convert each line of a file into a string */
private void lineReader() {

    /* We start with an ArrayList because we don't know the number of lines
     * in the file
     */
    ArrayList lineList = new ArrayList();

    try {

        /* Iterate over every line; we will know we have read in the
         * whole file when readLine returns null
         */
        String line = null; //Contains each individual line as read in
        int lineNumber = 0; //Keeps track of which line we are on

        while ((line = bufferedFile.readLine()) != null) {
        lineList.add(lineNumber, line);
        lineNumber++;
        }

    } catch (IOException e) {

      /* If this block executes it means that the program is somehow
       * unable to read in lines from the specified file
```

```
       */
      System.out.println(”Error reading ” + bufferedFile);
      System.exit(0); //Exit because we can’t recover from this
    }

    /* Convert lineList to an array of Strings */
    lineArray = (String[])lineList.toArray(new String[0]);
}

/* Simple class to close the bufferedFile and deal with the exception
 * handling.
 */
private void closeFile() {

    try {
        bufferedFile.close();
    } catch(IOException e) {

        /* This block should never execute unless something has gone
         * seriously wrong with file IO
         */
        System.out.println(”Error closing ” + fileName);
        System.exit(0); //Dangerous to continue if file IO is messed up

    }
}
```

```
    /* Returns the String array containing each line of the file specified
     * when FileInput was initalized.
     */
    String[] lineReturner() {
        return lineArray;
    }
}
```

A.1.3 Parser.java

```
/*
 * Parser
 *
 * Version 1.1
 *
 * 01/30/09
 *
 */

package edu.missouri.stardust.absscat;

import java.util.ArrayList;

/**
 * Parser contains methods that parse a given String array in a variety of
```

```
 * ways useful to the rest of the package.
 *
 * @author Adrian Corman
 * @version 1.1
 */
class Parser {

    /* The given String array */
    private final String[] unparsedArray;

    /*The only constructor for this class. Initializes the initial unparsed
     * String array, preparing it for parsing.
     */
    Parser(String[] unparsedArray) {
        this.unparsedArray = unparsedArray;
    }

    /**
     * Parses a parameter file into a String array of the individual parameters.
     * The parameter file is structured as follows. There are always two
     * parameters at the beginning of the file corresponding to the number
     * of nk data files and then the interpolation parameter. If
     * interpolation is requested, then there is a third parameter
     * containing the wavelength grid the data will be interpolated to.
     * After these lines are blocks of parameters for each nk data file.
     * First is the filename, then the grain shape distribution, then
```

```
* the grain size distribution. If the size distribution is single,
* then there is one additional parameter (corresponding to the
* single value for size), but for the others there are three. Finally,
* each block ends with the weight used for the given nk file when
* the weighted average is taken. The parser will ignore any line
* not containing an = sign.
*
* @return a String array containing the parsed parameters.
*/
String[] parseParameters() {

   /* Create an ArrayList to hold the parsed parameters one by one. The
    * maximum size it can be at the end is the length of the unparsed
    * array.
    */
   ArrayList initialArray = new ArrayList(unparsedArray.length);

   /* Keeps track of which line of data we are on, as opposed to the
    * overall line number (which can contain comments).
    */
   int dataLineNumber = 0;
   boolean interpolationNeeded = false;
   String sizeDistribution = null;

   /* Iterate through each of the members of unparsedArray, discarding
    * lines that do not contain an = sign.
```

```
 */
for (int i = 0; i < unparsedArray.length; i++) {
    if (unparsedArray[i].startsWith("#")){

        /* Ignore lines starting with # − this comes first because
         * a line starting with # could be a commented out line with a
         * = sign in it.
         */
        continue;
    }
    if (unparsedArray[i].contains("=")) {
        if (dataLineNumber == 0) {

            /* The number of nk data files */
            initialArray.add(0,
                    this.parseAndClean(unparsedArray[i], "="));
            dataLineNumber++;
        } else if (dataLineNumber == 1) {

            /* Interpolation flag */
            String interpolation = this.parseAndClean(unparsedArray[i],
                    "=");
            initialArray.add(1, interpolation);
            dataLineNumber++;

            /* Set interpolationNeeded for later use */
```

```
        if (interpolation.equalsIgnoreCase(”yes”)) {
            interpolationNeeded = true;
        } else if (interpolation.equalsIgnoreCase(”no”)){
            interpolationNeeded = false;
        } else {

            /* If this block executes it means that the input file
             * is not formatted correctly */
            ConsoleOutput.interpolationFlagError();
            System.exit(0); //This is a fatal error
        }

    /* The rest of the parameters are more complicated to
     * parse because if interpolation is not required the
     * rest of the parameters will be shifted up one (due
     * to the absence of the wavelength file) and if a single
     * grain size distribution is selected it only takes
     * one parameter instead of the usual three (thus shifting
     * the rest of the parameters up two every time this
     * happens).
     */
    } else if (dataLineNumber == 2) {

        /* A block to fill the third element (index 2) of the array
         * with either the wavelength file name if interpolation
         * is needed or null otherwise.
```

```
     */
    if (interpolationNeeded) {
        initialArray.add(2,
            this.parseAndClean(unparsedArray[i], ”=”));
        dataLineNumber++;
    } else {
        initialArray.add(2, null);
        dataLineNumber++;
        i−−; //In this case we shouldn’t advance the file line
    }
} else if ((dataLineNumber − 3) % 7 == 0 &&
        (dataLineNumber − 3) >= 0) {

    /* This block stores in the nk data file names, which
     * after the initial parameters are found every 7th line
     */
    initialArray.add(dataLineNumber,
            this.parseAndClean(unparsedArray[i], ”=”));
    dataLineNumber++;
} else if ((dataLineNumber − 4) % 7 == 0 &&
        (dataLineNumber − 4) >= 0) {

    /* This block stores in the desired grain shape
     * distribution for this nk data file.
     */
    initialArray.add(dataLineNumber,
```

```
            this.parseAndClean(unparsedArray[i], ”=”));
    dataLineNumber++;
} else if ((dataLineNumber − 5) % 7 == 0 &&
        (dataLineNumber − 5) >= 0) {

    /∗ This block stores the desired grain size distribution ∗/
    sizeDistribution =
            this.parseAndClean(unparsedArray[i], ”=”);
    initialArray.add(dataLineNumber, sizeDistribution);
    dataLineNumber++;
} else if ((dataLineNumber − 6) % 7 == 0 &&
        (dataLineNumber − 6) >= 0) {

    /∗ This block stores the first grain size distribution
     ∗ parameter. In the case of a single grain size,
     ∗ there is only one parameter so it will fill in the
     ∗ other two spots with null.
     ∗/
    if (sizeDistribution.equalsIgnoreCase(”single”)) {
        initialArray.add(dataLineNumber,
                this.parseAndClean(unparsedArray[i], ”=”));
        dataLineNumber++;
        initialArray.add(dataLineNumber, null);
        dataLineNumber++;
        initialArray.add(dataLineNumber, null);
        dataLineNumber++;
```

```
    } else if (sizeDistribution.equalsIgnoreCase(”MRN”) ||
            sizeDistribution.equalsIgnoreCase(”KMH”)) {
        initialArray.add(dataLineNumber,
                this.parseAndClean(unparsedArray[i], ”=”));
        dataLineNumber++;
    } else {

        /* If this block executes it means that the parameter
         * file has not been correctly formatted.
         */
        System.out.println(”Size distribution must be one of” +
                ” single, MRN, or KMH”);
        System.exit(0); //This is a fatal error
    }
} else if ((dataLineNumber − 7) % 7 == 0 &&
        (dataLineNumber − 7) >= 0) {

    /* This block will only execute in the case of either the
     * MRN or KMH size distribution, in which case it will
     * obtain the second distribution parameter.
     */
    initialArray.add(dataLineNumber,
            this.parseAndClean(unparsedArray[i], ”=”));
    dataLineNumber++;
} else if ((dataLineNumber − 8) % 7 == 0 &&
        (dataLineNumber − 8) >= 0) {
```

```
                /* This block will also only execute in the case of either
                 * the MRN or KMH size distribution, in which case it
                 * will obtain the third and final distribution
                 * parameter.
                 */
                initialArray.add(dataLineNumber,
                        this.parseAndClean(unparsedArray[i], "="));
                dataLineNumber++;
            } else if ((dataLineNumber − 9) % 7 == 0 &&
                    (dataLineNumber − 9) >= 0) {

                /* This block obtains the weighting factor */
                initialArray.add(dataLineNumber,
                        this.parseAndClean(unparsedArray[i], "="));
                dataLineNumber++;
            }
        } else {
            continue; //No data on this line so go to the next one
        } //This ends the = checking block
    } //This ends the for loop iterating over all the file lines

    return (String[])initialArray.toArray(new String[0]);
}

/* Parses a string at the given regex and returns the string to the
```

```
 * right of the regex, removing any whitespace.
 */
private String parseAndClean(String unparsedString, String regex){
    String[] parsed = unparsedString.trim().split(regex);
    String parsedAndCleanedString = parsed[1].trim();

    return parsedAndCleanedString;
}

/* Parses a nk data file into an array containing the data. The nk data
 * files are formatted as follows. It must contain exactly three
 * columns, which may be delimited by any of comma, space, or tab. The
 * first column contains the wavelengh, and must be arranged from
 * lowest wavelength to highest wavelength. The second column contains the
 * n data, and the third column contains the k data. Any line in this
 * file beginning with the # symbol is ignored. The returned array
 * is structured as follows: the first index represents the line number
 * of the data file (note: only lines of actual data are counted, not
 * lines starting with # which are not stores), and the second index
 * represents the column - 0 for wavelength, 1 for n, and 2 for k.
 */
double[][] parseNK() {

    /* Contains the parsed nk data */
    double parsedNK[][] = new double[unparsedArray.length][3];
```

```
/∗ Contains the line number we are on when only lines containing data
 ∗ are considered (so there will be no gaps when a line is blank or
 ∗ if a line starts with #).
 ∗/
int dataLineNumber = 0;
for (int i = 0; i < unparsedArray.length; i++) {

    /∗ Ignore lines starting with # ∗/
    if (unparsedArray[i].startsWith(”#”)) {
        continue;

    /∗ Ignore blank lines ∗/
    } else if (unparsedArray[i].isEmpty()) {
        continue;
    } else {

        /∗ Split the columns. They can be delimited by any comma,
         ∗ tab, or space. Then convert the column values into
         ∗ doubles and store these values in parsedNK.
         ∗/
        String[] conversionArray =
                unparsedArray[i].trim().split(”\\,|\\s+”);
        for (int j = 0; j < 3; j++) {
            parsedNK[dataLineNumber][j] =
                    Double.parseDouble(conversionArray[j]);
        }
```

```
                dataLineNumber++;
            }
        }

        /* If there were any lines starting with #, parsedNK is larger than it
         * needs to be (complicating length measurements later). If this is
         * the case, copy the data over to a new array of the proper size
         * and return that.
         */
        if (dataLineNumber == unparsedArray.length) {
            return parsedNK;
        }
        else {
            double[][] trimmedArray = new double[dataLineNumber][3];
            System.arraycopy(parsedNK, 0, trimmedArray, 0, dataLineNumber);
            return trimmedArray;
        }
    }

    /* Parses a wavelength grid file into an array. This file can have any
     * number of columns, but only the first is read in. This column must
     * contain the wavelengths in order from lowest to highest, and any line
     * starting with # is ignored. The only index of the returned array
     * represents the line number of the wavelength grid file (not storing or
     * counting lines with # as with the nk data files).
     */
```

```
double[] parseWavelengths() {

    /* Containes the parsed wavelength values */
    double[] parsedWavelengths = new double[unparsedArray.length];

    /* Contains the line number we are on when only lines containing
     * data are considered.
     */
    int dataLineNumber = 0;
    for (int i = 0; i < unparsedArray.length; i++) {

        /* Ignore lines starting with # */
        if (unparsedArray[i].startsWith("#")) {
            continue;
        } else {

            String[] conversionArray =
                    unparsedArray[i].trim().split("\\,|\\s+");
            parsedWavelengths[dataLineNumber] =
                    Double.parseDouble(conversionArray[0]);
            dataLineNumber++;
        }
    }

    /* If there were any lines starting with #, parsedWavelengths
     * is larger than it needs to be (complicating length measurements
```

```
     * later). If this is the case, copy the data over to a new array of
     * the proper size and return that.
     */
    if (dataLineNumber == unparsedArray.length) {
        return parsedWavelengths;
    }
    else {
        double[] trimmedArray = new double[dataLineNumber];
        System.arraycopy(parsedWavelengths, 0, trimmedArray, 0,
                dataLineNumber);
        return trimmedArray;
    }
}

/* Parses the command line arguments and sets the appropriate values in
 * Main accordingly.
 */
void parseArguments() {
    if (unparsedArray.length == 0) {
        ConsoleOutput.noArguments();
        System.exit(0); //The input filename has to be specified.
    }

    /* A series of variables that let us keep track of which arguments
     * were given.
     */
```

```
boolean inputFound = false; boolean outputFound = false;
boolean verboseFound = false; boolean silentFound = false;
boolean epsilonFound = false; boolean precisionFound = false;

/* Iterate through all the members of args */
for (int i = 0; i < unparsedArray.length; i++) {
    if (unparsedArray[i].equals(”−help”)) {

        /* Look for help first of all because if it is given then
         * absscat will only output the help message and exit without
         * doing anything else.
         */
        ConsoleOutput.helpMessage();
        System.exit(0);
    } else if (unparsedArray[i].equals(”−inputfile”)) {
        Main.inputFilename = unparsedArray[++i];
        inputFound = true;
    } else if (unparsedArray[i].equals(”−outputfile”)) {
        Main.outputFilename = unparsedArray[++i];
        outputFound = true;
    } else if (unparsedArray[i].equals(”−verbose”)) {
        Main.outputLevel = 2;
        verboseFound = true;
    } else if (unparsedArray[i].equals(”−silent”)) {
        Main.outputLevel = 0;
        silentFound = true;
```

```
    } else if (unparsedArray[i].equals("−overwrite")) {
        Main.overwrite = true;
    } else if (unparsedArray[i].equals("−epsilon")) {
        Main.epsilon = Double.parseDouble(unparsedArray[++i]);
        epsilonFound = true;
    } else if (unparsedArray[i].equals("−outputinterpolation")){
        Main.outputInterpolation = true;
    } else if (unparsedArray[i].equals("−onlyinterpolate")){
        Main.onlyInterpolate = true;
    } else if (unparsedArray[i].equals("−precision")) {
        Main.precision = Integer.parseInt(unparsedArray[++i]);
        precisionFound = true;
    } else {
        ConsoleOutput.unrecognizedArgument(unparsedArray[i]);
        System.exit(0); //Because we don't know what the user wanted
    }
}

/∗ Check for the case where both the −silent and −verbose flags
 ∗ were given. absscat will assume −verbose was meant.
 ∗/
if (verboseFound && silentFound){
    Main.outputLevel = 2;
    ConsoleOutput.verboseSilent();
}
```

```
/* Check if the mandatory input file was found */
if (!inputFound) {

    /* Executes if the required input file was not found */
    ConsoleOutput.noArguments();
    System.exit(0);
} else {
    ConsoleOutput.inputGiven(); //Displays a message if verbose is on
}

/* Check if the output file argument was found, and if not set the
 * output filename to the default inputFilename_out.dat
 */
if (!outputFound) {
    if (Main.inputFilename.contains(”.”)) {

        /* If inputFilename has a . extention, get rid of it so
         * the outputFilename doesn’t have two of them.
         */
        String[] inputSplit = Main.inputFilename.split(”\\.”);
        Main.outputFilename = inputSplit[0] + ”_out.dat”;
    } else {
        Main.outputFilename = Main.inputFilename + ”_out.dat”;
        ConsoleOutput.outputGiven();
    }
}
```

```
        /* Output messages for the other various arguments if present. */
        if (verboseFound){
            ConsoleOutput.verboseActivated();
        }
        if (Main.overwrite){
            ConsoleOutput.overwrite();
        }
        if (epsilonFound){
            ConsoleOutput.epsilonSpecified();
        }
        if (Main.outputInterpolation){
            ConsoleOutput.outputInterpolation();
        }
        if (Main.onlyInterpolate){
            ConsoleOutput.onlyInterpolate();
        }
        if (precisionFound){
            ConsoleOutput.precisionSpecified();
        }
    }
}
```

A.1.4 Interpolator.java

```
/*
```

```
 * Interpolator
 *
 * Version 2.4
 *
 * 01/30/10
 *
 */

package edu.missouri.stardust.absscat;

import java.util.ArrayDeque;
import java.util.Arrays;

/**
 * Interpolator interpolates a given set of (x,y) values to a given x grid.
 * Linear interpolation is used where the domains of the original values and
 * the new grid overlap, and linear extrapolation is used when the new grid
 * extends beyond the original data set.
 *
 * @author Adrian Corman
 * @version 2.4
 */
class Interpolator {

    /* The x values of the original data */
    private final double[] originalX;
```

```
/* The y values of the original data */
private final double[] originalY;

/* The grid the data set will be interpolated to */
private final double[] newX;

/* The final result of the interpolation */
private double[] newY;

/* The only constructor for this class. The index of the inputs should
 * correspond to the lines of the data, and initX and initY must contain
 * the same number of elements.
 */
Interpolator(double[] originalX, double[] originalY,
        double[] newX) {

    /* Check to see that the wavelengths are in order from smallest on
     * top to biggest on bottom; if not, reverse them.
     */
    if (newX[0] > newX[1]){
        this.newX = this.reverse(newX);
    } else {
        this.newX = newX;
    }
    if (originalX[0] > originalX[1]){
```

```
        this.originalX = this.reverse(originalX);
        this.originalY = this.reverse(originalY);
    } else {
        this.originalX = originalX;
        this.originalY = originalY;
    }

    /∗ Set the size of newY now that we have a wavelength grid to measure ∗/
    newY = new double[newX.length];

    this.interpolate();
}

/∗ Performs all the steps needed for the linear interpolation, calling on
 ∗ the other specific methods in this class.
 ∗/
private void interpolate() {

    /∗ Check to see if the data is already matched to the new x grid;
     ∗ if so no interpolation is required.
     ∗/
    if (Arrays.equals(originalX, newX)) {
        newY = originalY; //No interpolation required in this case
        return;
    }
```

```
/∗ If the new x grid extends beyond the original data set, we need
 ∗ to perform a linear extrapolation and fill in newY with these
 ∗ extrapolated values for the extended region(s).
 ∗/

/∗ Integer corresponding to the lowest index of newX corresponding
 ∗ to a value greater than or equal to the lowest x value in
 ∗ originalX. The default case is 0 (meaning that no filling is
 ∗ required).
 ∗/
int lowestIndex = 0;

/∗ Equivalent integer for the highest x. Default value in this case is
 ∗ the largest index in newX (i.e. newX.length − 1).
 ∗/
int highestIndex = (newX.length − 1);

if (originalX[0] > newX[0]) {
    lowestIndex = this.extrapolateLess();
} else if (originalX[originalX.length − 1] < newX[newX.length − 1]) {
    highestIndex = this.extrapolateMore();
}

/∗ Now that we've dealt with these cases, we can perform the
 ∗interpolation proper.
 ∗/
```

```
    this.linearInterpolation(lowestIndex, highestIndex);
}


/* Fills in all values where the new x grid has values below the lowest
 * x point in the original grid with a linear extrapolation, and
 * returns the index of newX corresponding to lowest x value in minX not
 * less than the lowest x value in originalX.
 */
private int extrapolateLess() {
    int minline = 0;

    /* Iterate through newX to find the lowest x value not less than the
     * lowest x value in originalX. The iteration starts at index 1 because
     * if index 0 was the lowest value, there would be no need for
     * filling (and thus this method would not be called).
     */
    for (int i = 1; i < newX.length; i++) {
        if (newX[i] < originalX[0]) {
            continue; //Keep searching
        } else {

            /* This block executes when we have found the min value */
            minline = i;
            break;
        }
    }
```

```
   /∗ Fill in the newY array with the values of the linear
    ∗ extrapolation below the lowest data point.
    ∗/
    for (int j = minline − 1; j >= 0; j−−) {
        newY[j] = this.interpolatedValue(newX[j], originalX[1],
                        originalX[0], originalY[1], originalY[0]);
            }



    return minline;
}

/∗ Fills in all values where the new x grid has values above the highest
 ∗ x point in the original grid with a linear extrapolation, and
 ∗ returns the index of newX corresponding to highest x value in minX not
 ∗ greater than the highest x value in originalX.
 ∗/
private int extrapolateMore() {
    int maxline = newX.length − 1;

    /∗ Iterate through newX (from the bottom up) to find the highest index
     ∗ for which newX has an x value not greater than the value at
     ∗ originalX[originalX.length − 1]. The iteration starts at
     ∗ newX.length − 2 because if newX.length − 1 was the max
     ∗ index, there would be no need for filling and thus this method
     ∗ would not be called.
```

```
     */
    for (int i = (newX.length − 2); i > 0; i−−) {
        if (newX[i] > originalX[originalX.length − 1]) {
            continue; //Keep searching
        } else {

            /* This block executes when we have found the max index */
            maxline = i;
            break;
        }
    }

    /* Fill in the newY array with the linear extrapolation above
     * the highest data point.
     */
    for (int j = maxline + 1; j < newX.length; j++) {
        newY[j] = this.interpolatedValue(newX[j],
        originalX[originalX.length − 2],
        originalX[originalX.length − 1],
        originalY[originalX.length − 2],
        originalY[originalX.length − 1]);
    }
    return maxline;
}

/* Performs the linear interpolation proper, between indices min and
```

```
 * max applied to newX.
 */
private void linearInterpolation(int min, int max) {

    /* First deal with the special cases where newX[min] = originalX[0]
     * and/or newX[max] = originalX[originalX.length − 1] (as opposed
     * to simply being greater than or less than respectively, which
     * is all we checked for when calculating min and max). If either of
     * these is the case we have to directly copy the original y values
     * over. Integers minshift and maxshift keep track of if this happens
     * so that we can iterate properly in the next step.
     */
    int minshift = 0;
    int maxshift = 0;
    if (newX[min] == originalX[0]) {
        newY[min] = originalY[0];
        minshift++;
    }
    if (newX[max] == originalX[originalX.length − 1]) {
        newY[max] = originalY[originalY.length − 1];
        maxshift++;
    }

    /* Iterate over all the remaining values, performing the linear
     * interpolation.
     */
```

```
    /∗ Keeps track of where we previously 'split' the old x and y values
     ∗ so we can save time searching for the new splitpoint.
     ∗/
    int oldSplit = 0;
    for (int i = min + minshift; i < max + 1 − maxshift; i++) {

        /∗ Find the point at which to 'split' originalX and originalY (i.e.
         ∗ we want the x and y values to each side of the new x value.
         ∗/
        int splitPoint = this.findIndex(newX[i], oldSplit);
        newY[i] = this.interpolatedValue(newX[i], originalX[splitPoint],
                originalX[splitPoint + 1], originalY[splitPoint],
                originalY[splitPoint + 1]);
        oldSplit = splitPoint;
    }
}

/∗ Finds the index of the x value in originalX that is closest to but
 ∗ not above the given double. Additionally takes an integer argument
 ∗ indicating where it should start the search.
 ∗/
private int findIndex(double comparator, int startpoint) {
    int index = 0;

    /∗ Iterate through originalX to search for the desired index, stopping
```

```
     * when we find the first x value greater than comparator, then
     * returning that index minus one. If there is an index in originalX
     * for which the x value is equal to comparator, then return that
     * index.
     */

    for (int i = startpoint; i < originalX.length - 1; i++) {
        if (originalX[i] < comparator) {
            continue; //Keep searching
        } else if (originalX[i] == comparator) {
            index = i;
            break;
        } else if (originalX[i] > comparator) {
            index = i - 1;
            break;
        }
    }
    return index;
}

/* Calculates the interpolated value for these points */
private double interpolatedValue(double x, double x_0, double x_1,
        double y_0, double y_1) {

    double slope = (y_1 - y_0)/(x_1 - x_0);
```

```
        return y_0 + ((x − x_0) ∗ slope);
    }


    /∗ Returns the new interpolated y values corresponding to the x values
     ∗ specified when the class was initialized.
     ∗/
    double[] returnInterpolation() {
        return newY;
    }


    /∗ Reverses the order of elements in an array, using a stack ∗/
    private double[] reverse(double[] xArray) {
        double[] reversedArray = new double[xArray.length];
        ArrayDeque <Double>stack = new ArrayDeque();

        for (int i = 0; i < xArray.length; i++){
            stack.push(xArray[i]);
        }
        for (int j = 0; j < xArray.length; j++){
            reversedArray[j] = stack.pop().doubleValue();
        }
        return reversedArray;
    }
}
```

A.1.5 Complex.java

```
/*
 * Complex
 *
 * Version 1.3
 *
 * 01/30/10
 *
 */

package edu.missouri.stardust.absscat;

/**
 * Complex is a simple utility class to more easily handle the required complex
 * operations for the rest of the package. No optimizations have been made
 * for speed.
 *
 * @author Adrian Corman
 * @version 1.3
 */
public class Complex {

    private final double real;
    private final double imaginary;

    /**
     * The only constructor for this class. Initializes the real and imaginary
```

```
 * parts of this complex number.
 *
 * @param real the real part of this complex number.
 * @param imaginary the imaginary part of this complex number.
 */
public Complex(double real, double imaginary) {

    this.real = real;
    this.imaginary = imaginary;

}
/**
 * Returns the real part of this complex number.
 *
 * @return Re(this).
 */
public double real() {
    return real;
}

/**
 * Returns the imaginary part of this complex number.
 *
 * @return Im(this).
 */
public double imaginary() {
```

```
        return imaginary;
    }

    /**
     * Returns a new complex number whose value is (this + addend), when
     * addend is another complex number.
     *
     * @param addend the complex number to be added to this complex number.
     * @return this + addend.
     */
    public Complex plus(Complex addend) {
        double real_sum = real + addend.real();
        double imaginary_sum = imaginary + addend.imaginary();

        return new Complex(real_sum, imaginary_sum);
    }

    /**
     * Returns a new complex number whose value is (this + addend), when
     * addend is a double. This eliminates the need to convert addend
     * to a new Complex object for simple addition.
     *
     * @param addend the real double value to be added to this complex number.
     * @return this + addend.
     */
    public Complex plus(double addend) {
```

```
    double real_sum = real + addend;

    return new Complex(real_sum, imaginary);
}

/**
 * Returns a new complex number whose value is (this - subtrahend), when
 * subtrand is another complex number.
 *
 * @param subtrahend the complex number to be subtracted from this complex
 * number.
 * @return this - subtrahend.
 */
public Complex minus(Complex subtrahend) {
    double real_difference = real - subtrahend.real();
    double imaginary_difference = imaginary - subtrahend.imaginary();

    return new Complex(real_difference, imaginary_difference);
}

/**
 * Returns a new complex number whose value is (this - subtrahend), when
 * subtrahend is a double. This eliminates the need to convert
 * subtrahend into a new Complex object for simple subtraction.
 *
 * @param subtrahend the real double to be subtracted from this complex
```

```
 ∗ number.
 ∗ @return this − subtrahend.
 ∗/
public Complex minus(double subtrahend) {
    double real_difference = real − subtrahend;

    return new Complex (real_difference, imaginary);
}

/∗∗
 ∗ Returns a new complex number whose value is (this ∗ factor), when
 ∗ factor is another complex number.
 ∗
 ∗ @param factor the complex number to be multiplied with this complex
 ∗ number.
 ∗ @return this ∗ factor.
 ∗/
public Complex times(Complex factor) {
    double real_product = (real ∗ factor.real())
                        − (imaginary ∗ factor.imaginary());
    double imaginary_product = (real ∗ factor.imaginary()) +
                             (imaginary ∗ factor.real());

    return new Complex (real_product, imaginary_product);
}
```

```
/**
 * Returns a new complex number whose value is (this * factor), when
 * factor is a double. This elimainates the need to convert factor into
 * a new Complex object for simple multiplication.
 *
 * @param factor the double to be multiplied with this complex number.
 * @return this * factor.
 */
public Complex times(double factor) {
    double real_product = real * factor;
    double imaginary_product = imaginary * factor;

    return new Complex (real_product, imaginary_product);
}

/**
 * Returns a new complex number whose value is (this / divisor), when
 * divisor is another complex number.
 *
 * @param divisor the complex number by which this will be divided.
 * @return this / divisor.
 */
public Complex divide(Complex divisor) {
    double real_quotient = ((real * divisor.real())
                            + (imaginary * divisor.imaginary()))
                            / ((divisor.real() * divisor.real())
```

```
                              + (divisor.imaginary() * divisor.imaginary()));
    double imaginary_quotient = ((imaginary * divisor.real())
                                 - (real * divisor.imaginary()))
                                 / ((divisor.real() * divisor.real())
                               + (divisor.imaginary() * divisor.imaginary()));

    return new Complex(real_quotient, imaginary_quotient);
}

/**
 * Returns a new complex number whose value is (this / divisor), when
 * divisor is a double. This elimainates the need to convert divisor
 * into a new Complex object for simple division.
 *
 * @param divisor the double by which this will be divided.
 * @return this / divisor.
 */
public Complex divide(double divisor) {
    double real_quotient = real / divisor;
    double imaginary_quotient = imaginary / divisor;

    return new Complex(real_quotient, imaginary_quotient);
}

/**
 * Returns the square of a complex number.
```

```
 *
 * @return this * this.
 */
public Complex squared() {
    double real_value = (real * real) - (imaginary * imaginary);
    double imaginary_value = (2 * real * imaginary);

    return new Complex(real_value, imaginary_value);
}

/**
 * Returns the absolute value of a complex number.
 *
 * @return |this|
 */
public double abs() {

    return Math.sqrt((real * real) + (imaginary * imaginary));
}

/**
 * Returns the square of the absolute value of a complex number.
 *
 * @return |this|^2
 */
public double absSquared() {
```

```
        return ((real * real) + (imaginary * imaginary));
    }

    /**
     * Returns the principle value of the natural logarithm of a complex
     * number, given by ln(z) = ln(|z|) + i tan^-1(Im(z)/Re(z)).
     *
     * @return ln(this).
     */
    public Complex ln() {
        double real_part = Math.log(this.abs());
        double imaginary_part = Math.atan2(imaginary, real);

        return new Complex(real_part, imaginary_part);
    }

}
```

A.1.6 Calculations.java

```
/*
 * Calculations
 *
 * Version 1.3
 *
```

```
 * 01/30/10
 *
 */

package edu.missouri.stardust.absscat;

/**
 * Calculations takes a prepared set of n and k data and generates the
 * absorption and scattering coefficients corresponding to those sets, combined
 * with a user-supplied weighting factor for each set. Calculations performs
 * most of the needed mathematics itself, but the required integrands are
 * generated by calling on the SizeIntegrator class. The required complex
 * mathematics is provided by the included Complex class.
 *
 * These calculations are based on theoretical work found in Min, M.,
 * Hovenier, J. W., and de Koter, A., Astronomy and Astrophysics, v. 404,
 * p. 35-46, 2003.
 *
 * @author Adrian Corman
 * @version 1.3
 * @see Complex
 * @see SizeIntegrator
 * @see <a href="http://www.aanda.org/index.php?option=article&access=
 * bibcode&bibcode=2003A%2526A...404...35MFUL">Min et al.</a>
 */
class Calculations {
```

```
/* A note on the methodology used in these calculations: for all cases,
 * it is possible to split the equations for the absorption and scattering
 * coefficients into three parts. The first part is comprised of constants
 * and wavelength data, the second is comprised of the part involving
 * operations on complex numbers, and the third is dependant on r and
 * thus is subject to integration over the grain size distribution. This
 * class calculates the first two of these parts, calling on the class
 * SizeIntegrator to calculate the third. Then this class combines the
 * three parts and as a final step calculates the weighted average
 * of all the nk data files.
 */

/* The parameters of the calculations */
private final String[] parameterArray;

/* The number of nk files */
private final int numberOfNKFiles;

/* The data from the nk data files */
private final double[][][] nkData;

/* Holds the n and k values from nkData after conversion into Complex
 * objects. The first index represents the number of the original nk data
 * file, and the second represents the line number of each data set.
 */
```

```
private final Complex[][] complexNK;

/* The final set of absorption and scattering coefficients. The first
 * index represents the line number of the data set, and the second
 * represents the column of the data set (0 = wavelengths, 1 = absorption
 * coefficients, 2 = scattering coefficients).
 */
private final double[][] finalResult;

/* The only constructor for this class. Takes the String array representing
 * the parameters of the calculations, and a double array with the n and
 * k data from each data file.
 */
Calculations(String[] parameterArray, double[][][] nkData) {
    this.parameterArray = parameterArray;
    numberOfNKFiles = Integer.parseInt(parameterArray[0]);
    this.nkData = nkData;
    complexNK = this.complexConversion();
    finalResult = this.applyWeighting(this.unweightedCalculation());
}

/* Converts the array of n and k values into an array of Complex objects */
private Complex[][] complexConversion() {
    Complex[][] complexArray = new Complex[nkData.length][nkData[0].length];
    for (int i = 0; i < nkData.length; i++) {
        for (int j = 0; j < nkData[0].length; j++) {
```

```
                complexArray[i][j] = new Complex(nkData[i][j][1],
                        nkData[i][j][2]);
            }
        }
        return complexArray;
    }

    /* A wrapper method to correctly select and call on the various other
     * methods of this class, in order to obtain the set of final results
     * before the weighted average.
     */
    private double[][][] unweightedCalculation() {

        /* The results before the unweighted average */
        double[][][] unweightedResult =
                new double[numberOfNKFiles][nkData[0].length][2];

        /* Perform the grain shape and size calculations on each of the
         * nk data files.
         */
        for (int i = 0; i < numberOfNKFiles; i++) {

            /* The shape distribution for this data set */
            String shape = parameterArray[(i * 7) + 4];

            /* The size distribution for this data set */
```

```
String size = parameterArray[(i * 7) + 5];

/* The size distribution parameters for this data set */
double[] distributionParameters = new double[3];
distributionParameters[0] =
        Double.parseDouble(parameterArray[(i * 7) + 6]);
if (size.equalsIgnoreCase(”single”)) {

    /* Double.parseDouble can’t handle a null input so in the
     * case of a single grain size don’t do anything for the
     * indices 1 and 2 (they are already filled with 0 when
     * the array is created.
     */
} else {
distributionParameters[1] =
        Double.parseDouble(parameterArray[(i * 7) + 7]);
distributionParameters[2] =
        Double.parseDouble(parameterArray[(i * 7) + 8]);
}

/* Send the data set to the proper method, along with the size
 * distribution.
 */
if (shape.equalsIgnoreCase(”spherical”)) {
    unweightedResult[i] = this.calculateSpherical(size,
            distributionParameters, i);
```

```
        } else if (shape.equalsIgnoreCase(”cde”)) {
            unweightedResult[i] = this.calculateCDE(size,
                    distributionParameters, i);
        } else if (shape.equalsIgnoreCase(”cds”)) {
            unweightedResult[i] = this.calculateCDS(size,
                    distributionParameters, i);
        } else if (shape.equalsIgnoreCase(”dhs”)) {
            unweightedResult[i] = this.calculateDHS(size,
                    distributionParameters, i);
        } else {
            /* If this block executes there has been a formatting error
             * in the input file.
             */
            ConsoleOutput.incorrectShape();
            System.exit(0); //Fatal error
        }
    }
    return unweightedResult;
}

/* Calculates the absorption and scattering coefficients for a nk data
 * set in the case of spherical grains, with a given size distribution.
 * The set parameter refers to the number of the data set we are working
 * with.
 */
private double[][] calculateSpherical(String size,
```

```
        double[] parameters, int set) {

    /* Holds the result of the calculation for this set */
    double[][] sphericalResult =
            new double[nkData[0].length][2];

    /* Gets and holds the result of the integration. integral[0] is the
     * result for the absorption coefficient, integral[1] is the result for
     * the scattering coefficient. Additionally, output a status message
     * if verbose mode is active.
     */
    ConsoleOutput.integrating(size);
    SizeIntegrator sphericalIntegrator = new SizeIntegrator(size,parameters);
    double []integral = sphericalIntegrator.getIntegration();

    ConsoleOutput.nonRTerms(”spherical”); //Output status for verbose
    for (int i = 0; i < nkData[0].length; i++){
    sphericalResult[i][0] = this.sphericalAbsNonR(nkData[set][i][0],
            complexNK[set][i]) * integral[0];
    sphericalResult[i][1] = this.sphericalScaNonR(nkData[set][i][0],
            complexNK[set][i]) * integral[1];
    }
    return sphericalResult;
}

/* Calculates the alpha value needed in the equations for spherical dust
```

```
 * grains.
 */
private Complex calculateSphericalAlpha(Complex m) {
            Complex numerator = (m.squared()).minus(1.0);
            Complex denominator = (m.squared()).plus(2.0);
            return numerator.divide(denominator);
}

/* Calculates the absorption and scattering coefficients for a nk data set
 * in the case of a continuuous distribution of ellipsoids, for a given
 * size distribution. The set parameter refers to the data set we are
 * working with.
 */
private double[][] calculateCDE(String size, double[] parameters, int set) {
    /* Holds the result of the calculation for this set */
    double[][] cdeResult =
            new double[nkData[0].length][2];

    /* Gets and holds the result of the integration. integral[0] is the
     * result for the absorption coefficient, integral[1] is the result for
     * the scattering coefficient.Additionally, output a status message
     * if verbose mode is active.
     */
    ConsoleOutput.integrating(size);
    SizeIntegrator cdeIntegrator = new SizeIntegrator(size,parameters);
    double[] integral = cdeIntegrator.getIntegration();
```

```
    ConsoleOutput.nonRTerms(”CDE”); //Output a status message for verbose
    for (int i = 0; i < nkData[0].length; i++){
    cdeResult[i][0] = this.otherAbsNonR(nkData[set][i][0],
            complexNK[set][i],”cde”) ∗ integral[0];
    cdeResult[i][1] = this.otherScaNonR(nkData[set][i][0],
            complexNK[set][i],”cde”) ∗ integral[1];
    }
    return cdeResult;
}

/∗ Calculates the alpha value needed in the equations for a continuuous
 ∗ distribution of ellipsoids.
 ∗/
private Complex calculateCDEAlpha(Complex m) {
        Complex numerator = (m.squared()).times(2.0).times(m.squared().ln());
        Complex denominator = (m.squared()).minus(1.0);
        return numerator.divide(denominator).minus(2.0);
}

/∗ Calculates the absorption and scattering coefficients for a nk data set
 ∗ in the case of a continuuous distribution of sphereoids, for a given
 ∗ size distribution. The set parameter refers to the data set we are
 ∗ working with.
 ∗/
private double[][] calculateCDS(String size, double[] parameters, int set) {
```

```
    /* Holds the result of the calculation for this set */
    double[][] cdsResult =
            new double[nkData[0].length][2];

    /* Gets and holds the result of the integration. integral[0] is the
     * result for the absorption coefficient, integral[1] is the result for
     * the scattering coefficient.Additionally, output a status message
     * if verbose mode is active.
     */
    ConsoleOutput.integrating(size);
    SizeIntegrator cdsIntegrator = new SizeIntegrator(size,parameters);
    double[] integral = cdsIntegrator.getIntegration();

    ConsoleOutput.nonRTerms("CDS"); //Output a status message for verbose
    for (int i = 0; i < nkData[0].length; i++){
    cdsResult[i][0] = this.otherAbsNonR(nkData[set][i][0],
            complexNK[set][i],"cds") * integral[0];
    cdsResult[i][1] = this.otherScaNonR(nkData[set][i][0],
            complexNK[set][i],"cds") * integral[1];
    }
    return cdsResult;
}

/* Calculates the alpha value needed in the equations for a continuuous
 * distribution of sphereoids.
 */
```

```
private Complex calculateCDSAlpha(Complex m) {
        Complex firstTerm = (m.squared().ln()).times(1.0/3.0);
        Complex secondTerm =
                (m.squared().plus(1.0).divide(2.0).ln()).times(4.0/3.0);
        return firstTerm.plus(secondTerm);
}

/* Calculates the absorption and scattering coefficients for a nk data set
 * in the case of a distribution of hollow spheres. The set parameter
 * refers to the data set we are working with.
 */
private double[][] calculateDHS(String size, double[] parameters, int set) {
    /* Holds the result of the calculation for this set */
    double[][] dhsResult =
            new double[nkData[0].length][2];

    /* Gets and holds the result of the integration. integral[0] is the
     * result for the absorption coefficient, integral[1] is the result for
     * the scattering coefficient.Additionally, output a status message
     * if verbose mode is active.
     */
    ConsoleOutput.integrating(size);
    SizeIntegrator dhsIntegrator = new SizeIntegrator(size,parameters);
    double[] integral = dhsIntegrator.getIntegration();

    /* Will perform the needed numerical integration for the scattering
```

```
      * case.
      */
     IterativeSimpsons dhs_sca_Integrator =
               new IterativeSimpsons(1.0, 0, Main.epsilon);

     ConsoleOutput.nonRTerms(”DHS”); //Output a status message for verbose
     for (int i = 0; i < nkData[0].length; i++){
          double wavelength = nkData[set][i][0];
          Complex m = complexNK[set][i];
          dhsResult[i][0] =
                    this.otherAbsNonR(wavelength, m ,”dhs”) * integral[0];

     /* Unfortunately, the simple relationship between the scattering and
      * absorption coefficients present in the other shape distributions
      * does now hold here, so we have to perform a numerical integration.
      */
          Function f = new Function.f_DHS_sca(m);
          dhsResult[i][1] = dhs_sca_Integrator.integrate(f) *
                    (8.0 * Math.pow(this.k(wavelength), 4.0) *
                    Math.PI * integral[1]) / 9;
          }
     return dhsResult;
}

/* Calculates the alpha value needed in the equations for a distribution
 * of hollow spheres.
```

```
 */
private Complex calculateDHSAlpha(Complex m) {
            Complex firstNumerator = (m.squared()).times(6.0).plus(3.0);
            Complex firstDenominator = (m.squared()).times(2.0).minus(2.0);
            Complex firstTerm = firstNumerator.divide(firstDenominator);
            Complex secondTerm = (m.squared()).times(2.0).plus(1.0);
            Complex thirdNumerator = (m.squared()).plus(2.0);
            Complex thirdDenominator = (m.squared()).times(9.0);
            Complex thirdTerm = thirdNumerator.divide(thirdDenominator);
            return firstTerm.times(secondTerm.times(thirdTerm).ln());
}

/* Calculates the part of the equation for the absorption coefficient
 * of spherical shaped particles that does not depend on r (the part
 * that does is handled in the integration).
 */
private double sphericalAbsNonR (double wavelength, Complex m) {
      double firstTerm = 4.0*Math.PI*this.k(wavelength);
      double secondTerm = this.calculateSphericalAlpha(m).imaginary();
      return firstTerm*secondTerm;
}

/* Calculates the part of the equation for the scattering coefficient
 * of spherical shaped particles that does not depend on r (the part
 * that does is handled in the integration).
 */
```

```
private double sphericalScaNonR (double wavelength, Complex m) {
    double firstTerm = 8.0∗Math.PI∗Math.pow(this.k(wavelength), 4.0) ∗
            (1.0/3.0);
    double secondTerm = this.calculateSphericalAlpha(m).absSquared();
    return firstTerm∗secondTerm;
}

/∗ Calculates the part of the equation for the absorption coefficient
 ∗ for CDE, CDS, and DHS shape distributions that does not depend
 ∗ on r (the part that does is handled in the integration).
 ∗/
private double otherAbsNonR (double wavelength, Complex m, String shape) {
    Complex alpha = null;
    if (shape.equalsIgnoreCase(”CDE”)) {
        alpha = this.calculateCDEAlpha(m);
    } else if (shape.equalsIgnoreCase(”CDS”)) {
        alpha = this.calculateCDSAlpha(m);
    } else if (shape.equalsIgnoreCase(”DHS”)) {
        alpha = this.calculateDHSAlpha(m);
    }
    double firstTerm = 4.0∗Math.PI∗this.k(wavelength) ∗ (1.0/3.0);
    double secondTerm = alpha.imaginary();
    return firstTerm∗secondTerm;
}

/∗ Calculates the part of the equation for the scattering coefficient
```

```
 * for the CDE and CDS shape distributions that does not depend on
 * r (the part that does is handled in the integration).
 */
private double otherScaNonR(double wavelength, Complex m, String shape) {
    Complex alpha = null;
    if (shape.equalsIgnoreCase(”CDE”)) {
        alpha = this.calculateCDEAlpha(m);
    } else if (shape.equalsIgnoreCase(”CDS”)) {
        alpha = this.calculateCDSAlpha(m);
    }
    double firstNumerator = 4.0*Math.PI*this.k(wavelength);
    double firstDenominator = 3.0*this.sigma(wavelength, m);
    double firstTerm = firstNumerator / firstDenominator;
    double secondTerm = alpha.imaginary();
    return firstTerm*secondTerm;
}

/* Calculates the part of sigma (needed for the non-spherical cases) that
 * is not dependant on the size. The part that is dependant on the size
 * (a factor of 1/r^3) has been incorporated into the integrations.
 */
private double sigma (double wavelength, Complex m) {
    double firstTerm = 9.0 /(2.0*Math.pow(this.k(wavelength), 3.0));
    double secondTerm = m.squared().imaginary();
    double thirdTerm = 1.0 /(m.squared().minus(1.0).absSquared());
    return firstTerm * secondTerm * thirdTerm;
```

```
}

/* A very simple method to calculate the k [i.e. (2 * pi)/(wavelength)] for
 * a given wavelength, to help simplify the rest of the calculations.
 */
private double k(double wavelength) {
   return (2.0 * Math.PI)/(wavelength);
}

/* Performs the averaging over all the grain species, using the weights
 * specified in the parameter file.
 */
private double[][] applyWeighting(double[][][] uncombinedArray) {

    /* Holds the final result of the weighted averaging */
    double[][] weightedAverage = new double[nkData[0].length][3];

    for (int i = 0; i < nkData[0].length; i++) {
        double sumOfWeights = 0;
        double weightedAbs = 0;
        double weightedSca = 0;
        weightedAverage[i][0] = nkData[0][i][0]; //The wavelengths
        for (int j = 0; j < numberOfNKFiles; j++) {
            double weight = Double.parseDouble(parameterArray[(j * 7) + 9]);
            weightedAbs = weightedAbs + (weight * uncombinedArray[j][i][0]);
            weightedSca = weightedSca + (weight * uncombinedArray[j][i][1]);
```

```
                sumOfWeights = sumOfWeights + weight;
            }
            weightedAverage[i][1] = weightedAbs/sumOfWeights;
            weightedAverage[i][2] = weightedSca/sumOfWeights;
        }
        return weightedAverage;
    }

    /* Returns the array containing the final results of the absorption and
     * scattering calculations.
     */
    double[][] returnResult() {
        return finalResult;
    }


}
```

A.1.7 Integrator.java

```
/*
 * SizeIntegrator
 *
 * Version 3.1
 *
 * 01/30/10
```

```
 *
 */

package edu.missouri.stardust.absscat;

/**
 * SizeIntegrator calculates the integral over the part of the equations for
 * the absorption and scattering coefficients that depend only on r. This
 * essentially involves the r-dependant term from the single grain size
 * distribution equations, the size distribution formula, and the cross
 * sectional area (2*pi*r^2). These elements are combined to produce
 * the equations in this class. The elements not depending on r are calculated
 * by the Calculations class, where additional description of the mathematics
 * can be found.
 *
 * For the single grain size case, or for the
 * MRN grain size distribution, the integral over these equations has a
 * closed form solution so those equations are evaluated directly.
 * In the case of the KMH grain size distribution, there is no general closed
 * form solution so a numerical integration is performed, subject to the
 * error bound in the Main class (either a default value, or specified on the
 * command line when absscat is called).
 *
 * @author Adrian Corman
 * @version 3.1
 * @see Calculations
```

```
 */
class SizeIntegrator {

    /* The grain size distribution parameters */
    private final double[] parameters;

    /* The result of the integration of this grain size distribution over
     * the specified parameters.
     */
    private final double[] integrationResult;


    /* The only constructor for this class. Takes the array of size distribution
     * parameters, and a String representing which distribution is being
     * integrated over.
     */
    SizeIntegrator(String size, double[] parameters) {
        this.parameters = parameters;

        if (size.equalsIgnoreCase(”single”)) {
            integrationResult = this.singleIntegral();
        } else if (size.equalsIgnoreCase(”MRN”)) {
            integrationResult = this.mrnIntegral();
        } else {
            integrationResult = this.kmhIntegral();
        }
```

```
}

/* Calculates the value of the integral for a single grain size */
private double[] singleIntegral() {

    /* Check the parameter array for errors */
    ParameterChecker.checkSingle(parameters);
    double[] integral = new double[2];
    integral[0] = parameters[0]/Math.PI;
    integral[1] = Math.pow(parameters[0], 4.0)/Math.PI;
    return integral;
}

/* Calculates the value of the integral for the MRN grain size
 * distribution.
 */
private double[] mrnIntegral() {

    /* Check the parameter array for errors */
    ParameterChecker.checkMRN(parameters);
    double[] integral = new double[2];

    double q = parameters[1];
    double min = parameters[0];
    double max = parameters[2];
```

```
/∗ Calculate the normalization constant ∗/
double normalization = (1/(1.0 − q)) ∗ (Math.pow(max,(1.0 − q)) −
                                        Math.pow(min,(1.0 − q)));

/∗ If q = 2 for the absorption case, we have to be careful because
 ∗ the integrand becomes (1/x) which has a different solution
 ∗ for the q!=2 situation. The same holds true for the scattering
 ∗ case when q=5.
 ∗/
if (q == 2) {

    /∗ Special (1/x) case for absorption ∗/
    integral[0] = ((Math.log(max / min))/Math.PI) / normalization;

    /∗ The normal scattering integral (as q != 5 here) ∗/
    double scaFirstTerm = 1/(Math.PI ∗ (5.0 − q));
    double scaSecondTerm = Math.pow(max,(5.0 − q));
    double scaThirdTerm = Math.pow(min, (5.0 − q));
    integral[1] =
            scaFirstTerm∗(scaSecondTerm − scaThirdTerm) / normalization;
} else if (q == 5) {

    /∗ Special (1/x) case for scattering ∗/
    integral[1] = ((Math.log(max / min))/Math.PI) / normalization;

    /∗ The normal absorption integral (as q != 2 here) ∗/
```

```
        double absFirstTerm = 1/(Math.PI ∗ (2 − q));
        double absSecondTerm = Math.pow(max,(2 − q));
        double absThirdTerm = Math.pow(min, (2 − q));
        integral[0] =
                absFirstTerm∗(absSecondTerm − absThirdTerm) / normalization;
    } else {
        /∗ The integral for absorption in all other cases ∗/
        double absFirstTerm = 1/(Math.PI ∗ (2 − q));
        double absSecondTerm = Math.pow(max,(2 − q));
        double absThirdTerm = Math.pow(min, (2 − q));
        integral[0] =
                absFirstTerm∗(absSecondTerm − absThirdTerm) / normalization;

        /∗ The integral for scattering in all other cases ∗/
        double scaFirstTerm = 1/(Math.PI ∗ (5 − q));
        double scaSecondTerm = Math.pow(max,(5 − q));
        double scaThirdTerm = Math.pow(min, (5 − q));
        integral[1] =
                scaFirstTerm∗(scaSecondTerm − scaThirdTerm) / normalization;
    }
    return integral;
}

/∗ Calculates the value of the integral in the case of the KMH grain size
 ∗ distribution, by calling on the methods forming the algorithm for
 ∗ the iterative adaptive Simpson’s method.
```

```
 */
private double[] kmhIntegral() {

    /* Holds the results of the calculations */
    double[] results = new double[3];

    /* Check the parameter array for errors */
    ParameterChecker.checkKMH(parameters);

    /* The integrals for both the absorption and scattering cases when
     * the size distribution is KMH does not have a closed form
     * solution for arbitrary values of the parameters. Thus, we must
     * perform a numerical integration. Because this integration is
     * otherwise simple, we will use an adaptive Simpsons method,
     * with the accuracy of the integration given by the epsilon in the Main
     * class. The normalization constant will also be obtained in this
     * way.
     */
    double q = parameters[1];
    double r_0 = parameters[2];
    Function f_norm = new Function.f_KMH_norm(q, r_0);
    Function f_abs = new Function.f_KMH_abs(q, r_0);
    Function f_sca = new Function.f_KMH_sca(q, r_0);

    IterativeSimpsons kmhIntegrator =
            new IterativeSimpsons(1.0/parameters[0],0,Main.epsilon);
```

```
    double normalization = kmhIntegrator.integrate(f_norm);
    results[0] = kmhIntegrator.integrate(f_abs) / normalization;
    results[1] = kmhIntegrator.integrate(f_sca) / normalization;

    return results;
}

/* Returns the value of the integration calculated when this class
 * was initialized.
 */
double[] getIntegration(){
    return integrationResult;
}



/* A small nested class to check the size parameters for errors */
private static class ParameterChecker {

    /* Checks the given parameters in the case of a single grain
     * size.
     */
    private static void checkSingle(double[] parameters) {
        if (parameters[0] == 0) {
            /* Grain size has to be greater than zero! */
            ConsoleOutput.zeroGrainSize();
```

```
        System.exit(0); //The result would just be zero
    } else if (parameters[0] < 0) {
        ConsoleOutput.negativeGrainSize();
        System.exit(0); //The result would be meaningless
    } else {
        return; //Everything is fine in this case
    }
}

/* Checks the given parameters in the case of a MRN grain size
 * distribution.
 */
private static void checkMRN(double[] parameters) {
      if (parameters[0] < 0) {
        /* The minimum grain size must be positive */
        ConsoleOutput.negativeMinGrainSize();
        System.exit(0); //The result would be meaningless
    } else if (parameters[2] == 0) {
        /* The maximum grain size shouldn't be zero */
        ConsoleOutput.zeroMaxGrainSize();
        System.exit(0); //The result would be meaningless
    } else if (parameters[2] < 0) {
        /* The maximum grain size must be positive */
        ConsoleOutput.negativeMaxGrainSize();
        System.exit(0); //The result would be meaningless
    } else if (parameters[0] > parameters[2]) {
```

```
            /* The maximum grain size has to be larger than the minimum
             * grain size.
             */
            ConsoleOutput.minMoreThanMax();
            System.exit(0); //The result would be meaningless
        } else {
            return; //Everything is fine in this case
        }
    }

    /* Checks the given parameters in the case of a KMH grain size
     * distribution.
     */
    private static void checkKMH(double[] parameters) {
        if (parameters[0] < 0) {
            /* The minimum grain size must be positive */
            ConsoleOutput.negativeMinGrainSize();
            System.exit(0); //The result would be meaningless
        } else if (parameters[2] == 0) {
            /* The falloff grain size cannot be zero */
            ConsoleOutput.zeroFalloffGrainSize();
            System.exit(0); //Would include a division by zero.
        } else if (parameters[2] < 0) {
            /* The falloff grain size must be positive */
            ConsoleOutput.negativeFalloffGrainSize();
            System.exit(0); //The integral would diverge
```

```
            } else if (parameters[0] > parameters[2]) {
                /* The falloff grain size has to be larger than the minimum
                 * grain size.
                 */
                ConsoleOutput.falloffLessThanMin();
                System.exit(0); //The result would be meaningless
            } else {
                return; //Everything is fine in this case
            }
        }
    }
}
```

A.1.8 Function.java

```
/*
 * To change this template, choose Tools | Templates
 * and open the template in the editor.
 */

package edu.missouri.stardust.absscat;

interface Function {

  double evaluate(double x);
```

```
/* Because the KMH integral has limits from r_min to infinity, it
 * is necessassary to do a change of variables on the integral
 * in order to obtain an integral of finite limits. This is done
 * by replacing r with 1/t => dr = -(1/t^2), and the limits change
 * into 1/r_min and 0. This can be integrated using Simpson's
 * method. The next three classes reflect this.
 */

/* Inner class representing the normalization integrand for a KMH
 * distribution.
 */
class f_KMH_norm implements Function {

    private final double q;

    /* The falloff size parameter */
    private final double r_0;

    f_KMH_norm(double q, double r_0){
      this.q = q;
      this.r_0 = r_0;
    }
    public double evaluate(double x){
        return Math.pow(x, q) * Math.pow(Math.E, -(1.0/(x*r_0)));
      }
}
```

```
/* Inner class representing the r-term function to be integrated for a KMH
 * distribution, in the case of absorption.
 */
class f_KMH_abs implements Function {

    private final double q;

    /* The falloff size parameter */
    private final double r_0;

    f_KMH_abs(double q, double r_0){
      this.q = q;
      this.r_0 = r_0;
    }

    public double evaluate(double x){

      /* This function is straightforward when parameters[1] >= power,
       * because in this case f(0) = 0. In the case where parameters[2]
       * is less than the power, the first term has a negative exponent
       * and the numerical integration fails when x = 0 because
       * f(0) has an indeterminant form. However, because the limit of
       * f(x) as x->0 from the right is 0, we can set f(0) = 0 in this
       * case as well, giving us an accurate result when used as part
       * of the numerical integration.
```

```
        */
         if (x == 0){
              return 0;
         } else {
              return Math.pow(x, (q − 3.0)) ∗
                        Math.pow(Math.E, −(1.0/(x∗r_0)));
         }

      }

  }

/∗ Inner class representing the r−term function to be integrated for a KMH
 ∗ distribution, in the case of scattering.
 ∗/
class f_KMH_sca implements Function{

     private final double q;

     /∗ The falloff size parameter ∗/
     private final double r_0;

     f_KMH_sca(double q, double r_0){
        this.q = q;
        this.r_0 = r_0;
     }
```

```
    public double evaluate(double x){

      /* This function is straightforward when parameters[1] >= power,
       * because in this case f(0) = 0. In the case where parameters[2]
       * is less than the power, the first term has a negative exponent
       * and the numerical integration fails when x = 0 because
       * f(0) has an indeterminant form. However, because the limit of
       * f(x) as x−>0 from the right is 0, we can set f(0) = 0 in this
       * case as well, giving us an accurate result when used as part
       * of the numerical integration.
       */
        if (x == 0){
            return 0;
        } else {

            return Math.pow(x, (q − 6.0)) *
                    Math.pow(Math.E, −(1.0/(x*r_0)));
        }

    }
}

/* Inner class representing the DHS scattering function that must be
 * integrated (i.e. |alpha|^2.
 */
```

```
  class f_DHS_sca implements Function {

    private final Complex m;

    /* The only constructor for this class, initializes it for a given
     * Complex object m.
     */
    f_DHS_sca(Complex m){
      this.m = m;
    }

    public double evaluate(double x){

      Complex numerator =
           (m.squared().minus(1.0)).times(m.squared().times(2.0).plus(1.0));
      Complex denominatorOne =
            (m.squared().plus(2.0)).times(m.squared().times(2.0).plus(1.0));
      Complex denominatorTwo =
              (m.squared().minus(1.0)).squared().times(2.0).times(x);
      Complex alpha =
              numerator.divide(denominatorOne.minus(denominatorTwo));

      return alpha.absSquared();
    }
  }
}
```

A.1.9 IterativeSimpsons

```
/*
 * IterativeSimpsons
 *
 * Version 1.0
 *
 * 02/08/10
 *
 */

package edu.missouri.stardust.absscat;

import java.util.ArrayDeque;

/**
 * IterativeSimpsons performs an adaptive Simpson's method itegration on a
 * given function between given limits. The algorithm used is iterative, rather
 * than the more common recursive technique; this helps prevent runaway
 * memory problems.
 *
 * @author Adrian Corman
 * @version 1.0
 */
public class IterativeSimpsons {
```

```
/* The upper limit of the integration */
private final double upperLimit;

/* The lower limit of the integration */
private final double lowerLimit;

/* The desired error bound for this numerical integration */
private final double errorBound;

/**
 * The only constructor for this class. Initializes with the upper and
 * lower limits to the numerical integration, and a desired error bound.
 *
 * @param upperLimit the upper limit of the integration
 * @param lowerLimit the lower limit of the integration
 * @param errorBound the desired error bound for this integration
 */
public IterativeSimpsons(double upperLimit,
        double lowerLimit, double errorBound){

    this.upperLimit = upperLimit;
    this.lowerLimit = lowerLimit;
    this.errorBound = errorBound;
}
```

```
/* Calculates the numerical integration, using an iterative form of the
 * adaptive Simpson's method.
 *
 * Classically, the adaptive Simpson's method has been presented in a
 * recursive form; however, the recursive form can have
 * serious memory issues in the Java Virtual Machine's stack if the
 * integration does not quickly converge. If this happens, the
 * program will crash. Though this iterative method also uses a stack,
 * each element of the stack only contains 4 double values instead of the
 * entire memory footprint of the method, and so this danger is decreased.
 */
double integrate(Function f) {

    /* The methodology behind this particular iterative (not recursive)
     * implementation of the adaptive Simpson's method is as follows.
     * An ArrayDeque is used as a stack to hold a series of arrays,
     * each representing one division of the integration interval. As long
     * as there is an element inside the stack, there is at least one
     * division of the interval that has not yet been evaluated. So,
     * a while loop checks if the stack is empty or not, and if not
     * it performs a loop (and the integration is finished when the
     * stack is empty). Inside the loop, the top element of the stack
     * is removed for processing. Simpson's rule is used to evaluate
     * both sides of this interval, and then the error bound is checked.
     * If the error check passes, then the sum of the two calls to
     * Simpson's rule over this interval are added to the integration
```

```
 * sum, and then the next element of the stack is processed. If the
 * error check does not pass, then further subdivision is needed
 * and the loop adds two more elements into the stack, each representing
 * half of the previous subdivision. This process continues until all
 * the elements are processed, and the final sum is the value of the
 * integral to within the specified error bound.
 */

/* The stack */
ArrayDeque <double[]> stack = new ArrayDeque();

/* The next series of variables are used as placeholders for values
 * in each iteration of the loop over the stack. They are defined
 * here because to define them inside the loop would create redundant
 * object creation calls.
 */
double error; //The error, which is divided by two in each subdivision
double difference; //
double midpoint; //The middle of the subdivision
double left; //The minimum value of the subdivision
double right; //The maximum value of the dubdivision
double[] old = new double[5]; //Holds the stack arrays as removed

/* The initial values needed to begin the integration */
double[] initialCalcs = new double[5];
initialCalcs[0] = simpsonsRule(f,lowerLimit,upperLimit);
```

```
initialCalcs[1] = lowerLimit;
initialCalcs[2] = upperLimit;
initialCalcs[3] = errorBound;

stack.push(initialCalcs); //Push these values onto the stack
double integralSum = 0; //Holds the value of the integral as we sum

while (!stack.isEmpty()){
    old = stack.pop(); //Pop the top subdivision from the stack
    midpoint = (old[1] + old[2])/2.0;
    error = old[3];
    left = simpsonsRule(f,old[1],midpoint);
    right = simpsonsRule(f,midpoint,old[2]);
    difference = left + right − old[0];

    if (Math.abs(difference) <= 15.0 ∗ error){

        /∗ Executes when a subdivision is within the error bound ∗/
        integralSum += left + right + (difference / 15.0);
    } else {
        /∗ The new left hand subdivision ∗/
        double[] newLeft = new double[5];
        newLeft[0] = left;
        newLeft[1] = old[1];
        newLeft[2] = midpoint;
        newLeft[3] = error/2.0;
```

```
            stack.push(newLeft); //Push it to the stack

            /* The new right hand subdivision */
            double[] newRight = new double[5];
            newRight[0] = right;
            newRight[1] = midpoint;
            newRight[2] = old[2];
            newRight[3] = error/2.0;
            stack.push(newRight); //Push it to the stack
        }
    }
    return integralSum;
}

/* Calculates the Simpson's rule value for a given minimum and
 * maximum, with power representing the term in f that varies
 * over absorption and scattering.
 */
private double simpsonsRule(Function f, double min, double max) {
    double midpoint = (max + min) / 2.0;
    double height = (max - min);
    return (height/6.0) * (f.evaluate(min) + 4.0 * f.evaluate(midpoint) +
            f.evaluate(max));
}
```

```
}
```

A.1.10 FileOutput.java

```
/*
 * FileOutput
 *
 * Version 2.2
 *
 * 01/30/10
 *
 */

package edu.missouri.stardust.absscat;

import java.io.*;



/**
 * FileOutput outputs an array of data into a three column file of the
 * specified filename.
 *
 * @author Adrian Corman
 * @version 2.2
 */
```

```
class FileOutput {

    /* The file name to save this data to */
    private final String fileName;

    /* The data to be saved */
    private final double[][] dataArray;

    /* Flag indicating if an already existing file should be overwritten */
    private final boolean overwrite;

    /* The File object that will be manipulated */
    private File outputFile;

    /* The BufferedWriter that writes the file */
    private BufferedWriter bufferedOutput;

    /* The only constructor for this class */
    FileOutput(String fileName, double[][] dataArray, boolean overwrite){
        this.fileName = fileName;
        this.dataArray = dataArray;
        this.overwrite = overwrite;
    }

    /* Attempts to create and open fileName. If the file already exists, it
     * will output an error message and exit if the overwrite flag is set to
```

```
 * false, or delete the old file and create a new one of the same name
 * if it is set to true.
 */
private void createFile() {
    outputFile = new File(fileName);
    try {
        if (outputFile.createNewFile()) {

            /* This block executes if the file did not already exist and
             * the system was able to create it.
             */
            bufferedOutput = new BufferedWriter(new FileWriter(outputFile));
        } else {
            if (overwrite) {
                if (outputFile.delete()) {
                    outputFile.createNewFile();
                    /* This block executes if the file already exists,
                     * the overwrite flag is set to true, and the
                     * system was successfully able to delete the file.
                     */
                    bufferedOutput =
                            new BufferedWriter(new FileWriter(outputFile));
                } else {

                    /* This block executes if the file already exists,
                     * the overwrite flag is set to true, but the system
```

```
                 * was unable to delete the file (usually indicating
                 * a permissions error).
                 */
                ConsoleOutput.unableToDelete(fileName);
                System.exit(0); //Exit so the user can make changes
            }
        } else {

            /* This block executes if the file already exists, but
             * the overwrite flag is set to false (so the program
             * won't delete it and will exit.
             */
            ConsoleOutput.fileExistsNoOverwrite(fileName);
            System.exit(0);
        }
    }

} catch (IOException e) {

    /* This means there was an error trying to create and/or open the
     * file.
     */
    ConsoleOutput.unknownOutputError(fileName);
    System.exit(0);
}
```

```
}

/* Writes lines to the output file through bufferedOutput */
private void lineWriter() {
    for (int i = 0; i < dataArray.length; i++){
        try {
            for (int j = 0; j < 3; j++){
                String output = String.format(”%.” + Main.precision + ”E”,
                        dataArray[i][j]);
                bufferedOutput.write(output);
                if (j != 2) {
                    bufferedOutput.write(” ”);
                } else {
                    bufferedOutput.newLine();
                }
            }
        } catch (IOException e) {

            /* This block executes if there has been an error writing to
             * the file.
             */
            ConsoleOutput.writingError(fileName);
            System.exit(0);
        }
            }
}
```

```
    /* Closes bufferedOutput */
    private void closeFile() {
        try {
            bufferedOutput.close();
        } catch (IOException e) {

            /* This block executes if the system is unable to close the file,
             * which will happen if there is another Java program running
             * at the same time with this file open (for example, another
             * instance of absscat).
             */
            ConsoleOutput.closeError(fileName);
            System.exit(0);
        }

    }

    /* Activates the actual outputting process */
    void output() {
        this.createFile();
        this.lineWriter();
        this.closeFile();
    }

}
```

A.1.11 ConsoleOutput.java

```
/*
 * ConsoleOutput
 *
 * Version 2.3
 *
 * 01/30/10
 *
 */

package edu.missouri.stardust.absscat;

/**
 * ConsoleOutput contains the various messages that can be passed to the
 * console, both for ordinary operation and in the case of an error.
 *
 * @author Adrian Corman
 * @version 2.3
 */
class ConsoleOutput {

    /* The message to be displayed if more than one nk data file is present but
     * the files do not all use the same wavelength grid, and interpolation
     * has not been selected in the input file.
     */
```

```
static void needsInterpolation() {
    System.out.println();
    System.out.println(”The specified nk data files do not all have the ” +
            ”same wavelength grids. Please correct this,”);
    System.out.println(”or if interpolation by absscat is desired, ” +
            ”please specify yes for interpolation in the input”);
    System.out.println(”file and also provide a wavelength grid to ” +
            ”interpolate to. Exiting.”);
}

/∗ The file not found error message ∗/
static void fileNotFound(String filename) {
    System.out.println();
    System.out.println(”File ” + filename + ”cannot be located. Please ” +
            ”check that the input file contains the”);
    System.out.print(”proper path to this file and the correct filename. ” +
            ”Exiting.”);
}

/∗ The message displayed when the −help argument is given when absscat is
 ∗ called.
 ∗/
static void helpMessage() {
    System.out.println();
    System.out.println(”Usage: java −j absscat −inputfile [filename] ” +
            ”<optional flags>”);
```

```
System.out.println();
System.out.println(”absscat is a program designed to convert a set” +
        ” of n and k optical constants into a single”);
System.out.println(”file containing absorption and scattering ” +
        ”coefficients, with the grain shape distribution and”);
System.out.println(”size distribution specified for each n and k data ” +
        ”set. Please consult the readme file distributed”);
System.out.println(”with this program for additional instructions. ” +
        ”absscat accepts the following command line”);
System.out.println(”parameters: ”);
System.out.println();
System.out.println(” −inputfile [filename] (specifies which input ” +
        ”file absscat should use for processing, the”);
System.out.println(” only required parameter. Consult the readme ” +
        ”file for the format of this file.)”);
System.out.println();
System.out.println(” −verbose (outputs a series of messages ” +
        ”indicating the status of various operations as”);
System.out.println(” absscat operates, primarily intended for ” +
        ”resolving errors.)”);
System.out.println();
System.out.println(” −silent (suppresses all non−error messages” +
        ” generated by absscat, intended for batch”);
System.out.println(” processing.)”);
System.out.println();
System.out.println(” −overwrite (if this flag is enabled, ” +
```

```
        ”absscat will overwrite any existing file with”);
System.out.println(” the same name as the output file it generates”+
        ” Otherwise, absscat will display an error”);
System.out.println(” message and not produce output in order to ” +
        ”prevent accidental overwrites.)”);
System.out.println();
System.out.println(” −outputfile [filename](optionally specifies ” +
        ”an output file. If not specified, absscat”);
System.out.println(” will generate an outputfile that follows the” +
        ” format [inputfilename]_output.dat.)”);
System.out.println();
System.out.println(” −epsilon (optionally supplies a value for the” +
        ”desired error bound for the numerical integration”);
System.out.println(” which occurs if a KMH grain size” +
        ”distribution is selected.”);
System.out.println();
System.out.println(” −outputinterpolation (when selected, absscat” +
        ” will, in addition to outputting the final result,”);
System.out.println(” output the interpolated nk data files it” +
        ” used for the calculations. The interpolated”);
System.out.println(” files are named [nkdatafilename]_interp.dat.” +
        ” Please note that if this option is selected,”);
System.out.println(” the interpolation flag must be set as yes” +
        ” in the input file, and a wavelength grid to”);
System.out.println(” be interpolated to must also be provided in” +
        ” that file. If not, the program will output an”);
```

```
    System.out.println(” error and exit. See the readme file for more” +
            ”information.”);
    System.out.println();
    System.out.println(” −onlyinterpolate (when selected, absscat will” +
            ” perform interpolation, but instead of continuing”);
    System.out.println( ”the calculations will output the ” +
            ”interpolated nk data files and quit processing.”);
    System.out.println(” See the −outputinterpolation option or the” +
            ”readme file for more information.”);
    System.out.println();
    System.out.println(” −help (displays this help message.)”);
}

/∗ The error message displayed when the −inputfile argument is not
 ∗ given when absscat is called.
 ∗/
static void noArguments() {
    System.out.println();
    System.out.println(”The input file absscat is to process has not” +
            ” been specified. Please use the”);
    System.out.println(”−inputfile [filename] option when calling absscat.”+
            ” Additional instructions are available by”);
    System.out.println(”calling absscat with the −help flag or in the ” +
            ”readme file distributed with this program.”);
}
```

```
/∗ The message displayed when absscat starts to read in the input file,
 ∗ if −verbose has been selected.
 ∗/
static void beginWorking() {
    if (Main.outputLevel != 2) {
        return; //This message is only for verbose mode
    }
    System.out.println();
    System.out.println(”absscat initializing using input file ”
            + Main.inputFilename + ”.”);
}

/∗ The message displayed when absscat reads in a file (for example, a
 ∗ nk data file) if −verbose has been selected.
 ∗/
static void fileInputMessage(String fileName) {
    if(Main.outputLevel != 2) {
        return; //This message is only for verbose mode
    }
    System.out.println();
    System.out.println(”Reading in ” + fileName + ”.”);
}

/∗ Outputs an error if the interpolation line in the input file is either
 ∗ missing or incorrectly formatted.
 ∗/
```

```
static void interpolationFlagError() {
     System.out.println(”The line in the input file indicating if ” +
               ”interpolation is desired is either missing”);
     System.out.println(”or has not been set correctly to yes or no. ” +
               ”Exiting.”);
}

/∗ Outputs a verbose version of the finishing message, including the
 ∗ runtime of the program.
 ∗/
static void verboseFinish(double time) {
     System.out.println();
     System.out.println(”absscat has successfully outputted the scattering” +
               ” and absorption coefficients to”);
     System.out.println(Main.outputFilename + ”. Approximate run time: ” +
               String.format(”%.3G”, time) + ” seconds. Exiting.”);
}

/∗ Outputs the standard version of the finishing message if the default
 ∗ output level is selected, no message if −silent was selected, and
 ∗ calls on verboseFinish if −verbose was selected.
 ∗/
static void nonVerboseFinish(double time) {
     if (Main.outputLevel == 0) {
          return; //No non−error output is desired at this output level
     } else if (Main.outputLevel == 1) {
```

```
        System.out.println();
        System.out.println(”absscat has successfully outputted the ” +
                ”scattering and absorption coefficients to ”
                + Main.outputFilename + ”.”);
    } else {
        verboseFinish(time); //Call on the more verbose message
    }
}

/* Outputs an error if a line specifying the shape distribution was
 * incorrectly formatted.
 */
static void incorrectShape() {
    System.out.println();
    System.out.println(”The shape distribution specified must be one of” +
            ” spherical, CDE, CDS, or DHS. Exiting.”);
}

/* Outputs an error message if the size given for a single grain size
 * ’distribution’ is zero.
 */
static void zeroGrainSize() {
    System.out.println();
    System.out.println(”The grain size specified for a distribution of” +
            ” grains of a single size cannot be zero. Exiting.”);
}
```

```
/∗ Outputs an error message if the size given for a single grain size
 ∗ ’distribution’ is negative.
 ∗/
static void negativeGrainSize() {
    System.out.println();
    System.out.println(”The grain size specified for a distribution of ” +
            ”grains of a single size cannot be negative. Exiting.”);
}

/∗ Outputs an error message if the minimum grain size specified for a MRN
 ∗ or KMH grain size distribution is negative.
 ∗/
static void negativeMinGrainSize() {
    System.out.println();
    System.out.println(”The minimum grain size specified for a grain size” +
            ” distribution cannot be negative. Exiting.”);
}

/∗ Outputs an error message if the maximum grain size specified for a MRN
 ∗ grain size distribution is negative.
 ∗/
static void negativeMaxGrainSize() {
    System.out.println();
    System.out.println(”The maximum grain size specified for a grain size” +
            ” distribution cannot be negative. Exiting.”);
```

```
}

/* Outputs an error message if the maximum grain size specified for a MRN
 * distribution is zero.
 */
static void zeroMaxGrainSize() {
    System.out.println();
    System.out.println(”The maximum grain size specified for a grain size” +
            ” distribution cannot be zero. Exiting.”);
}

/* Outputs an error message if the falloff grain size specified for a KMH
 * grain size distribution is zero.
 */
static void zeroFalloffGrainSize() {
    System.out.println();
    System.out.println(”The exponential falloff size specified for a MRN” +
            ” grain size distribution cannot be zero. Exiting.”);
}

/* Outputs an error message if the falloff grain size specified for a KMH
 * grain size distribution is negative.
 */
static void negativeFalloffGrainSize() {
    System.out.println();
    System.out.println(”The exponential falloff size specified for a MRN” +
```

```
                ” grain size distribution cannot be negative. Exiting.”);
}

/∗ Outputs an error message if the minimum grain size specified for a MRN
 ∗ grain size distribution is larger than the maximum grain size specified
 ∗ for that distribution.
 ∗/
static void minMoreThanMax() {
    System.out.println();
    System.out.println(”The maximum grain size specified for a grain size” +
                ” distribution cannot be less than the minimum”);
    System.out.println(”grain size specified for that distribution. ” +
                ”Exiting.”);
}

/∗ Outputs an error message if the falloff grain size specified for a KMH
 ∗ grain size distribution is smaller than the minimum grain size
 ∗ specified for that distribution.
 ∗/
static void falloffLessThanMin() {
    System.out.println();
    System.out.println(”The falloff grain size specified for a MRN grain” +
                ” size distribution cannot be smaller than the”);
    System.out.println(”minimum grain specified for that distribution.” +
                ” Exiting.”);
}
```

```
/∗ Outputs an error message if absscat attempts to delete a file
 ∗ but is unable to.
 ∗/
static void unableToDelete(String fileName) {
    System.out.println();
    System.out.println(”The system was unable to delete ” + fileName +
            ” to prepare for new output. Please check the”);
    System.out.println(”permissions for this file. Exiting.”);
}

/∗ Outputs an error message if an output file absscat is trying to make
 ∗ already exists, but the −overwrite argument was not specified when
 ∗ absscat was called.
 ∗/
static void fileExistsNoOverwrite(String fileName) {
    System.out.println();
    System.out.println(”The output file ” + fileName + ” already exists,” +
            ” but the −overwrite flag was not specified.”);
    System.out.println(”Please either select a new file name using the” +
            ” −outputfile flag, or else select the −overwrite”);
    System.out.println(”flag if overwriting is desired. Exiting.”);
}

/∗ Outputs an error if some unknown error happens during the output of
 ∗ a file.
```

```
 */
static void unknownOutputError(String fileName) {
    System.out.println();
    System.out.println(”absscat encountered an unknown error while trying” +
            ”to output to ” + fileName + ”. Please check the”);
    System.out.println(”directory permissions for the working directory” +
            ”in which abscat is running.”);
}

/* Outputs an error if absscat was unable to write to a file */
static void writingError(String fileName) {
    System.out.println();
    System.out.println(”absscat was able to open ” + fileName + ” but was” +
            ”unable to write to it. Exiting.”);
}

/* Outputs an error if absscat was unable to close a file */
static void closeError(String fileName) {
    System.out.println();
    System.out.println(”absscat was unable to close ” +fileName+ ” after” +
            ” writing. Please check that no other instance of”);
    System.out.println(”abscat is running, and that this file is not open” +
            ”in any other program. Exiting.”);
}

/* Outputs a message if −verbose was given */
```

```
static void verboseActivated() {
    System.out.println();
    System.out.println(”Verbose mode active.”);
}

/* Outputs a status message for verbose mode */
static void verboseInterpolating(String wavelengthsFilename){
    if (Main.outputLevel == 2) {
        System.out.println();
        System.out.println(”Beginning interpolation using ” +
                wavelengthsFilename + ” as the new”);
        System.out.println(”wavelength grid.”);
    }
}

/* Outputs an error message if the number of n and k data file specified
 * in the input file does not match up with the number of parameter
 * blocks in that input file.
 */
static void wrongNumberOfNKFiles(int numberOfNKFiles,
        int parametersSpecified) {
    System.out.println();
    System.out.println(”The number of nk data files specified in ”
            + Main.inputFilename + ” does not correspond to the number of”);
    System.out.println(”parameters specified in ” + Main.inputFilename +
            ”. The number of nk data files specified was ” + numberOfNKFiles
```

```
            + ” but the”);
    System.out.println(”number of files corresponding to the given ” +
            ”parameters is ” + parametersSpecified + ”.”);
    System.out.println (”Please check that the number of nk data files ” +
            ”specified is correct, and if so that the”);
    System.out.println(”correct number of parameters has been specified in ” +
            ”the rest of the file. See the readme file”);
    System.out.println(”for further assistance. Exiting.”);
}

/∗ Outputs a message saying the output of the interpolated data files
 ∗ was selected.
 ∗/
static void outputInterpolation() {
    if (Main.outputLevel == 0) {

        /∗ Don’t output anytihing here when −silent is selected ∗/
        return;
    } else {
        System.out.println();
        System.out.println(”Output of interpolated nk data files ” +
                ”selected.”);
    }
}

/∗ Outputs a message saying only the output of the interpolated data files
```

```
 * was selected.
 */
static void onlyInterpolate() {
    if (Main.outputLevel == 0) {

        /* Don’t output anything here when −silent is selected */
        return;
    } else {
        System.out.println();
        System.out.println(”Output of only the interpolated nk data files” +
            ”selected.”);
    }
}

/* Outputs a message when an only interpolate run is finished */
static void onlyInterpolateExit() {
    if (Main.outputLevel == 0) {

        /* Don’t output anything here when −silent is selected */
        return;
    } else {
        System.out.println();
        System.out.println(”Interpolation of nk data files finished. The” +
                ” new interpolated nk data files have been”);
        System.out.println(”output to [nkdatafilename]_interp.dat. ” +
                ”Exiting.”);
```

```
    }
}

/* Outputs a message when a −outputinterpolation run has output the
 * interpolated data files.
 */
static void outputInterpolationFinished() {
    if (Main.outputLevel == 0) {

        /* Don't output anything here when − silent is selected */
        return;
    } else {
        System.out.println();
        System.out.println("Interpolation of nk data files finished. The" +
                " new interpolated nk data files have been");
        System.out.println("output to [nkdatafilename]_interp.dat. " +
                "Calculation of absorption and scattering");
        System.out.println("coefficients continuing.");

    }
}

/*Outputs an error message when either −outputinterpolation or
 * −only interpolation was selected but interpolation was not selected
 * in the specified input file.
 */
```

```
static void interpOptionsDontMatch() {
    System.out.println();
    System.out.println(”One of the command line arguments indicating that” +
            ” the interpolated nk data files should be”);
    System.out.println(”output was selected, but in ” + Main.inputFilename +
            ” the flag for interpolation was set for no.”);
    System.out.println(”Please either set this flag for yes and also ” +
            ”provide a wavelength grid to interpolate to,”);
    System.out.println(”or do no select the output of interpolated files” +
            ” when calling absscat. Exiting.”);
}

/∗ Outputs an error message if an unrecognized argument is given to
 ∗ absscat when it is called.
 ∗/
static void unrecognizedArgument(String argument) {
    System.out.println();
    System.out.println(”Argument ” + argument + ” is not recognized. ” +
            ”Please check the command line arguments for”);
    System.out.println(”errors. Exiting.”);
}

/∗ Outputs the specified precision for verbose mode ∗/
static void precisionSpecified() {
    if (Main.outputLevel != 2){
        return; //This message is only for verbose mode
```

```
    } else {
        System.out.println();
        System.out.println(”Output precision specified as ” + Main.precision
                + ”.”);
    }
}

/* Outputs the given input filename for verbose mode */
static void inputGiven() {
    if (Main.outputLevel != 2){
        return; //This message is only for verbose mode
    } else {
        System.out.println();
        System.out.println(”Input filename given as ” + Main.inputFilename +
                ”.”);
    }

}

/* Outputs the given output filename for verbose mode */
static void outputGiven() {
    if (Main.outputLevel != 2){
        return; //This message is only for verbose mode
    } else {
        System.out.println();
        System.out.println(”Output filename given as ” +
```

```
                    Main.outputFilename + ”.”);
     }
}

/∗ Deals with the case where both the −silent and −verbose flags were given.
 ∗ absscat will output this message and then continue as if only the
 ∗ −verbose flag had been given.
 ∗/
static void verboseSilent() {
    System.out.println();
    System.out.println(”Both the −silent and the −verbose flags were ” +
              ”given! absscat will assume −verbose was meant.”);
}

/∗ Indicates if overwrite mode is active for verbose mode ∗/
static void overwrite() {
     if (Main.outputLevel !=2){
          return; //This message is only for verbose mode
     } else {
          System.out.println();
          System.out.println(”Output file overwrite mode activated.”);
     }
}

/∗ Outputs the given epsilon for verbose mode ∗/
static void epsilonSpecified() {
```

```
    if (Main.outputLevel !=2){
        return; //This message is only for verbose mode
    } else {
        System.out.println();
        System.out.println(”Epsilon specified as ” + Main.epsilon + ”.”);
    }
}

/∗ Outputs a status message for verbose mode ∗/
static void parsingParameters() {
    if (Main.outputLevel !=2){
        return; //This message is only for verbose mode
    } else {
        System.out.println();
        System.out.println(”Parsing ” + Main.inputFilename + ”.”);
    }
}

/∗ Outputs a status message for verbose mode ∗/
static void beginningCalculations() {
    if (Main.outputLevel !=2){
        return; //This message is only for verbose mode
    } else {
        System.out.println();
        System.out.println(”Beginning to calculate the absorption” +
                ” and scattering coefficients.”);
```

```
    }
}

/∗ Outputs a status message for verbose mode ∗/
static void integrating(String size) {
    if (Main.outputLevel !=2) {
        return; //This message is only for verbose mode
    } else if (size.equals(”single”)){
        System.out.println();
        System.out.println(”Integrating over a single grain size.”);
    } else {
        System.out.println();
        System.out.println(”Integrating over the ” + size + ” grain size” +
                ” distribution.”);
    }
}

/∗ Outputs a status message for verbose mode ∗/
static void nonRTerms(String shape) {
    if (Main.outputLevel != 2) {
        return; //This message is only for verbose mode
    } else {
        System.out.println();
        System.out.println(”Calculating the non r−dependant terms for a ” +
                shape + ” grain shape distribution.”);
    }
```

```
    }
}
```

A.2 Supplementary material and examples

A.2.1 Readme file

absscat

Overview

absscat is a Java program that takes any number of data files, containing the wavelength-dependent n and k optical constants for a particular grain species, and combines them to produce the shape and size dependent absorption and scattering coefficients.

absscat requires the Java runtime environment; this is already installed on many systems, but if not it can be downloaded and installed from http://java.com/en/.

To call absscat, from the command line of your system:
java -jar absscat -inputfile [inputfilename] (optional arguments)

The only required argument is the -inputfile flag followed by the input filename, but several other optional arguments are also available (described below).

The input file requires elements in a specified order, though it ignores any comment lines indicated by starting with the # symbol and any lines not containing an = sign.

The first line contains the number of nk files that will be processed, and the second indicates if interpolation is desired. If interpolation is desired, the next line gives the filename for the wavelength grid the data will be interpolated to. Following this is a block of lines for each set of grain parameters; the first is the name of the n and k data file, the second is the desired grain shape distribution (spherical, CDE, CDS, or DHS - see below) to be used for that set, the third is the desired grain size distribution (single, MRN, or KMH - see below) to be used for that set. Next comes lines giving the parameters of the grain size distribution - in the case of a single grain size this is only one line giving the grain size, but for MRN it is three lines (the minimum grain size, the exponent, and the maximum grain size) and for KMH it is also three lines (the minimum grain size, the exponent, and the 'falloff' grain size). Finally, the final line in each set is the weighting factor to be used when combining all the sets into a single set of coefficients. After this, for each additional set of grain parameters the block repeats itself.

After absscat has calculated the absorption and scattering efficiencies for each block, it will combine them into a single set of absorption and scattering efficiencies through the use of a weighted average, with the weight given to each block specified by the weighting factor that is given on the last line of the block. The total weight is normalized (for example, if two blocks were given with weights of 1 and 4, the first block would be 1/5 of the total and the second would be 4/5 of the total).

Two example configuration files are provided for reference, example1.inp and example2.inp.

The supplied sets of n and k data should have three columns; the first column is the wavelength (any units, but the units must be the same for all n and k files to be used in that call of absscat), the second is the n data, and the third is the k data. The columns may be delimited, by any of tab, space, or comma. Additionally, the files are required to have the wavelengths in order either from largest to smallest or smallest to largest. If interpolation is desired, and the appropriate flag (on the second line of the input file) is selected as 'yes', then a file containing the wavelength grid it is desired to interpolate to must be supplied and that file name must be given in the input file. This file should have one column containing the wavelengths (of any units), in order from largest to smallest or from smallest to largest. absscat will perform a linear interpolation on the data files (and a linear extrapolation for regions where the new wavelength grid goes beyond the original) before performing the absorption and scattering calculations; if it is desired to obtain these interpolated files, one of -outputinterpolation or -onlyinterpolate can be given as command line arguments, as shown below. Note that if the n and k data files have different wavelength grids, then interpolation must be performed. If it is not selected, absscat will exit with an error message.

The default output filename generated by absscat is [inputfilename - extension]˙output.dat . However, there is an optional command line argument described below that can be used to specify the desired output filename. If a file with the output filename already exists, then absscat will display an error message and exit, not overwriting the file (unless this option is selected when absscat with the -overwrite argument, described below). The equations used in this program are based on theoretical work found in Min, M., Hovenier, J. W., and de Koter, A., Astronomy and Astrophysics, v. 404, p. 35-46, 2003.

Command Line Arguments

absscat may take any of the following command line arguments:

-inputfile [inputfilename]

Specifies the input file, as described above. If this is not provided, absscat will exit displaying an error message.

-outputfile [outputfilename]

Optionally specifies the output filename desired. If not provided, absscat will default to [inputfilename -extension]˙output.dat.

-overwrite

When absscat attempts to generate an output file, if that file already exists it will output an error message and exit without overwriting. If this argument is selected, then absscat will automatically overwrite any pre-existing file with the same name as the output file it is attempting to generate.

-outputinterpolation

If this argument is given, when absscat performs interpolation it will output the interpolated versions of the n and k data files it generated internally, as well as the output file. In order to select this argument, interpolation must have been selected in the input file and a wavelength grid to interpolate to must have also been provided.

-onlyinterpolate

Identical to -outputinterpolation, but does not generate the final absorption and scattering coefficients (that is, absscat will only calculate the interpolation, output the interpolated data files, and then exit without further output.

-silent

If this argument is given, then absscat will suppress all console output except for errors. If both -silent and -verbose are given, then absscat will assume -verbose was meant.

-verbose

If this argument is given, absscat will output additional console messages indicating the progress of the program through the required operations. If both -silent and -verbose are given, then absscat will assume -verbose was meant.

-epsilon [desired error bound for numerical integration]

In order to calculate values related to the MRN grain size distribution (used only when MRN is selected in one of the sets of grain parameters) absscat uses a numerical integration. The default value for the error bound is 1E-10, but if a different error bound is desired it can be specified using this argument. Larger values can make absscat take significantly longer to run.

-precision [desired precision of output]

If this argument is given, absscat will change the precision of the output values (which in this case means the number of digits after the decimal) to the desired value. The default value is 3. Note that this argument only affects the output; internally absscat always uses the maximum possible precision.

-help

Displays a help message describing the usage of absscat and these arguments.

A.2.2 Example configuration files

A.2.2.1 Example1.inp

This is an example of an input file for absscat. Any line not containing an equal sign, or one starting with a #, will be ignored. Also, the only thing absscat looks for is the value to the right of the equals sign; the descriptions to the left of the sign are simply for convenience and can be changed to anything. The case for parameters is also ignored, except for file names.

```
Number of nk files = 2
Interpolation Desired = no

First nk file = example1.nk
Desired shape distribution = spherical
Desired size distribution = MRN
MRN minimum grain size = 0.1
MRN q value = 3.5
MRN maximum grain size = 1
Weighting Factor = 0.5

Second nk file = example2.nk
Desired shape distribution = DHS
Desired size distribution = single
Single grain size = 0.1
Weighting Factor = 0.5
```

A.2.2.2 Example2.inp

This is a second example file to illustrate the usage of input files with absscat. In this file, interpolation to the wavelength grid found in wavelengths.example is selected.

Number of nk files = 2
Interpolation desired = yes
Interpolation wavelength grid = wavelengths.example

First nk file = example1.nk
Desired shape distribution = DHS
Desired size distribution = MRN
MRN minimum grain size = 0.1
MRN q value = 3.5
MRN maximum grain size = 1
Weighting factor = 0.5

Second nk file = example2.nk
Desired shape distribution = CDS
Desired size distribution = KMH
KMH minimum grain size = 0.1
KMH q value = 3.5
KMH falloff value = 1
Weighting factor = 0.6

This block has been commented out and won't be read by absscat

```
#Third nk file = example3.nk
#Desired shape distribution = CDE
#Desired size distribution = KMH
#KMH minimum grain size = 0.1
#KMH q value = 3.5
#KMH falloff value = 1
#Weighting factor = 0.3
```

Bibliography

Amedro, B., Bodnartchouk, V., Caromel, D., Delbe, C., Huet, F., & Taboada, G. 2008, Current State of Java for HPC, Technical Report RT-0353, INRIA

Andersen, A. C., Jäger, C., Mutschke, H., Braatz, A., Clément, D., Henning, T., Jørgensen, U. G., & Ott, U. 1999a, Astronomy and Astrophysics, 343, 933

Andersen, A. C., Loidl, R., & Höfner, S. 1999b, Astronomy and Astrophysics, 349, 243

Andersen, A. C., Mutschke, H., Posch, T., Min, M., & Tamanai, A. 2006, Journal of Quantitative Spectroscopy and Radiative Transfer, 100, 4

Aoki, W., Tsuji, T., & Ohnaka, K. 1999, Astronomy and Astrophysics, 350, 945

Bagnulo, S., Doyle, J. G., & Andretta, V. 1998, Monthly Notices of the Royal Astronomical Society, 296, 545

Bagnulo, S., Doyle, J. G., & Griffin, I. P. 1995, Astronomy and Astrophysics, 301, 501

Bagnulo, S., Skinner, C. J., Doyle, J. G., & Camphens, M. 1997, Astronomy and Astrophysics, 321, 605

Baron, Y., Papoular, R., Jourdain de Muizon, M., & Pegourie, B. 1987, Astronomy and Astrophysics, 186, 271

Begemann, B., Dorschner, J., Henning, T., Mutschke, H., & Thamm, E. 1994, Astrophysical Journal Letters, 423, L71

Bernatowicz, T., Fraundorf, G., Ming, T., Anders, E., Wopenka, B., Zinner, E., & Fraundorf, P. 1987, Nature, 330, 728

Bernatowicz, T. J., Akande, O. W., Croat, T. K., & Cowsik, R. 2005, Astrophysical Journal, 631, 988

Bernatowicz, T. J., Croat, T. K., & Daulton, T. L. 2006, Origin and Evolution of Carbonaceous Presolar Grains in Stellar Environments, ed. Lauretta, D. S. & McSween, H. Y., Jr., 109–126

Berreman, D. W. 1963, Physical Review, 130, 2193

Berzelius, J. J. 1824, Annalen der Physick, B77:209

Bevington, P. R. 1969, Data reduction and error analysis for the physical sciences, ed. Bevington, P. R.

Bohren, C., & Huffman, D. 1983, Absorption and Scattering of Light by Small Particles, 1st edn. (New York: Wiley)

Borghese, F., Denti, P., & Saija, R. 1994, Applied Optics, 33, 484

Borghese, F., Denti, P., Saija, R., & Sindoni, O. I. 1992, Journal of the Optical Society of America A, 9, 1327

Borghesi, A., Bussoletti, E., Colangeli, L., & de Blasi, C. 1985, Astronomy and Astrophysics, 153, 1

Bowey, J. E., Lee, C., Tucker, C., Hofmeister, A. M., Ade, P. A. R., & Barlow, M. J. 2001, Monthly Notices of the Royal Astronomical Society, 325, 886

Burns, G. 1990, Solid State Physics (San Diego: Academic Press), 810

Carroll, B. W., & Ostlie, D. A. 1996, An Introduction to Modern Astrophysics (New York: Addison-Wesley)

Chan, S. J., & Kwok, S. 1990, Astronomy and Astrophysics, 237, 354

Chandrasekhar, S. 1950, Radiative Transfer (Oxford: Clarendon Press)

Cherchneff, I. 2006, Astronomy and Astrophysics, 456, 1001

Chigai, T., & Yamamoto, T. 2003, Geochimica et Cosmochimica Acta, 67, 64

Clayton, D. D., & Nittler, L. R. 2004, Annual Review of Astronomy and Astrophysics, 42, 39

Clément, D., Mutschke, H., Klein, R., & Henning, T. 2003, Astrophysical Journal, 594, 642

Clément, D., Mutschke, H., Klein, R., Jäger, C., Dorschner, J., Sturm, E., & Henning, T. 2005, Astrophysical Journal, 621, 985

Clube, K. L., & Gledhill, T. M. 2004, Monthly Notices of the Royal Astronomical Society, 355, L17

Cohen, M. 1984, Monthly Notices of the Royal Astronomical Society, 206, 137

Comelli, G., Stöhr, J., Robinson, C. J., & Jark, W. 1988, Physical Review B, 38, 7511

Daulton, T. L., Bernatowicz, T. J., Lewis, R. S., Messenger, S., Stadermann, F. J., & Amari, S. 2002, Science, 296, 1852

—. 2003, Geochimica et Cosmochimica Acta, 67, 4743

de Graauw, T., et al. 1996, Astronomy and Astrophysics, 315, L49

DePew, K., Speck, A., & Dijkstra, C. 2006, Astrophysical Journal, 640, 971

Dijkstra, C., & Speck, A. K. 2006, Astrophysical Journal, 651, 288

Dijkstra, C., Speck, A. K., Reid, R. B., & Abraham, P. 2005, Astrophysical Journal Letters, 633, L133

Dominik, C., Gail, H., & Sedlmayr, E. 1989, Astronomy and Astrophysics, 223, 227

Dorschner, J., Friedemann, C., & Guertler, J. 1977, Astronomische Nachrichten, 298, 279

Draine, B. T., & Lee, H. M. 1984, Astrophysical Journal, 285, 89

Fahrenfort, J. 1961, Spectrochimica Acta, 17, 698

Feldman, D. W., Parker, J. H., Choyke, W. J., & Patrick, L. 1968, Physical Review, 173, 787

Fontaine, G., Brassard, P., & Bergeron, P. 2001, Publications of the Astronomical Society of the Pacific, 113, 409

Forrest, W. J., Gillett, F. C., & Stein, W. A. 1975, Astrophysical Journal, 195, 423

Forrest, W. J., Houck, J. R., & McCarthy, J. F. 1981, Astrophysical Journal, 248, 195

Freedman, R., & Kaufmann, W. 2005, Universe, 7th edn. (New York: W. H. Freeman and Company)

Friedemann, C. 1969, Physica, 41, 139

Friedemann, C., Guertler, J., Schmidt, R., & Dorschner, J. 1981, Astrophysics and Space Science, 79, 405

Gaines, R. V., Skinner, H. C., Mason, E. E., & Rosenzweig, A. 1997, Dana's New Mineralogy (John Wiley & Sons, Inc.)

Gauba, G., & Parthasarathy, M. 2004, Astronomy and Astrophysics, 417, 201

Giesting, P. A., & Hofmeister, A. M. 2002, Physical Review B, 65, 144305

Gilman, R. C. 1969, Astrophysical Journal Letters, 155, L185+

Goebel, J. H., Cheeseman, P., & Gerbault, F. 1995, Astrophysical Journal, 449, 246

Goebel, J. H., & Moseley, S. H. 1985, Astrophysical Journal Letters, 290, L35

Goldberg, Y., Levinshtein, M. E., & Rumyantsev, S. L. 2001, Properties of Advanced Semiconductor Materials, ed. M. E. Levinshtein, S. L. Rumyantsev, & M. S. Shur (New York: Wiley), 93

Goncharenko, A. V., Venger, E. F., & Vlaskina, S. I. 1996, Institute of Physics Conference Series, 142, 369

Griffin, I. P. 1990, Monthly Notices of the Royal Astronomical Society, 247, 591

—. 1993, Monthly Notices of the Royal Astronomical Society, 260, 831

Groenewegen, M. A. T. 1994, Astronomy and Astrophysics, 290, 207

—. 1995, Astronomy and Astrophysics, 293, 463

Groenewegen, M. A. T., Baas, F., Blommaert, J. A. D. L., Stehle, R., Josselin, E., & Tilanus, R. P. J. 1999, Annual Review of Astronomy & Astrophysics, 140, 197

Groenewegen, M. A. T., Oudmaijer, R. D., Goudfrooij, P., van den Hoek, L. B., & van Kerkwijk, M. H. 1996, Astronomy and Astrophysics, 305, 475

Groenewegen, M. A. T., Sevenster, M., Spoon, H. W. W., & Pérez, I. 2002, Astronomy and Astrophysics, 390, 511

Groenewegen, M. A. T., Whitelock, P. A., Smith, C. H., & Kerschbaum, F. 1997, Astrophysics and Space Science, 251, 89

—. 1998, Monthly Notices of the Royal Astronomical Society, 293, 18

Hackwell, J. A. 1972, Astronomy and Astrophysics, 21, 239

Hanner, M. 1988, Grain optical properties, Tech. rep.

Henning, T. 2003, in Solid State Astrochemistry, ed. V. Pirronello, J. Krelowski, & G. Manicò, 85–103

Hoare, M. G. 1990, Monthly Notices of the Royal Astronomical Society, 244, 193

Hofmann, M., Zywietz, A., Karch, K., & Bechstedt, F. 1994, Physical Review B, 50, 13401

Hofmeister, A. M., Keppel, E., & Speck, A. K. 2003, Monthly Notices of the Royal Astronomical Society, 345, 16

Hony, S., Tielens, A. G. G. M., Waters, L. B. F. M., & de Koter, A. 2003, Astronomy and Astrophysics, 402, 211

Hony, S., Waters, L. B. F. M., & Tielens, A. G. G. M. 2002, Astronomy and Astrophysics, 390, 533

Hoppe, P., & Ott, U. 1997, in American Institute of Physics Conference Series, Vol. 402, American Institute of Physics Conference Series, ed. E. K. Zinner & T. J. Bernatowicz, 27–58

Huang, K. 1987, Statistical Mechanics, 2nd edn. (Wiley)

Huffman, D. R. 1988, in Astrophysics and Space Science Library, Vol. 149, Experiments on Cosmic Dust Analogues, ed. E. Bussoletti, C. Fusco, & G. Longo, 25–+

Iatì, M. A., Cecchi-Pestellini, C., Williams, D. A., Borghese, F., Denti, P., Saija, R., & Aiello, S. 2001, Monthly Notices of the Royal Astronomical Society, 322, 749

Il'in, M. A., Kukharskii, A. A., Rashevskaya, E. P., & Subashiev, V. K. 1972, Soviet Physics - Solid State, 13, 2078

Ivezic, Z., & Elitzur, M. 1995, Astrophysical Journal, 445, 415

—. 1997, Monthly Notices of the Royal Astronomical Society, 287, 799

Jackson, J. D. 1975, Classical electrodynamics, ed. Jackson, J. D.

Jiang, B. W., Zhang, K., & Li, A. 2005, Astrophysical Journal Letters, 630, L77

Jones, A. P. 1988, Monthly Notices of the Royal Astronomical Society, 234, 209

Jones, B., Merrill, K. M., Puetter, R. C., & Willner, S. P. 1978, Astronomical Journal, 83, 1437

Jørgensen, U. G., Hron, J., & Loidl, R. 2000, Astronomy and Astrophysics, 356, 253

Jura, M. 1994, Astrophysical Journal, 434, 713

Jura, M., Turner, J. L., Van Dyk, S., & Knapp, G. R. 2000, Astrophysical Journal Letters, 528, L105

Kelires, P. C. 1993, Physical Review B, 47, 1829

Kerker, M., Scheiner, P., & Cooke, D. D. 1978, Journal of the Optical Society of America, 68, 135

Kessler, M. F., et al. 1996, Astronomy and Astrophysics, 315, L27

Kholopov, P. N., et al. 1998, in Combined General Catalogue of Variable Stars, 4.1 Ed (II/214A). (1998), 0–+

Kim, S., Martin, P. G., & Hendry, P. D. 1994, Astrophysical Journal, 422, 164

Kohn, M., & Spear, F. S. 1991, American Mineralogist, 76, 128

Kwok, S. 2000, Origin and Evolution of Planetary Nebulae (Cambridge: Cambridge University Press)

Kwok, S. 2004, Nature, 430, 985

Lagadec, E., & Zijlstra, A. A. 2008, Monthly Notices of the Royal Astronomical Society, 390, L59

Lagadec, E., et al. 2007, Monthly Notices of the Royal Astronomical Society, 376, 1270

Lambert, D. L., Gustafsson, B., Eriksson, K., & Hinkle, K. H. 1986, Astrophysical Journal Suppliment Series, 62, 373

Lamers, H., & Cassinelli, J. 1999, Introduction to Stellar Winds (Cambridge: Cambridge University Press)

Laor, A., & Draine, B. T. 1993, Astrophysical Journal, 402, 441

Lee, O. J., Baldwin, R. B., Hamlin, D. W., & Kinnaird, R. F. 1943, Annals of the Dearborn Observatory, 4, 133

Leech, K., e. a. 2003 (Noordwijk: ESA)

Leisenring, J. M., Kemper, F., & Sloan, G. C. 2008, Astrophysical Journal, 681, 1557

LeVan, P. D., & Sloan, G. 1989, Publications of the Astronomical Society of the Pacific, 101, 1140

Levinshtein, M. E., Rumyantsev, S. L., & Shur, M. S., eds. 2001, Properties of Advanced Semiconductor Materials (New York: Wiley)

Li, A. 2005, Astrophysical Journal, 622, 965

Lipson, H. 1960 (New York: Pergamon Press), 371–375

Liu, Z., Xu, J., Scott, H. P., Williams, Q., Mao, H., & Hemley, R. J. 2004, Review of Scientific Instruments, 75, 5026

Lodders, K., & Fegley, Jr., B. 1995, Meteoritics, 30, 661

Lodders, K., & Fegley, Jr., B. 1999, in IAU Symposium, Vol. 191, Asymptotic Giant Branch Stars, ed. T. Le Bertre, A. Lebre, & C. Waelkens, 279–+

Lorenz-Martins, S., de Araújo, F. X., Codina Landaberry, S. J., de Almeida, W. G., & de Nader, R. V. 2001, Astronomy and Astrophysics, 367, 189

Lorenz-Martins, S., & Lefevre, J. 1993, Astronomy and Astrophysics, 280, 567

—. 1994, Astronomy and Astrophysics, 291, 831

Loup, C., Forveille, T., Omont, A., & Paul, J. F. 1993, Astronomy and Astrophysics Suppliment Series, 99, 291

Lunttila, T., & Juvela, M. 2007, Astronomy and Astrophysics, 470, 259

Lynch, D. K., & Mazuk, S. 1999, Applied Optics, 38, 5229

Martin, P. G., & Rogers, C. 1987, Astrophysical Journal, 322, 374

Mathews, J. H., & Fink, K. D. 1999, Numerical methods using MATLAB, 3rd edn. (Upper Saddle River, New Jersey: Prentice-Hall)

Mathis, J. S. 1996, Astrophysical Journal, 472, 643

Mathis, J. S., Rumpl, W., & Nordsieck, K. H. 1977, Astrophysical Journal, 217, 425

Matsuura, M., et al. 2005, Astronomy and Astrophysics, 434, 691

McKenna, L. W., & Hodges, K. V. 1988, American Mineralogist, 73, 1205

Meixner, M., Ueta, T., Bobrowsky, M., & Speck, A. 2002, Astrophysical Journal, 571, 936

Meixner, M., Zalucha, A., Ueta, T., Fong, D., & Justtanont, K. 2004, Astrophysical Journal, 614, 371

Meixner, M., et al. 1999, Astrophysical Journal Suppliment Series, 122, 221

Min, M., Hovenier, J. W., & de Koter, A. 2003, Astronomy and Astrophysics, 404, 35

Mitra, S. S., Brafman, O., Daniels, W. B., & Crawford, R. K. 1969, Physical Review, 186, 942

Moissan, H. 1904, Comptes rendus hebdomadaires des séances de l'Académie des Sciences, 139, 773

Molster, F. J. 2000, PhD thesis, FNWI: Sterrenkundig Instituut Anton Pannekoek, Postbus 19268, 1000 GG Amsterdam, The Netherlands

Mutschke, H., Andersen, A. C., Clément, D., Henning, T., & Peiter, G. 1999, Astronomy and Astrophysics, 345, 187

Nenkova, M., Ivezić, Ž., & Elitzur, M. 2000, Thermal Emission Spectroscopy and Analysis of Dust, Disks, and Regoliths, 196, 77

Neugebauer, G., et al. 1984, Science, 224, 14

Noguchi, K., Kawara, K., Kobayashi, Y., Okuda, H., Sato, S., & Oishi, M. 1981, Publications of the Astronomical Society of Japan, 33, 373

Nuth, J. A., Moseley, S. H., Silverberg, R. F., Goebel, J. H., & Moore, W. J. 1985, Astrophysical Journal Letters, 290, L41

O'Connor, J. R., & Smiltens, J., eds. 1960, Silicon Carbide A High Temperature Semiconductor (New York: Pergamon Press)

Olofsson, H., Eriksson, K., Gustafsson, B., & Carlstroem, U. 1993a, Astrophysical Journal Suppliment Series, 87, 305

Olofsson, H., Eriksson, K., Gustafsson, B., & Carlstrom, U. 1993b, Astrophysical Journal Suppliment Series, 87, 267

Omont, A., Loup, C., Forveille, T., Te Lintel Hekkert, P., Habing, H., & Sivagnanam, P. 1993, Astronomy and Astrophysics, 267, 515

Omont, A., et al. 1995, Astrophysical Journal, 454, 819

Orofino, V., Blanco, A., Mennella, V., Bussoletti, E., Colangeli, L., & Fonti, S. 1991, Astronomy and Astrophysics, 252, 315

Papoular, R., Cauchetier, M., Begin, S., & Lecaer, G. 1998, Astronomy and Astrophysics, 329, 1035

Patrick, L. 1968, Physical Review, 167, 809

Pègourié, B. 1988, Astronomy and Astrophysics, 194, 335

Philipp, H. R., & Taft, E. A. 1960 (New York: Pergamon Press), 366–370

Pitman, K. M., Hofmeister, A. M., Corman, A. B., & Speck, A. K. 2008, Astronomy and Astrophysics, 483, 661

Pitman, K. M., Speck, A. K., & Hofmeister, A. M. 2006, Monthly Notices of the Royal Astronomical Society, 371, 1744

Roessler, D. M. 1965, British Journal of Applied Physics, 16, 1359

Rouleau, F., & Martin, P. G. 1991, Astrophysical Journal, 377, 526

Rowan-Robinson, M., & Harris, S. 1982, Monthly Notices of the Royal Astronomical Society, 200, 197

—. 1983a, Monthly Notices of the Royal Astronomical Society, 202, 797

—. 1983b, Monthly Notices of the Royal Astronomical Society, 202, 767

Saada, D. 2000, PhD thesis, Israel Institute of Technology

Saddow, S., & Agarwal, A. 2004, Advances in Silicon Carbide Processing and Applications; electronic version (Norwood: Artech House)

Sahai, R. 2004, in Astronomical Society of the Pacific Conference Series, Vol. 313, Asymmetrical Planetary Nebulae III: Winds, Structure and the Thunderbird, ed. M. Meixner, J. H. Kastner, B. Balick, & N. Soker, 141–+

Schaffer, P. T. B., & Naum, R. 1969, Journal of the Optical Society of America, 59, 1498

Shaffer, P. T. B. 1971, Applied Optics, 10, 1034

Sharp, C. M., & Wasserburg, G. J. 1995, Geochimica et Cosmochimica Acta, 59, 1633

Skinner, C. J., Meixner, M., & Bobrowsky, M. 1998, Monthly Notices of the Royal Astronomical Society, 300, L29

Skinner, C. J., et al. 1997, Astronomy and Astrophysics, 328, 290

Skrutskie, M. F., Reber, T. J., Murphy, N. W., & Weinberg, M. D. 2001, in Bulletin of the American Astronomical Society, Vol. 33, Bulletin of the American Astronomical Society, 1437–+

Sloan, G. C., Kraemer, K. E., Matsuura, M., Wood, P. R., Price, S. D., & Egan, M. P. 2006, Astrophysical Journal, 645, 1118

Sloan, G. C., Little-Marenin, I. R., & Price, S. D. 1998, Astronomical Journal, 115, 809

Soker, N., & Subag, E. 2005, Astronomical Journal, 130, 2717

Speck, A. K. 1998, PhD thesis, University College London

Speck, A. K., Barlow, M. J., & Skinner, C. J. 1997, Monthly Notices of the Royal Astronomical Society, 288, 431

Speck, A. K., Barlow, M. J., Sylvester, R. J., & Hofmeister, A. M. 2000, Astronomy and Astrophysics Supplement, 146, 437

Speck, A. K., Cami, J., Markwick-Kemper, C., Leisenring, J., Szczerba, R., Dijkstra, C., Van Dyk, S., & Meixner, M. 2006, Astrophysical Journal, 650, 892

Speck, A. K., Corman, A. B., Wakeman, K., Wheeler, C. H., & Thompson, G. 2009, Astrophysical Journal, 691, 1202

Speck, A. K., & Hofmeister, A. M. 2004, Astrophysical Journal, 600, 986

Speck, A. K., Hofmeister, A. M., & Barlow, M. J. 1999, Astrophysical Journal Letters, 513, L87

Speck, A. K., Thompson, G. D., & Hofmeister, A. M. 2005, Astrophysical Journal, 634, 426

Spitzer, W. G., Kleinman, D., & Walsh, D. 1959a, Physical Review, 113, 127

Spitzer, W. G., Kleinman, D. A., & Frosch, C. J. 1959b, Physical Review, 113, 133

Spitzer, W. G., Kleinman, D. A., Frosch, C. J., & Walsh, D. J. 1960 (New York: Pergamon Press), 347–365

Szczerba, R., Omont, A., Volk, K., Cox, P., & Kwok, S. 1997, Astronomy and Astrophysics, 317, 859

Tanaka, K. K., Tanaka, H., & Nakazawa, K. 2000, in Lunar and Planetary Institute Science Conference Abstracts, Vol. 31, Lunar and Planetary Institute Science Conference Abstracts, 1408–+

Taylor, A., & Jones, R. M. 1960 (New York: Pergamon Press), 147–154

Thomas, G. B., & Finney, R. 1996, Calculus, 9th edn. (New York: Addison-Wesley)

Thompson, G. D., Corman, A. B., Speck, A. K., & Dijkstra, C. 2006, Astrophysical Journal, 652, 1654

Treffers, R., & Cohen, M. 1974, Astrophysical Journal, 188, 545

van de Hulst, H. 1957, Light Scattering by Small Particles (New York: Wiley) van der Veen, W. E. C. J., & Habing, H. J. 1988, Astronomy and Astrophysics, 194, 125

Vassiliadis, E., & Wood, P. R. 1993, Astrophysical Journal, 413, 641

Villaver, E., García-Segura, G., & Manchado, A. 2002a, Astrophysical Journal, 571, 880

Villaver, E., Manchado, A., & García-Segura, G. 2002b, Astrophysical Journal, 581, 1204

Virag, A., Wopenka, B., Amari, S., Zinner, E., Anders, E., & Lewis, R. S. 1992, Geochimica et Cosmochimica Acta, 56, 1715

Volk, K., Kwok, S., & Langill, P. P. 1992, Astrophysical Journal, 391, 285

Volk, K., Kwok, S., Stencel, R. E., & Brugel, E. 1991, Astrophysical Journal Supplement, 77, 607

Volk, K., Xiong, G., & Kwok, S. 2000, Astrophysical Journal, 530, 408

Waelkens, C., & Waters, L. B. F. M. 1999, in IAU Symposium, Vol. 191, Asymptotic Giant Branch Stars, ed. T. Le Bertre, A. Lebre, & C. Waelkens, 519

Whittet, D. C. B., Duley, W. W., & Martin, P. G. 1990, Monthly Notices of the Royal Astronomical Society, 244, 427

Willacy, K., & Cherchneff, I. 1998, Astronomy and Astrophysics, 330, 676

Willems, F. J. 1988, Astronomy and Astrophysics, 203, 51

Woitke, P. 2006, Astronomy and Astrophysics, 452, 537

Yang, X., Chen, P., & He, J. 2004, Astronomy and Astrophysics, 414, 1049

Zijlstra, A. A., et al. 2006, Monthly Notices of the Royal Astronomical Society, 370, 1961

Zorba, T. 1996, Applied Surface Science, 102, 120

VITA

Adrian Burgin Corman was born on October 13, 1979 in Meridian, Mississippi. His parents are Andrew and Beverly Roche of Summerville, South Carolina. Adrian attended the College of Charleston in Charleston, South Carolina and graduated with bachelors degrees in physics and mathematics in May of 2001. He earned his master's degree in physics at the University of Missouri in 2005 with Dr. Sergei Kopeikin, and then went on to work with Dr. Angela Speck for his doctorate in physics, conducting astronomical research. Adrian is going on to a postdoctoral position with Dr. Anne Hofmeister at Washington University in St. Louis, Missouri.